Primitive melt recharge, and magma-mush mixing in the weeks and months preceding the 2005-06 eruption, EPR, 9˚46'N-9˚56'N

by

Aerona Moore
B.Sc., University of St Andrews, 2010

A Thesis Submitted in Partial Fulfilment
of the Requirements for the Degree of

MASTER OF SCIENCE

in the School of Earth and Ocean Sciences

© Aerona Moore, 2013
University of Victoria
All rights reserved. This thesis may not be reproduced in whole or in part, by photocopy
or other means, without the permission of the author.

Supervisory Committee

Primitive melt recharge, and magma-mush mixing in the weeks and months preceding the 2005-06 eruption, EPR, 9˚46'N-9˚56'N

by

Aerona Moore
B.Sc., University of St Andrews, 2010

Supervisory Committee

Dr. Laurence Coogan (School of Earth and Ocean Sciences)
Supervisor

Dr. Kathryn Gillis (School of Earth and Ocean Sciences)
Departmental Member

Dr. Dante Canil (School of Earth and Ocean Sciences)
Departmental Member

Abstract

Supervisory Committee

Dr. Laurence Coogan (School of Earth and Ocean Sciences)
Supervisor

Dr. Kathryn Gillis (School of Earth and Ocean Sciences)
Departmental Member

Dr. Dante Canil (School of Earth and Ocean Sciences)
Departmental Member

At fast spreading ridges such as the East Pacific Rise (EPR) volcanic eruptions are predicted to occur on a decadal timescale. Due to the limited ability to observe submarine eruptions, little is known about the magmatic processes occurring in the underlying magma chamber leading up to a volcanic event, including differentiation and magma mixing. The recent 2005-06 eruption at 9˚46'N-9˚56'N along the EPR provides a unique opportunity to gain a better understanding of rates of magma transport and magma replenishment associated with a typical eruption. This study examines the geochemistry of phenocrysts from the 2005-06 eruption in order to determine if they are in equilibrium with their host melt, or if magma mixing occurred prior to eruption. A diffusion model is used to model those crystals which are out of equilibrium with their erupted host to determine timescales of magma mixing. The major and trace element contents of plagioclase and olivine phenocrysts provides evidence for melts both more evolved (> 3.5 wt % MgO) and more primitive (< 8.8 wt % MgO) than those found within the host lava (7.7-8.3 wt % MgO; Goss et al., 2010). Glomerocrysts and resorbed crystals in equilibrium with evolved melts (3.5-6.5 wt % MgO) suggests an origin in a roof mush zone, and were disrupted and entrained into their host melt within days of eruption.

Modelling of the zoning profiles of phenocrysts suggest the 2005-06 eruption was likely triggered by an influx of hotter, more primitive melt (~ 9.0 wt % MgO) which was injected into the melt lens a few weeks to months prior to the eruption. With decreasing time before eruption, there is an overall increase in the number of crystals with modelled timescales representing mixing events in the magma chamber. This increase in modelled timescales appears to correlate with the increase in seismic activity recorded prior to the eruption (Tolstoy et al., 2006). This suggests magma mixing events within the underlying magma chamber may be linked to seismic activity at fast spreading ridges.

Table of Contents

Supervisory Committee.....ii
Abstract.....iii
Table of Contents.....v
List of Tables.....x
List of Figures.....xi
Acknowledgments.....xiii
Dedication.....xiv

Chapter 1: Introduction to the geology of the East Pacific Rise mid-ocean ridge 1
1.1 Introduction to mid-ocean ridges.....1
1.1.1 Magma chambers and magma accretion at fast spreading ridges.....3
1.1.2 Mid-ocean ridge basalt differentiation.....5
1.2 Geology and structure of the EPR between 9º and 10ºN.....7
1.2.1 Location and structure.....7
1.2.2 Size and depth of the magma chamber in the 9-10ºN region.....8
1.2.3 Documented volcanic eruptions in the past two decades.....11
1.2.4 The 1991-1992 Volcanic Eruption, 9º46'-9º51'N.....13
1.2.4.1 Geochemistry and Petrology of the 1991-92 eruption.....13
1.2.5 The 2005-2006 Volcanic Eruption, 9º46'-9º56'N.....14
1.2.5.1 Pre- and syn-eruption induced seismicity 14
1.2.5.2 Eruption dynamics and morphology.....14
1.2.5.3 Petrology and Geochemistry of lavas from the 2005-2006 eruption.....16
1.2.5.4 Petrogenesis of the 2005-06 lavas.....17
1.3 Aims and approach of this study 18

Chapter 2: Primitive melt recharge, and magma-mush mixing in the weeks and months preceding the 2005-06 eruption, EPR, 9˚46'N-9˚56'N.....20
2.1 Introduction.....20

2.2 Analytical Techniques..... 20
2.2.1 Electron microprobe analysis (EMP).....21
2.2.2 Laser ablation inductively coupled plasma mass spectrometry (LA-ICP-MS) 22
2.3 Petrology of samples from the 2005-06 eruption.....24
2.4 Parameters for calculating equilibrium plagioclase and olivine compositions. 27
2.4.1 Melt compositions of 2005-06 lavas.....28
2.4.2 Parameters controlling partition coefficients in plagioclase and olivine.....29
2.4.2.1 Calculating melt temperatures 29
2.4.2.2 Equilibrium plagioclase anorthite content 30
2.4.2.3 Defining Mg, Sr, and K partition coefficients in plagioclase.....31
2.4.2.4 Partition coefficients of Fe-Mg, Mn, Ni, and Cr in olivine.....37
2.5 Compositional zoning profiles and equilibrium melt concentrations in plagioclase and olivine. 39
2.5.1 Evidence of intra- and inter- crystalline disequilibria seen through plagioclase An, Mg, Sr, and K content 40
2.5.1.1 Disequilibria observed in plagioclase An contents..... 40
2.5.1.2 Disequilibria observed in plagioclase Mg, Sr, and K contents.....48
2.5.1.2.1 *EUHEDRAL PLAGIOCLASE*..... 50
2.5.1.2.2 *RESORBED PLAGIOCLASE*.....52
2.5.1.2.3 *GLOMEROCRYSTS*..... 53
2.5.2 Evidence of intra- and inter- crystalline disequilibria seen through measured concentrations of Fo, Mn, Ni, and Cr within olivine 55
2.6 Diffusion modelling to determine timescales of magma mixing processes.....58
2.6.1 Diffusion modelling in plagioclase..... 58
2.6.1.1 Parameters used for diffusion modelling in plagioclase.....58
2.6.1.2 Diffusion models used and uncertainties..... 60
2.6.2 Results of diffusion modelling in plagioclase.....61
2.6.2.1 Euhedral plagioclase..... 61
2.6.2.2 Resorbed plagioclase..... 70

2.6.2.2.1 *SOUTHERN FISSURE*.....70
2.6.2.2.2 *BULL'S EYE AND NORTHERN FISSURE*.....75
2.6.3 Parameters used for diffusion modelling in olivine.....76
2.6.3.1 Diffusion modelling in euhedral olivine 77
2.6.4 Diffusion modelling in plagioclase and olivine from the Southern Fissure glomerocryst 79
2.6.4.1 A model to explain the elemental zoning observed in the glomerocryst . .79
2.6.4.2 Modelled timescales from plagioclase and olivine in the glomerocryst from the Southern Fissure.....84
2.7 Discussion.....94
2.7.1 Petrogenetic Model.....94
2.7.2 Comparison of modelled timescales to previous work.....98
2.7.2.1 Comparison of timescales with seismic data from Tolstoy et al. (2006)…98
2.7.2.2 Comparisons between the timescales derived from previous diffusion modelling studies in oceanic basalts.....100
2.7.3 Broader implications 101

Chapter 3.0 Conclusions and Future Work.....103
3.1 Conclusions.....103
3.2 Future Work.....103

References.....106

Appendix.....124
Appendix A.1: Analytical Techniques, Precision and Accuracy.....124
A.1.1: Electron microprobe analysis (EMP).....124
A.1.2: Accuracy and precision of data.....125
A.1.2.1: Precision of LA-ICP-MS data.....125
A.1.2.1.1: Precision within an analytical session.....125

A.1.2.1.2: Precision between analytical sessions.....126
A.1.2.2: Comparison of data from different sources.....127
A.1.2.2.1: EMP versus LA-ICP-MS..... 127
A.1.2.2.2: Singapore EMP data compared to Barcelona EMP data.....129
A.1.2.2.3: LA-ICP-MS multiple isotope comparison in olivine.....131
A.1.2.2.4: Analysed glass data compared to values published in Goss et al. (2010) 131
A.1.3: Differences in calculated melt temperatures 135
Appendix A.2: Major and trace element data 137
Appendix A.3: Sample locations, petrography and techniques used on each sample.....137
Appendix A.4: Errors in partition coefficients and diffusion models.....139
A.4.1: Error of the plagioclase-melt partition coefficients.....139
A.4.2: Calculating the misfit between a diffusion model and analysed data.....140
Appendix A.5: Photomicrographs of plagioclase and olivine, and elemental zoning profiles.....140
A.5.1: Northern Fissure.....140
A.5.1.1: Sample 4204_9.....140
A.5.1.2: Sample 4204_8.....144
A.5.2: Bull's eye.....147
A.5.2.1: Sample 4206_2.....147
A.5.2.2: Sample 4202_1.....151
A.5.2.3: Sample 4203_2.....155
A.5.2.4: Sample 4202_6.....164
A.5.3: Southern Fissure.....165
A.5.3.1: Sample 4205_5.....165
A.5.3.2: Sample 4205_5.....178
Appendix A.6: Explanations and examples of diffusion models. 181
A.6.1: A 1D diffusion model.....181
A.6.1.1: Plagioclase.....182

A.6.1.2: Olivine.....188
A.6.2: A 2D diffusion model: Plagioclase..... 193
A.6.3: A 1D diffusion plus crystal growth model: Plagioclase.....200

List of Tables

Table 1: A summary of the number and location of plagioclase crystals with cores, rims, or the entire crystal with MgO, Sr or K contents out of equilibrium with its host melt.....49

Table A.1: Details of analytical conditions for plagioclase and olivine analysed at (a) the University of Barcelona, (b) the Earth Observatory of Singapore, and (c) the University of British Columbia.....124

Table A.2: Details of analytical conditions used for elemental maps of olivine and plagioclase obtained on the EMP at the Earth Observatory of Singapore.....125

Table A.3: Precision of analysed elements for NIST 611, 613, and 615 within each analytical session.....126

Table A.4: Precision of Sr, K, and Ba within synthetic plagioclase glasses and natural plagioclase crystals.....127

Table A.5: Concentrations of MgO, Sr, K, MnO, NiO, and Cr in the lavas from the 2005-06 eruption analysed by LA-ICP-MS and taken from bulk glass data in Goss et al. (2010).....134

Table A.6: Locations of each sample from the 2005-06 eruption, petrographic phase abundances in each sample, and analytical techniques performed.....138

List of Figures

Figure 1: Location map of the 9-10°N region of the East Pacific Rise (EPR).....2
Figure 2: Magma chamber and crustal accretion models at fast spreading ridges.....4
Figure 3: Cross-sectional views through the EPR ridge between 9°'N and 9°58'N.....10
Figure 4: Bathymetric map of the 9°46'N-9°56'N region of the EPR showing the location of the 2005-06 eruption.....12
Figure 5: Plot of the number of seismic events recorded per day up to three years prior to the 2005-06 eruption.....15
Figure 6: Plots showing the distribution of plagioclase phenocrysts textures, and sizes from 2005-06 lavas.....25
Figure 7: Partition coefficients of Mg in plagioclase as a function of plagioclase anorthite content.....33
Figure 8: The partition coefficients of K in plagioclase, and the activity coefficient of K, as a function of plagioclase anorthite content.....36
Figure 9: Plagioclase MgO data against anorthite content from 2005-06 lavas.....41
Figure 10: Plagioclase Sr data against anorthite content from 2005-06 lavas.....42
Figure 11: Plagioclase K data against anorthite content from 2005-06 lavas.....43
Figure 12: Histogram of the frequency of calculated MgO concentrations in equilibrium with plagioclase.....44
Figure 13: Histogram of the frequency of calculated Sr concentrations in equilibrium with plagioclase.....45
Figure 14: Histogram of the frequency of calculated K concentrations in equilibrium with plagioclase.....46
Figure 15: Results of diffusion models in euhedral plagioclase.....63
Figure 16: Photomicrograph and EMP maps of the resorbed plagioclase from the Southern Fissure and results of diffusion models.....71
Figure 17: Photomicrograph of a euhedral olivine from the Bull's eye and results of diffusion models.....78

Figure 18: Photomicrograph and EMP maps of the glomerocryst from the Southern Fissure.....80
Figure 19: Model of the history of the glomerocryst from the Southern Fissure.....82
Figure 20: Photomicrographs of plagioclase in the glomerocryst from the Southern Fissure and results of diffusion modelling.....85
Figure 21: Results of diffusion modelling from olivine in the glomerocryst from the Southern Fissure.....89
Figure 22: Petrogenic model illustrating the five main stages occurring in the magma chamber leading up to the 2005-06 eruption.....95
Figure 23: Histogram of the number of timescales modelled from phenocrysts in the 2005-06 lavas overlain with the seismic data recorded prior to the eruption.....99
Figure A.1: Mn and Ni concentrations in olivine analysed by EMP against those analysed by LA-ICP-MS.....128
Figure A.2: Normalised stoichiometric values of Si, Al, Na, and Ca in plagioclase plotted against one another.....130
Figure A.3: Plots of Cr and Ni isotopes analysed in olivine.....132
Figure A.4: Plots of Sr, K, Mn, Ni and Cr analysed in glass by LA-ICP-MS against bulk glass data from Goss et al. (2010).....133
Figure A.5: Plot illustrating the range of melt temperatures calculated using four methods.....136

Acknowledgments

I would like to thank Laurence Coogan for giving me this research opportunity and for all his help, advice and support along the way. I would like to thank Fidel Costa for his insights and suggestions throughout this project, and for his time and help using the EMP in Singapore. Thanks to Jody Spence for his help using the LA-ICP-MS at the University of Victoria, and Mati Raudsepp and Edith Czech for their assistance with using the EMP at the University of British Columbia. I would also like to thank Stephen for his help with modelling and for reviewing this thesis.

Dedication

I would like to dedicate this thesis to my late best friend Christopher W. Bell.

Chapter 1: Introduction to the geology of the East Pacific Rise mid-ocean ridge

1.1 Introduction to mid-ocean ridges

The global chain of mid-ocean ridges (MOR) are the most volcanically active system in the world, extending to a length of ~ 70 000 km. It is estimated that an average volume of 3 km^3 of lava is erupted annually on to the seafloor (Crisp, 1984). Our understanding of the character of the oceanic crust has been obtained from marine geophysical studies, deep sea drilling, direct observations through submersibles, and studies of uplifted segments of the ocean floor (ophiolites; e.g. Detrick et al., 1987; Renard et al., 1985; Hall, 1979; Cann, 1974). These studies show that the volcanic and tectonic characteristics of the ridges at spreading centres differ primarily with spreading rates and magma supply (e.g. Macdonald et al., 1992; Perfit and Chadwick, 1998). At fast-spreading ridges, the flux of magma into the crust is larger than at slow-spreading ridges, with eruptions occurring on decadal timescales (Macdonald et al., 1988; Sinton and Detrick, 1992; Perfit and Chadwick, 1998). Due to the limited ability to observe submarine eruptions, little is known about eruption dynamics, their exact number and location, and the time interval between them. This information is crucial in order to understand how the oceanic crust is formed.

Multidisciplinary research programs which link many aspects of a MOR system are helping to increase our knowledge of the processes associated with a spreading event. The Ridge 2000 program coordinates research on selected Integrated Study Sites in order to understand the interactions between complex ridge systems such as volcanic and magmatic activity, hydrothermal circulation, and seafloor topography (http://www.ridge2000.org). The East Pacific Rise (EPR) between 8 and 11°N was selected as an Integrated Studies Site due to it being one of the world's most well understood MOR, having been intensively studied since the late 1970's (e.g. Lonsdale, 1977; Renard et al., 1985; Detrick et al., 1987; Figure 1). An interdisciplinary approach has revealed much about the EPR's hydrothermal systems, geophysical structure,

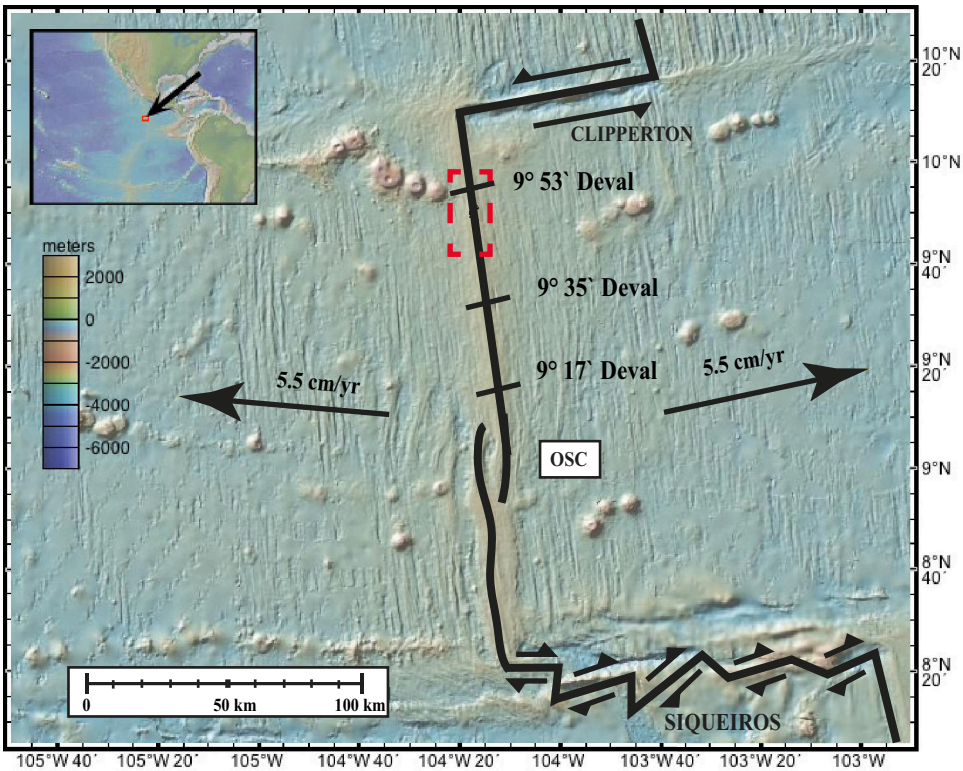

Figure 1. A bathymetric map of the 8°N-10°N area of the EPR. Bathymetry data is from the Marine Geoscience Data System (MGDS) database (www.marine-geo.org). The location of the 2005-06 eruption at ~9°50'N is shown by the red box (see Figure 4 for details). The locations of the Clipperton and Siqueiros Faults, Overlapping Spreading Centers (OCS), and areas that deviate from axial linearity are shown (Devals; Langmuir et al 1986; Kent et al, 1993a,b). The black arrows represent the direction of sea floor spreading and are labelled with their spreading rates.

tectonics and geochemistry (e.g. Macdonald and Fox, 1988; Perfit and Chadwick, 1998; Macdonald et al., 1992; Von Damm et al., 1994; Fornari et al., 1998; Goss et al., 2010). The EPR is classified as a fast-spreading mid-ocean ridge with full rates ranging from up to ~ 160 mm/year in the southern super-fast EPR (Detrick et al., 1993), to ~ 50 mm/year in the northern region (Carbotte and Macdonald, 1992). The 9º50'N region of the EPR has been designated as the 'Bull's eye' of the Ridge 2000 EPR Integrated Study Site, and is the area of focus in this study. This portion of the EPR has been subjected to numerous extensive investigations with repeat eruptions being documented at the site, the first in 1991-92 (Haymon et al., 1993), and the second in 2005-06 (Tolstoy et al., 2006). However, there is still much to learn about the physical and geochemical processes occurring within the magma chamber underlying the EPR, and the steps leading up to volcanic events, including crystallization, differentiation and magma mixing.

1.1.1 Magma chambers and magma accretion at fast spreading ridges

The oceanic crust at fast spreading ridges such as the EPR, have a simple layered stratigraphy which has been inferred from ophiolite (Geotimes conference, 1972) and seismic studies (e.g. Raitt, 1963; Shor et al., 1970). With increasing depth the oceanic crust consists of an extrusive volcanic section, a sheeted dyke complex, and an intrusive plutonic section (e.g. Karson, 1998; Karson, 2002). To account for this crustal stratigraphy, traditional models of MOR axial magma chambers (AMC) consisted of a large molten melt reservoir in which melt accumulates and undergoes differentiation prior to eruption on to the seafloor (e.g. Cann, 1974; Figure 2A). Freezing of this melt reservoir produces the plutonic portion, whilst eruption from the chamber forms the dykes and extrusive volcanics. This traditional model has been proven to be too simplistic, with geophysical studies showing the AMC is comprised of a volumetrically small melt lens, ~ 1-3 km below the seafloor, less than a few hundred meters thick, and ~ 1 km wide (Detrick et al., 1987; Hooft et al., 1997; Rohr et al., 1988; Detrick et al., 1993; Kent et al., 1993a). This narrow melt lens is surrounded by a crustal low velocity zone defined by low compressional and shear wave velocities and is interpreted to be a partially solidified crystal mush zone (e.g. Detrick et al., 1987; Toomey et al., 1990; Rohr

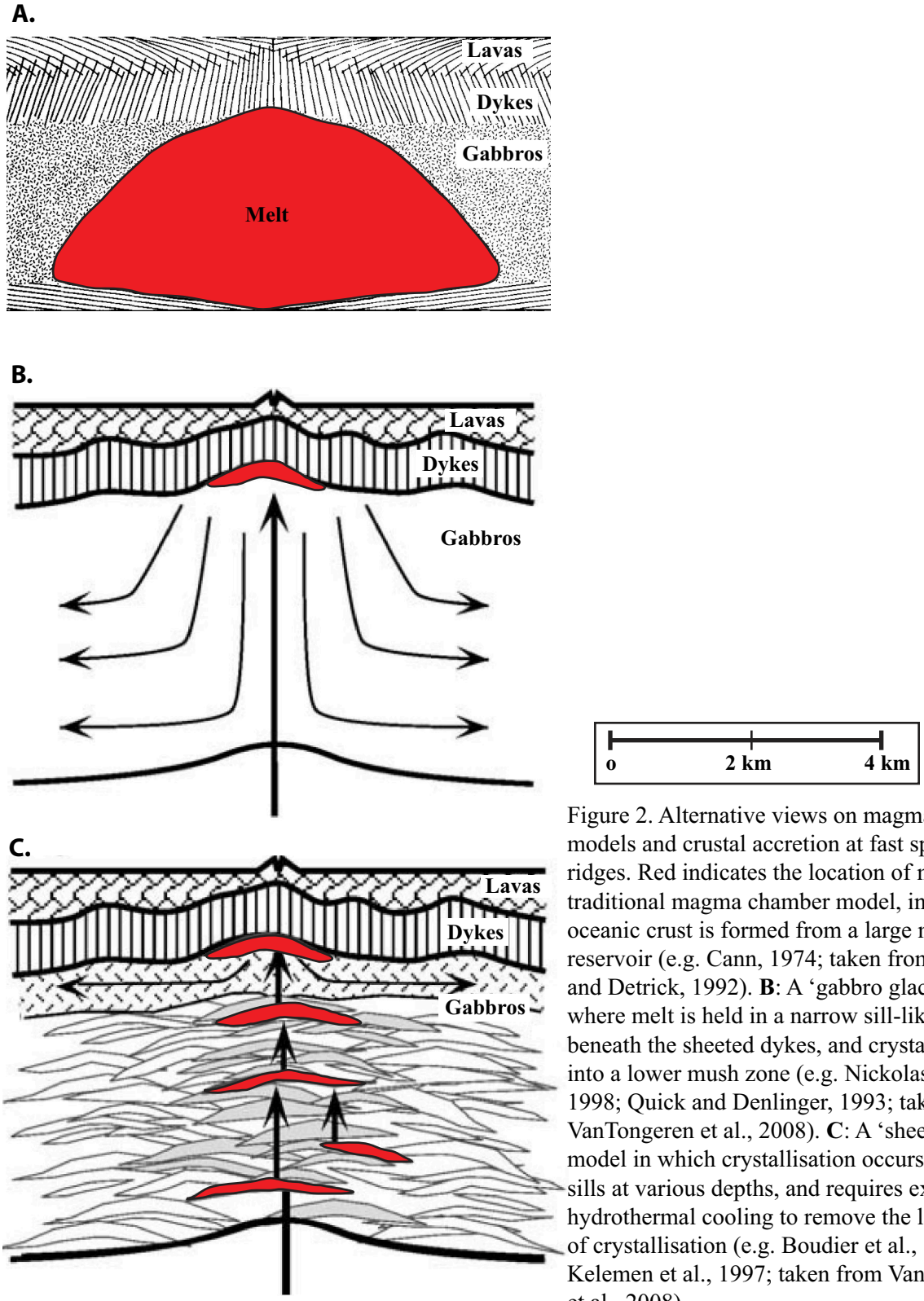

Figure 2. Alternative views on magma chamber models and crustal accretion at fast spreading ridges. Red indicates the location of melt. **A**: A traditional magma chamber model, in which the oceanic crust is formed from a large molten melt reservoir (e.g. Cann, 1974; taken from Sinton and Detrick, 1992). **B**: A 'gabbro glacier' model where melt is held in a narrow sill-like body beneath the sheeted dykes, and crystals subside into a lower mush zone (e.g. Nickolas et al., 1998; Quick and Denlinger, 1993; taken from VanTongeren et al., 2008). **C**: A 'sheeted sill' model in which crystallisation occurs in multiple sills at various depths, and requires extensive hydrothermal cooling to remove the latent heat of crystallisation (e.g. Boudier et al., 1996; Kelemen et al., 1997; taken from VanTongeren et al., 2008).

et al., 1988; Dunn et al., 2000). The AMC along fast spreading ridges can vary significantly in its width and depth, for example at 13°N on the EPR a 400 m depth variation is recorded within 2 km along axis (e.g. Babcock et al., 1998). Such changes in magma chamber depth may be linked to magma chamber dynamics with replenishment events causing assimilation of the roof portion inducing upwards migration of the chamber (e.g. Coogan et al., 2003). Evidence of the assimilation of hydrothermally altered roof material is seen in chlorine enrichments within erupted basalts (e.g. Micheal and Schilling, 1989). Reductions in magma chamber depth may be due to crystallization at its roof induced by periods of reduced magma activity (Detrick et al., 1987). These findings were incorporated into a revised magma chamber model by Sinton and Detrick (1992). The model consists of narrow, sill-like bodies of melt ~1-2 km below the ridge axis, which merges into a lower crystal mush zone (Sinton and Detrick, 1992).

At present two general models exist to predict the style of crustal accretion at fast spreading ridges. In the first, called the gabbro glacier model, crystallization occurs primarily within the melt lens, with the latent heat of crystallization being lost to the overlying hydrothermal system (Figure 2B). Crystals subside into the mush zone which extends outwards and downwards to form the lower oceanic crust (e.g. Nicolas et al., 1988; Quick and Denlinger, 1993; Figure 2B). In the second model, crystallization occurs within multiple sills in the lower crust at various depths (e.g. Boudier et al., 1996; Figure 2C). This model has subsequently been called the sheeted sill model and requires extensive hydrothermal cooling throughout the lower crust to remove the latent heat of crystallization (e.g. Kelemen et al., 1997; Figure 2C). Information on magma chamber dynamics, such as magma mixing and differentiation, are essential in order to understand how the oceanic crust is formed.

1.1.2 Mid-ocean ridge basalt differentiation

Studies of the geochemistry and petrography of basalts erupted along mid-ocean ridges provide essential information on crystallization and differentiation processes within the magma chamber. Examination of the phenocrysts, glomerocrysts and xenoliths

found within mid-ocean ridge basalts (MORBs) from fast spreading ridges indicate low crystal abundances (1-5 vol %). The dominant phases found in MORBs are commonly plagioclase followed by olivine, whilst clinopyroxene is usually scarce (e.g. Harp, 1995; Pan and Batiza, 2003; Soule et al., 2007). Glomerocrysts or xenoliths of partially molten crustal rock are rare, and provide excellent opportunities to study the processes occurring in the lower crust. These glomerocrysts and xenoliths are usually not in equilibrium with the melt that brought them to the surface and likely represent mixing within the mush zone beneath fast spreading ridges (e.g. Davis and Clague, 1990; Dixon et al., 1986; Hekinian et al., 1985; Ridley et al., 2006). Chemical and textural information from phenocrysts in MORBs provide further evidence for disequilibria existing with their erupted host and can provide evidence of mixing events. The lava chemistry and presence of resorbed crystals lead Dungan and Rhodes (1978) to suggest magma mixing plays an important role in the genesis of lavas from the Mid-Atlantic Ridge. Chemically diverse populations of plagioclase and olivine have been used as indicators of magma mixing within lavas from the EPR (Pan and Batiza, 2003). Trace element zoning in plagioclase from lavas from the Mid-Atlantic Ridge and the Costa Rica Rift (Costa et al., 2009), and in plagioclase from the Juan de Fuca, North Gorda Ridge and Gakkel Ridge (Zellmer et al., 2011), provide evidence of disequilibria existing between crystals and their host which are interpreted to be caused by magma mixing. This reinforces the idea that magma mixing is an important process affecting the petrology of MORB (O'Hara 1977; Dungan and Rhodes, 1978; Rhodes et al., 1979).

The time between a magma mixing event and eruption onto the seafloor can be examined by modelling the amount of diffusive re-equilibration between crystals and melt (e.g. Pan and Batiza, 2002; Costa et al., 2009). Uncertainties that arise from using this approach usually involve the choice of diffusion model and parameters. For example, whether crystal growth or dissolution accompanied diffusion, or the estimated initial and boundary conditions used (e.g. whether the crystal grew in an open versus closed system). Despite these uncertainties diffusion modelling has proven to be a useful tool in determining timescales of magmatic processes such as magma mixing, and has been exploited by a growing number of studies. Previous work using this method on crystals

within MORB's have indicated that mixing can predate an eruption by a few days, up to tens of years (Pan and Batiza, 2002; Costa et al., 2009; Zellmer et al., 2011, 2012).

A detailed examination of the petrology and geochemistry of MORB's, followed by diffusion modelling on those crystals which provide evidence of disequilibria existing between their host melt, can provide important information on crystal residence times and timescales of magma mixing. This information is essential in helping us understand magma transport, and magma replenishment rates associated with a typical MOR eruption.

1.2 Geology and structure of the EPR between 9º and 10ºN

The area studied in this dissertation (9˚46'N-9˚56'N) lies within the well studied 9º to 10ºN region of the EPR. The following sections provide details of the tectonic structure and morphology of the axial magma chamber beneath the ridge from 9° to 10°N. This is followed by a description of the recent eruptions that have been documented along this portion of the ridge.

1.2.1 Location and structure

The EPR between 9º-10ºN is spreading at a full rate of ~ 110 mm a year (Carbotte and Macdonald, 1992). The study area (9º46'N-9º56'N) lies on a first-order ridge segment bounded by the right-stepping Clipperton and left-stepping Siqueuiros transform faults (Figure 1; Fornari et al., 2004). This first order segment is divided into two second-order segments, separated by an Overlapping Spreading Centre (OSC) at 9º03'N (Detrick et al., 1987; Mutter et al., 1988). A number of smaller segments, or deviations in axial linearity (Devals), correspond to bends and offsets at intervals of 5-25 km (Figure 1; Langmuir et al., 1986; Kent et al., 1993b). These are thought to be associated with different tectonic, volcanic and hydrothermal systems with petrologic data suggesting differences between magma compositions can exist between segments (Langmuir et al., 1986; Haymon et al., 1991; Smith et al., 2001).

Evidence of a high magmatic budget in the 9º-10ºN region is seen through the correlation of a number of features (Macdonald and Fox, 1988). Seismic reflection data indicate the presence of a shallow and laterally near-continuous axial magma chamber which can vary in depth and continuity (AMC; Detrick et al., 1987). Those regions with shallow level magma reservoirs are linked to areas exhibiting an inflated axial cross section and shallow bathymetry (minimum depth of ~ 2540 m at 9º50'N), plus the presence of a narrow axial summit trough (< 200 m; Macdonald and Fox, 1988). The trough was previously believed to have a tectonic origin and was termed an axial summit graben (Gente et al., 1986). It has since been renamed an axial summit caldera (Haymon et al., 1991) or an axial summit collapse trough (Fornari et al., 1998), and has been interpreted to be caused by gravitational collapse following magma withdrawal post eruption (Macdonald and Fox, 1988; Haymon et al., 1991; Fornari et al., 1998). Fornari et al. (1998) suggested this can be enclosed within a wider, fault bounded trough with a primarily tectonic origin, termed an axial summit graben (300-2000 m wide).

Hydrothermal plume distribution is thought to be a good indicator of a high magmatic budget (e.g. Urabe et al., 1995; Baker and Urabe, 1996). The area between 9º29'-10ºN was found to have a high proportion of intense and continuous hydrothermal plumes, whilst the 8°58'-9°29'N region exhibits a weak and discontinuous plume distribution (Baker et al., 1994). This suggests the ridge area to the north of 9º29'N has a higher magmatic budget than to the south. This is supported by this portion of the ridge having the shallowest and most continuous AMC, with a ~ 600 m decrease in AMC depth from ~ 9°20'N to ~ 9°50'N (Detrick et al., 1987).

1.2.2 Size and depth of the magma chamber in the 9-10ºN region

Seismic studies in the 9º-10ºN area have provided detailed constraints on the depth, dimension, shape, and along axis variation of the AMC underlying the ridge crest (Detrick et al., 1987; Dunn et al., 2000; Crawford and Webb, 2002; Kent et al., 1993a, b; Kent et al., 2000; Collier and Singh, 1997). Seismic reflection studies indicate the presence of a shallow melt lens at a depth of ~ 1.4 km, which is on average 700 m wide

and 10-50 m thick (Detrick et al., 1987; Kent et al., 1993b; Harding et al., 1993). Seismic studies have been used to determine the along-axis variations in width and continuity of the AMC (Kent et al., 1993a, b; Smith et al., 2001). These studies reveal narrowing of the melt lens occurs beneath Devals at 9º35'N, 9º53'N, and 9º58'N (width of ~ 250 m; Kent et al., 1993b; Smith et al., 2001). Seismic tomography indicates that estimated melt fractions (~ 3-38 %) at mid-lower crustal depths (~ 2-8 km) are greater at segment centres suggesting a greater delivery of melt from the mantle (Toomey et al., 1990; Dunn et al., 2000).

Seismic tomography reveals the low velocity, crystal mush zone beneath the AMC has a width of 4-6 km at 9º33'N (Dunn et al., 2000; Crawford and Webb, 2002; Figure 3). Compressional and shear wave velocities indicate ≤ 18 % melt is present in the mush zone (Dunn et al., 2000; Crawford and Webb, 2002). Seafloor compliance is a measure of the extent of deformation of the seafloor under pressure forcing from ocean waves. Compliance measurements of the crystal mush zone reveal a similar width of 5-8 km at 9º48'N and 9º33'N, but in an asymmetric form, with a greater amount of melt towards the west of the axis (Figure 3B; Crawford and Webb, 2002). Further south, towards the overlapping spreading centre (OSC; 9º08'N) the mush zone broadens out, extending up to 10 km west of the axis and spanning the distance between the limbs of the OSC (Crawford and Webb, 2002). This asymmetry could be explained by asymmetric near-axis faulting initiating more efficient cooling via the penetration of hydrothermal fluids at a deep crustal level (Figure 3B; Crawford and Webb, 2002). Along axis variation in melt to mush proportions has been documented in the southern EPR, with both crystal-rich zones (> 60 %) and pure melt zones occurring at a spacing of 15-20 km (Singh et al., 1998). The pure melt zones are thought to correspond to zones of fresh magma from the mantle (Singh et el., 1998). Compliance data indicates the presence of Moho melt sills beneath the crystal mush zone in certain locations (9º48', 9º05' and 9º02'N; Figure 3B; Crawford and Webb, 2002). These melt bodies are not seen through seismic tomography, suggesting a very thin (50-200 m) layer less than 2 km wide (Crawford and Webb, 2002). Their formation mechanism and role in melt differentiation at mid-ocean ridges remains ambiguous. and it is unclear whether significant crystallization can occur here due to the high temperature of the wall rock (Crawford and Webb, 2002).

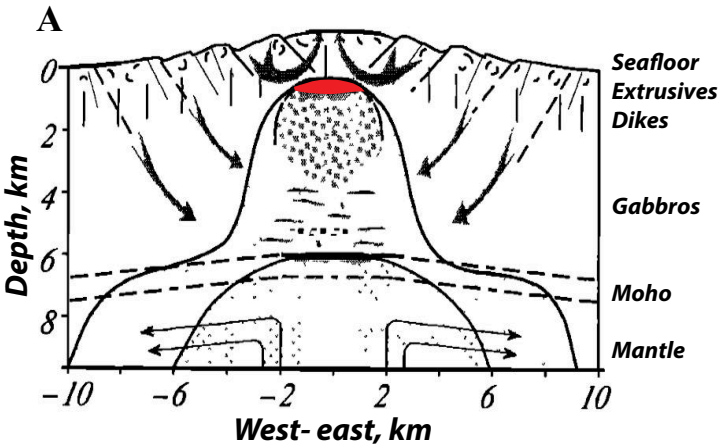

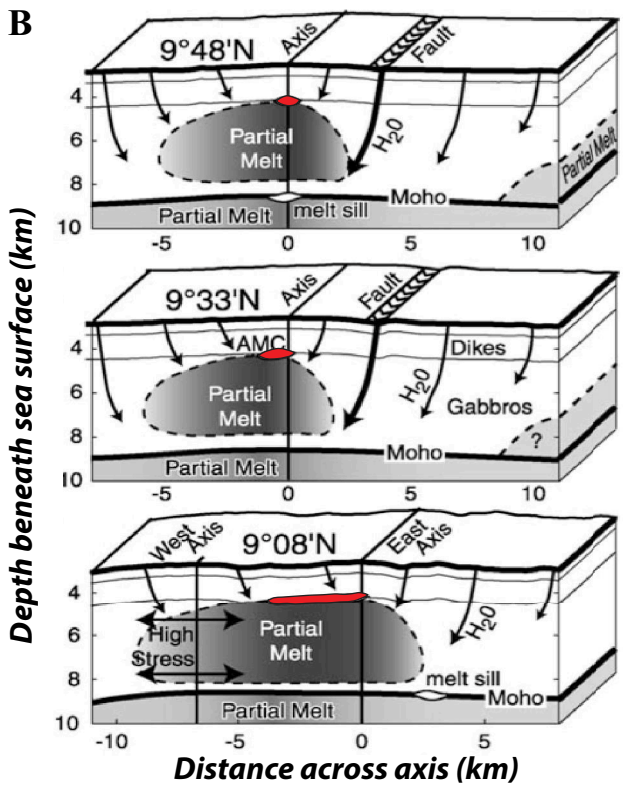

Figure 3. **A**: A schematic cross-sectional view through the EPR ridge at 9º30'N based on seismic tomography data from Dunn et al. (2000). Melt is highlighted in red and arrows represent hydrothermal circulation.

B: Interpretive cross-sectional views through the EPR ridge at 9º48'N, 9º33'N and at the OSC 9º08'N based on sea floor compliance data from Crawford and Webb (2002). The AMC (red) sits beneath the axis with an asymmetric underlying crystal mush zone. Curved arrows represent hydrothermal flow penetrating the crust and horizontal arrows indicate high stress (Crawford and Webb, 2002).

An increase in compressional wave velocity with depth is seen through compliance data (Crawford and Webb, 2002). Compressional wave velocities vary with varying melt distributions, indicating the observed increase in velocity with depth could be attributed to either differences in melt distribution or a decrease in melt fraction. It was proposed by Crawford and Webb (2002) that the ratio of compressional to shear wave velocities suggest melt in the lower crust is not held in isolated sills, but instead are connected in grain boundary regions with high aspect ratios.

1.2.3 Documented volcanic eruptions in the past two decades

The EPR between 9º46'N and 9º56'N is the first location to document repeat eruptions along a MOR; one in 1991-92 (Haymon et al., 1993) and a second in 2005-06 (Tolstoy et al., 2006). This 13 year gap is consistent with estimates of an eruption occurring every ~ 10 years along fast spreading ridges. Multiple eruptions on the same ridge segment have only been located in one other location, at Axial Seamount on the Juan de Fuca ridge, where an eruption was recorded in 1998 (Fox et al., 2001; Dziak et al., 1999), and again in 2011 (Dziak et al., 2012; Chadwick et al., 2012).

Previous analysis of lavas erupted around 9º46'N and 9º56'N along the EPR show they are primarily normal MORBs (N-MORBs) with MgO contents between 7 and 9 wt % (e.g. Langmuir et al, 1986; Batiza and Niu, 1992; Perfit et al., 1994). The petrology of lavas from this region are similar to those found on other fast spreading ridges, and contain less than 5 vol % phenocrysts consisting of predominantly plagioclase (~ 80 %), with minor olivine (~ 8 %) and clinopyroxene (~ 13 %; Pan and Batiza, 2003). To spatially characterize the lavas erupted between 9º46'N and 9º56'N the following terms are used (Goss et al., 2010): the Bull's eye (9º49'-51'N), the Northern Fissure region (9º53'-56'N), the Southern Fissure region (9º49-46'N) and an off-axis eruption that lies approximately 600 m east of the ridge (9º54.5'N; Soule et al., 2007; Figure 4A). Cross sections perpendicular to the ridge axis at the Northern Fissure, the Bull's eye, and the Southern Fissure are shown in Figure 4B. The central Bull's eye region is seen to have a slightly shallower bathymetry in comparison to further north or south (Figure 4B). The

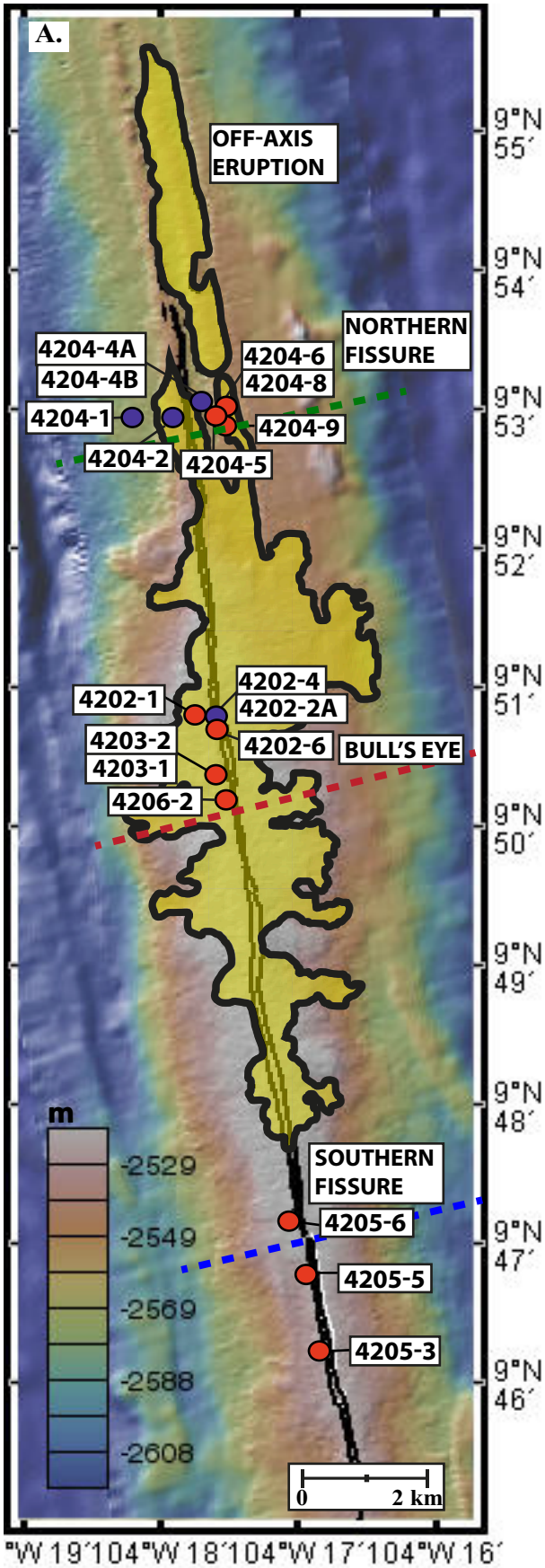

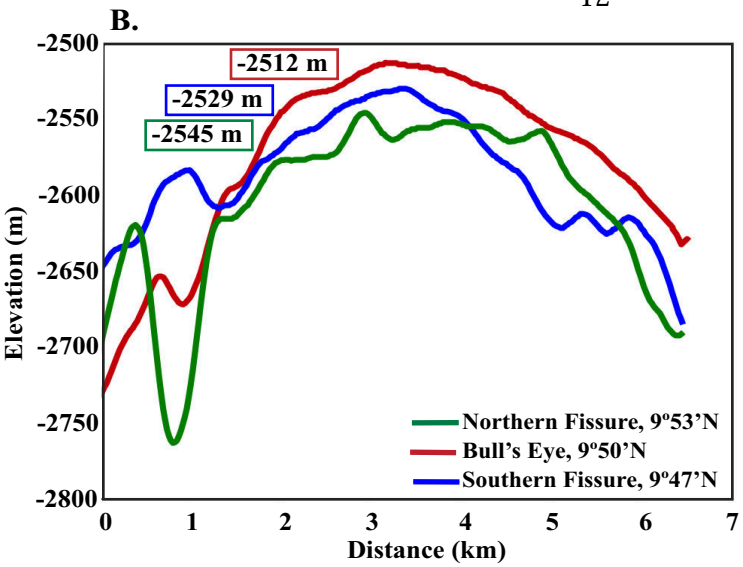

Figure 4. **A**: Bathymetric map of the 9°46'N-9°56'N region of the East Pacific Rise with the extent of the products from the 2005-06 eruption highlighted in yellow as determined from the Marine Geoscience Data System (MGDS) database (www.marine-geo.org; Soule et al., 2007; Fundis et al., 2010). The bathymetry is high resolution EM300 multibeam data from White et al. (2006). The axial summit trough (AST) is outlined in black trending north-south. Sample names and locations used in this report are indicated by circles. Red circles highlight those samples that have undergone geochemical analyses plus petrographic observations, and purple those samples that have only been examined petrographically. The dashed lines perpendicular to the AST show the location of the cross sections in **B**.

B: Cross sections perpendicular to the ridge axis at the Bull's eye (9°50'N), Northern Fissure (9°53'N), and the Southern Fissure (9°47'N). Numbers in boxes are the maximum elevation found across each section.

bathymetry along the ridge axis at the Southern Fissure and Northern Fissure are ~17 m and ~ 33 m deeper than the Bull's eye respectively. This suggests the Bull's eye (9º50'N) region may have a higher magmatic flux than regions to the north or south.

The following section describes the previous work completed on the dynamics, petrography and geochemistry of lavas from both the 1991-91 and 2005-06 eruption between 9º46'N and 9º56'N along the EPR.

1.2.4 The 1991-1992 Volcanic Eruption, 9º46'-9º51'N

Comparisons of seafloor imaging and bathymetric data collected in 1989 and 1991 at 9º09'-54'N provided evidence of an eruption having occurred recently (Haymon et al., 1993). Subsequent ^{210}Po-^{210}Pb dating of lava samples suggest the eruption lasted for at least one year, with an event in early 1991 at ~ 9º50'N, and in late 1991 to early 1992 at ~ 9º53'N (Rubin et al., 1994). Modelling of the morphology of the 1991 eruption suggested ~ 4-6 x 10^6 m^3 of lava was emplaced between 9º46'-51'N in a fissure-controlled eruption (Gregg et al., 1996, Fornari et al., 2004). A significant amount of disruption was documented along the ridge, including changes to the distribution and nature of hydrothermal vents (Haymon et al. 1993; Baker et al., 1994). Venting of fluids became dominated by diffuse venting of grey-black smoke directly from cracks and fissures in the newly erupted lava (Haymon et al., 1993). This unfocused 'syn-eruption venting' has been linked to shallow dyke intrusions (Haymon et al., 1993; Butterfield et al., 1997). The destruction and disappearance of numerous vent communities was recorded following the eruption, in particular the 'Tubeworm Barbecue' site at 9º50.6'N (Haymon et al., 1993).

1.2.4.1 Geochemistry and Petrology of the 1991-92 eruption

Samples from the 1991 lavas (~ 9º50'N) are aphyric to slightly phyric with < 5 vol % phenocrysts (details not reported; Gregg et al., 1996), and are classified as N-MORBs (Perfit et al., 1994; Rubin et al., 1994; Sims et al., 2002). Lavas erupted from the Bull's eye in 1991 are primitive with compositions between 7.9-8.9 wt % MgO, and high

TiO_2 (1.2-1.5 wt %) and CaO/Al_2O_3 ratios (0.77-0.80), and Sr and K contents between 118-127 ppm and 710-890 ppm respectively (Sims et al., 2002). The lavas erupted near the Northern Fissure in 1992 (9º53'N) are more evolved (~ 8.0 wt % MgO) than the central 1991 lavas (Rubin et al., 1994; 2001). It was concluded that this eruption represented a separate event and is derived from a different magma reservoir than the 1991 eruption (Rubin et al., 1994).

1.2.5 The 2005-2006 Volcanic Eruption, 9º46'-9º56'N

1.2.5.1 Pre- and syn-eruption induced seismicity

Due to the predicted decadal timescales of eruptions occurring along the EPR, an ocean-bottom seismometer (OBS) monitoring program was initiated in the 9ºN area, beginning in October 2003 (Tolstoy et al., 2006). Indications that a second eruption had taken place came from 8 out of 12 OBSs failing to return to the surface upon electronic release in April 2006 (Tolstoy et al., 2006). Ocean-bottom seismometers record the velocity of ground motion, which at fast spreading ridges are dominated by small-scale cracking events driven by hydrothermal cooling, crustal inflation and extensional stresses associated with the AMC (Tolstoy et al., 2006). Seismic data from 2 of the 4 recovered OBSs show increases in the number of earthquakes per day occurred from October 2003 to May 2005, which was interpreted as reflecting conditions building up towards an eruption (Tolstoy et al., 2006; Figure 5). This period of increased seismic activity continued throughout the eruption between 2005 and early 2006 (Figure 5; Tolstoy et al., 2006). A period of very high amplitude seismic signals lasting 6 hours occurred on the 22 January 2006, and was inferred to be the propagation of the primary dyke that fed the eruption near 9º50'N (Tolstoy et al., 2006).

1.2.5.2 Eruption dynamics and morphology

The 2005-06 eruption was established as occurring in pulses beginning in June 2005 and culminating in an event in late January 2006 based on ages determined from ^{210}Po-^{210}Pb disequilibria in lava samples (Rubin et al., 2006, 2008). More recently Soule

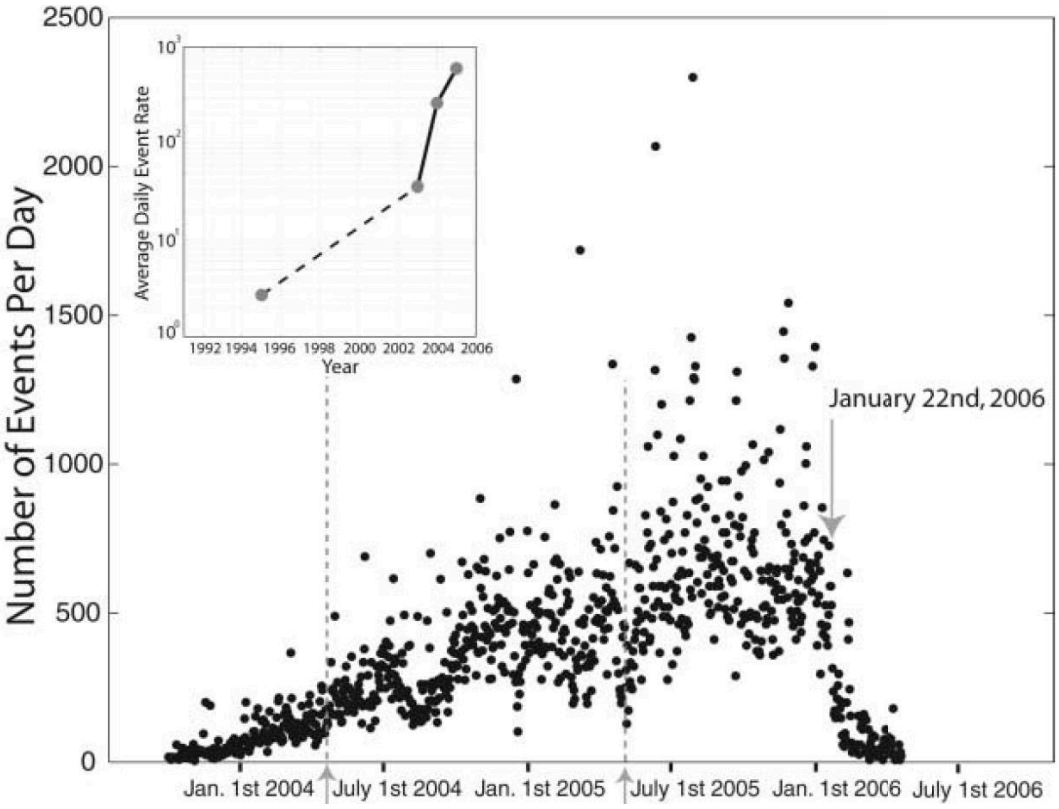

Figure 5. Plot of the number of seismic events recorded per day from 3 October 2003 to 23 April 2006 from Tolstoy et al. (2006). The inset plot shows the average daily event rates including data from a 1995 deployment by Sohn et al. (1999).

et al. (2012) measured volatiles, helium, vesicularity and crystallinity within basaltic glasses in 2005-06 lavas from the Bull's eye in order to understand the dynamics of magma ascent and emplacement. Using a model of diffusion controlled bubble growth rate they calculated flow rates between 0.02 to 0.12 m s^{-1}, with minimum ascent rate of 0.15 m s^{-1} and eruption duration of ~ 30 h for this portion of the eruption (Soule et al., 2012). Soule et al. (2007) were able to successfully identify and map the products of the 2005-06 eruption using seafloor imagery due to their black colour and lack of sediment on the flow surfaces, which resulted in highly visible boundaries between older flows and the newer 2005-06 lavas (Figure 4.). The 2005-06 lava flows extended for ~18 km along the axis between 9º46'-56'N and had an average flow thickness of 1.5 m (Soule et al., 2007). These flow thicknesses implies ~ 22 x 10^6 m^3 of lava was erupted, which is 5-6 times more voluminous than the 1991 eruption, although the area covered was similar (Gregg et al., 1996, Soule et al., 2007). Similar to the 1991 eruption, the emplacement of 2005-06 lavas was controlled by fissures within the AST between 9º49'-9º52'N (Fornari et al., 1998, Soule et al, 2007). The morphology of the 2005-06 lavas was examined using deep-towed camera surveys and high-resolution bathymetric profiles by Fundis et al. (2010). Due to a high percentage of lavas showing high-flow rate morphologies (i.e. sheet and hackly flows), it was concluded the eruption was characterized by higher effusion rates than previous eruptions (Fundis et al., 2010). The 2005-06 lavas were centred near the inferred region of primary dyke propagation at the Bull's eye (~ 9º50'N; Fundis et al., 2010) and is also where lava was transported farthest from the axial summit trough (Fundis et al., 2010). This is consistent with the suggestion that the Bull's eye region has a higher magmatic budget than the Southern or Northern Fissure (Section 1.2.3).

1.2.5.3 Petrology and Geochemistry of lavas from the 2005-2006 eruption

The 2005-06 lavas are mostly aphyric with less than 5 vol % phenocrysts of plagioclase and olivine (Soule et al., 2007), similar to the 1991 eruption. The geochemistry of lavas from the 2005-06 eruption was investigated in detail by Goss et al. (2010). The lavas are typical N-MORB, with variations in major and trace element concentrations along-axis (Goss et al., 2010). The 2005-06 lavas are slightly more

evolved than the 1991 eruption with lower MgO contents of between 7.3 and 8.4 wt %, higher CaO/Al_2O_3 ratios (0.78-0.82) and TiO_2 (1.4-1.6 wt %) concentrations (Perfit et al., 1994; Rubin et al., 1994; Goss et al., 2010). Their Sr and K contents vary between 103-117 ppm and 800-912 ppm respectively (Goss et al., 2002). The Northern and Southern Fissure regions are more evolved than the central Bull's eye, with higher concentrations of incompatible elements and lower magnesium concentrations (7.3-8.0 wt % MgO in comparison to 7.9-8.4 wt % MgO). A similar spatial pattern was observed in the 1991-92 eruption (Rubin et al., 1994; 2001). Goss et al. (2010) suggested this geochemical heterogeneity provides evidence of variations in melt differentiation and magma mixing along-axis. This may be a consequence of the low aspect ratio and segmentation seen along-axis in the AMC, which may inhibit magma mixing (Sinton and Detrick, 1992; Goss et al., 2010). In contrast, radiogenic isotope ratios from 2005-06 lavas do not display much variation, indicating a common isotopically homogenous mantle source which is typical of the EPR (Goss et al., 2010). Soule et al. (2012) measured the volatile content of lavas from the Bull's eye region of the 2005-06 eruption. Lavas contained a wide range of CO_2 concentrations (163-295 ppm) with H_2O contents between 0.15 and 0.19 wt % (Soule et al., 2012). The dissolved CO_2 contents in near-vent samples were found to be in equilibrium with pressures that correspond to the depth of the AMC underlying the 9°50'N region (~ 1.4 km; Soule et al., 2012). The lava Cl contents (50-63 ppm) increased with down-flow distance from the ridge axis, which Soule et al. (2012) attributed to contamination of seawater during flow emplacement.

1.2.5.4 Petrogenesis of the 2005-06 lavas

Based on the geochemical data, Goss et al. (2010) suggested that the more primitive magmas from the 1991 eruption could be parental to the 2005-06 magmas. They describe a petrogenetic model which involves residual magma from the 1991 eruption evolving through fractional crystallization and mixing with evolved melts leaked into the AMC from the deeper mush zone. From their data, Goss et al. (2010) suggests there is no evidence to indicate the involvement of a hotter, more primitive magma, and therefore the 2005-06 eruption could not have been initiated by the injection of hot,

primitive melt into the AMC. Instead, they suggest continuous or episodic replenishment of the AMC occurred since 1991, via the infiltration of evolved residual melts from the mush zone, which produced magmatic overpressure (Goss et al., 2010). The eruption was then triggered from fractionated melt being expelled into the overlying AMC from the mush zone, in conjunction with local and external extensional forces along the ridge axis (Goss et al., 2010).

1.3 Aims and approach of this study

The primary objective of this thesis is to gain a better understanding of the dynamics of the magma plumbing system beneath fast spreading ridges. This is achieved through examining the geochemistry of phenocrysts and lavas from the recent 2005-06 eruption along the EPR. The chemical zoning profiles in crystals from the 2005-06 lavas are modelled in an attempt to unravel magma mixing histories and crystal residence timescales within the underlying magma chamber. The three main aims of this dissertation are:

1. To use the major and trace element compositions of phenocrysts and their host melt from the 2005-06 lavas to establish if crystals are in equilibrium with their host melts, or if magma mixing occurred prior to this eruption.
2. To determine crystal residence times and timescales of magma mixing for those crystals that hold evidence of disequilibria with their host melt by using diffusion modelling.
3. To determine if there is a link between processes happening in the magma chamber, as determined by phenocryst composition and the seismic activity recorded prior to the 2005-2006 eruption (Tolstoy et al., 2006).

The second chapter of this thesis begins by describing the analytical techniques used to retrieve the chemical composition of phenocrysts and glass from the 2005-06 eruption. Details of these analytical techniques are in Appendix A.1, and a compilation of the raw data is in Appendix A.2. Subsequent sections describe the petrography of the samples,

followed by the geochemical data of the phenocrysts and lavas from the 2005-06 eruption along with the results of diffusion modelling. Details of the petrography and sample locations are in Appendix A.3, and the chemical zoning profiles for all the analysed crystals are in Appendix A.5. Appendix A.6 contains examples and explanations of the diffusion models used in this thesis. The final section outlines a petrogenic model that describes the events occurring within the AMC prior to the 2005-06 eruption. The third chapter outlines the primary conclusions of this thesis along with a list of further work to be completed.

Chapter 2: Primitive melt recharge, and magma-mush mixing in the weeks and months preceding the 2005-06 eruption, EPR, 9˚46'N-9˚56'N.

2.1 Introduction

In this chapter geochemical data is presented from phenocrysts and lavas from the 2005-06 eruption on the EPR, 9°46'N to 9°56'N. This data is used to quantify timescales of magma mixing in the magma chamber beneath the EPR prior to eruption. Such data will provide important constraints on the rates of magma replenishment, and details of the magma plumbing system beneath fast spreading ridges. These magma mixing timescales are compared to the increase in the number of seismic events recorded up to two years prior to the eruption by Tolstoy et al. (2006). This information is used to investigate if there is a link between processes happening in the magma chamber and seismic activity.

This chapter begins with describing the analytical techniques used to determine the chemical composition of phenocrysts and glass from 2005-06 lavas. Later sections examine the petrography of the 2005-06 samples, along with the retrieved geochemical data. This is followed by the results of diffusion modelling completed on those crystals that are out of equilibrium with their host melt. This information is put together in a petrogenic model which outlines the events occurring within the magma chamber prior to the 2005-06 eruption.

2.2 Analytical Techniques

In order to determine the major and trace element zoning profiles of phenocrysts and lavas from the 2005-06 eruption, two analytical techniques where employed; the electron micro-probe (EMP) and laser ablation inductively coupled plasma mass spectrometry (LA-ICP-MS). The following sections describe the analytical conditions used for each technique and the errors associated with the analyses. Full details of the analytical conditions, and accuracy and precision of the analyses are in Appendix A.1 and a compilation of the data is in Appendix A.2.

2.2.1 Electron microprobe analysis (EMP)

Rim-to-core and rim-to-rim transects through plagioclase and olivine crystals were analysed using the EMP at the University of Barcelona (UB; Cameca SX-50) by analyst Dr. Fidel Costa, and the EMP at the Earth Observatory of Singapore (Nanyang Technological University [NTU]; JOEL JXA-8530F) by analyst Aerona Moore. Due to a poor correlation between the stoichiometry of plagioclase analysed from UB and NTU, points from each transect where re-analysed at the University of British Columbia (UBC; Cameca SX-50) by analyst Aerona Moore. The data from UB and NTU were normalized to the data analysed from UBC. This involved plotting each element analysed in an analytical session from UB and NTU, against the corresponding data analysed at UBC. The regression line from each plot was used to calculate the corrected values for each element (Appendix A.1.2). This process has ensured that all the plagioclase data are internally consistent (Appendix A.1.2).

A total of 48 plagioclase crystals were analysed (57 traverses totalling 3025 analyses) and 10 olivine crystals (15 traverses totalling 1165 analyses; data is available in Appendix A.2). For both plagioclase and olivine an accelerating voltage of 15-20 kV was used, with a ~ 2 μm spot size and 3-5 μm spacing between spots. For plagioclase a counting time of between 10-60 s and a beam current of between 15-100 nA was used for the elements Na, Ca, Al, Si, K, Fe, and Ti. A counting time of 60 s and beam current of between 60-100 nA was used for all Mg analyses. Na was analysed first to minimize Na-loss. For olivine a counting time of 20-30 s was used for Si, Mg, and Mn, between 20-60 s for Ca, Ni, Fe, and 100 s for Cr, Al, and P. On all analyses half the peak counting time was used on background measurements either side of the peak. Elemental maps of olivine and plagioclase were obtained on the EMP at the Earth Observatory of Singapore. A resolution of 1 μm/step, and current of between 100-200 nA was used for both plagioclase and olivine. The elements Mg, Fe, Ca, Ni, Ti, Al, Cr, P, Co, F, and V were analysed in olivine using a dwell time of between 10-70 msec/point. The Co, F and V olivine EMP maps do not show any zoning and the elements have not been analysed during EMP transects, therefore they are not discussed here. The elements Al, Ca, Mg, Fe, and Ti were analysed in plagioclase using a dwell time of between 10-13 msec/point.

The precision (2σ) of the plagioclase MgO contents analysed at the NTU and UBC varies between 2 and 4 %. The precision of the plagioclase MgO contents analysed at UB could not be determined due to a lack of raw data. However, due to the similar analytical conditions used for Mg analyses at both UB and NTU, the precision is likely to be similar. Data from plagioclase displaying up to a 20 % increase in Fe within ≤ 40 μm from the crystal rim, most likely reflects disequilibrium partitioning during rapid growth during emplacement on the seafloor, and are not considered in this study. Full details of the instrument conditions and a comparison between instruments are given in Appendix A.1.

2.2.2 Laser ablation inductively coupled plasma mass spectrometry (LA-ICP-MS)

Trace element abundances in plagioclase, olivine and the surrounding basaltic glass were determined using LA-ICP-MS at the University of Victoria using a New Wave 213 nm Nd-YAG UV laser and a Thermo X-series ICP-MS. A gas blank analysis of 30 s was measured followed by 50 s of sample analysis. Analyses where calibrated against NIST 611, 613, and 615 which were analysed before and after every sample change, after every 5 analysis, and at the beginning and end of the analytical session in order for any drift to be corrected.

The isotopes ^{88}Sr, ^{39}K, and ^{137}Ba in plagioclase were analysed using a laser power of 0.7-0.8 mJ, a spot size of 30 μm, and rastered over a ~ 80 μm line four times using a laser pulse frequency of 10 Hz. The isotope ^{43}Ca was used as the internal standard. NIST 611, 613, and 615 were assumed to contain 11.5, 11.9, and 11.8 wt % CaO, 497.4, 76.15, and 45 ppm Sr, 486 and 66.26 ppm K, and 424.1, 37.74, and 3.02 ppm Ba respectively (the concentration of K is unknown in NIST 615; Pearce et al., 1997; Horn et al., 1997). The absolute concentration of the trace element was determined using plagioclase CaO concentrations obtained prior to LA-ICP-MS analysis on the same plagioclase traverse by electron microprobe.

The isotopes ^{52}Cr, ^{53}Cr, ^{55}Mn, ^{60}Ni, ^{61}Ni, and ^{62}Ni were analysed in olivine using a laser power of 0.5 mJ, a spot size of 15 μm, and rastered over a ~ 80 μm line four times

using a laser pulse frequency of 10 Hz. The isotope ^{29}Si was used as the internal standard with the SiO_2 concentrations having been obtained prior to analysis on the same olivine traverse by electron microprobe. The samples were calibrated against NIST 611, 613, and 615, assumed to contain 69.9, 71.9, and 72.0 wt % SiO_2 , 433.3, 38.43, and 1.37 ppm Mn, 405.2 and 39.88 ppm Cr, and 443.9 and 38.44 ppm Ni (the concentrations of Cr and Ni are unknown in NIST 615; Pearce et al., 1997; Horn et al., 1997).

The isotopes ^{88}Sr, ^{39}K, ^{137}Ba, ^{52}Cr, ^{53}Cr, ^{55}Mn, ^{60}Ni, ^{61}Ni, and ^{62}Ni were analysed in the glassy rims of six samples using a laser power of 0.5 mJ, a spot size of 15-30 μm, and rastered over a ~ 80 μm line four times using a laser pulse frequency of 10 Hz. The isotope ^{43}Ca was used as the internal standard, with the samples being calibrated against NIST 611, 613, and 615 which were assumed to contain the same concentrations stated above (Pearce et al., 1997; Horn et al., 1997). The absolute concentration of the trace element in glass were determined using the glass CaO contents measured by Goss et al. (2010).

Precision within an analytical session was based on the relative standard deviation of the analysed NIST glass with the closest concentration to that in the sample. Precision was better than 4.0 % for Sr, 13.9 % for K, 29.8 % for Ba, 1.5 % for Cr, 1.0 % for Mn, and 3.7 % for Ni. Precision between analytical sessions for plagioclase analyses was based on the standard deviation of Sr, K, and Ba concentrations analysed within synthetic plagioclase glasses and natural plagioclase crystals at the beginning and end of each session. Synthetic plagioclase glasses and natural plagioclase crystals contained between 225-1500 ppm Sr, 24-2755 ppm K, and 0.2-50 ppm Ba. The calculated precision was based on the synthetic plagioclase glass or natural plagioclase with the closest concentrations to that in the samples, and was better than 6.5 % for Sr, 9.2 % for K, and 34.2 % for Ba. Worse precision was calculated from standards with low elemental concentrations. Due to the poor precision of Ba analyses, these are not included in the results or interpretation of this thesis. All olivine analyses were performed in a single analytical session. Details of the accuracy and precision of LA-ICP-MS data are given in Appendix A.1.2.

2.3 Petrology of samples from the 2005-06 eruption

Thin sections of 18 representative samples from the 2005-06 eruption were examined under a petrographic microscope. The samples extended across all geographic regions (eight from the Northern Fissure, seven from the Bull's eye, and three from the Southern Fissure), and showed variation in major and trace element contents (Goss et al., 2010). The volume percentage of phenocrysts was measured using image analysis of whole scanned thin sections with the image processing program Image-J. The total area of thin section calculated over the 18 thin sections was 11 000 mm^2. The numbers of phenocrysts were counted, with a phenocryst defined as a crystal over 100 μm along its longest dimension. A full description of the phenocrysts phases in each sample is reported in Appendix A.3.

Samples are sparsely phyric to aphyric and contain a total of 795 plagioclase crystals and 10 olivine crystals. Samples contain less than 2 vol % phenocrysts (99 % plagioclase, < 1 % olivine), and less than 0.1 vol % glomerocrysts (30 % plagioclase, 70 % olivine). Clinopyroxene and spinel are absent in all samples. The matrix is largely devitrified glass with thin-laths of fine-grained plagioclase and skeletal olivine, consistent with quenching and fast mineral growth after eruption onto the seafloor. Fresh glass is present in 11 of the 18 samples. The volume percent of phenocrysts reported here is consistent with previous observations of 2005-06 lavas by Soule et al. (2007; < 5 vol %), those lavas erupted in 1991-92 (< 5 vol %; Gregg et al., 1996), and lavas from on and off-axis at ~ 9°30'N (2.6-3.0 vol %; Pan and Batiza, 2003). Pan and Batiza (2003) report modal mineral proportions in 9°30'N lavas of 78 % plagioclase, 8 % olivine, and 13 % clinopyroxene, notably different to proportions found in 2005-06 lavas, which are free of clinopyroxene, and have plagioclase to olivine ratios that are close to one order of magnitude lower than those found at 9°30'N (Pan and Batiza, 2003).

Plagioclase is the dominant phenocryst phase, with 92 % of plagioclase occurring as single euhedral crystals (> 1 mm) or aggregates of between 2 and 20 crystals (> 3 mm) within all geographic areas (Figure 6A). Rounded and resorbed plagioclase crystals (> 1 mm) are rare, making up 3.5 % of the total number of plagioclase phenocrysts and occur within all three regions (this is equal to ~ 0.07 vol % of the total crystal content; Figure

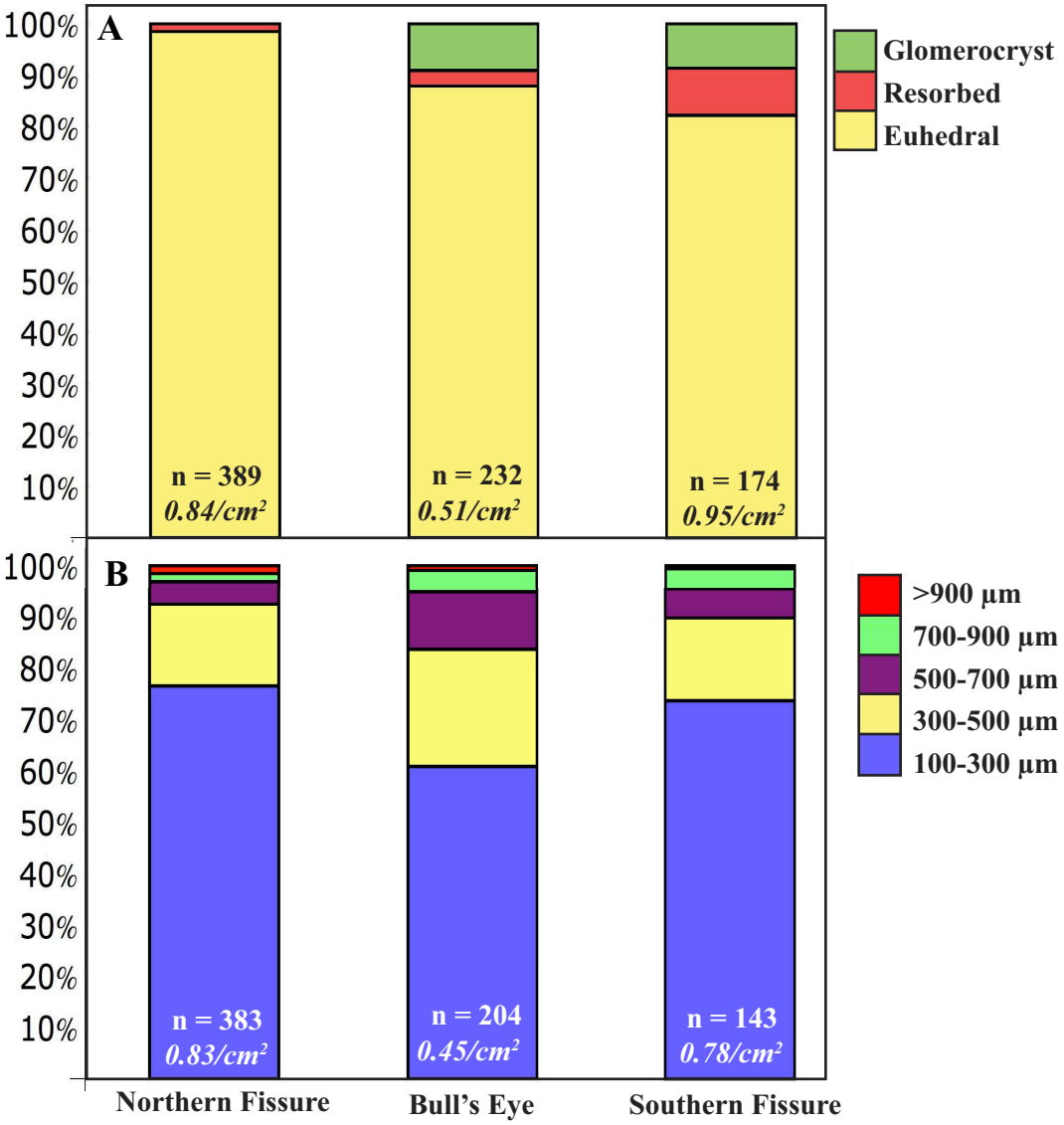

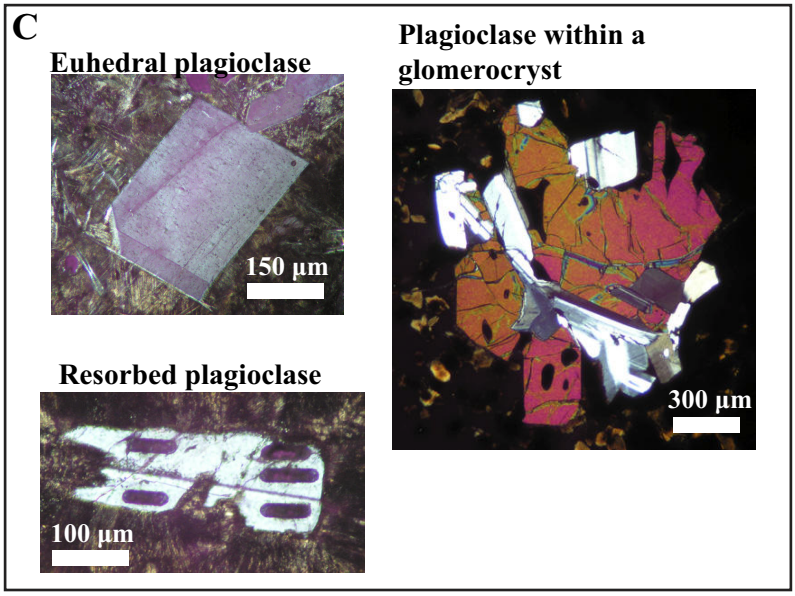

Figure 6. **A (i)**: The total number of counted plagioclase phenocrysts that exist within glomerocrysts, as resorbed crystals, or euhedral crystals. Where **n** is the total number of plagioclase phenocrysts counted, and numbers in italics are the number of crystals per square centimeter. **B**: The size distribution of the number of euhedral plagioclase phenocrysts counted in the Northern Fissure, Bull's eye and Southern Fissure. The majority of euhedral crystals (~71 %) are between 100-300 µm in all regions. **C:** Photomicrographs of examples of three plagioclase textures; a euhedral plagioclase, a resorbed plagioclase and plagioclase residing in a glomerocryst.

6A). Their presence suggests dissolution, most simply explained by being in disequilibrium with their host melt. An alternative explanation would be dissolution occurring in a different melt prior to being mixed into their host melt. The proportion of resorbed crystals found in 2005-06 lavas is within error of the number of crystals displaying obvious disequilibrium texture reported by Pan and Batiza (2003) in 9°30'N lavas (0.57 ± 0.7 vol %, where the error is one standard deviation). The remaining 4.5 % of the total number of plagioclase phenocrysts counted reside alongside olivine within glomerocrysts (Figure 6A). In all geographic regions the majority (71 %) of euhedral plagioclase phenocrysts are between 100 and 300 μm along their longest dimension, with 28 % being between 300-900 μm, and 1 % being over 900 μm (Figure 6B). This is consistent with an average plagioclase size of 200 μm found in the 9°30'N lavas by Pan and Batiza (2003). There is no significant difference in the size distribution of phenocrysts between the different geographic regions. There are ~ 40 % fewer plagioclase crystals counted per unit area in the Bull's eye in comparison to the Northern or Southern Fissure. The Southern Fissure contains six times more resorbed plagioclase per unit area than both the Bull's eye and Northern Fissure.

Three subhedral to euhedral olivine phenocrysts (< 600 μm) occur in two samples within the Bull's eye. No olivine phenocrysts are observed in the Northern or Southern Fissure regions. The proportion of euhedral olivine is not recorded in previous studies of 2005-06 lavas.

Glomerocrysts of olivine and plagioclase exist in two samples, the first in the Southern Fissure (Sample 4205_5), and the second in the Bull's eye (Sample 4203_2). The Southern Fissure glomerocryst (~ 2 mm in diameter) consists of three olivine crystals (~ 75 %), with the largest olivine (~ 1.5 mm) poikilitically enclosing sub-anhedral plagioclase crystals (~ 25 %). Portions of the olivine have a rounded, anhedral margin suggesting dissolution. This is likely due to being in disequilibria with its host melt. The glomerocryst from the Bull's eye consists of an olivine (~ 1 mm) poikilitically enclosing four smaller plagioclase crystals (~ 100 μm). The total size of the glomerocryst cannot be determined due to it residing on the edge of the thin section. Some portions of the olivine appear to have a more rounded margin suggesting dissolution, although it is not as distinctive as the rounded margin in the Southern Fissure glomerocryst. A large xenolith

(~ 90 cm^3) from lavas erupted in 1991 was examined in detail by Ridley et al. (2006), and consists of plagioclase (~ 70 %), olivine (~ 9 %), intergranular glass (~ 21 %), and minor sulphide and spinel (~ 0.2 %). Note, Ridley et al. (2006) uses the term xenolith to describe what has been termed in this thesis as a glomerocryst. The 1991 xenolith is considerably larger than the glomerocrysts found in 2005-06 lavas, and the proportion of plagioclase to olivine is over an order of magnitude higher, although clinopyroxene is noticeably absent in all three. The plagioclase within the 1991 xenolith has corroded margins and shows signs of being internally remelted (Ridley et al., 2006), suggesting it is in disequilibria with its host melt. This is consistent with the textures and interpretations made from the glomerocrysts in 2005-06 lavas.

Small crystals of plagioclase and olivine (< 40 μm) appear to have nucleated around vesicles (20-100 μm in diameter) in ten of the eighteen samples. The presence of small vesicles is consistent with Soule's et al. (2007) observations from 2005-06 lavas. Rare sulphide minerals are present as small sub-spherical globules (> 100 μm diameter) in three samples. Sulphide globules are not reported in previous examinations of 2005-06 lavas (Soule et al., 2007), or 1991-92 lavas (Gregg et al., 1996), but are present in the 1991 xenolith (Ridley et al., 2006).

2.4 Parameters for calculating equilibrium plagioclase and olivine compositions.

In order to determine if phenocrysts are in equilibrium with their host melt we require knowledge of the major and trace element contents of minerals and melts, along with the partition coefficients (Kd) of the element of interest. The major and trace element compositions of phenocrysts have been analysed by EMP and LA-ICP-MS (Section 2.2). The elements Mg, Sr and K were examined in plagioclase, and Fe, Mg, Mn, Ni, and Cr were examined in olivine for three reasons: (i) we have information on their partition coefficients and diffusion coefficients; (ii) the diffusion rates of these elements are sufficiently rapid enough to show changes in concentration on relatively short timescales (i.e. from weeks up to tens of years); (iii) the majority of these elements have different diffusion rates and can therefore provide information about magmatic

process that occurred on different timescales. The following sections provide information on the 2005-06 melt compositions, and details on the parameters required to calculate Mg, Sr and K partition coefficients in plagioclase, and Fe-Mg, Mn, Ni, and Cr partition coefficients in olivine

2.4.1 Melt compositions of 2005-06 lavas

Melt compositions are required in order to calculate the major and trace element contents in equilibrium with plagioclase and olivine. The compositions of 2005-06 lavas are classified as normal-MORBs (N-MORB). This is consistent with the N-MORB classification of 1991-92 lavas (Perfit et al., 1994; Rubin et al., 1994; Sims et al., 2002), and the majority of lavas examined at 9°30'N (93 %; Pan and Batiza, 2003). Samples examined in this study which contained fresh glass were analysed by LA-ICP-MS for their trace element contents. Samples of fresh glass have also been analysed by Goss et al. (2010) for their major and trace element contents. A compilation of the melt compositions retrieved from both methods and a comparison between the two is in Appendix A.1.2.2.4. Throughout this study, major element compositions are taken from the minimum and maximum values from bulk glass data analysed by Goss et al. (2010). Trace element melt contents (Sr, K, Mn, Ni, and Cr) are taken from the minimum and maximum values from both LA-ICP-MS glass analysis (Section 2.2), and bulk glass data in Goss et al. (2010). The maximum and minimum melt compositions of 2005-06 lavas from both methods for all regions are; 7.73 to 8.29 wt % MgO, 103 ± 6.7 to 117 ± 3.5 ppm Sr, 500 ± 70 to 950 ± 133 ppm K, 0.16 to 0.20 wt % Mn, 0.009 to 0.015 wt % Ni, and 266 ± 9.3 to 320 ± 11.2 ppm Cr (Table A.5; Appendix A.1.2.2.4).

2.4.2 Parameters controlling partition coefficients in plagioclase and olivine

Partition coefficients are required in order to calculate the major and trace element contents in equilibrium with plagioclase and olivine, and are known to be dependent on a number of parameters. The partition coefficients of Mg, Sr and K in plagioclase are dependent on temperature and anorthite content (An = 100*Ca/[Ca+Na+K], in mol %;

e.g. Blundy and Wood, 1991; Bindeman et al., 1998). The partition coefficients of Fe-Mg, Mn, Ni, and Cr in olivine are also dependent on temperature in addition to olivine and melt composition (e.g. Beattie et al., 1991; Beattie,1994; Toplis, 2005). The methods used to determine melt temperature, equilibrium plagioclase An contents, and partition coefficients are outlined in the following sections.

2.4.2.1 Calculating melt temperatures

Temperature is an essential parameter to quantify not only for calculating partition coefficients (2.4.2.3), and diffusion coefficients (Section 2.6), but for an overall understanding of a magmatic system. Melt temperatures for each sample were calculated using the methods described by Sinton and Detrick (1992), Wilson et al. (1988), and the MELTs (Ghiorso and Sack, 1995) and PetroLog (Danyushevsky and Plechov, 2011) algorithms. The methods of Sinton and Detrick (1992) and Wilson et al. (1988) use linear regressions of temperature and melt MgO content from experiments on MORB. The MELTs algorithm uses a free energy minimization procedure, and the PetroLog software uses mineral-melt equilibrium models. The following mineral-melt models were used for the PetroLog algorithm; Ariskin et al. (1993), Danyushevsky (2001), Langmuir et al. (1992), Nielsen (1985), and Weaver and Langmuir (1990). The inputs for the MELTs and PetroLog models are melt composition, pressure, and oxygen fugacity. In these calculations the temperature was calculated at the pressure of the axial magma chamber beneath the ridge at 9ºN (assumed 800 bars), at the quartz-magnetite-fayalite (QFM) oxygen fugacity buffer, and assuming 0.19 wt % H_2O. The QFM buffer was chosen as previous studies have shown this to be a likely oxidation state for MORB's (Mallmann and O'Neill, 2009; Cottrell and Kelley, 2011). This H_2O content is the average taken from the range measured in 2005-06 lavas by Soule et al. (2012). Melt compositions were taken from bulk glass data in Goss et al. (2010). For each melt composition, a maximum temperature difference of 16°C is seen between the results of the four methods. For each method, a maximum difference of 16°C is seen between different melt compositions (Figure A.5; Appendix A.1.3). The method of Sinton and Detrick (1992) gave the highest temperature estimates for each melt composition (1202-1212°C), whilst the PetroLog

algorithm gives the lowest temperature estimates for each composition (1180-1196°C; Figure A.5; Appendix A.1.3). The melt temperatures retrieved from all four methods were averaged for each melt composition giving a maximum and minimum value of 1195°C and 1204°C. Due to the similarities in melt temperature calculated from all areas, and by all methods, a temperature of 1200°C is used to calculate partition coefficients (Section 2.4.2.3) and diffusion coefficients (Section 2.6)

The same methods and parameters described above can be used to calculate the melt temperatures for the 1991-92 lava compositions (Sims et al., 2002). For each melt composition a maximum difference of 15°C is seen between the four methods. For each method used, a maximum difference of 19°C is seen between melts of different compositions. The melt temperatures determined from all four methods was averaged for each melt composition giving a minimum and maximum value of 1205°C and 1217°C. These temperatures are up to 22°C higher than those calculated from the 2005-06 lavas, with the average temperature from 1991-92 lavas being ~ 10°C higher than the average from 2005-06 lavas (~1200°C). This is consistent with 1991-92 lavas having MgO contents up to 1.2 wt % higher than 2005-06 lavas (Sims et al., 2002; Goss et al., 2010). The average MgO melt content in 1991-92 lavas is ~ 0.5 wt % higher than the average MgO melt content in 2005-06 lavas (7.9 wt % MgO; Goss et al., 2010).

2.4.2.2 Equilibrium plagioclase anorthite content

The anorthite content of plagioclase in equilibrium with the melt compositions from each sample is calculated using the method described by Grove et al. (1992), which requires knowledge of the melt composition (taken from Goss et al., 2010), and both the MELTs (Ghiorso and Sack, 1995) and PetroLog algorithms (Danyushevsky and Plechov, 2011). The latter two models use the plagioclase liquidus temperature and the same inputs described in Section 2.4.2.1. The mineral-melt models from Langmuir et al. (1992) and Danyushevsky (2001) are used in the PetroLog algorithm here and in other Petrolog calculations as they contained models for both plagioclase and olivine. For a melt of the same composition, a maximum difference of 4 mol % is seen in the equilibrium An content between the different methods. The range of equilibrium An contents calculated

for different melt compositions using the Grove et al. (1992) approach is An_{71-73}, using the MELTs algorithm is An_{73-75}, and using the PetroLog algorithm is An_{71-75}. Due to the similar equilibrium An contents calculated from each melt composition, an average is taken from each method giving a minimum and maximum value of An_{70} and An_{75}. This range of equilibrium An contents are compared to the An contents from phenocrysts in the 2005-06 lavas to determine whether they are in equilibrium with their host melts (Section 2.5.1.1). Using the approach described by Grove et al. (1992), a 50°C increase in melt temperature increases the calculated equilibrium An content by up to 10 mol %. Using the MELTs algorithm an increase in H_2O content from 0.2 to 0.5 wt % increases the equilibrium An content by ~ 3 mol %.

2.4.2.3 Defining Mg, Sr, and K partition coefficients in plagioclase.

This section provides details on the methods used to determine the partition coefficients of Mg, Sr and K in plagioclase, which are dependent on melt temperature and plagioclase An content. The partition coefficients of Mg and K in plagioclase increase with decreasing An content and increasing temperature, whereas the Kd_{Sr} increases with decreasing An and decreasing temperature (Blundy and Wood, 1991; Bindeman et al., 1998).

It is common for partition coefficients to be taken from experimental studies, for example the results of Mg partitioning in plagioclase from Bindeman et al. (1998) are widely used (e.g. Costa et al., 2003; Smith et al., 2009; Costa et al., 2009; Druitt et al., 2012). Using the Kd_{Mg} from Bindeman et al. (1998) all the euhedral plagioclase have Mg contents in equilibrium with a higher MgO melt (~ 10.0 wt %) then their host (~ 7.73-8.29 wt %). Two possible interpretations are: (1) Bindeman's et al. (1998) Kd_{Mg} are correct, therefore the MgO content of all euhedral plagioclase crystals, in all samples, are in equilibrium with a higher MgO melt than their host; or (2), the MgO content of most euhedral plagioclase are in equilibrium with the MgO content of their host, therefore the Kd_{Mg} defined by Bindeman et al. (1998) are 15-20 % too low. This is likely as the 15-20 % difference in absolute Kd_{Mg} values is within the associated error (14-22 %; Appendix A.4) of the Kd_{Mg} calculated from Bindeman et al. (1998). In the first model, due to the

fast diffusion rates of Mg in plagioclase (LaTourrette and Wasserburg, 1998), all euhedral plagioclase would have had to be mixed into the more evolved melt that hosts them within days of eruption; this seems unlikely and hence the second hypothesis is favoured. As an alternative approach an empirical partition coefficient for Mg in euhedral plagioclase ($Kd_{Mg\ euhedral}$) from the 2005-06 eruption is calculated using the MgO contents of euhedral plagioclase and the glass MgO concentration of each sample from Goss et al. (2010), and plotted against the plagioclase An content (Figure 7). When comparing the $Kd_{Mg\ euhedral}$ with the Kd_{Mg} from Bindeman et al. (1998) it can be seen they both show a similar pattern of increasing MgO with decreasing An content (Figure 7). This pattern is consistent with previous observations of Mg zoning in plagioclase phenocrysts (e.g. Costa et al., 2003; Costa et al., 2009). Consequently, throughout this study Kd_{Mg} is determined from the linear regression of the observed Kd_{Mg} for euhedral plagioclase (Figure 7), although results using the Kd_{Mg} from Bindeman et al. (1998) are shown in Section 2.5 for comparison. Plots of $RT\ln(Kd_{Mg\ euhedral})$ against XAn illustrate that the compositional and temperature influences on Kd_{Mg} can be shown in the following linear form which follows that of Bindeman et al. (1998);

$$RT \ln (Kd_{Mg}) = -21800\ (\pm 430)\ XAn\ -26300\ (\pm 340) \qquad (1)$$

where R is the gas constant, T is temperature in Kelvin, and the numbers in parentheses are the standard error (Figure 7).

This approach of using natural sample data to define the Kd_{Mg} is supported by a comparison with the composition of plagioclase analysed in a cumulate xenolith from the 1991 eruption at 9°50'N (Ridley et a., (2996), and phenocrysts from Ocean Drilling Program (ODP) Hole 648B in the Mid Atlantic Ridge (Costa et al., 2009; Figure 7). Those from ODP Hole 896A from the Costa Rica Rift in Costa et al. (2009) were not included due to the MgO content of the host melt not being well defined (7.5-9.4 wt % MgO; Brewer et al., 1996 *in* Costa et al., 2009). The Kd_{Mg} calculated from the xenolith data (Ridley et al., 2006) and from Hole 648B (Costa et al., 2009) show a similar pattern of increasing Kd_{Mg} with decreasing An. However, the absolute values of Kd_{Mg} are up to 20 % lower at the same An content than the $Kd_{Mg\ euhedral}$ from Equation (1). This ~ 20 % discrepancy is within, or greater than, the calculated uncertainties (7-22 %; Appendix

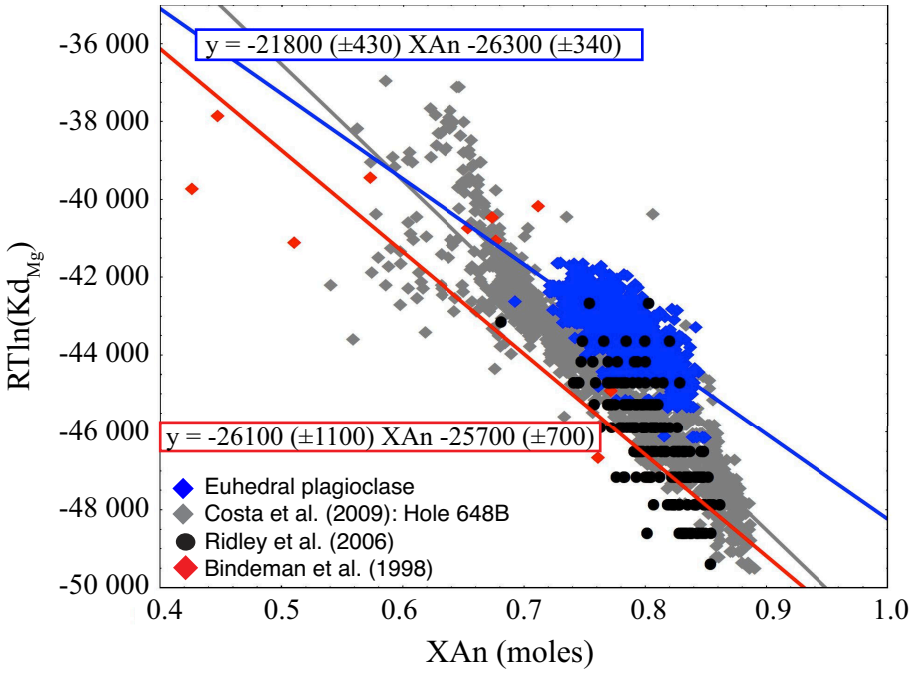

Figure 7. Partition coefficients of Mg as a function of plagioclase anorthite content (XAn). The $Kd_{Mg\ euhedral}$ (blue) are calculated from the MgO concentrations in the euhedral plagioclase and the surrounding glass (from Goss et al., 2010), R is the gas constant and T is the temperature in Kelvin. A temperature of 1200°C is used for all calculations. A regression through the euhedral plagioclase data gives a linear relationship between $RTln(Kd_{Mg})$ and XAn. For comparison, linear regressions are shown using parameters that fit Kd_{Mg} data from Bindeman et al. (1998; red), the Kd_{Mg} data from plagioclase in Costa et al. (2009; ODP Hole 648B, Mid Atlantic Ridge; grey), and the Kd_{Mg} data from a xenolith in 1991 lavas (Ridley et al., 2006; black). The data follow a similar trend of increasing Kd with decreasing An, however there are discrepancies in the absolute Kd_{Mg} values which are discussed in the main text. The equations shown are for regressions through Bindeman et al. (1998) data (red) and through euhedral plagioclase data (blue).

A.4) of Equation (1) and Bindeman's et al. (1998) equation. An alternative explanation for the discrepancy between Equation (1) and the data from Ridley's et al. (2006) data could be the plagioclase MgO contents being out of equilibrium with its host melt. This is supported by textural evidence of corroded plagioclase margins suggesting it is in disequilibrium with its host melt (Ridley et al., 2006). Using a Kd_{Mg} from Equation (1) the MgO contents of plagioclase in the 1991 xenolith would be in equilibrium with a melt containing ~ 1.6 wt % lower MgO contents than its host (8.6 wt %; Ridley et al., 2006). The discrepancy between the $Kd_{Mg\ euhedral}$ and ODP Hole 648B data (Costa et al., 2009) could be a result of uncertainties in the host melt MgO content or melt temperatures. In order to remove this discrepancy the reported MgO host melt contents would have to be 0.6 % lower than the reported 7.6 wt % MgO (Shipboard Scientific Party, 1988 *in* Costa et al., 2009), or ~ 50°C lower temperature than the 1200°C predicted in Costa et al. (2009). An alternative explanation is the Hole 648B plagioclase equilibrated with a ~ 7.0 wt % MgO melt prior to being mixed into their host melt (~ 7.6 wt % MgO) a short time before eruption. This would result in the MgO contents at crystal rims having insufficient time to equilibrate with their host melt. However, this seems unlikely due to the fast diffusion rates of Mg in plagioclase (LaTourette and Wasserburg, 1998) requiring crystals to have being mixed into the higher MgO melt within a few days of eruption.

The empirical approach used to define the compositional dependence of the Kd_{Mg} in plagioclase from the observed dependence in euhedral plagioclase cannot be applied to Sr or K because they do not define a well constrained correlation with An content. This may reflect greater analytical uncertainty or that different processes control the concentration of these elements in plagioclase. The Kd_{Sr} is defined using the equation in Blundy and Wood (1991), although the Kd_{Sr} from Bindeman et al. (1998) are shown as a comparison (Sections 2.5). Both equations take into account the roles of temperature and plagioclase An content on the partition coefficient.

The Kd_K can be defined using the equation from Bindeman et al. (1998). However using this approach, the K contents of all euhedral plagioclase are in equilibrium with a melt containing much higher K contents (> 3500 ppm) than their host (500-950 ppm). Aigner-Torres et al. (2007) published experimental data on the Kd_K with values that are up to 56 % higher than those calculated using the equation from Bindeman et al. (1998)

at An_{75} and the same temperature. Using the Kd_K values from Aigner-Torres et al. (2007), the majority of euhedral plagioclase would be in equilibrium with the K contents found in the host melts (500-950 ppm). However, the dependence of Kd_K on plagioclase An content cannot be accurately defined using the experimental data from Aigner-Torres et al. (2007) due to the small range in plagioclase An contents (An_{73-79}). Due to this uncertainty, the An dependence on the Kd_K was calculated from the thermodynamic model of anorthite-albite-orthoclase mixing of Elkins and Grove (1990). This model allows the compositional dependence of the activity coefficient of K (γ_K) on An content to be determined. Using Equation (9) and the excess free-energy terms for feldspar from Table 4, both in Elkins and Grove (1990), this has been calculated for the following conditions: (1) a temperature and pressure of 1200°C and 800 bars which were best estimates for the axial magma chamber; (2) the range of observed plagioclase An contents from 2005-06 lavas (An_{50-90}); (3) the orthoclase component (Or) calculated from the average K concentrations found in euhedral plagioclase from 2005-06 lavas ($Or_{0.001}$). The γK increases with increasing plagioclase An content. Since the partition coefficient is proportional to one over γK, the change in Kd_K with An can be determined from this (Figure 8). For a decrease in An content from An_{90} to An_{50}, the plagioclase K content has to increase by ~ 48 % for the activity of K in plagioclase to remain constant. This can be compared to a ~ 56 % increase in the Kd_K from An_{90} to An_{50} using the equation in Bindeman et al. (1998; Figure 8). Based on this, the An dependence predicted by Bindeman et al. (1998) is similar to the An dependence predicted using the thermodynamic model. The compositional dependence term determined from the change in Kd_K with γK is used along with the Kd_K experimental data from Aigner-Torres et al. (2007) to give (Figure 8);

$$RT \ln (Kd_K) = -25360\, XAn + 360\ (\pm 110) \qquad (2)$$

where the y-intercept of Equation (2) is calculated from the average Kd_K value in Aigner-Torres's experimental data, and the number in parentheses is the standard error of the difference between each data point and the regression line. In the results section the Kd_K in plagioclase is determined from both Equation (2) and Bindeman et al. (1998; Sections 2.5 & 2.6) for comparison.

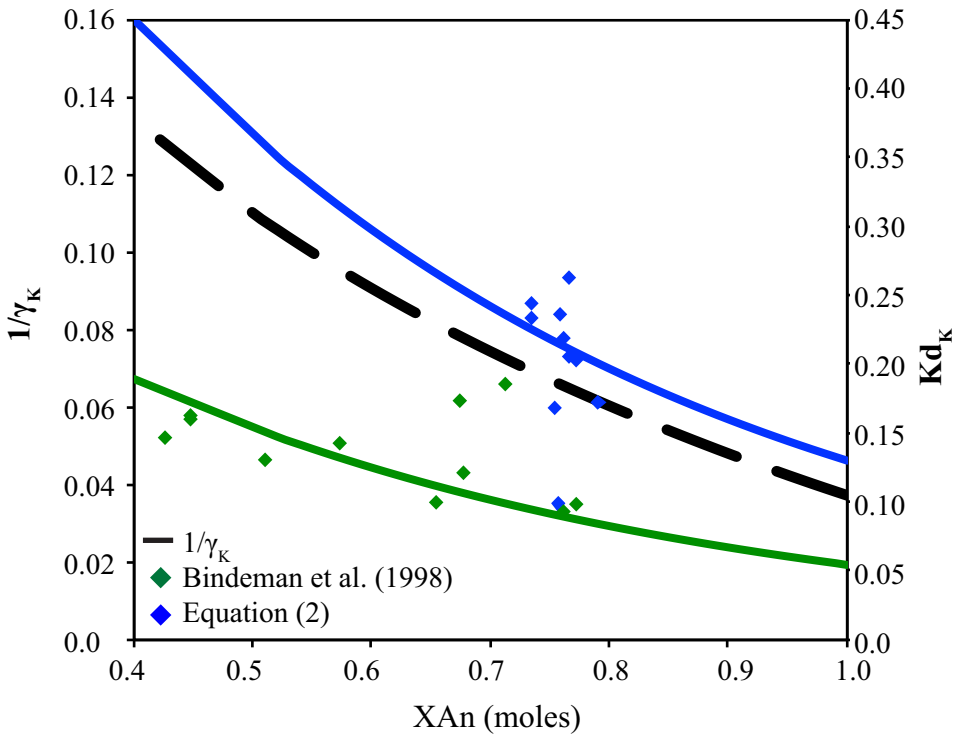

Figure 8. One over the activity coefficient of K ($1/\gamma_K$) is plotted against plagioclase An content (XAn; black). The activity of K is calculated using equation (9) in Elkins and Grove (1990), at a temperature of 1200°C and a pressure of 800 bars, with a plagioclase orthoclase (Or) content of $Or_{0.001}$. The slope of increasing $1/\gamma_K$ with decreasing An can be compared to the An dependence on Kd_K using the equation from Bindeman et al. (1998; green), and Equation (2) which combines the slope from the Elkins and Grove (1990) model with the Kd_K data from Aigner-Torres et al. (2007; blue). See text for details.

The uncertainties (two sigma standard error) associated with the parameters used to obtain the partition coefficients was calculated for An contents between An_{50-100} at 1200°C by error propagation (assuming independent errors; Taylor, 1982) of the uncertainties in the regressed parameters. The derived equation (Equation A.2; Appendix A.4) does not take into consideration the errors associated with the estimated temperature or the EMP analysis of An contents. The errors associated with the partition coefficients are between 14 % and 22 % for Mg, Sr and K from equations in Bindeman et al. (1998), and between 25 % and 35 % for the Kd_{Sr} from Blundy and Wood (1991), and 7-10% for the $Kd_{Mg\ euhedral}$ from Equation (1). In a plagioclase of An_{80}, a change in the melt temperature of ± 50°C will vary the Kd_{Sr} by ~ 2 %, Kd_{Mg} by ~ 12 % and Kd_K by ~ 6 %. Using the MELTs algorithm, a change in melt temperature from 1200°C to 1130°C will decrease the crystallised plagioclase An content from An_{75} to An_{60}. This 70°C change in temperature corresponds to a ~ 14 % difference in the activity of K in the Elkins and Grove model, which translates to a ~ 14 % difference in Kd_K. The Kd_{Mg} from Equation (1) and Bindeman et al. (1998), the Kd_{Sr} from Blundy and Wood (1991) and Bindeman et al. (1998), and the Kd_K from Equation (2) and Bindeman et al. (1998), are used to calculate the Mg, Sr, and K concentrations that are in equilibrium with the host melt and are compared to the measured concentrations within plagioclase (Section 2.5).

2.4.2.4 Partition coefficients of Fe-Mg, Mn, Ni, and Cr in olivine

Partition coefficients for Fe-Mg, Mn, Ni, and Cr in olivine must be known in order to determine the compositions in equilibrium with the host melt. Roeder and Emslie (1970) proposed the widely used average value for the exchange coefficient (K) of Fe-Mg of 0.3 for all temperatures and pressures. However, later studies have shown this value can vary a small amount with changes in pressure and temperature, and more substantially with melt composition (e.g. Toplis, 2005 and references therein). Melt components such as alkalis (e.g. Sack et al., 1987; Gee and Sack, 1988), titanium (e.g. Jones, 1988; Wagner and Grover, 1997), silica (e.g. Longhi et al., 1978), and melt polymerisation state (Kushiro and Walter, 1998; Kushiro and Mysen, 2002), have also been used to explain the variation seen in $K_{Fe-Mg,}$. More recently Toplis (2005) derived K_{Fe-}

$_{Mg}$ using a thermodynamic expression involving the chemical potentials of the fayalite and forsterite components in olivine and liquid. Oxygen fugacity (fO_2) is a critical factor in calculating K_{Fe-Mg} as it controls the ratio of Fe^{2+} and Fe^{3+}, and therefore how much Fe^{2+} is available to partition into the olivine. The total iron in this study was separated into Fe^{2+} and Fe^{3+} using the MELTs algorithm at the QFM oxygen buffer. To evaluate the uncertainty in whether an olivine is in Mg-Fe exchange equilibrium with its host melt four methods are used: (1) a K_{Mg-Fe} value of 0.3 from Roeder and Emslie (1970); (2) the K_{Mg-Fe} derived from Toplis (2005); (3) the MELTs algorithm (Ghiorso and Sack, 1995); and (4) the PetroLog algorithm (Danyushevsky and Plechov, 2011) using the mineral-melt models from Langmuir et al. (1992) and Danyushevsky (2001). The latter two methods use the same inputs as described in Section 2.4.2.1. The maximum and minimum K_{Fe-Mg} found using each method is used to calculate the range of equilibrium olivine forsterite contents (Fo = 100*Mg/[Mg+Fe], in mol %; Section 2.5.2). The MgO melt contents in equilibrium with the forsterite contents of olivine is calculated using the maximum and minimum K_{Fe-Mg} found using the four methods described above, and assuming a constant FeO content of 10 wt %. An FeO content of 10 wt % is taken from the average FeO contents analysed in 2005-06 lavas by Goss et al. (2010).

Experimental studies of the partitioning of Mn and Ni between olivine and melt have shown they are primarily influenced by melt temperature, and olivine and melt composition (Watson, 1977; Arndt, 1977; Irving, 1978; Hart and Davis 1978; Kinzler et al., 1990; Beattie et al., 1991; Beattie, 1993; Hanson and Jones, 1998). The Kd_{Mn} is determined using the equation from Beattie et al. (1991) due to limited studies on the partitioning of Mn in olivine. The Kd_{Ni} is determined using equations by Arndt (1977), Hart and Davis (1978), Kinzler et al., (1990) and Beattie et al. (1991). The methods of Arndt (1977) and Hart and Davis (1978) use a regression involving melt MgO content, whereas Kinzler et al., (1990) use the forsterite content of olivine and melt MgO content to compute the Kd_{Ni}. Beattie et al. (1991) uses an equation to describe Kd_{Mn} and Kd_{Ni} involving the Kd_{Mg} in olivine, and the Fe and Mg content of the melt.

The controls on Cr partitioning in olivine are less well constrained than Fe-Mg, Mn or Ni, which in part is due to the different partitioning behaviour of Cr^{2+} and Cr^{3+} (Kennedy et al., 1993; Gaetani and Grove, 1997; Hanson and Jones, 1998; Beattie, 1994;

Spandler and O'Neill, 2010). Hanson and Jones (1998) examined the partitioning of Cr into olivine taking into consideration both Cr^{2+} and Cr^{3+} and predicted that at oxygen fugacities above the QFM buffer Cr is predominantly trivalent. They gave an equation to calculate the Kd_{Cr3+} based on the ratio of non-bridging oxygens to tetrahedrally coordinated cations (NBO/T; Hanson and Jones, 1998). The Kd_{Cr} is calculated using this equation, where NBO/T is determined using the melt compositions from Goss et al. (2010). The Kd_{Cr} from each melt compositions is used to calculate the range of equilibrium olivine Cr contents (Section 2.5.2).

2.5 Compositional zoning profiles and equilibrium melt concentrations in plagioclase and olivine.

This section compares the analysed concentrations of elements found in plagioclase and olivine with concentrations calculated to be in equilibrium with their host melts. This is followed by a detailed description of the melt compositions in equilibrium with plagioclase and olivine that are outside the range of host melt compositions. Results are presented for 47 euhedral plagioclase phenocrysts (11 from the Northern Fissure, 19 from the Bull's eye, and 17 from the Southern Fissure), 4 resorbed plagioclase (one from the Northern Fissure, two from the Bulls eye, and one from the Southern Fissure), and 3 euhedral olivine phenocrysts (all from the Bull's eye). A further two resorbed crystals were analysed in the Southern Fissure, however these are not included in the results due to low overall totals caused by analytical problems. Additionally, the compositions of plagioclase and olivine analysed from both the glomerocrysts in the Bull's eye area, and the Southern Fissure, are compared to those of the phenocrysts. The elemental zoning profiles for each crystal are given in Appendix A.5.

The anorthite content of all plagioclase phenocrysts ranges between An_{50-94}, and the forsterite content of all olivine phenocrysts ranges between Fo_{72-86}. These values are similar to those found in ~ 9°30'N lavas (An_{55-85} and Fo_{82-88}; Batiza and Niu, 1992; Pan and Batiza, 2003). However, there is a noticeable absence of olivine containing forsterite contents lower than Fo_{80} in ~ 9°30'N lavas (Batiza and Niu, 1992; Pan and Batiza, 2003). The An zoning within plagioclase is categorized into four types; normal, reverse,

unzoned, and oscillatory. Zoning is defined by a prominent and consistent change in anorthite of over 3 mol % An, with oscillatory zoning showing an increase and decrease of over 3 mol % more than once from rim to core. Examination of the An content of the euhedral plagioclase crystals reveals that 60 % exhibit oscillatory zoning, 23 % reverse zoning, 11 % normal zoning, and 6 % are unzoned. There is no difference in the percentage of zoning types seen between the Northern Fissure, the Bull's eye, and the Southern Fissure. These observations contrast with An zoning in plagioclase from 9º30'N lavas, which are reported to have primarily weak normal or reverse zoning (Batiza and Niu, 1992; Pan and Batiza, 2003).

2.5.1 Evidence of intra- and inter- crystalline disequilibria seen through plagioclase An, Mg, Sr, and K content

To determine whether plagioclase crystals are in equilibrium with one another, measured MgO, Sr and K concentrations are plotted against their An content and separated via their area of origin (Figures 9-11A) and texture (Figures 9-11B). The coloured diagonal bands in Figures 9-11 represent the trace element contents in equilibrium with the concentrations found within the host melt. The black lines in Figures 9-11B represent contour lines of MgO, Sr, and K concentrations in equilibrium with constant melt contents. Histograms of the frequency of calculated melt MgO, Sr and K contents in equilibrium with plagioclase are shown for each region (Figures 12-14A) and for each texture (Figures 12-14B). Shaded grey bands represent the range of MgO, Sr, and K concentrations found within the host melt taken from LA-ICP-MS glass data and bulk glass data from Goss et al. (2010; Table A.5). The following sections discuss the disequilibria observed in plagioclase An contents (Section 2.5.1.1), followed by Mg, Sr and K contents (Section 2.5.1.2).

2.5.1.1 Disequilibria observed in plagioclase An contents

The average equilibrium anorthite content of plagioclase calculated using the methods described in Section 2.4.2.2 provides a range of An_{70-75}. This range is compared

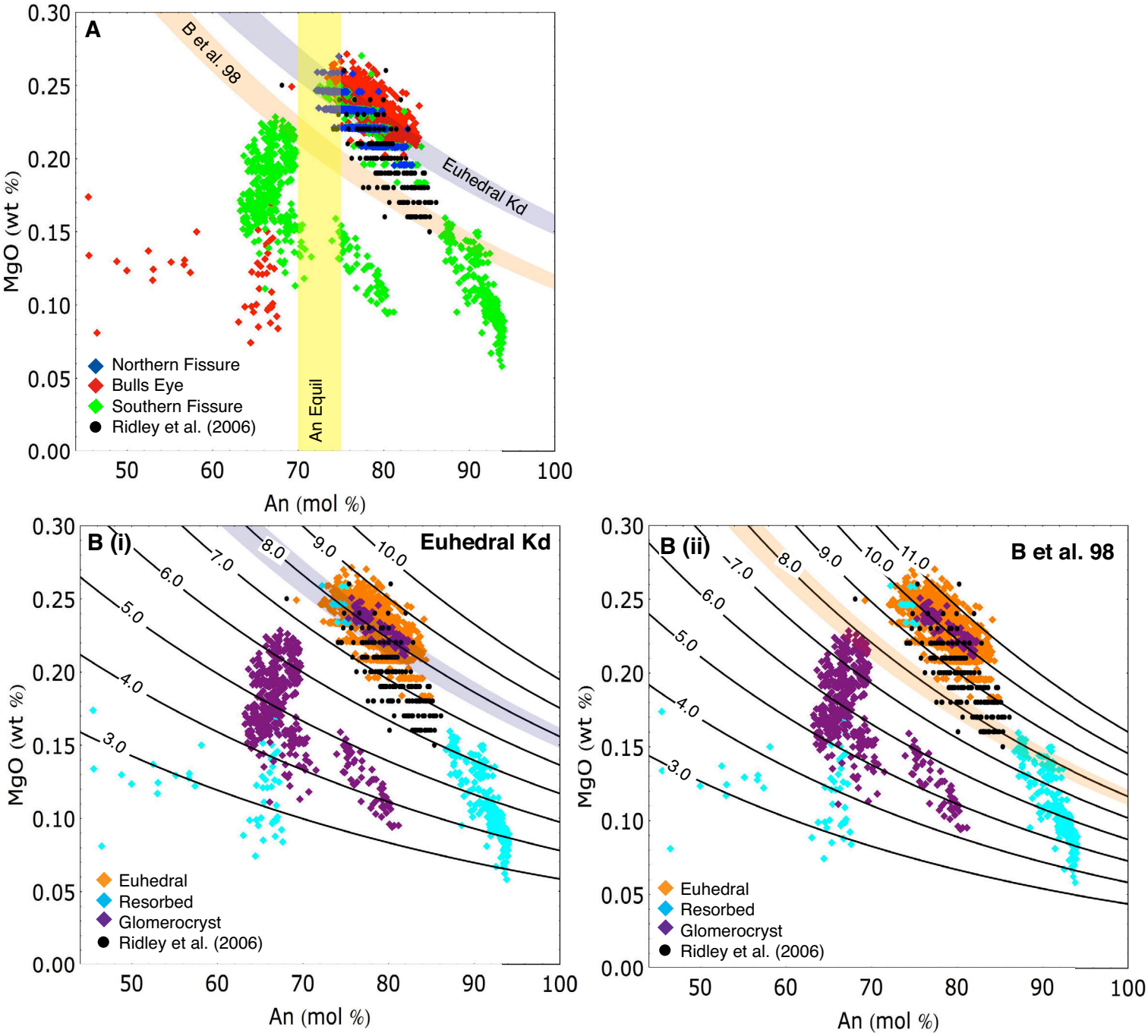

Figure 9. Plots of MgO against An content separated via **A**: Region and **B**: Texture. Plagioclase data from a xenolith from 1991 lavas (Ridley et al., 2006) is shown for comparison. In plot **A**, the yellow band represents the calculated range of equilibrium An contents averaged from all methods ($An_{70\text{-}75}$), the blue and orange diagonal bands represent the calculated MgO content in equilibrium with the host melts, where "Euhedral Kd" is using Kd_{Mg} defined by the euhedral plagioclase (Equation 1), and "B et al. 98" is using the Kd_{Mg} from Bindeman et al. (1998). The host melt compositions are the maximum and minimum values from bulk glass analysis by Goss et al. (2010; Table A.5). In plot **B**, the black diagonal lines represent the calculated MgO content in equilibrium with the stated melt concentration using the Kd_{Mg} from (i) euhedral plagioclase, and (ii) Bindeman et al. (1998; numbers on line). A temperature of 1200°C is used for all calculation, although it is noted temperature decreases with decreasing An and melt MgO content, and hence will decrease the partition coefficients and alter the calculated equilibrium melt compositions. A change in temperature of 50°C will change the Kd and calculated melt compositions by ~ 12 %. Note: due to software problems, the MgO data from the Northern Fissure and seven profiles from the Southern Fissure are rounded to two decimal places (Appendix A.1.1), and the MgO data from Ridley et al. (2006) is to two decimal places.

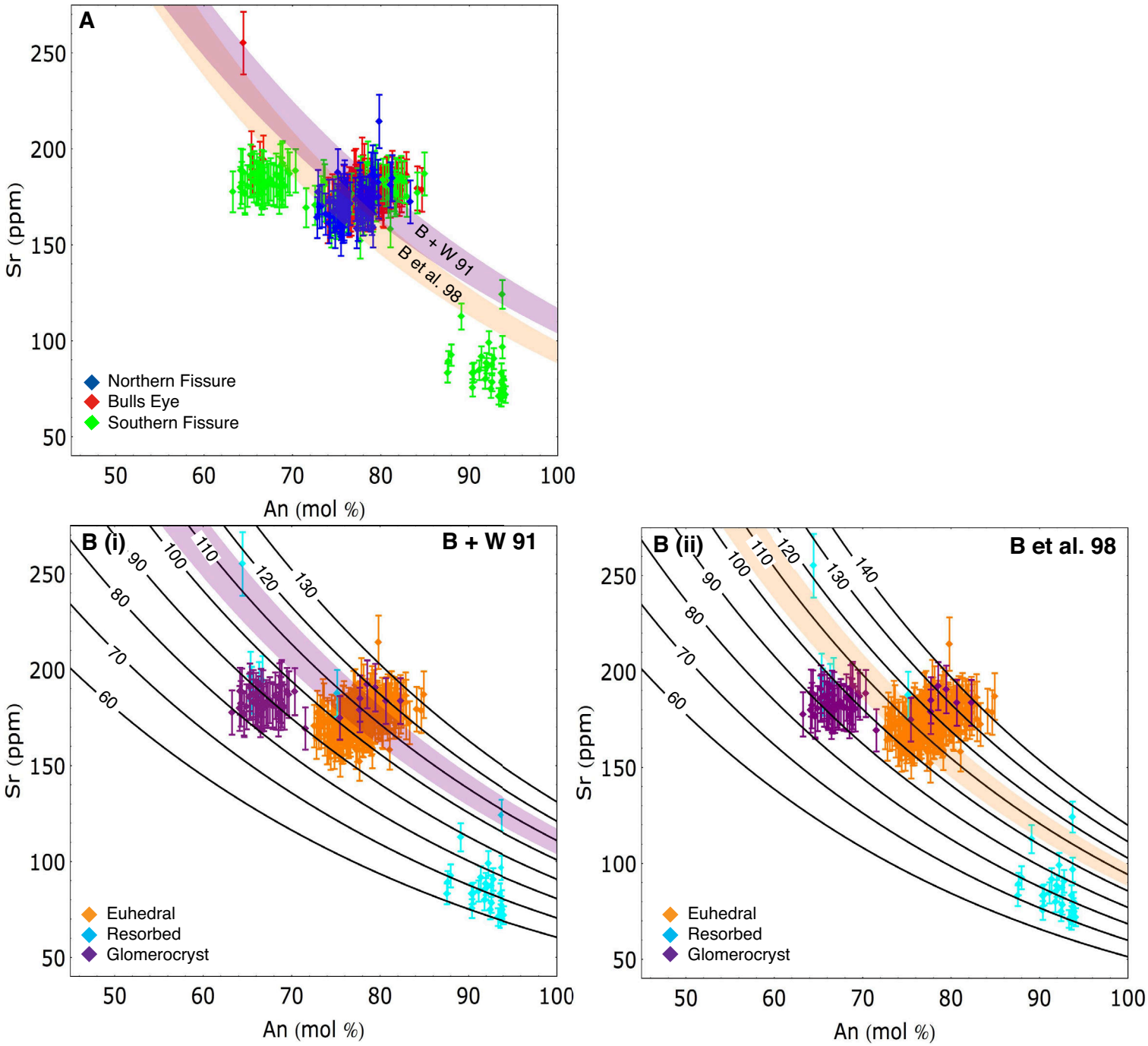

Figure 10. Plots of Sr against An content separated via **A**: Region and **B**: Texture. In plot **A**, the purple and orange diagonal bands represent the calculated Sr content in equilibrium with the host melts, where "B+W 91" and "B et al. 98" is using the Kd_{Sr} taken from Blundy and Wood (1991) and Bindeman et al. (1998) respectively. In plot **B**, the black diagonal lines represent the calculated Sr content in equilibrium with stated melt concentration using the Kd_{Sr} from (i) Blundy and Wood (1991) and (ii) Bindeman et al. (1998; numbers on line). A temperature of 1200°C is used for all calculations and melt concentrations are the maximum and minimum taken from LA-ICP-MS glass analysis and bulk glass data from Goss et al. (2010; Table A.5). Error bars represent the precision (6.5 %) of Sr analyses by LA-ICP-MS (Section 2.2.2).

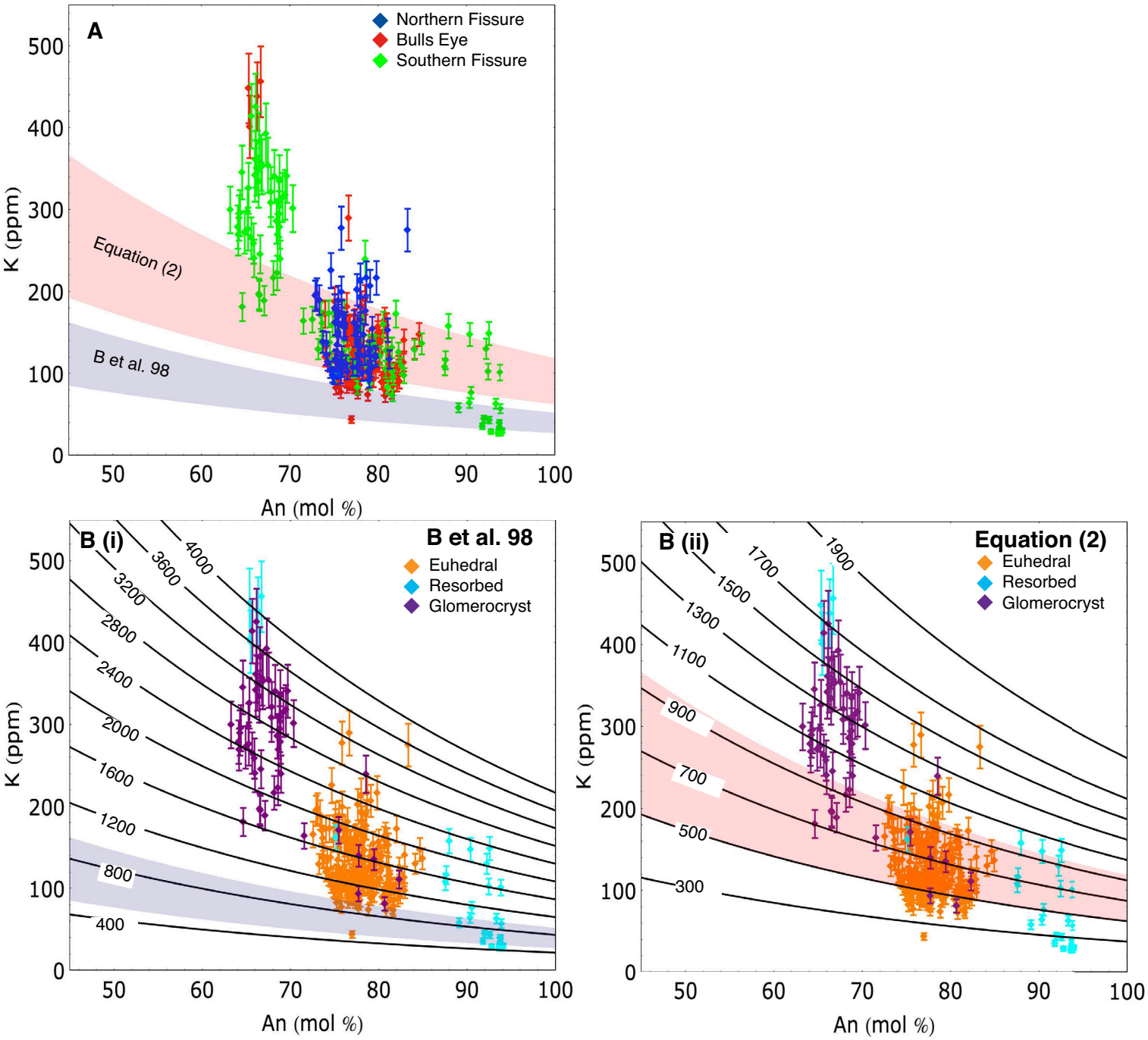

Figure 11. Plots of K against An content separated via **A**: Region and **B**: Texture. In plot A, the red and purple diagonal bands represent the calculated K content in equilibrium with the host melts,where "Euhedral Kd" is using Kd_K defined by the euhedral plagioclase, and "Equation (2)" is using the Kd_K from Equation (2) which is based on the model of Elkins and Grove (1990) and the Kd_K data from Aigner-Torres et al. (2007). In plot **B**, the black diagonal lines represent the calculated K content in equilibrium with stated melt concentration using the Kd_K from (i) Bindeman et al. (1998), and (ii) Equation (2; numbers on line). A temperature of 1200°C is used for all calculations and melt concentrations are the maximum and minimum taken from LA-ICP-MS glass analysis and bulk glass analysis from Goss et al. (2010; Table A.5). Error bars represent the precision (9.2 %) of K analyses by LA-ICP-MS (Section 2.2.2).

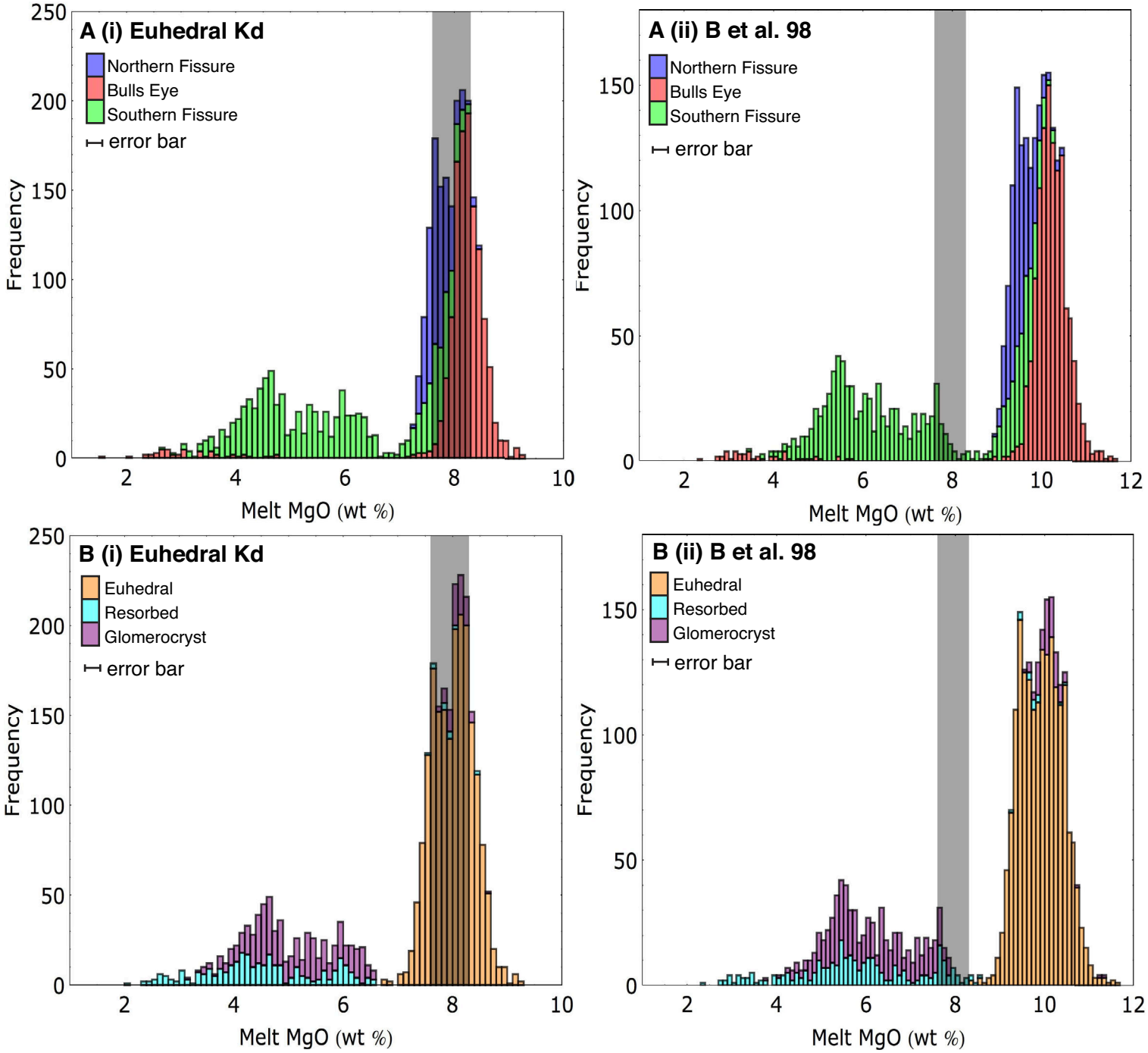

Figure 12. Histogram of the frequency of calculated melt MgO concentrations in equilibrium with plagioclase analyses separated via **A**: Region, and **B**: Texture. The melt MgO concentrations are calculated using the Kd_{Mg} from (i) defined by euhedral plagioclase, and (ii) Bindeman et al. (1998), at a temperature of 1200°C. The grey band represents the MgO melt concentrations found in the host melt and are taken from bulk glass analysis in Goss et al. (2010; 7.73-8.28 wt % MgO; Table A.5). The error bar represents the precision (4 %) of MgO analyses by EMP (Section 2.2.1).

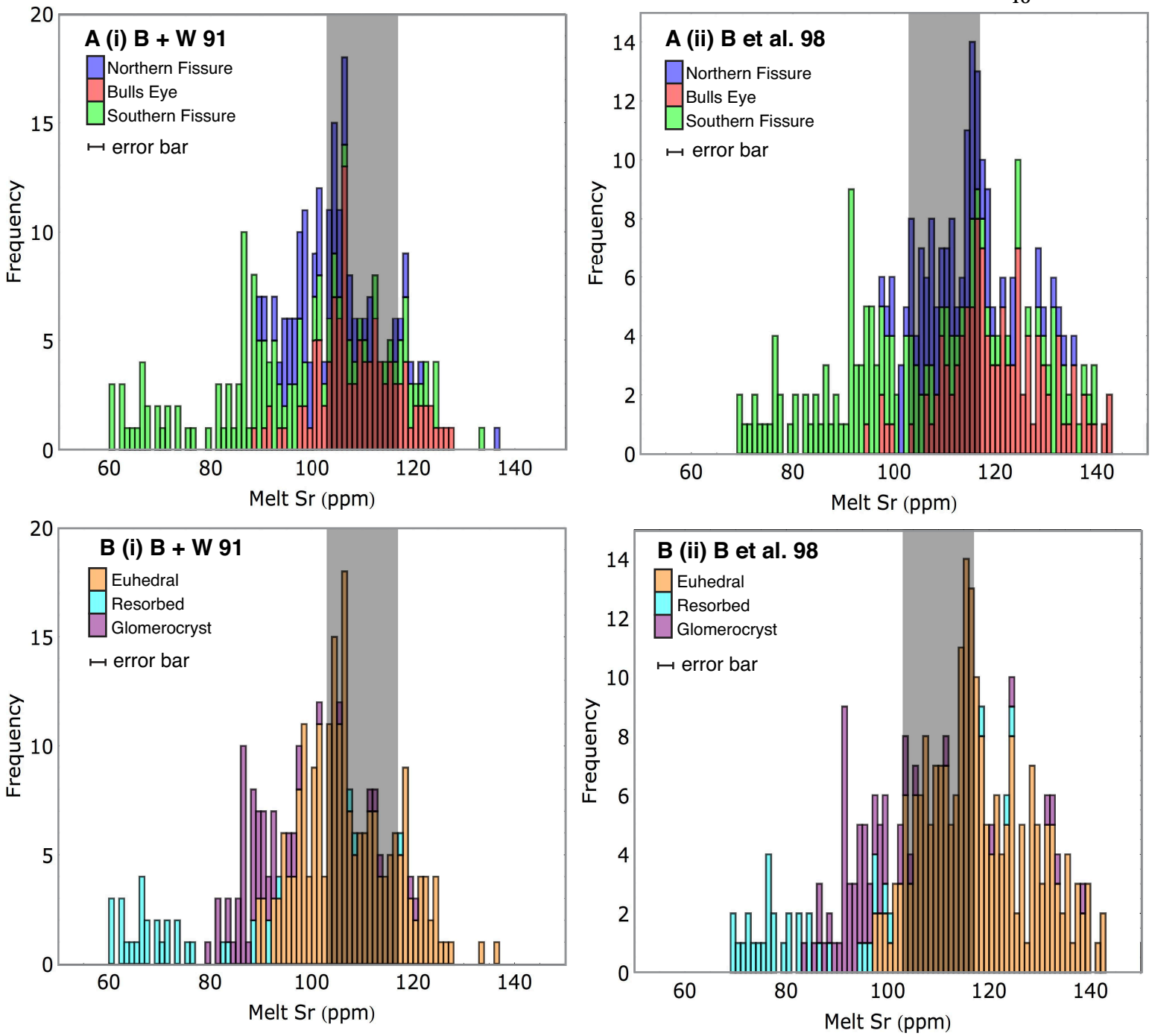

Figure 13. Histogram of the frequency of calculated melt Sr concentrations in equilibrium with plagioclase analyses separated via **A**: Region, and **B**: Texture. Melt Sr concentrations are calculated using the Kd_{Sr} defined by equations in (i) Blundy and Wood (1991), and (ii) Bindeman et al. (1998), at a temperature of 1200°C. The grey band represents the Sr melt concentrations found in the host melt and are taken from glass analysis by LA-ICP-MS (103 ± 6.7 ppm to 113 ± 7.3 ppm) and bulk glass data from Goss et al. (2010; 103 ± 3.1 ppm to 117 ± 3.5 ppm; Table A.5). The error bar represents the precision (6.5 %) of Sr analyses by LA-ICP-MS (Section 2.2.2).

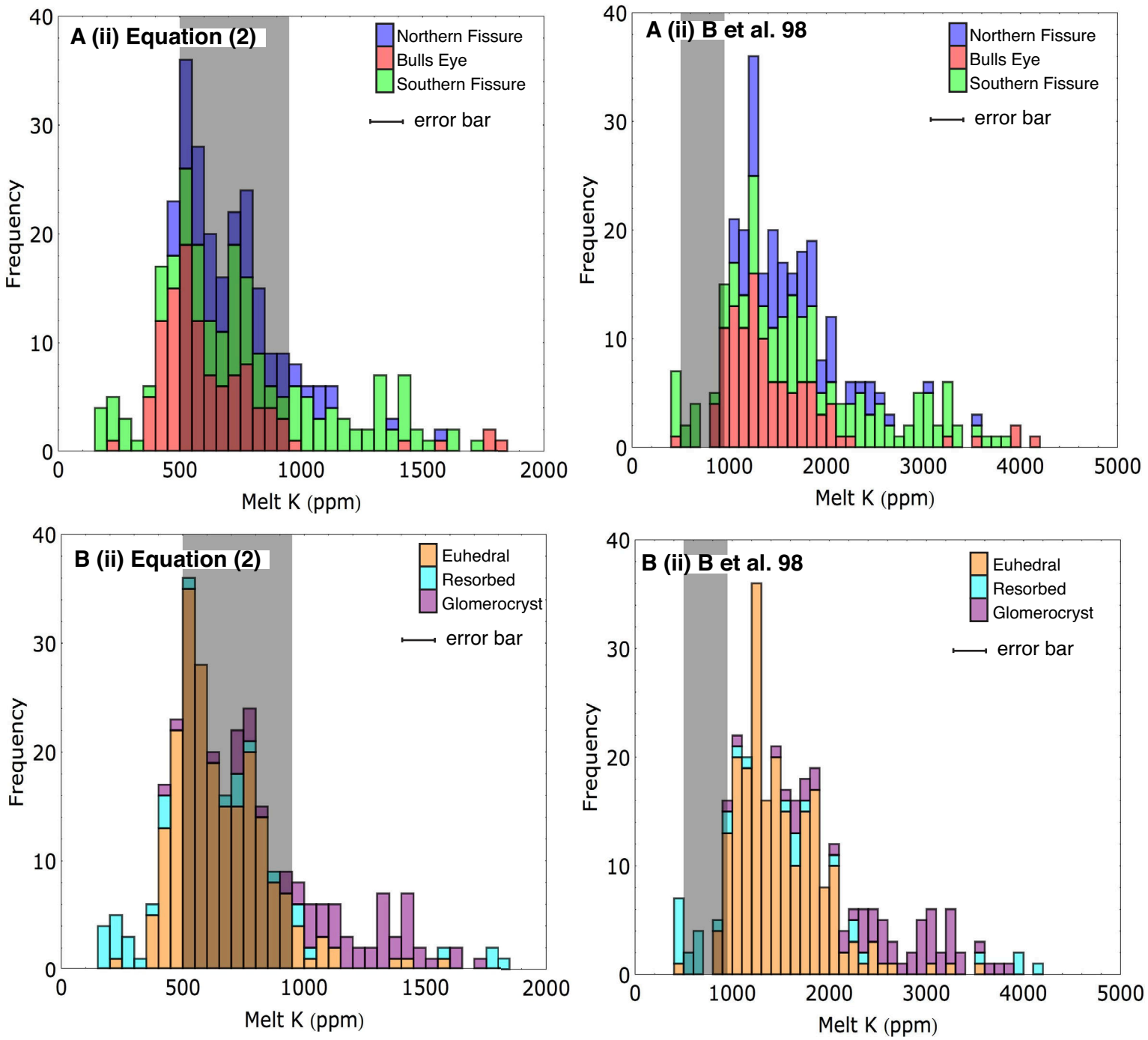

Figure 14 Histogram of the frequency of calculated melt K concentrations in equilibrium with plagioclase analyses separated via **A**: Region, and **B**: Texture. Melt K concentrations are calculated using the Kd_K defined by (i) Equation (2) using the model in Elkins and Grove (1990) and Kd_K data in Aigner-Torres et al. (2007), and (ii) Bindeman et al. (1998), at a temperature of 1200°C. The grey band represents the K melt concentrations found in the host melt and are taken from glass analysis by LA-ICP-MS (500 ± 70 ppm to 950 ± 133 ppm) and bulk glass data from Goss et al. (2010; 860 to 870 ppm; Table A.5). The error bar represents the precision (9.2 %) of K analyses by LA-ICP-MS (Section 2.2.2).

to the An contents found within euhedral plagioclase, resorbed plagioclase, and those within glomerocrysts from the Bull's eye and Southern Fissure (Figure 9).

Euhedral plagioclase have An contents within the range of An_{73-84}, which are up to 14 mol % greater than the An content calculated to be in equilibrium with the host melt (An_{70-75}; yellow band in Figure 9A). This suggests the crystals grew from a more primitive melt and a higher melt temperature, and/or a higher Ca/Na melt, and/or a magma with a higher H_2O content (Fisk, 1984; Panjasawatwong et al., 1995; Sisson and Grove, 1993). The MELTs algorithm was used to model differentiation of a primitive MORB composition taken from an average of 39 primitive MORB glasses from Atlantic and Pacific Oceans (Presnall and Hoover, 1987). Plagioclase with An contents matching the most primitive observed in euhedral crystals (~ An_{82-84}), was found to crystallise at a temperature of ~ 1220°C assuming zero water content, or in a melt with 0.6 wt % H_2O at a temperature of ~ 1200°C. This H_2O content is ~0.4 wt % higher than those measured within 2005-06 lavas by Soule et al. (2012). This suggests that plagioclase with An contents within this range (~ An_{82-84}) are unlikely to have crystallised from the melts erupted in 2005-06.

A total of four resorbed plagioclase crystals were analysed, one in the Northern Fissure, two in the Bull's eye, and one in the Southern Fissure. The resorbed crystal in the Northern Fissure has An contents of An_{72-75} which are within the range calculated to be in equilibrium with the host melt (An_{70-75}). The first resorbed crystal in the Bull's eye has an An content of An_{50-67}, which is up to 26 mol % lower than equilibrium values. This indicates it grew from a more evolved melt and a lower melt temperature, and/or a melt with a lower Ca/Na. The second resorbed crystal in the Bull's eye has An contents between An_{81-84} which is within the range found in euhedral crystals (An_{73-84}). The resorbed plagioclase crystal from the Southern Fissure has an An content between An_{87-94}, which is up to 18 mol % higher than equilibrium values (Figure 9B). Plagioclase with An contents over An_{90} are not uncommon within mid ocean-ridge basalts, although they have not been experimentally reproduced from even the most primitive MORB starting material (e.g. Muir and Tilley, 1964; Ribbe, 1975; Natland, 1989; Allan et al., 1989; Sinton et al. 1993; Nielsen et al. 1995; Kohut and Nielsen, 2003; Adams et al., 2011).

Two plagioclase crystals were analysed from the glomerocryst in the Bull's eye and have cores of ~ An_{80} decreasing to rims of ~ An_{75}. These An contents are up to 10 mol % higher than equilibrium values, but are within the range found in euhedral plagioclase (An_{73-84}; Figure 9B). Seven plagioclase crystals were analysed in the glomerocryst from the Southern Fissure and have An contents in the range of An_{63-70}, with four crystal cores containing between An_{73-81} (Figure 9). These are up to 12 mol % lower than equilibrium values, indicating they grew from a more evolved melt and a lower melt temperature, and/or a melt with a lower Ca/Na. The An contents within plagioclase from the 1991 xenolith are between An_{70-87} (Ridley et al., 2006). Note, the range of An contents published in Ridley et al. (2006) are incorrectly reported as being between An_{70-94} due to errors in the An calculation on some analyses. The ranges reported here are calculated using the plagioclase data from Ridley et al. (2006). The An contents in the 1991 xenolith are similar to those found in the Bull's eye glomerocryst, but are up to 24 mol % higher than those in the glomerocryst from the Southern Fissure.

2.5.1.2 Disequilibria observed in plagioclase Mg, Sr, and K contents

The partition coefficients of Mg, Sr, and K increase with decreasing An content (Section 2.4.2.3), therefore crystals in intra-crystalline equilibrium will have low MgO, Sr, and K contents in portions of crystals with high An contents, and higher concentrations of these elements in more albitic portions of the crystal. Crystals that are in equilibrium with each other (i.e. inter-crystalline equilibrium) should have trace element data that fall parallel to the constant melt contour lines (Figures 9-11B). These contour lines represent the MgO, Sr, or K contents of plagioclase in equilibrium with a constant MgO, Sr, or K melt content. The following sections discuss evidence of intra- and inter-crystalline disequilibrium in euhedral plagioclase, followed by the resorbed plagioclase, and plagioclase in the glomerocrysts from the Bull's eye and Southern Fissure. Each section discusses in detail the calculated equilibrium melt concentrations in plagioclase that are different to those found in their host melts. Table 1 provides a summary of the number and location of crystals with MgO, Sr and K contents at crystal rims or cores that are out of equilibrium with those found in their host melts. Those

crystals showing significant disequilibria with their host melt are modelled in Section 2.6 to determine timescales of magma mixing.

Table 1. A summary of the number (#) and location of plagioclase crystals with cores, rims, or the entire crystal with MgO, Sr or K contents out of equilibrium with its host melt. Highlighted in red are the entire crystals, rims or cores that have equilibrium melt compositions different to their host melt. The corresponding rim and core equilibrium melt compositions are also shown, along with the range of melt compositions in each region from glass analysis by LA-ICP-MS and bulk glass data by Goss et al. (2010; Table A.5; Note, no reported error for glass K data from Goss et al., 2010). Equilibrium melt compositions are calculated using the partition coefficient from Equation 1 for Mg, the equation in Blundy and Wood (1991) for Sr, and Equation (2) for K.

Crystal Texture	Element	Location	#	Equilibrium Melt Contents			Host melt composition
				Rim	Core	Entire	
Euhedral	MgO (wt %)	*Northern Fissure*	0	-	-	-	7.76 to 7.78
		Bull's eye	5	7.8-8.1	8.4-8.8	-	8.02 to 8.28
			1	8.6	8	-	
		Southern Fissure	1	7.9	7	-	7.73 to 7.94
	Sr (ppm)	*Northern Fissure*	6	104-115	90-97	-	104 ± 6.7 to 110 ± 7.1
			2	90-98	104-108	-	
			1	-	-	100	
		Bull's eye	3	121-120	105-115	-	103 ± 6.7 to 113 ± 7.3
			6	107-115	94-125	-	
		Southern Fissure	1	-	-	120	106 ± 6.9 to 117 ± 3.5
			3	100-110	120-133	-	
			1	96	106	-	
	K (ppm)	*Northern Fissure*	3	600-890	950-1150	-	590 ± 82 to 880
			1	680	460	-	
		Bull's eye	2	-	-	450	500 ± 70 to 900 ± 126
			2	400-450	500-550	-	
		Southern Fissure	3	770-900	400-450	-	870 ± 80 to 950 ± 133
Resorbed	MgO (wt %)	*Northern Fissure*	0	-	-	-	7.76 to 7.78
		Bull's eye	1	-	-	3.0	8.02 to 8.28
		Southern Fissure	1	4.3-6.3	4.3	-	7.73 to 7.94
	Sr (ppm)	*Northern Fissure*	0	-	-	-	104 ± 6.7 to 110 ± 7.1
		Bull's eye	1	-	-	95	103 ± 6.7 to 113 ± 7.3

		Southern Fissure	1	-	-	60-80	106 ± 6.9 to 117 ± 3.5
	K (ppm)	*Northern Fissure*	0	-	-	-	590 ± 82 to 880 ± 26
		Bull's eye	1	-	-	1600	500 ± 70 to 900 ± 126
		Southern Fissure	1	-	-	250	870 ± 80 to 950 ± 133
Glomerocryst	**MgO (wt %)**	*Southern Fissure*	7	3.8-4.3	4.5-6.3	-	7.73 to 7.94
	Sr (ppm)		1	96	83	-	106 ± 6.9 to 117 ± 3.5
			4	-	-	85-91	
			2	85-95	120	-	
	K (ppm)		3	700-750	1080	-	870 ± 80 to 950 ± 133
			4	-	-	1100-1400	

2.5.1.2.1 EUHEDRAL PLAGIOCLASE

The majority of euhedral plagioclase have MgO, Sr, and K contents that fall within the region of concentrations calculated to be in equilibrium with their host melts (Figures 9-11B(i)). However, a number of crystals provide evidence of being out of equilibrium with their hosts, and are described in the following paragraphs.

The MgO contents in most euhedral crystals are parallel to the contour lines representing constant MgO melt contents, indicating they are in inter-crystal equilibrium (Figure 9B; Table 1). The euhedral crystals from the Bull's eye have slightly higher MgO contents at the same An content than those from the Southern or Northern Fissure (Figure 9A). This is consistent with the melt in the Bull's eye having a slightly higher MgO content (8.02-8.28 wt % compared to 7.73-7.94 wt %). As noted in Section 2.4.2.3, there is a clear overall trend of increasing MgO content with decreasing An within the euhedral plagioclase crystals from all regions, indicating they are close to being in internal equilibrium (i.e. intra-crystalline equilibrium; Figure 9A). This is the case whether the Kd_{Mg} is taken from Bindeman et al. (1998), or from Equation (1). However, there are seven euhedral crystals (six in the Bull's eye and one in the Southern Fissure) with MgO contents in internal disequilibria, i.e. with concentrations at their core or rim in equilibrium with a different MgO melt content than their host melt (Table 1). Six

euhedral plagioclase in the Bull's eye have MgO contents either at the rim (n=1), or the core (n=5), in equilibrium with a melt containing up to 8.8 wt % MgO (Figure 12B(i)). The corresponding rim/core of each crystal having MgO contents in equilibrium with a similar MgO content to its host melt (8.02-8.28 wt % MgO). One euhedral crystal from the Southern Fissure has MgO contents at rims in equilibrium with a similar MgO content to its host melt. However, its core is in equilibrium with a 7.0 wt % MgO melt, which is 0.90 wt % lower than its host melt (Figure 12B(i)). These seven crystals with MgO contents displaying internal disequilibria are modelled in Section 2.6 to determine timescales of magma mixing.

Within euhedral plagioclase, different Sr concentrations are found at the same An content suggesting that inter-crystalline disequilibria may exist within the population (Figure 10). The Sr concentrations from all regions do not show any clear correlation with the anorthite content, which may suggest intra-crystalline disequilibria, or may reflect analytical precision limits (Figure 10A). There are a total of twenty-three euhedral plagioclase with Sr contents at rims, cores or the entire crystal in equilibrium with either a higher or lower Sr melt than its host (Table 1). Ten of these crystals have equilibrium melt Sr contents within analytical uncertainty of the range found in the host melts (103 ± 6.7 ppm to 117 ± 3.5 ppm; Table 1). Therefore, they may represent variations in Sr host melts contents. The remaining thirteen plagioclase have Sr contents at rims or cores in equilibrium with a lower (90-96 ppm; n=10), or higher (122-133 ppm; n=3) Sr melt than the range found in the host (103 ± 6.7 ppm to 117 ± 3.5 ppm; Figure 13(i); Table 1). This suggests that melts containing different Sr contents to those erupted at the surface were involved in the history of these crystals.

The K contents in euhedral plagioclase show a scattered trend of increasing K contents with decreasing An content, suggesting the majority of crystals are close to being in internal equilibrium (Figure 11). A number of K profiles in euhedral plagioclase show spikes of higher K concentrations in an otherwise homogeneous K profile. These likely reflect LA-ICP-MS analyses of altered material in cracks and are not thought to represent disequilibria within the crystal, although they are shown in Figures 11 and 14. Outside of these analyses, there are a number (n=11) of euhedral crystals with K contents in equilibrium with a lower or higher K melt than their host melt. Six of these crystals

have equilibrium K melt concentrations at their core, rims, or entire crystal that are within the analytical error of the range found in the host melts (500 ± 70 ppm to 950 ± 87 ppm; Table 1). These equilibrium melt concentrations could reflect K variations within the host melt. The remaining five crystals are in internal disequilibrium, with equilibrium melt contents at rims or cores that are higher (~ 1150 ppm; n=2), or lower (~ 400 ppm; n=3) than the range found within their host melts (500 ± 70 ppm to 950 ± 133 ppm; Figure 14B(i); Table 1). This suggests the involvement of melts both higher and lower in K than those erupted at the surface.

In summary, the majority of euhedral plagioclase have MgO, Sr and K contents in equilibrium with the melt that brought them to the surface. However, six crystals from the Bull's eye lavas provide evidence of a more primitive melt (8.8 wt % MgO) than its host, and one crystal from the Southern Fissure provides evidence of a more evolved melt (7.0 wt % MgO) than its host. Euhedral plagioclase from all three regions suggest that melts with Sr and K contents both higher (~ 133 ppm Sr, ~ 1150 ppm K), and lower (~ 90 ppm Sr, ~ 400 ppm K) than those observed in the erupted lavas were involved in the history of these crystals. There is little consistency seen in Mg, Sr and K elemental trends within the same crystal. Modelling is completed on those crystals displaying pronounced internal disequilibria in order to determine timescales of magma mixing (Section 2.6).

2.5.1.2.2 RESORBED PLAGIOCLASE

A total of four resorbed plagioclase were analysed; one in the Northern Fissure, two in the Bull's eye, and one in the Southern Fissure. The resorbed crystal from the Northern Fissure has MgO, Sr, and K contents in equilibrium with its host melt (Figure 9-11), consistent with An contents (An_{72-75}) being within the range of equilibrium An values (Section 2.5.1.1). This suggests the crystal may have been resorbed by a melt with a different composition, prior to being entrained into its host melt. The first resorbed crystal in the Bull's eye has MgO contents in equilibrium with its host melt (Sr and K contents not analysed). Its equilibrium An contents (An_{82-85}) are higher than those calculated to be in equilibrium with its host but are within the range found in the euhedral crystals (Section 2.5.1.1; Figures 9-11). In contrast, the remaining two resorbed crystals have

MgO, Sr, and K contents that are substantially outside those determined to be in equilibrium with their host melts (Figure 9-11). Their MgO, Sr and K contents also do not follow a trend that is parallel to the contour lines representing constant MgO, Sr, and K melt contents, indicating they are in intra-crystalline disequilibria (Figure 9-11B(i)). This supports the textural evidence and indicates they must have a different history to the euhedral crystals. The second resorbed crystal from the Bull's eye has MgO, Sr and K contents in equilibrium with a much more evolved melt containing ~ 3.0 wt % MgO, 95 ppm Sr, and 1600 ppm K (Figures 12-14(i); Table 1). These evolved melt compositions are consistent with the crystal having lower An contents (An_{50-65}) than equilibrium values (Section 2.5.1.1). The resorbed crystal from the Southern Fissure has MgO and Sr contents in equilibrium with a melt containing lower MgO (4.3-6.3 wt %), Sr (60-80 ppm) and K (~ 250 ppm) contents than its host (Figures 12-13B(i); Table 1). These low MgO melt contents contradict the suggested primitive melt composition required to explain it's very high An contents (An_{87-94}; Section 2.5.1.1). This high An, low MgO resorbed plagioclase has a particularly complex history which is discussed in detail in Section 2.6.2.2.

In summary, two resorbed crystals have MgO, Sr, and K contents in equilibrium with their host melts. One resorbed crystal has MgO, Sr, K and An contents in equilibrium with its host melt indicating it may have been resorbed in a different melt composition to its host. Two resorbed crystals provide evidence of being in equilibrium with much more evolved melts (3.0-6.3 wt % MgO, 60-95 ppm Sr) than their host melts. These crystals are modelled in Section 2.6 in order to retrieve timescales of magma mixing processes.

2.5.1.2.3 GLOMEROCRYSTS

Two plagioclase crystals were analysed in the glomerocryst from the Bull's eye and have MgO, Sr, and K contents that are similar to those found in euhedral plagioclase (Figure 9-11). This is consistent with their An contents (An_{80-75}) being within the range found in euhedral crystals, although they are higher than the An range calculated to be in equilibrium with their host melts (Section 2.5.1.1).

Seven plagioclase crystals were analysed in the glomerocryst from the Southern Fissure. The majority of their MgO, Sr, and K contents do not follow a trend that is parallel to the contour lines of constant MgO, Sr, and K melt contents (Figure 9-11B(i)). This suggests they are not in internal equilibrium, and supports the textural evidence which indicates they must have a different history to the euhedral crystals. Their MgO and Sr contents are lower than the euhedral crystals from all geographic areas, and are outside the range calculated to be in equilibrium with their host melt, indicating they equilibrated with a more evolved melt (Figures 9-10B(i)). Plagioclase from this glomerocryst have MgO concentrations at their rims in equilibrium with a melt of between 3.8-4.3 wt % MgO (Figure 12B(i); Table 1). Whereas the MgO contents within plagioclase cores, or at rims in contact with the olivine, are in equilibrium with a 4.5-6.3 wt % MgO melt. This is up to ~ 4 wt % lower than those found in the host melt in the Southern Fissure (7.73-7.94 wt %; Table 1). The majority of crystals (n=5) are in equilibrium with a lower Sr melt (83-96 ppm) than their host, with two crystal cores in equilibrium with a higher Sr melt (>120 ppm; Figure 13B(i); Table 1). Their K concentrations are higher than euhedral plagioclase, and are in equilibrium with a melt containing up to 1400 ppm K using the Kd_K from Equation (2), which is up to 450 ppm higher than the host melt (Figure 14B(i); Table 1). Using the Kd_K from Bindeman et al. (1998) they are in equilibrium with a melt containing up to 3600 ppm (Figure 14B(ii)).

In summary, the plagioclase crystals from the glomerocryst in the Southern Fissure have equilibrated with a highly evolved melt (3.8-6.5 wt % MgO, 83-96 ppm Sr, and 700-1400 ppm K). These concentrations are similar to those found to be in equilibrium with two of the four resorbed crystals discussed above. The textures and evolved equilibrium melt contents of these crystals suggest the glomerocryst and resorbed crystals may have resided in an evolved crystal mush zone. It is likely the crystals were mixed into their host melts not long prior to eruption due to the important observation of their crystal rims being out of equilibrium with their host melt. These mixing times are quantified by modelling their zoning profiles in Section 2.6. The plagioclase within the Bull's eye glomerocryst have MgO, Sr, and K contents in equilibrium with its host melt. The geochemistry and texture of this glomerocryst suggests an origin in a primitive crystal-mush zone.

2.5.2 Evidence of intra- and inter- crystalline disequilibria seen through measured concentrations of Fo, Mn, Ni, and Cr within olivine

Three euhedral olivine crystals in the Bull's eye, and the olivine within glomerocrysts from the Bull's eye and Southern Fissure were analysed. The olivine forsterite, MnO, NiO and Cr contents in equilibrium with the host melt was calculated using the methods described in Section 2.4.2.4. A maximum difference of 5 mol % Fo is found between these different methods for a melt of the same composition. A maximum difference of 1.5 mol % Fo is found between the different melt compositions erupted in 2005-06 (Goss et al., 2010) using the same method. The minimum and maximum equilibrium Fo contents using all methods and for all the melt compositions is $Fo_{82.3}$ and $Fo_{87.8.}$ The calculated equilibrium Ni contents varies by 0.06 wt % between the four methods for a melt of the same composition, and varies by 0.09 wt % between the range of 2005-06 melt compositions analysed by Goss et al. (2010) and by LA-ICP-MS, using the same method. The minimum and maximum equilibrium NiO olivine values from all methods and for all melt compositions are 0.067 wt % and 0.22 wt %. The equilibrium MnO and Cr contents were each calculated using one method. The minimum and maximum MnO and Cr olivine concentrations in equilibrium with melts of differing compositions are 0.17 wt % and 0.27 wt %, and 220 ppm and 305 ppm respectively.

All olivine crystals (n=5) within the Bull's eye, including those within the glomerocryst, have forsterite contents of $Fo_{85\text{-}86.}$ These are within the range calculated to be in equilibrium with their host melt and are similar to the forsterite content of olivine found within the xenolith in the 1991 lavas ($Fo_{86\pm0.3}$; Ridley et al., 2006). All but one olivine within the Bull's eye are unzoned in Fo, MnO (0.18-0.20 wt %), NiO (0.17-0.18 wt %), and Cr (240-285 ppm), indicating that they are in intra-crystalline equilibrium. These MnO, NiO, and Cr contents are within the range calculated to be in equilibrium with their host melts. Calcium ranges between 0.3-0.46 wt %, and increases by 0.04-0.06 wt % in the outer 35 μm of olivine crystals adjacent to high CaO phases (i.e. glass or plagioclase). Part of this signal may represent compositional zoning in the olivine, although the majority is likely a consequence of the effects of secondary X-ray

fluorescence from the adjacent Ca-rich phase during EMP analysis (Dalton and Lane, 1996), and is not considered further here. One euhedral olivine from the Bull's eye displays slight normal zoning with a core of Fo_{86} and a rim of $Fo_{85.5}$, indicating it is in intra-crystal disequilibria. Trace element profiles show similar, but more pronounced, zoning with MnO increasing from core-to-rim (0.19 to 0.21 wt %), and NiO (0.22 to 0.16 wt %), Cr (390 to 220 ppm), and Al_2O_3 (0.075 to 0.05 wt %) decreasing from core-to-rim (Appendix A.5.2.3; 4203_2 Ol3). The divalent elements appear to be less zoned than Cr or Al_2O_3, with differences between the core and rim compositions of 0.6, 9.5 and 27 % for Fo, MnO, and NiO respectively, compared to 44 % in Cr and 33 % in Al_2O_3. This is discussed further in Section 2.6, where the profiles are modelled to extract timescales. The MnO and NiO concentrations of this crystal are within the range calculated to be in equilibrium with its host melt. The Cr contents at the olivine rims are within the range calculated to be in equilibrium with its host, however its core contains up to 170 ppm higher Cr than equilibrium values. This suggests the involvement of a melt containing higher Cr contents (~ 410 ppm) than the range found in its host (266-318 ppm).

Olivine is only present within a glomerocryst in the Southern Fissure. The olivine crystals within the glomerocryst have normally zoned Fo profiles, with cores of Fo_{75-79} decreasing to rims of Fo_{72-73}. This is up to ~ 16 mol % lower than the range of forsterite contents calculated to be in equilibrium with their host melt ($Fo_{82.3}$ and $Fo_{87.8}$). The MgO content of the melt in equilibrium with these forsterite contents are calculated using the methods described in Section 2.4.2.4. A maximum difference of 1.2 wt % MgO is seen between methods for an olivine of the same forsterite composition. An olivine of Fo_{72} is found to be in equilibrium with a melt of between 3.5-4.5 wt % MgO, and an olivine of Fo_{77} to be in equilibrium with a melt of between 4.3-5.5 wt % MgO. These MgO melt compositions are similar to the range calculated to be in equilibrium with the plagioclase from this glomerocryst (Section 2.5.1). Trace elements show similar zoning patterns with Mn increasing from core-to-rim (0.3 to 0.38 wt %), and NiO (0.11 to 0.06 wt %), CaO (0.36 to 0.28 wt %), and Cr (120 to 20 ppm), decreasing from core-to-rim. The Mn concentrations are > 0.1 wt % higher than those calculated to be in equilibrium with the host melt, indicating the olivine equilibrated with a melt containing higher MnO concentrations than its host melt (0.22-0.26 wt %). Chromium concentrations in the

olivine (120-20 ppm) are lower than those calculated to be in equilibrium with its host melt by between 100 and 285 ppm. The Cr content at the rims of the crystal are in equilibrium with a ~ 20 ppm melt, whereas the core is in equilibrium with a ~ 125 ppm melt, which are lower than the range found in its host melt (278-320 ppm). The Ni concentrations however, are within the range calculated to be in equilibrium with the host melt.

The Fo, Mn and Cr content of olivine crystals in the glomerocryst from the Southern Fissure suggest they equilibrated with a more evolved melt than its host. This supports the evidence from plagioclase in the glomerocryst which indicates they equilibrated with a melt containing < 3.5 wt % MgO. Nickel contents in the olivine are higher than expected for such an evolved melt and are in equilibrium with a melt containing Ni content similar to that of its host. This could be explained by a model of olivine growth within a trapped melt (e.g. Barnes et al., 1986). An olivine with an initially primitive composition (i.e. high NiO contents) is held within a more evolved trapped melt. As the olivine grows, the surrounding melt evolves to lower MgO contents and lower amounts of compatible elements (e.g Ni). The crystal reacts with the evolving residual melt resulting in a continuous change in the olivine composition in most elements, e.g. decrease in forsterite contents towards the rim. However, due to Ni being a highly compatible trace element it will prefer to remain in the olivine structure. The end result is an olivine with low Fo contents which reflect the evolving composition of the trapped melt, but with high NiO contents reflecting the initial primitive crystal composition. This model is looked at further in Section 2.6.4, where the profiles are modelled to extract timescales.

In summary, the zoning profiles observed in the olivine from the Southern Fissure glomerocryst are consistent with the plagioclase data from this glomerocryst (Section 2.5.1.2) and supports the suggestion of the glomerocryst residing in a mush zone. The glomerocryst must have been disrupted from this mush zone and incorporated into its host melt prior to eruption in 2005-06. The idea of disrupted mush zone fragments corresponds with the interpretation made for the xenolith from 1991 lavas, which is reported to contain olivine which is unzoned in forsterite (Fo_{86}), and plagioclase (An_{70-87}) with corroded rims (Ridley et al., 2006). These compositions and textures led Ridley et

al. (2006) to suggest the xenolith was a fragment from the lower crystal mush zone where it equilibrated and grew from a primitive MORB before being disrupted and entrained into its host melt. The Southern Fissure glomerocryst differs from the 1991 xenolith in their more evolved olivine and plagioclase compositions due to it residing in a more evolved mush zone, and is discussed in Section 2.6.4.1. The plagioclase and olivine from the Bull's eye glomerocryst are in equilibrium with their host melt, and contain similar compositions to the 1991 xenolith. Therefore, the Bull's eye glomerocryst may represents a fragment of a mush zone underlying the AMC, where it grew and equilibrated with melts containing similar compositions to its host prior to being disrupted.

2.6 Diffusion modelling to determine timescales of magma mixing processes

For crystals that are not in equilibrium with their host melt, diffusion modelling can be used to provide estimates of the length of time between changes in their chemical environment. For example, this could be the time between a magma mixing event, and quenching of the erupted basalt on the sea floor (e.g. Costa et al., 2003; Costa et al., 2009). The redistribution of elements via diffusion effectively stops on eruption due to the extremely slow rates of diffusion at low temperatures. Crystal residence and magma mixing timescales are derived from modelling the extent of diffusive re-equilibration of major and trace elements between crystals and melts of differing compositions. The approach requires knowledge of the boundary conditions, initial concentrations of the element of interest, and their diffusion coefficient (D). Details of the diffusion model, boundary conditions and initial conditions used for modelling plagioclase and olivine are outlined in the following sections, followed by the results of diffusion modelling for each element.

2.6.1 Diffusion modelling in plagioclase

2.6.1.1 Parameters used for diffusion modelling in plagioclase

The parameters used for the Arrhenius relationship for diffusion ($D = D_0 \text{Exp}[-E/RT]$; E is the activation energy for diffusion and D_0 is diffusion coefficient at infinite

temperature) of Mg in plagioclase is taken from LaTourrette and Wasserburg (1998). No dependence of D_{Mg} on plagioclase An content is considered (Faak et al., 2013). It is noted that using the D_{Mg} with the theoretical An dependence of Equation (8) in Costa et al. (2003) changes the value of D_{Mg} by less than a factor of two for the An range found in the modelled plagioclase phenocrysts (An_{60}-An_{93}). LaTourrette and Wasserburg (1998) showed that Mg diffusion is anisotropic, with diffusion along the *c*-direction being around three times faster than the *b*-direction. Modelled timescales reported here use D parallel to the faster *c*-axis. The Arrhenius parameters used for Sr and K in plagioclase are taken from Giletti and Casserly (1994), and Giletti and Shanahan (1997) respectively, which are dependent on the An content. A temperature of 1200°C is used for calculating all the diffusion coefficients. The concentrations measured in the core of the plagioclase are taken as the initial concentrations, and those measured at the rim as the boundary conditions. The Mg, Sr and K melt compositions for the initial and boundary conditions are calculated using the Kd_{Mg} used is from Equation (1), the Kd_{Sr} is from Blundy and Wood (1991) and the Kd_K is from Equation (2).

Trace element zoning (e.g. MgO, Sr, K) in plagioclase has been shown to be dependent on anorthite content (e.g. Bindeman et al. 1998; Blundy and Wood, 1991). The initial An zoning profile within a plagioclase will remain unchanged due to the extremely slow diffusion rates of NaSi-CaAl (Grove et al., 1984). However, the initial zoning profile of MgO, Sr or K will change over time as it attempts to equilibrate to new conditions by diffusion. This results in an equilibrium profile with high An zones having a corresponding low MgO, Sr or K content at equilibrium, and vice versa. Therefore, knowledge of the An content of a plagioclase is required in order to determine the equilibrium profile of MgO, Sr and K. In order to account for the elemental fluxes driven purely by variation in An content on the final equilibrium profile of trace element in plagioclase, the diffusion model and Equation 7 from Costa et al. (2003) are used for all elements. The types of diffusion models used and the uncertainties are outlined in the following section and Appendix A.6 provides examples and explanations of the models.

2.6.1.2 Diffusion models used and uncertainties

A small number of euhedral plagioclase have rims in equilibrium with a composition similar to their host melt, but with cores in equilibrium with a different melt composition (Section 2.5). This could be explained by the crystal growing from, or equilibrating with, one melt, before being mixed into a melt with a similar composition to its host melt. This induces relative diffusive loss or gain of the element through the crystal rims as it attempts to re-equilibrate. The time between entrainment of these crystals into its host melt and eruption onto the seafloor is constrained by modelling the distribution of trace elements.

A number of euhedral and resorbed plagioclase, plus those within the glomerocryst from the Southern Fissure, have MgO, Sr or K contents at their rims that are out of equilibrium with their host melt (Table 1). For plagioclase that display disequilibria between crystal rims and their host melt, a maximum time between mixing of the crystals into their host and eruption onto the seafloor can be calculated. This is determined by establishing the time it would take for the trace element disequilibria seen between the rims and melt to be erased by diffusion. The results of this depend on the spatial resolution of the analysed transect. Concentrations of trace elements within ~ 5 µm of a crystal rim are retrieved from those analysed by EMP (e.g. MgO in plagioclase), compared to within ~ 30 µm of a rim from those analysed by LA-ICP-MS (e.g. Sr in plagioclase; Section 2.2). This will result in shorter maximum times being modelled for those trace elements analysed using EMP, and longer times for those analysed by LA-ICP-MS.

The main uncertainty associated with the calculations is the temperature estimation. An increase in temperature from 1200°C to 1250°C increases the diffusion coefficient of Mg, Sr and K by a factor of ~ 2, which will decrease timescales by a factor of ~ 2. The partition coefficients of Mg, Sr and K are required to calculate the equilibrium and initial profiles used in the diffusion models. As noted in Section 2.4.2.3, there is a 10-20 % uncertainty associated with the partition coefficients used here, which will translate into a ~ 10-20 % uncertainty in the calculated initial and equilibrium melt concentrations. An added uncertainty in the diffusion models is the effect of diffusion in multiple

dimensions, which if ignored can overestimate the timescales. Some of the plagioclase crystals modelled are small and prismatic, and the effects of diffusion in two dimensions (2D) may be prominent. A two dimensional diffusion model is used to model the distribution of trace elements in plagioclase where the analytical transect deviates from the centre line by a distance of one quarter of its width or less (Appendix A.6.1). To evaluate the effects of diffusion in a second dimension on the retrieved timescales, the results of diffusion modelling in both 1D and 2D are reported in the results. The results of 1D diffusion models can be taken as a maximum time constraint.

2.6.2 Results of diffusion modelling in plagioclase

In the following sections the results of diffusion modelling is described for euhedral and resorbed plagioclase using the parameters and models outlined above. The results of diffusion modelling in plagioclase from the Southern Fissure glomerocryst are combined with those retrieved from olivine within the glomerocryst in Section 2.6.4.

2.6.2.1 Euhedral plagioclase

Six euhedral plagioclase from the Bull's eye and one from the Southern Fissure, (none from the Northern Fissure), have MgO contents in intra-crystalline disequilibria, i.e. where the plagioclase rims are in equilibrium with a MgO melt content higher and lower than the cores respectively (Section 2.5; Table 1). Five of the six crystals from the Bull's eye have cores in equilibrium with a melt MgO content (8.1-8.3 wt %) that is similar to its host (8.02-8.28 wt %), and rims in equilibrium with a higher MgO melt (8.4-8.8 wt %). Diffusion modelling of these five crystals assumes they were initially homogenous and in equilibrium with 8.1-8.3 wt % melt, prior to being instantaneously mixed into a more primitive melt (> 8.8 wt % MgO). Modelled timescales are between 1.5 weeks (2D model) and 5.7 weeks (1D model). This corresponds to how long before eruption the crystals were mixed into the higher MgO melt (8.4-8.8 wt %; Figures 15 A, C, D, E, F). The maximum time these 5 crystals resided in its host melt before eruption is ~ 2 days. This is calculated by determining the time it would take for the disequilibria

between the rims and their host melt to be removed. The remaining sixth crystal from the Bull's eye shows the opposite trend, with a core in equilibrium with a higher MgO melt (8.6 wt %), than its rims (8.0 wt % MgO; Table 1). If it assumed this crystal was initially in equilibrium with a more primitive melt containing 8.6 wt % MgO melt, and was instantaneously mixed into a lower MgO melt (8.0 wt %), modelling this profile gives a time of between 3.5 weeks (1D model) and 1.0 week (2D model; Figure 15 B).

The MgO profile of one euhedral crystal from the Southern Fissure has a core in equilibrium with a 7.0 wt % MgO melt, and rims in equilibrium with a melt similar to that of its host (7.9 wt %; Figure 15 J). Modelling assumes this crystal was mixed into a melt with similar MgO contents to its host after initially being in equilibrium with a lower MgO melt. Retrieved times are 7.0 weeks (1D model) to 4 weeks (2D model), which corresponds to how long before eruption the crystal was entrained into its host-like melt (Figure 15 J).

Two euhedral plagioclase from the Northern Fissure, and three from the Bull's eye, (none from the Southern Fissure), have Sr contents in intra-crystalline disequilibria; in these the plagioclase rims are in equilibrium with a higher Sr melt (109-120 ppm) than their cores (90-105 ppm). Diffusion models assume the crystals were in equilibrium with a low Sr melt (90-105 ppm) prior to being immediately mixed into a higher Sr melt (over ~ 120 ppm). Retrieved timescales range between 12 and 32 years using 1D diffusion models, and 4 to 13 years using 2D models (Figures 15A, B, C, G, H). The time frame from four of these five modelled crystals (12-32 years) indicates they may have been mixed into a higher Sr melt (>120 ppm) prior to or during the 1991-92 eruption. This is supported by the 1991-92 lavas containing Sr contents over 120 ppm (118-127 ppm; Sims et al., 2002). Three crystals from the Northern Fissure and one from the Southern Fissure have rims in equilibrium with a lower Sr (90-102 ppm) melt than their host. These crystals must have resided in their host melts a maximum time of ~ 1 year prior to eruption.

One euhedral plagioclase from the Southern Fissure has K contents that display pronounced internal disequilibria, i.e. where the plagioclase rims are in equilibrium with a melt containing a higher K content (770 ppm) than the core (440 ppm) respectively.

Figure 15. **A** through to **J**: Euhedral plagioclase photomicrographs with An (blue), MgO, Sr, and K (red) chemical zoning profiles, and the results of diffusion modelling. The red arrows indicate the position of the electron microprobe traverse, and the pits from the LA-ICP-MS analyses are visible. The arrow direction is always left to right in relation to the x-axis on the underlying plots. The yellow band in the An plots represents the range of An contents in equilibrium with the host melts (An_{70-75}). The error associated with the MgO analyses is approximately 2-4 % (Appendix 1.2), which is smaller than the size of the symbol used in the zoning profiles. The errors associated with Sr and K analyses are based on the precision found in the corresponding analytical session (Appendix 1.2). The retrieved time (t) from a one-dimensional (1D) diffusion model is shown, plus a two-dimensional (2D) model when used. The diffusion model (Black) in the plots is from the 1D model (unless stated otherwise) and represents the best fit model. The best fit was determined by minimizing the square root of the misfit between the model and data (e_{RMS}; Shown in parentheses; Equation A.3 in Appendix 4.2). The stated host melt MgO concentrations are taken from bulk glass data from Goss et al. (2010). The stated host melt Sr and K concentrations are the average in that sample taken from both LA-ICP-MS glass analysis and bulk glass data in Goss et al. (2010; Table A.5 in Appendix 1.2).
The equilibrium profile (green) is defined by the melt composition in equilibrium with the lowest/highest concentration found at the crystal rim. The initial profile (blue) is defined by the melt composition in equilibrium with the lowest/highest concentration found in the crystal core. Boundary conditions at crystals rims that are in contact with the surrounding melt are open and set at the corresponding equilibrium value. For further details on the exact initial, equilibrium, and boundary conditions used for each model see their corresponding caption.

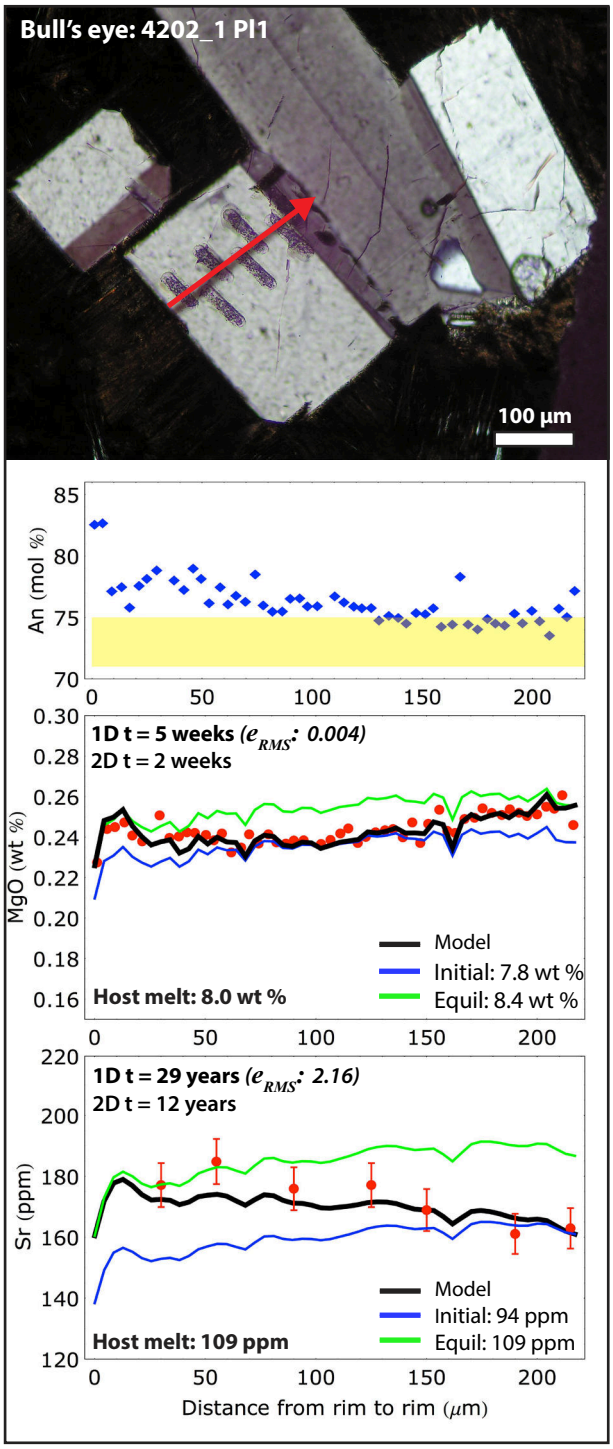

A: The crystal-crystal interface has an open boundary condition for the MgO profile, and a closed boundary condition for Sr. This assumes that Sr diffusion rates at the crystal-crystal interface is slower than Mg and could be explained by Sr diffusion being controlled by: (i) the fluid at the interface, in which the low Sr concentrations in the melt mean slow transport rates, (ii) slower Sr diffusion along the crystal-crystal interface due to the small flux between the melt and crystal (Dohmen and Chakraborty, 2003)

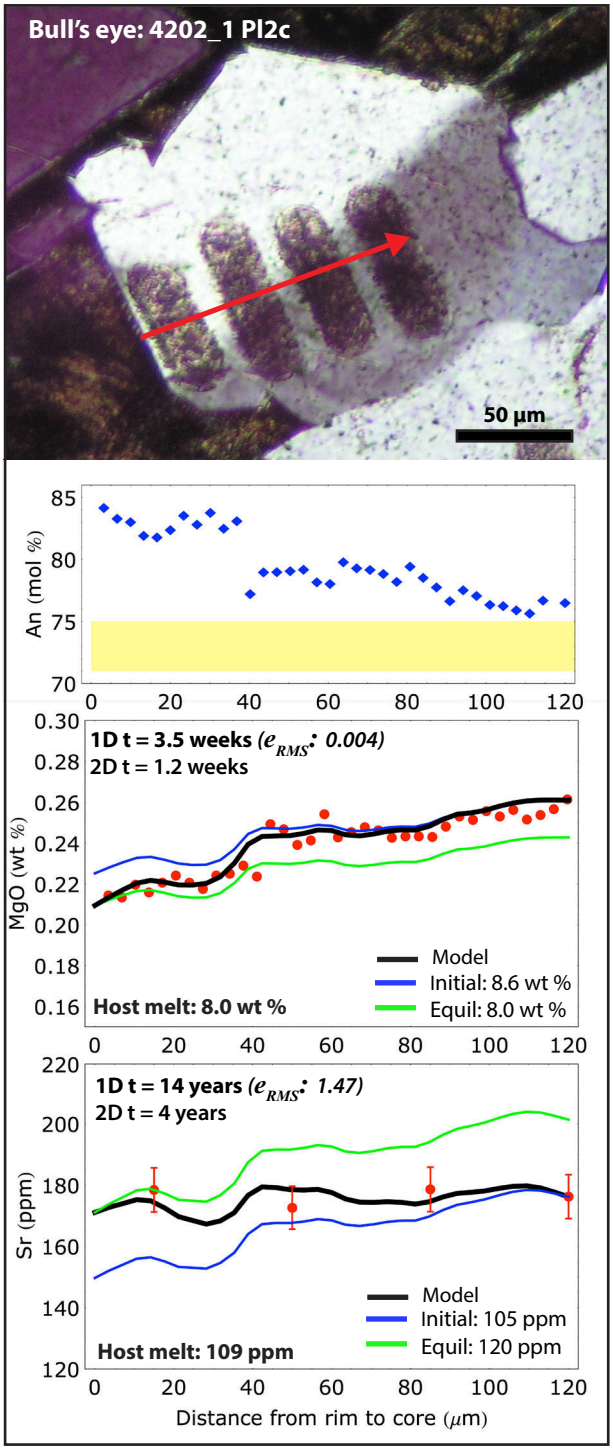

B: The crystal rim has an open boundary and the crystal core has a closed boundary in both MgO and Sr models.

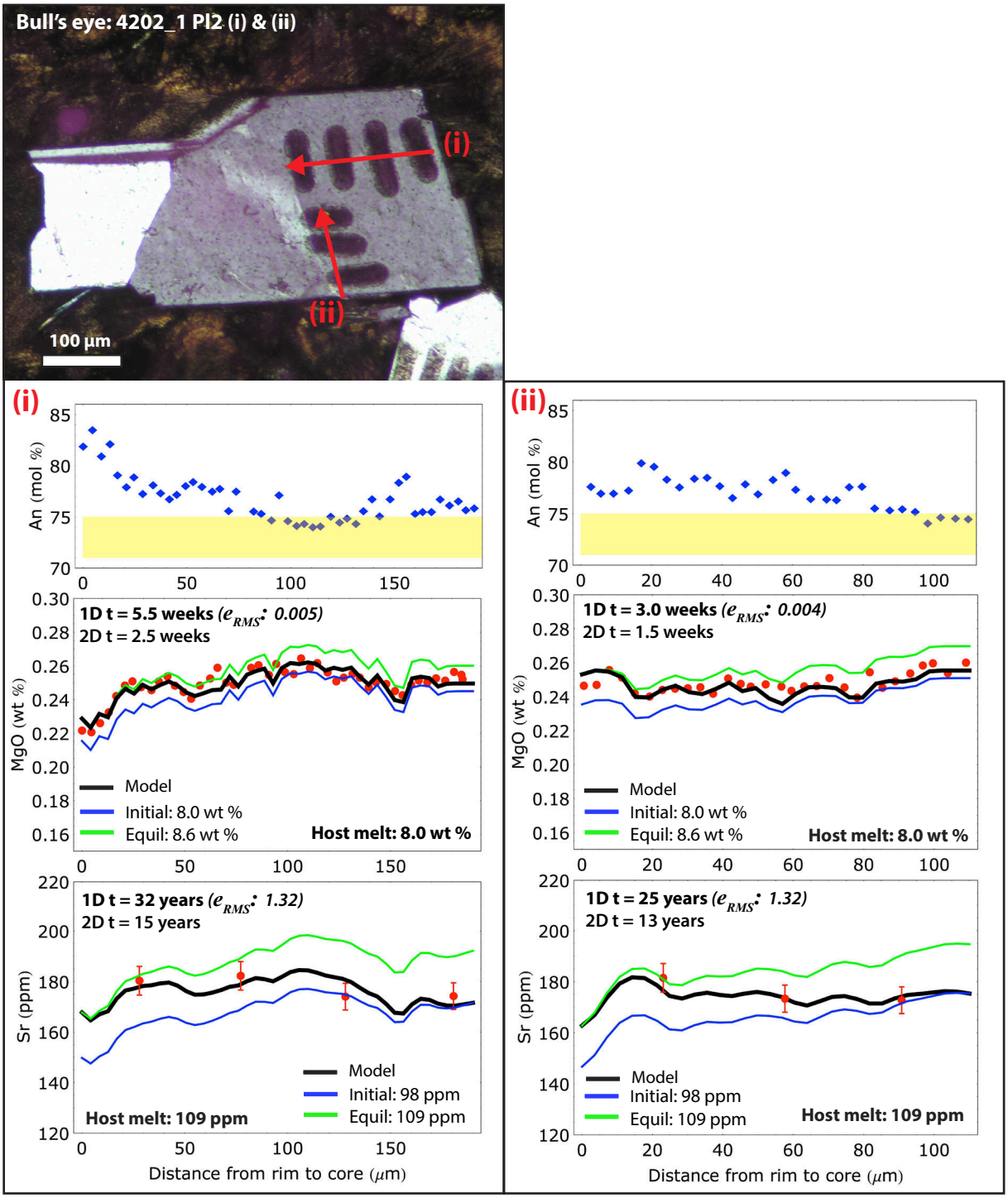

C. The crystal rims have an open boundary and the crystal cores have a closed boundary in both Sr and MgO models.

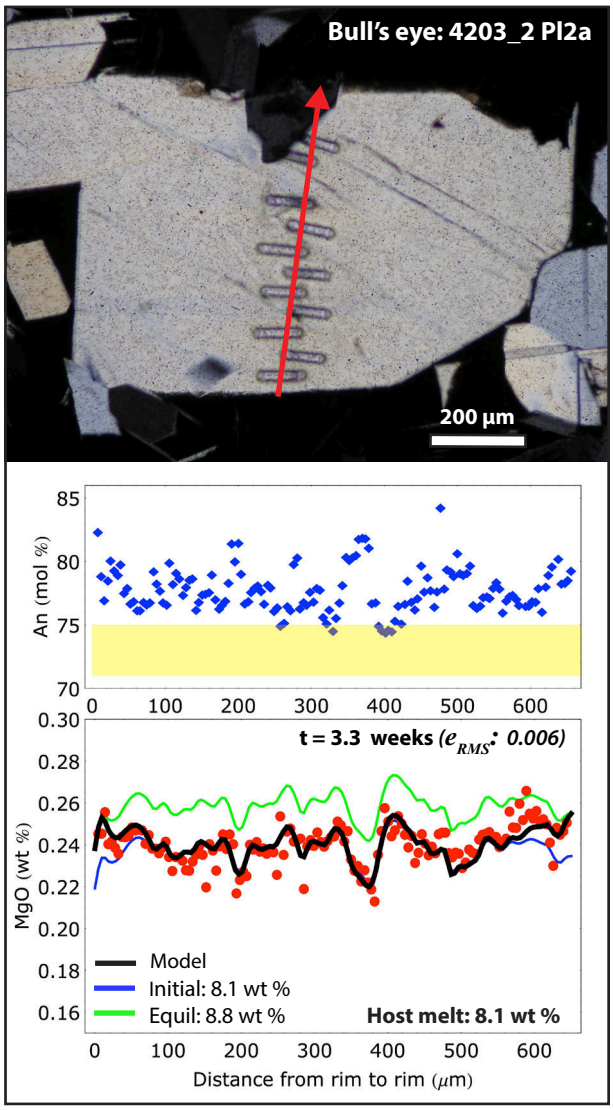

D. The crystal rims have open boundaries.

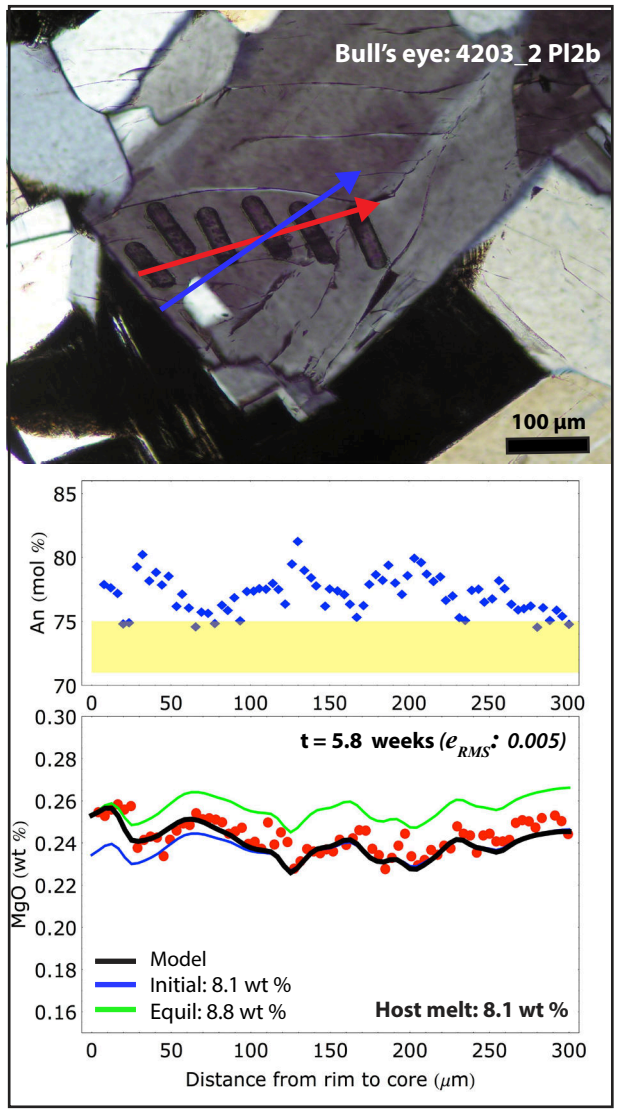

E: The crystal rim has an open boundary and the core has a closed boundary. This profile is modelled assuming it follows the transect highlighted by the blue arrow in order to model diffusion perpendicular to the crystal interface.

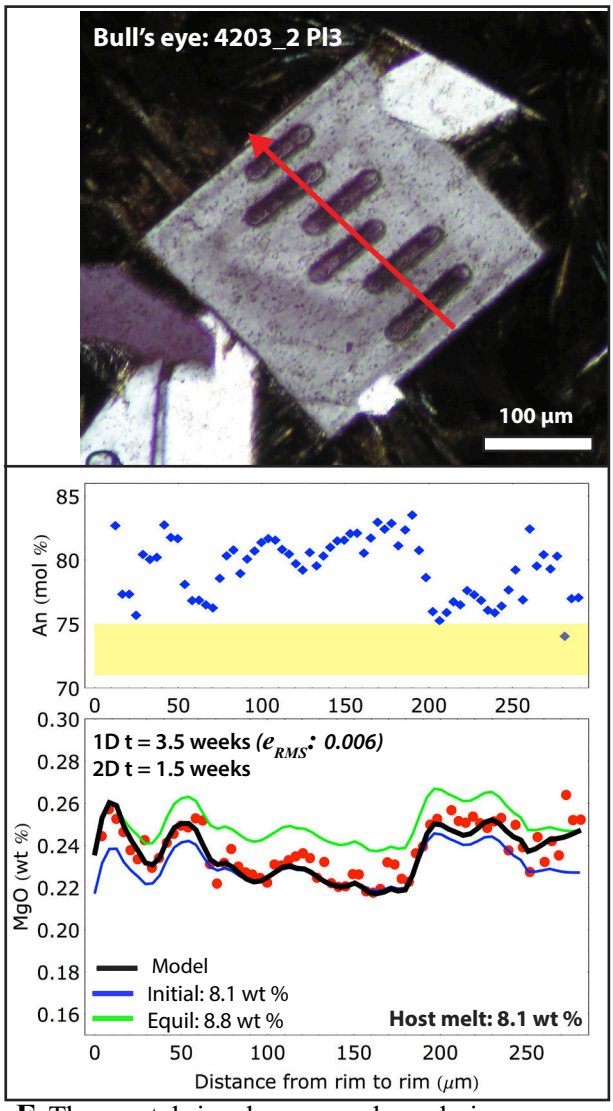

F. The crystal rims have open boundaries.

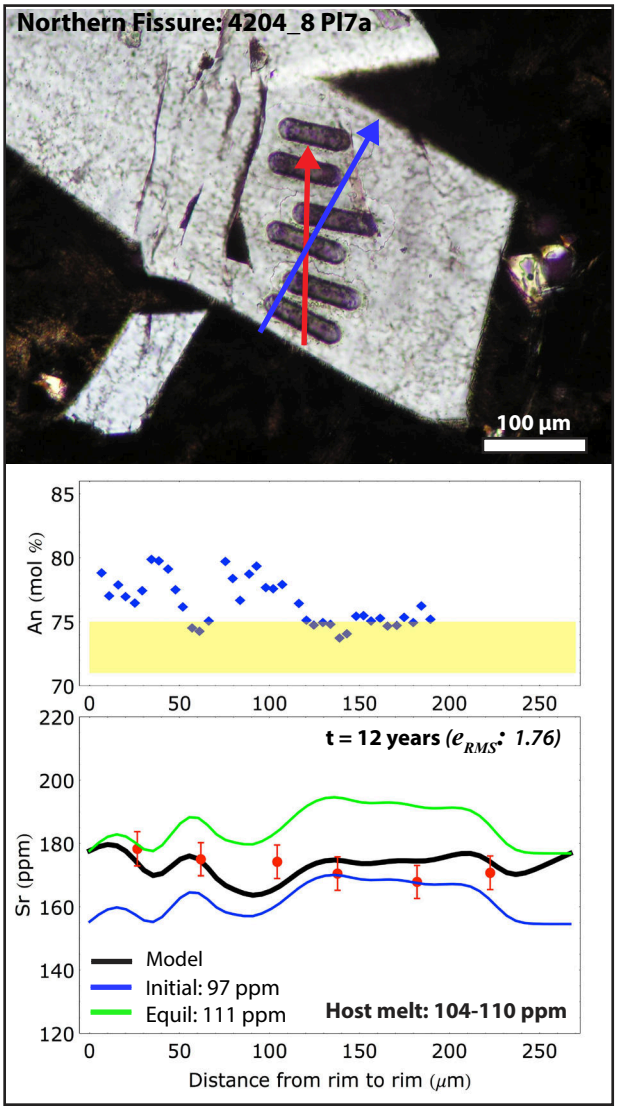

G. The profile is modelled assuming it follows the transect highlighted by the blue arrow (from rim to rim). The An concentrations that extend outside the EMP traverse were estimated using the scanning electron microscope (SEM) image of the crystal. The crystal rims have open boundaries.

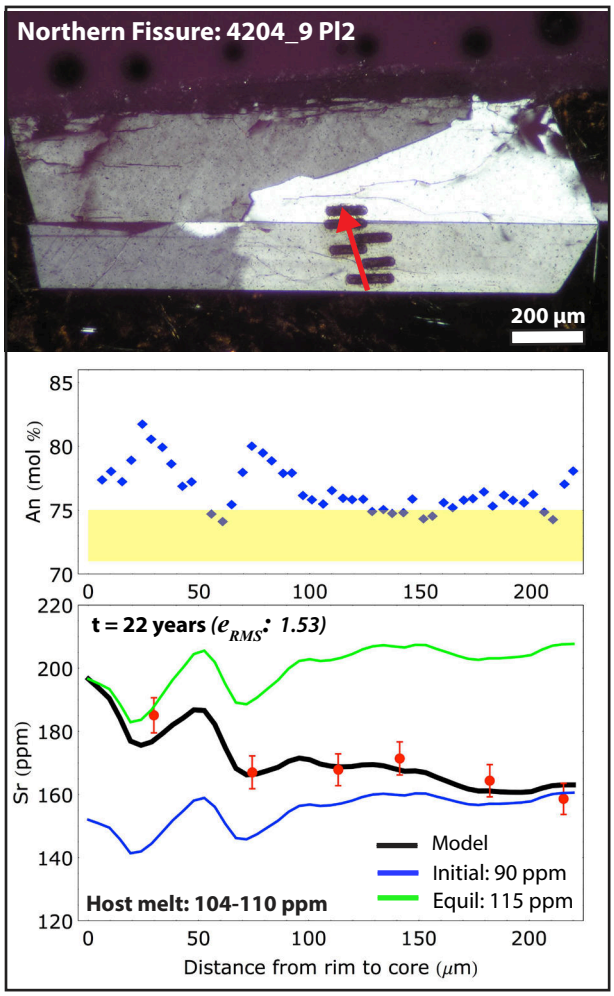

H: The boundary condition at the crystal rim is open and the core has a closed boundary.

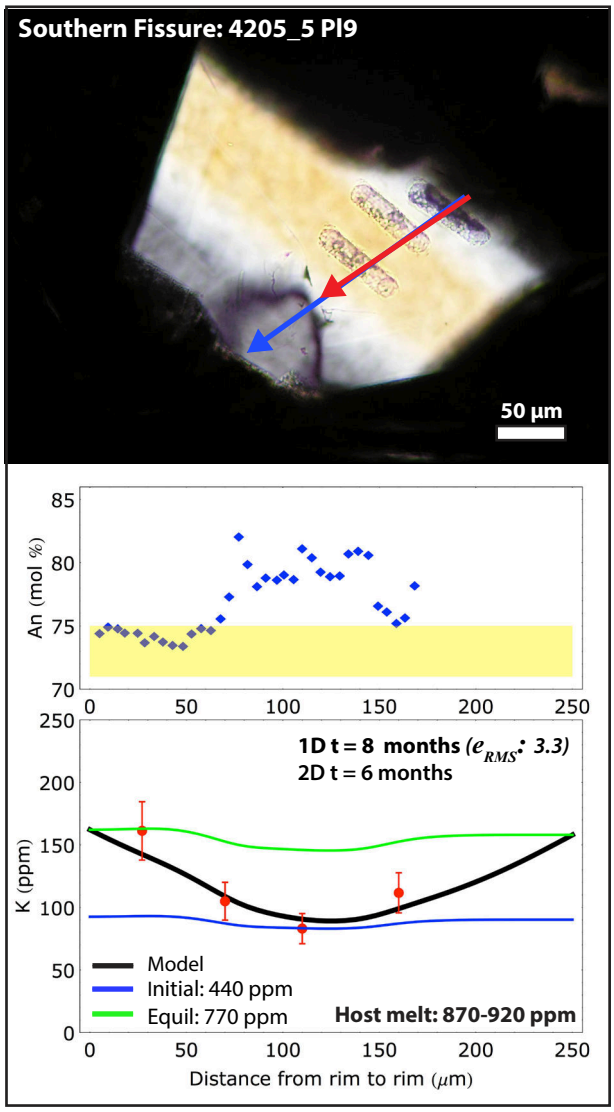

I: The profile is modelled assuming it follows the transect highlighted by the blue arrow (rim to rim). The An concentrations that extend outside the EMP traverse were estimated using the SEM image of the crystal. The crystal rims have open boundaries.

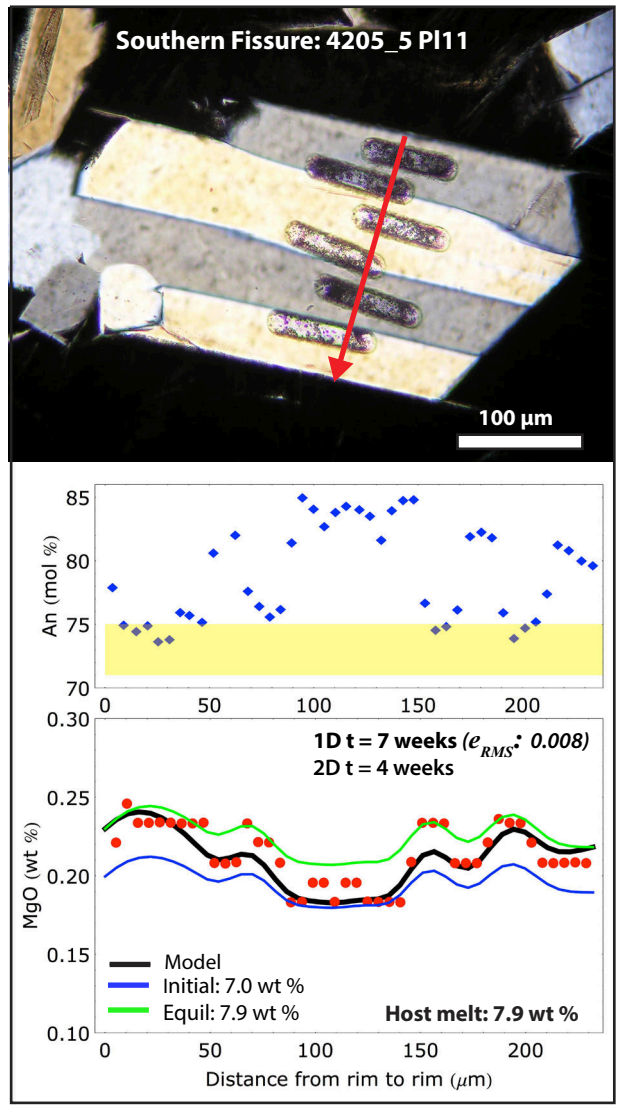

J. Boundary conditions at the crystal rims are set as open. EMP data is only 0.01 wt % precise due to problems with data collection.

Modelling assumes this crystal first equilibrated with a 440 ppm melt, prior to being mixed into a higher K melt. A time of between 6 months (2D model) and 8 months (1D model) is retrieved (Figure 15 I).

In summary, six euhedral crystals provide evidence of being mixed into a high MgO melt (> 8.8 wt %) between 1-6 weeks prior to 2005-06 eruption. Evidence of this more primitive melt is primarily seen within the Bull's eye region, which is the location where the most primitive lavas where erupted in 2005-06 (8.02-8.27 wt % MgO) and the region with the highest magmatic budget (Section 1.2.3). The Sr profiles of five crystals indicate they where mixed into a higher Sr melt (> 120 ppm) between 4 and 32 years prior to eruption. The timeframe from four of these five crystals (12-32 years) suggests a mixing event may have occurred between two melts with differing Sr contents prior to the 1991-92 eruption.

2.6.2.2 Resorbed plagioclase

2.6.2.2.1 SOUTHERN FISSURE

The resorbed crystal from the Southern Fissure has An contents up to 19 mol % higher (An_{87-94}) than those calculated to be in equilibrium with its host melt (4205_3 Pl3; Section 2.5.1.1; Figure 16). The crystal has very low MgO concentrations (0.09-0.15 wt %) which are in equilibrium with an evolved melt of 4.3-6.3 wt % MgO (Section 2.5.1.2). The crystals texture and major and trace element concentrations, as displayed by EMP elemental maps (Figure 16B), show the crystal is made up of a concentric array of zones of differing compositions. Dissolution of the crystal has left the remainders of what appears to be a core, an inner rim (rim 1), and an outer rim (rim 2), which are readily discernible in An and MgO (Figure 16B). The anorthite zoning is minor with the An contents of the core (~ An_{90}) increasing to ~ An_{94} in rim 1, before decreasing to ~ An_{87} in the outer rim 2 (Figure 16B). However, the zoning in MgO is very distinct with the core containing ~ 0.14 wt % MgO, decreasing to 0.09 wt % in rim 1, before increasing to 0.15 wt % in rim 2 (Figure 16). The MgO profile also displays sharp concentration gradients between zones, with different gradients being observed between zones (Figure 16). A shallow gradient is seen between the core and rim 1, whilst a sharper gradient exists

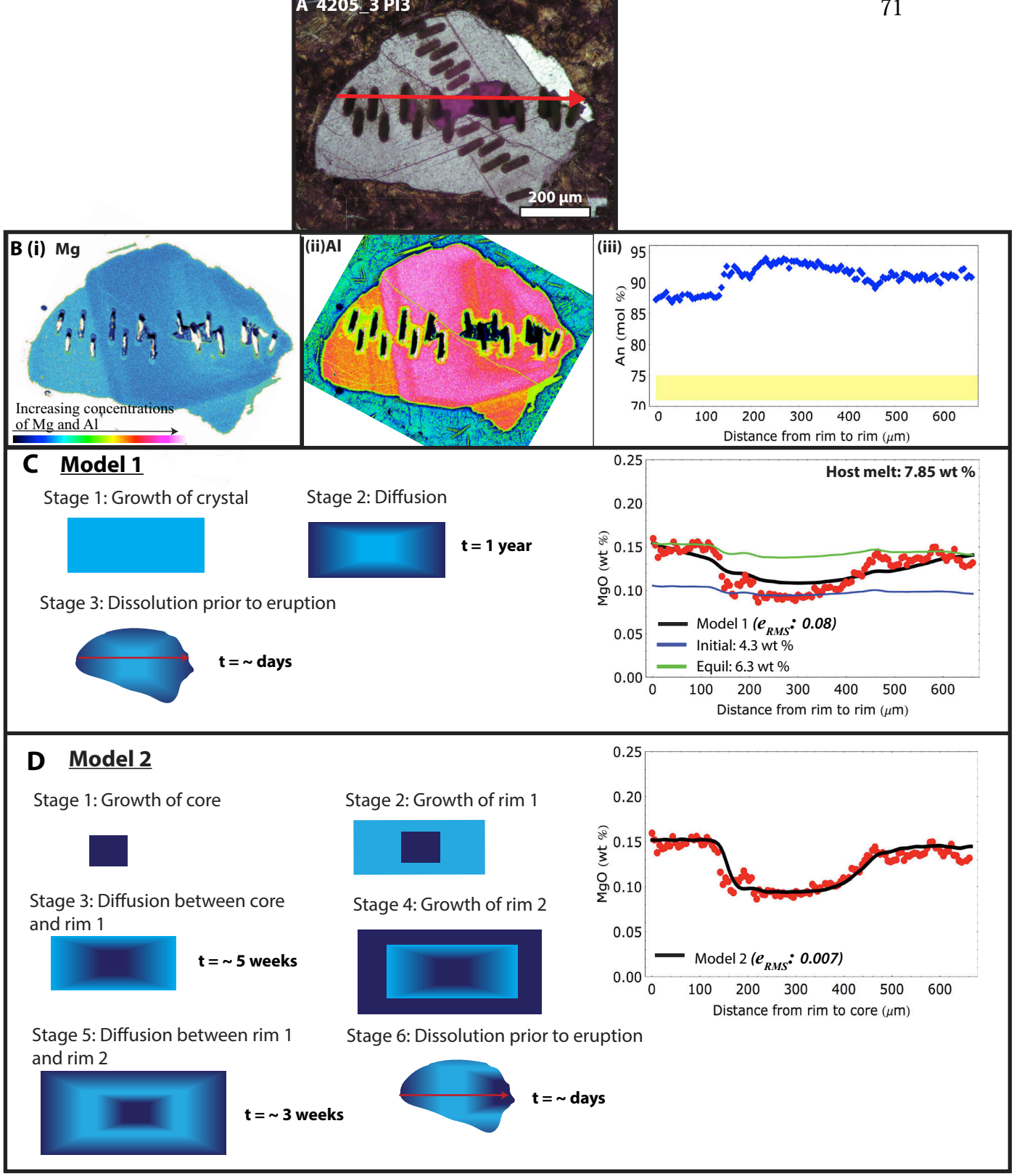

Figure 16. **A** (i) Photomicrograph of the resorbed plagioclase from the Southern Fissure (4205_3 Pl3). The red arrow indicates the location and direction of the EMP traverse (left to right in underlying plots), and the pits show the location of the LA-ICP-MS traverse. **B** (i) magnesium and (ii) aluminium intensity EMP maps. **B** (iii): The An profile (blue), with the calculated An range in equilibrium with its host melt (An_{70-75}; yellow band). **C** & **D** illustrate two potential models to explain the texture and zoning profiles in the resorbed plagioclase. The rectangles represents the crystal at various stages, with darker shades of blue corresponding to increasing MgO concentrations. The plots to the right show the analysed MgO zoning profiles (red), and the diffusion model (black), along the transect shown by the red arrow. The modeled timescales (t) are shown at the corresponding stage. **C**: In model 1, the plagioclase first grows from a 4.3 wt % MgO melt, prior to being mixed into a higher MgO melt (6.3 wt %) and is then dissolved. **D**: In model 2, a crystal core initially grows from a 4.3 wt % MgO melt, before being mixed into a 6.3 wt % melt where it grows rim one. Diffusion of Mg occurs between the core and rim one. The crystal is then mixed into a 4.3 wt % melt where it grows rim two. Diffusion of Mg occurs between rim one and rim two, before it is dissolved. This second model requires growth of a high An, low MgO plagioclase from the same melt and is discussed in the main text.

between rim 1 and rim 2 (Figure 16). The MgO content of the core and the outer rim 2 are both in equilibrium with a ~ 6.3 wt % melt, whereas the inner rim 1 is in equilibrium with a ~ 4.3 wt % melt. Due to this crystal being in intra-crystal disequilibria, it can provide information on the times of magma mixing which occurred prior to this crystal being entrained into the host melt.

There are two main features of this resorbed crystal that indicate it has had a more complex history than the euhedral crystals described above. (i) The plagioclase has high An contents which suggests a primitive origin, however its low MgO contents indicate it is in equilibrium with a very evolved melt (4.3-6.3 wt % MgO). (ii) The crystal has sharp gradients in its MgO profile which differ in their steepness between the core and rim 1, and rim 1 and rim 2 (Figure 16). We know from Section 2.4.2.3 that the Kd_{Mg} increases with decreasing An content, therefore the MgO equilibrium profile of a plagioclase will be a mirror image to its An profile. Over time diffusion will tend to decrease MgO concentration gradients outside of any zoning caused from a MgO equilibrium profile being dependent on its An profile. The crystal's An profile is not highly zoned, with a maximum difference between zones of 7 mol %, and so cannot be used to help explain the large difference in MgO concentrations between zones (0.09-0.15 wt %). It is therefore likely the two differing MgO gradients represent two changes in the crystals history. The steepness of the MgO concentration gradients suggests very short timescales between changing melt conditions, as diffusion has not had enough time to erase the sharp MgO gradients observed between the different zones. The complexities of this crystal make producing a diffusion model that fits its MgO profile more difficult than the euhedral crystals.

Two models are described in an attempt to unravel the history of this resorbed crystal (Figure 16). To begin with, a simple diffusion model was attempted which involves the crystal initially equilibrating with a 4.3 wt % MgO melt. Next, the crystal is mixed into a 6.5 wt % MgO melt, and Mg diffuses into the rims as it attempts to equilibrate with this higher MgO melt (Figure 16C: Model 1). Modelling provides a time of ~ 1 year, but gives a poor fit to the MgO profile and does not agree with the EMP maps which suggest the presence of a core and two rims (Figure 16). A diffusion model that produces a better fit to the MgO data involves two growth stages (Figure 16D; Model 2;

details of the model are in Appendix A.6.3). Initially the crystal core grows from, or completely equilibrates with, a melt containing 6.3 wt % MgO, before being mixed into and growing rim one from a melt containing 4.3 wt % MgO. The crystal is then mixed into a third melt of 6.3 wt % MgO and grows rim two (Figure 16D). The time the crystal spent in these evolved melts can be constrained by modelling the extent of diffusion between the core and rim one, and rim 1 and rim 2, providing times of 5 weeks and 3 weeks respectively (Figure 16D). These times correspond to a growth rate of 9.5 x 10^{-9} cm s^{-1} which is within the range reported from natural plagioclase growth rates in mafic melts (10^{-6} and 10^{-11} cm s^{-1}; Cashman, 1990,1993 and references therein).

There are problems associated with both models described above. The first simpler diffusion model does not produce a good fit to the MgO data and is inconsistent with the EMP zoning maps (Figure 16B). The second more complex growth model fits the MgO data well, however requires either; (i) an unusual melt composition, e.g. with a high Ca/Na ratio and low MgO concentrations (4.3-6.3 wt %), in order to grow plagioclase containing both high An and low MgO contents. Plagioclase crystals with compositions between An_{83-93} have been experimentally grown from synthetic mafic melts containing ~ 9-14 wt % MgO (Kohut and Nielsen, 2003). These MgO contents are substantially higher than the 4.3-6.3 wt % predicted to be equilibrium with the MgO contents of the resorbed crystal. An alternative explanation is (ii) the Kd_{Mg} is lower than what is predicted using Equation (1). In order for a plagioclase (An_{90}) containing 0.1 wt % MgO to be in equilibrium with a more primitive melt of ~ 10 wt % MgO, the Kd_{Mg} is required to be ~ 50 % lower than what is predicted using Equation (1). The Kd_{Mg} predicted from Bindeman et al. (1998), and from ODP Hole 648A data (Costa et al., 2009) are 15-20 % lower than those predicted by Equation (1) at An_{90} (Section 2.4.2.3; Figure 7). These partition coefficients are still not low enough for the MgO contents of this crystal to be in equilibrium with a high MgO, primitive melt. Two remaining options are: (i) the Kd_{Mg} determined from all the methods shown in Figure 7 are incorrect, this seems unlikely; or (ii) the Kd_{Mg} at high anorthite contents (~ An_{90}) is different to what is predicted by any of the trends seen in Figure 7.

A change in the Kd_{Mg} at high anorthite contents could potentially be caused by a change in structure at ~ An_{90}. High temperature experiments, along with calorimetric and

X-ray diffraction data, have shown that at over ~ 700°C intermediate plagioclase (An_{0-90}) have a triclinic structure with a $C\bar{1}$ space group, whilst more anorthitic compositions (An_{90-100}) have a triclinic symmetry with a $I\bar{1}$ space group (e.g. Carpenter and McConnell, 1984; Angel et al., 1990; Carpenter et al., 1990). Note, different space groups in a crystal are used to describe their symmetry. The transition from a $C\bar{1}$ to a $I\bar{1}$ space group occurs at temperatures above the liquidus in plagioclase of anorthitic compositions (Carpenter and McConnell, 1984). This structural transformation is coupled with a change in Al-Si ordering schemes in plagioclase. Aluminium-silicate ordering is a common process in Al-silicates and involves the tendency for Al and Si atoms to order themselves into specific sites with decreasing temperature. This process is driven by the avoidance of energetically unfavourable Al-O-Al bonds and is known as the Al-avoidance principle (Loewenstein, 1954; Yund and Tullis, 1980; Carpenter et al., 1990; Carpenter, 1992). The difference in Al-Si ordering schemes between anorthitic and intermediate plagioclase compositions are primarily due to their differing Al-Si ratios. For additional details on the transformations occurring in plagioclase crystals see Carpenter et al., (1990), Carpenter (1991; 1992), and Myers et al. (1998). The differences in structure and Al-ordering schemes between intermediate and high anorthite plagioclase may have direct consequences on how trace elements partition into the structure. Previous studies of Mg partitioning in plagioclase have indicated it can partition into the cation (M) site (e.g. Aigner-Torres et al., 2007), although increasing evidence suggests Mg prefers to partition into the tetrahedrally (T) coordinated site via an Al substitution (e.g. Longhi et al., 1978; Peters et al., 1995; Miller et al., 2006). A change in the structural state of a plagioclase may initiate a change in how and in which site Mg partitions into, resulting in a change in its partition coefficient. Further studies are required to provide information on trace element partitioning in high anorthite plagioclase. Note, if there is a change in how Mg partitions into anorthitic plagioclase, it is likely the diffusion coefficient of Mg will also change, which may alter the timescales modelled in this crystal.

In summary, the resorbed plagioclase from the Southern Fissure has a complex history. Its MgO contents indicate it equilibrated with an evolved melt, however its high An contents suggests an origin in a more primitive melt. A diffusion model that produces a good fit to the MgO profile suggests it grew from melts of differing compositions to its

host a few weeks before being erupted on to the sea floor. This requires either an unusual melt composition, or a different Kd_{Mg} at high anorthite contents than what is predicted by Equation (1) or Bindeman et al. (1998).

2.6.2.2.2 BULL'S EYE AND NORTHERN FISSURE

Out of the three remaining resorbed crystals that have been analysed, one from the Bull's eye has An, MgO, Sr, and K contents in equilibrium with a melt composition that is substantially different to its host melt (Section 2.5). This resorbed crystal from the Bull's eye, along with the high An resorbed plagioclase from the Southern Fissure detailed above, have rims with MgO, Sr and K contents out of equilibrium with their host melts. The *maximum* time interval between entrainment of these crystals into its host melt can be calculated from the amount of time it would take for the MgO disequilibria at crystal rims to be erased. Modelling indicates the crystals spent a maximum time of ~ 2 days in its host before being erupted on the sea floor, assuming no dissolution. If it is assumed the plagioclase were dissolved after being entrained into their host melts, this maximum time would increase depending on the area dissolved and the dissolution rate. A dissolution rate of 1.1×10^{-6} cm s^{-1} at 1200°C is calculated from a plot of plagioclase dissolution rates against temperature. Rates of dissolution are taken from experiments completed on $An_{52.5}$ plagioclase spheres in basalt by Donaldson (1985). Using this rate the time taken to dissolve 0.02 cm of plagioclase (a typical plagioclase size from the 2005-06 lavas; Section 2.3) is ~ 5 hours. Dissolution rates were also determined using the expression in Edwards and Russell (1996a,b; 1998) which relates experimentally determined mineral dissolution rates from Donaldson (1985, 1990), Thornber and Huebner (1985), Brearley and Scarfe (1986), and Zhang et al. (1989), to its affinity. Affinity is defined as the extent of disequilibria of that mineral with respect to the melt. Plagioclase affinity was calculated using the MELTs algorithm at 1200°C and a pressure of 800 bars, using the glass compositions from its host melt (Goss et al., 2010). Plagioclase dissolution rates were converted from moles cm^{-2} s^{-1} into cm s^{-1} using their molar volumes at the temperature and pressures stated above with the thermodynamic database from Holland and Powell (1998). This method gives a dissolution rate of 5.87 x

10^{-7} cm s^{-1} which would dissolve 0.02 cm of plagioclase in ~ 9.5 hours. This timeframe is similar to the maximum time determined using the dissolution rate from just the plagioclase data in Donaldson (1985). Therefore, it is unlikely that dissolution will substantially alter the calculated maximum time of ~ 2 days that the crystals spent in their host melts.

2.6.3 Parameters used for diffusion modelling in olivine

Experimental determinations of diffusion of Fe-Mg (Chakraborty, 1997; Dohmen et al. 2003; Dohmen and Chakraborty 2007a,b), Mn and, Ni (Petry et al. 2004) in olivine show they are dependent on temperature, fO_2, crystallographic direction, and olivine Fo content. Their diffusion coefficients are anisotropic, with diffusion parallel to the *c*-axis being approximately six times faster than parallel to the *a* or *b* axis (Chakraborty, 1997; Dohmen et al. 2003; Dohmen and Chakraborty 2007a,b; Petry et al. 2004). The diffusion coefficient for Cr in olivine is taken from Ito and Ganguly (2006), and is ~ 2 orders of magnitude slower than Fe-Mg, Mn, or Ni diffusion. Diffusion of Cr was found to be independent of fO_2 between wustite-iron (WI) buffer and WI + 2 (Ito and Ganguly, 2006). The D_{Cr} was also found to be anisotropic, with diffusion along the *c*-axis being ~ 4 times faster than along the *a*-axis (Ito and Ganguly, 2006). Unless stated otherwise, timescales are reported using diffusion coefficients parallel to the faster *c*-axis.

All the diffusion coefficients are calculated at 1200°C and assuming an oxygen fugacity at the QFM buffer, with the exception of Cr where it was assumed to be independent of fO_2 (Ito and Ganguly, 2006). In order to evaluate the variability in modelled timescales from different initial conditions, two initial profiles are used unless stated otherwise. The first is a homogenous initial condition at the maximum or minimum concentrations found in the core of each crystal. This assumes the crystal initially equilibrated with one melt, prior to being mixed into a melt with a different composition. The crystal will attempt to re-equilibrate which will result in the relative diffusive loss or gain of the element through the crystal rims. The second initial profile is zoned using the maximum/minimum concentrations found at the crystal rim and the core. This assumes the crystal core equilibrated or grew from one melt, prior to being mixed into a melt with

a different composition where it grew a rim. Diffusion will attempt to internally homogenise the zoning produced. In this second model, approximately 70 % of the initial profile is the core and 30 % is the rim. For each initial condition the compositions at crystal rims are taken as the boundary condition.

The main uncertainties associated with the calculations are related to temperature and fO_2. An increase in temperature from 1200°C to 1250°C will increase the diffusion coefficient and therefore decrease the modelled timescales by a factor of ~ 1.8, and an uncertainty in fO_2 of two log units (from QFM to QFM-2) decreases the diffusion coefficient by a factor of ~ 2 for Fe-Mg, Mn and Ni.

2.6.3.1 Diffusion modelling in euhedral olivine

The Fo, Mn, Ni and Cr contents in the euhedral olivine from the Bull's eye are within the range of compositions calculated to be in equilibrium with its host (Section 2.5.2). Their zoning profiles are also in intra-crystalline disequilibria, with some elemental profiles (e.g. Ni and Cr) having a concave upwards appearance (Figure 17). Concave upwards zoning profiles, with the rim concentration lower than the core concentration, cannot be reproduced by diffusion from a homogenous composition, indicating an initially zoned profile. The extent of zoning is different between different elements, with divalent cations exhibiting less zoning than Cr (Section 2.5.2). A simple model that explains these observations is crystal growth from a melt with similar Fo, Mn, Ni and Cr contents to its host. The crystal was then mixed into a slightly more evolved melt leading to growth of rims with lower Fo, Ni and Cr contents and higher Mn contents. Diffusion occurs as elements attempt to erase this zoning and internally homogenise. The zoning produced by this growth will be erased more rapidly for faster diffusing divalent cations (e.g. Fe-Mg; Dohmen and Chakraborty 2007a,b), whilst the slower diffusing elements such as Cr (Ito and Ganguly, 2006) will retain their initially zoned profile for longer. The crystal is then erupted before any of the elements can internally homogenise.

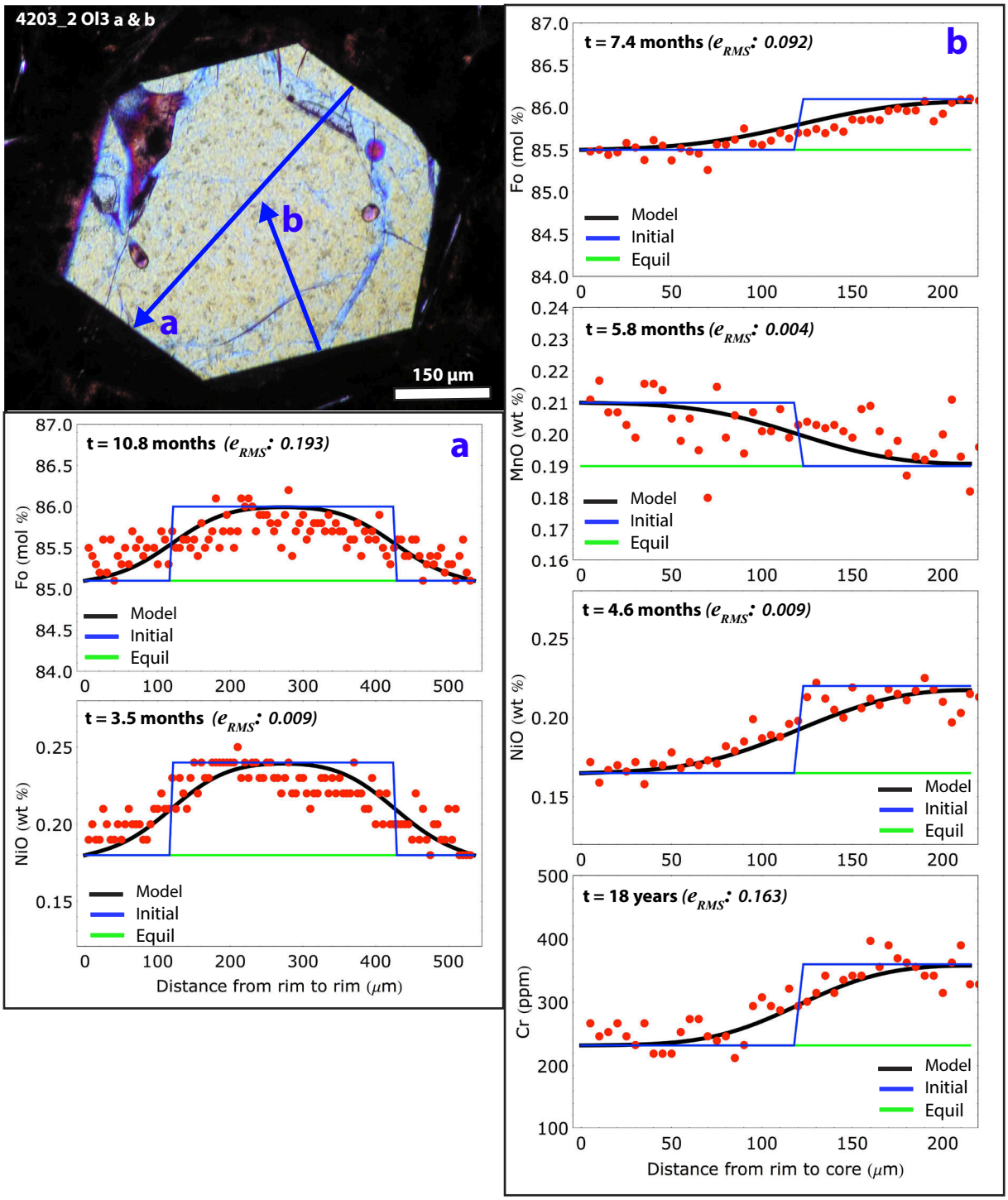

Figure 17. Photomicrograph of the euhedral olivine from the Bull's eye, with Fo, Mn, Ni and Cr chemical zoning profiles (red), and results of diffusion models (black) from transect-a and transect-b. The blue arrows indicate the position of the electron microprobe traverses. The arrow direction is left to right in relation to the x-axis on the underlying plots. An initial zoned profile is used due to the concave upwards appearance of zoning profile (e.g. NiO), which cannot be reproduced using an initial homogenous concentration. The boundary conditions at the crystal rims are open and set at the corresponding equilibrium rim composition. The diffusion model shown represents the best fit model which was determined by minimizing the square root of the misfit between the model and data (e_{RMS}; shown in parentheses; Equation A.3 in Appendix 4.2). Modeled times (t) are retrieved from the diffusion coefficients parallel to the *a/b*-axis due to the crystals euhedral shape. The rim of transect-**b** contains 0.3 mol % higher Fo, and 0.01 wt % lower NiO contents than rim two of transect-**a** (right of profiles). This could represent errors associated with the separate analyses, or be due to 2D effects.

Modelling of this crystal's elemental zoning profiles can provide a maximum constraint on the length of time between crystal growth and eruption onto the seafloor. Modelling of the Cr profile provides a time of ~ 18 years, whilst much shorter times of between 6 months and 11 months are retrieved from modelling the Fo, Mn, and Ni zoning profiles (Figure 17). The difference in modelled timescales between divalent elements and Cr is consistent with the proposed model of growth plus diffusion. Chromium diffusion in olivine is slow (Ito and Ganguly, 2006), and it is likely the olivine's Cr profile represents crystal growth. Consequently, the modelled timescales from the Cr profile will be longer than Fo, Mn, and Ni, which are likely to represent growth and diffusion due to their much faster diffusion rates (Dohmen and Chakraborty 2007a,b; Petry et al. 2004). If the olivine growth began much longer than 6-11 months prior to eruption, the observed zoning in the fast diffusing divalent cations would be erased. Therefore, the maximum possible time between crystal growth and eruption is approximately 11 months.

2.6.4 Diffusion modelling in plagioclase and olivine from the Southern Fissure glomerocryst

The Mg, Sr and K contents of plagioclase and Fo, Mn, Ni, and Cr of olivine in the glomerocryst from the Southern Fissure are in equilibrium with a much more evolved melt (e.g. 3.5-6.5 wt % MgO) than the melt that brought it to the surface (7.9 wt % MgO). Crystals are also in intra-crystalline disequilibria, with crystal rims in equilibrium with a lower MgO melt (3.5-4.3 wt %) than cores (4.5-6.5 wt %; Section 2.5). Portions of the glomerocryst display a rounded and embayed texture suggesting dissolution has occurred prior to it being erupted (Section 2.3; Figure 18). The following section describes a simple model that explains the textures and zoning profiles observed in the glomerocryst (Figure 19). The calculated timescales retrieved from modelling their elemental profiles are reported and put into context with this model (Figure 20).

2.6.4.1 A model to explain the elemental zoning observed in the glomerocryst

Due to the crystals having major and trace element contents in equilibrium with a very evolved melt, and the crystals resorbed texture, it has been proposed the

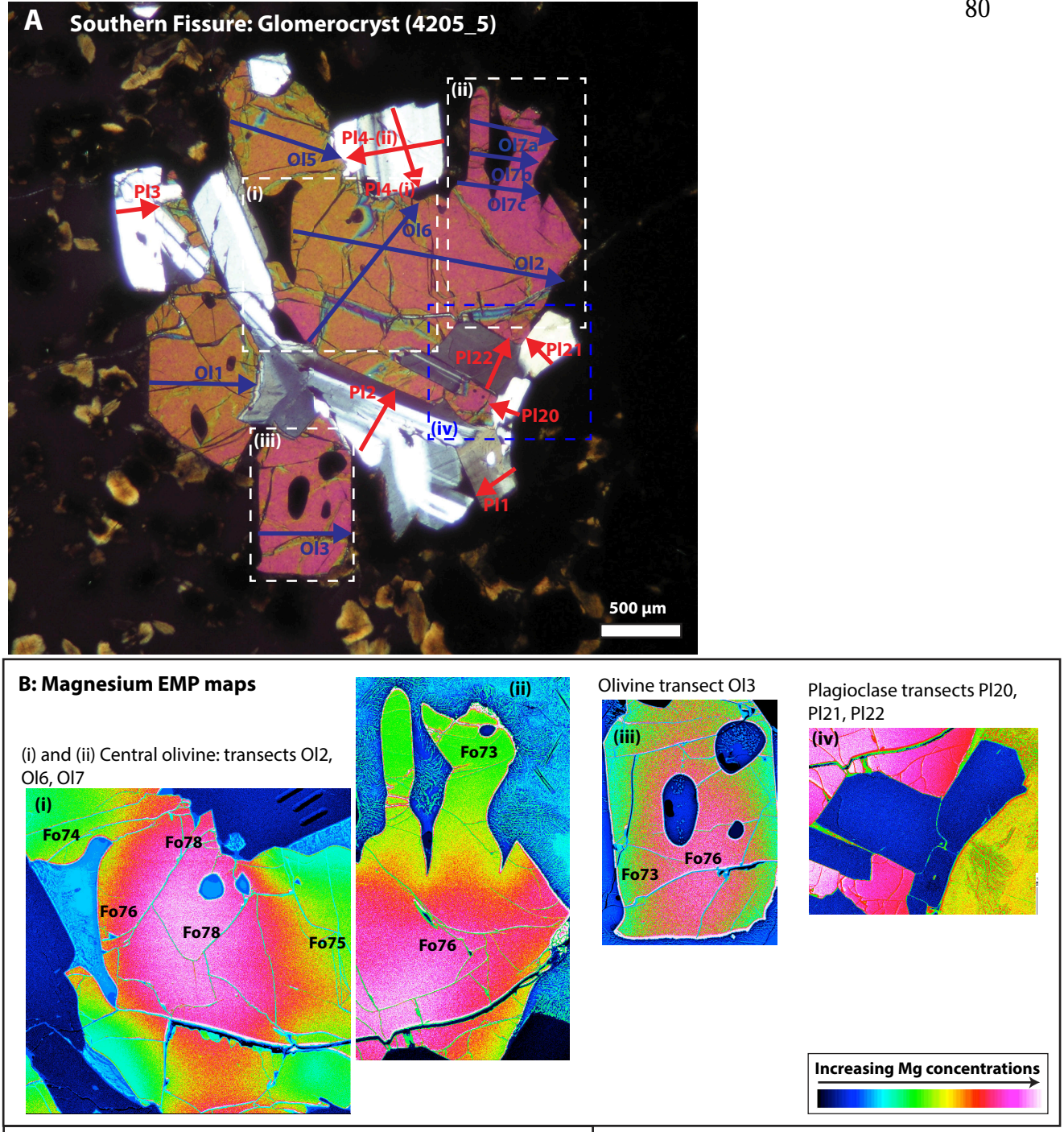

Figure 18. **A**: Photomicrograph of the glomerocryst from the Southern Fissure. Labeled red and blue arrows represent the location and direction of EMP transects on plagioclase and olivine. The dashed white and red boxes represent the location of the EMP maps shown in **B**.
B: Magnesium and **C:** Phosphorous EMP maps of plagioclase and olivine in the glomerocryst. EMP maps illustrate the large scale elemental zoning in Mg, and the irregular zoning patterns in P contents of olivine. Note, individual EMP maps have different concentration scales with colours representing relative increases and decreases in Mg or P. Numbers on the Mg EMP maps represent concentrations of forsterite in olivine analysed by EMP over the transects shown in A.

glomerocryst once resided in a mush zone (Sections 2.3 & 2.5). We know from seismic tomography that crystal mush zones exist beneath the ridge axis at ~9°50'N (Dunn et al., 2000; Crawford and Webb, 2002; Section 1.2.2). The extremely evolved melts in equilibrium with the glomerocryst (3.5-6.3 wt % MgO) suggests cooler melt temperatures than the ~ 1200°C predicted for the melt within the AMC from calculations using the compositions of 2005-06 lavas in Section 2.3.1. Thermal modelling by Liu and Lowell (2009) show that frequent magma replenishment of the melt lens is required in order to keep it from freezing and to maintain high hydrothermal vent temperatures. Goss et al. (2010) calculated that the AMC would completely crystallize in the repose period between the 1991-92 and 2006-06 eruptions in ~ 4.6 years without magma replenishment. This influx of melt upwards beneath the melt lens would inhibit any large decreases in temperature within the underlying mush zone. Therefore, it is suggested that the glomerocryst resided in a mush zone on the roof of the melt lens rather than the floor. Here, hydrothermal circulation can promote rapid cooling of the upper melt lens. Interactions between the hydrothermal system and the rocks overlying the AMC have been previously explored along fast spreading MOR's (e.g. Singh et al., 1999), with differences in hydrothermal cooling being used to explain along axis variations in AMC roof depths (Fontaine et al., 2011).

The first stages in the history of the glomerocryst involve fast growth of olivine (Figure 19). Initial fast growth of olivine produces a dendritic structure, evidence of which is seen within phosphorous EMP maps (Figure 18). These EMP maps show irregular P zoning patterns with high P concentrations emphasizing the dendritic projections (Figure 18). Previous work on growth and P zoning patterns in olivine suggests that skeletal and dendritic olivine structures are caused by rapid growth (e.g. Donaldson, 1976; Milman-Barris et al., 2008). This is also supported by studies of the textural evolution of olivine at different cooling rates, where fast cooling produced dendritic textures (Faure et al., 2006). Increased cooling rates have also been used to explain the dendritic texture and high P contents of olivine crystals from hot spot volcanoes (Welsch et al., 2013).

An initial rapid growth phase is consistent with the proposed model of crystallisation occurring in a roof mush zone where rapid decreases in temperature can

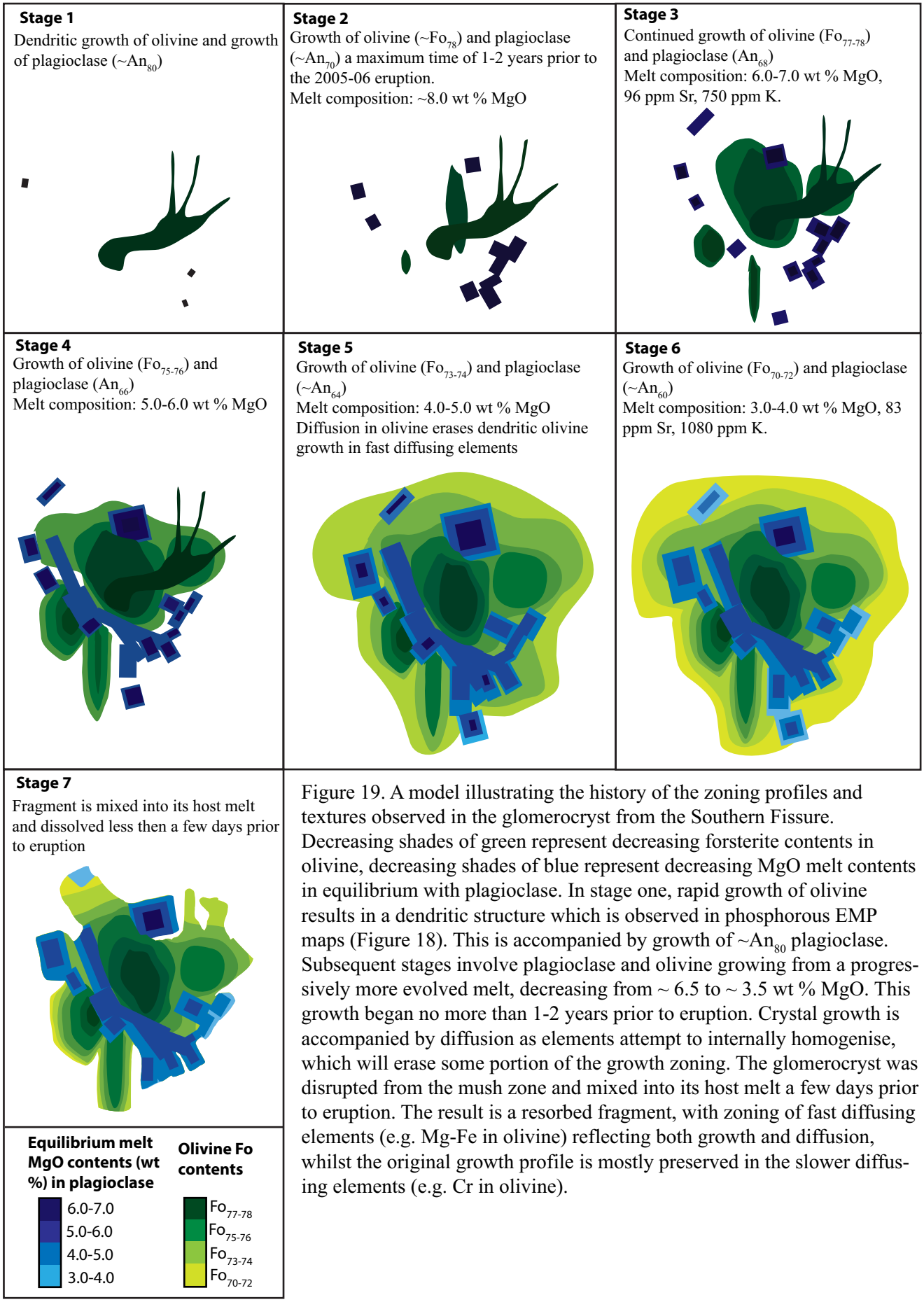

Figure 19. A model illustrating the history of the zoning profiles and textures observed in the glomerocryst from the Southern Fissure. Decreasing shades of green represent decreasing forsterite contents in olivine, decreasing shades of blue represent decreasing MgO melt contents in equilibrium with plagioclase. In stage one, rapid growth of olivine results in a dendritic structure which is observed in phosphorous EMP maps (Figure 18). This is accompanied by growth of ~An_{80} plagioclase. Subsequent stages involve plagioclase and olivine growing from a progressively more evolved melt, decreasing from ~ 6.5 to ~ 3.5 wt % MgO. This growth began no more than 1-2 years prior to eruption. Crystal growth is accompanied by diffusion as elements attempt to internally homogenise, which will erase some portion of the growth zoning. The glomerocryst was disrupted from the mush zone and mixed into its host melt a few days prior to eruption. The result is a resorbed fragment, with zoning of fast diffusing elements (e.g. Mg-Fe in olivine) reflecting both growth and diffusion, whilst the original growth profile is mostly preserved in the slower diffusing elements (e.g. Cr in olivine).

occur. However, the relatively high olivine Ni contents (0.06-0.11 wt %) is suggested to be a product of an initially more primitive crystal growing from an evolved trapped melt (Section 2.5.2; Barnes et al., 1986). This requires a certain proportion of the olivine to have grown from a primitive melt in a more open system prior to being completely trapped within the mush zone. The relative proportion of primitive olivine grown in a more open system versus the amount growing in a more evolved much zone will depend on its initial NiO contents. An initial NiO content of ~ 0.20 wt % is estimated for an olivine of Fo_{85} (the Fo value found in olivine phenocrysts from the 2005-06 lavas). This is calculated using a regression through NiO and Fo data from 763 olivine EMP analyses in basalts from spreading centres (taken from the PetDB database; www.earthchem.org/petdb). In order for the olivine within the glomerocryst to contain an average NiO content of 0.09 wt %, it would require ~ 20 % to have grown in an open system resulting in NiO olivine contents of 0.2 wt %. The remaining 80 % of the olivine would then have grown from a more evolved melt in the mush zone, with olivine NiO contents > 0.06 wt %. During this primary stage, plagioclase (~ An_{80}) crystallises, which is now observed in the cores of three crystals (Section 2.5.1; Figure 19). The composition of the melt these plagioclase crystallised from is unknown, however the high An contents (An_{80}) suggest it is likely to contain at least 8.0 wt % MgO. This is deduced from plagioclase An contents between An_{70-75} calculated to be in equilibrium with 2005-06 lavas containing ~ 8.0 wt % MgO (Section 2.4.2.2).

In the next stage, plagioclase (~ An_{70}) and olivine growth continues (Figure 19). Growth of olivine is initiated around the earlier dendritic texture in four main regions represented by the highest Fo concentrations (Fo_{78-76}; Figure 19). Subsequent stages involve further crystallisation of both plagioclase and olivine from a progressively more evolved melt in a crystal mush zone. This is observed in the decreasing olivine forsterite, Ni and Cr contents, and decreasing plagioclase An, MgO, and Sr contents from core to rim (Section 2.5). The low Sr melt contents (83-96 ppm) calculated to be in equilibrium with plagioclase also suggests extensive plagioclase crystallisation, with Sr preferentially partitioning into plagioclase producing a melt with low Sr contents. This is consistent with a model of growth within a crystal-mush zone.

During crystal growth, elements within plagioclase and olivine will attempt to erase their growth zoning and internally homogenise by diffusion (Figure 19). For fast diffusing elements (e.g. Fe-Mg in olivine; Dohmen and Chakraborty 2007a,b) eradication of growth zoning will be relatively rapid, however slow diffusing elements are more likely to preserve their initial growth profile (e.g. Cr in olivine; Ito and Ganguly, 2006). In a final stage the crystal mush fragment is mixed into its host melt and dissolved before being erupted. The preservation of the zoning profiles in fast diffusing elements suggests relatively short timescales between growth and eruption onto the sea floor. This time is quantified by modelling their zoning profile in the following section (Section 2.6.4.2). Dissolution of the mush zone is required in order to explain the embayed and irregular texture seen around the glomerocryst. Evolved melt contents (high P, low Mg) can be observed in confined pockets adjacent to rounded olivine in EMP maps, which provide evidence for either crystal growth in an evolved melt, or the dissolution of evolved crystals (Figure 18). The Fo, Mn and Cr contents of olivine rims and Mg, Sr and K content of plagioclase rims are not in equilibrium with their host melt. This suggests a short time between entrainment into the host melt, and eruption on to the sea floor.

In summary, the observed zoning profiles in the glomerocryst from the Southern Fissure represent crystal growth and differentiation from a progressively more evolved interstitial melt in a roof mush zone (Figure 19). Portions of this mush zone were disrupted and mixed into its host melt where it underwent dissolution prior to eruption in 2005-06. In the next section, diffusion modelling is completed on the crystals from the glomerocryst to retrieve estimates on the maximum time they spent in the mush zone, and the time between entrainment into its host melt and eruption.

2.6.4.2 Modelled timescales from plagioclase and olivine in the glomerocryst from the Southern Fissure

The previous section outlined a model involving growth of plagioclase and olivine in a crystal mush zone at the roof of the AMC. Here, the results of diffusion modelling are described which provide estimates of the timescales of the different stages in the model. Profiles from seven plagioclase crystals (Figure 20) and five olivine

Figure 20. **A** through to **F**: Plagioclase photomicrograph's from the glomerocryst in the Southern Fissure, with An (blue), MgO, Sr and K (red) chemical zoning profiles, and results of diffusion modelling. For the location of plagioclase within the glomerocryst refer to Figure 18.
The red arrows indicate the position of the electron microprobe traverse, and the pits show the location of LA-ICP-MS traverse. The arrow direction is always left to right in relation to the x-axis on the underlying plots. The yellow band in the An plot represents the calculated An range in equilibrium with their host melts (An_{70-75}). The error associated with the MgO analyses is between 2-4 % and is smaller than the size of the symbol used in the profiles (Appendix A.1). The errors associated with Sr and K analyses are based on the precision found in the corresponding analytical session (Appendix 1.2). The diffusion model (black) and the retrieved time (t) represents the best fit model, which was determined by minimizing the square root of the misfit between the model and data (e_{RMS}; Shown in the parenthesis; Equation A.3 in Appendix A.4.2). Times are shown from a 1D and 2D model when used, with the diffusion model shown being from a 1D model unless stated otherwise. The stated host melt MgO concentrations are taken from Goss et al. (2010). The Sr and K host melt concentrations are the average in that sample taken from both LA-ICP-MS glass analysis and bulk glass data in Goss et al., (2010; Table A.5 in Appendix 1.2).
The equilibrium profile (green) is defined by the melt composition in equilibrium with the lowest/highest concentration found at the crystal rim. The initial profile (blue) is defined by the melt composition in equilibrium with the lowest/highest concentration found in the crystal core. Boundary conditions at rims in contact with the surrounding melt are open and set at the corresponding equilibrium value. For further details on the exact initial conditions, equilibrium conditions, and boundary conditions used for each model see their corresponding caption.

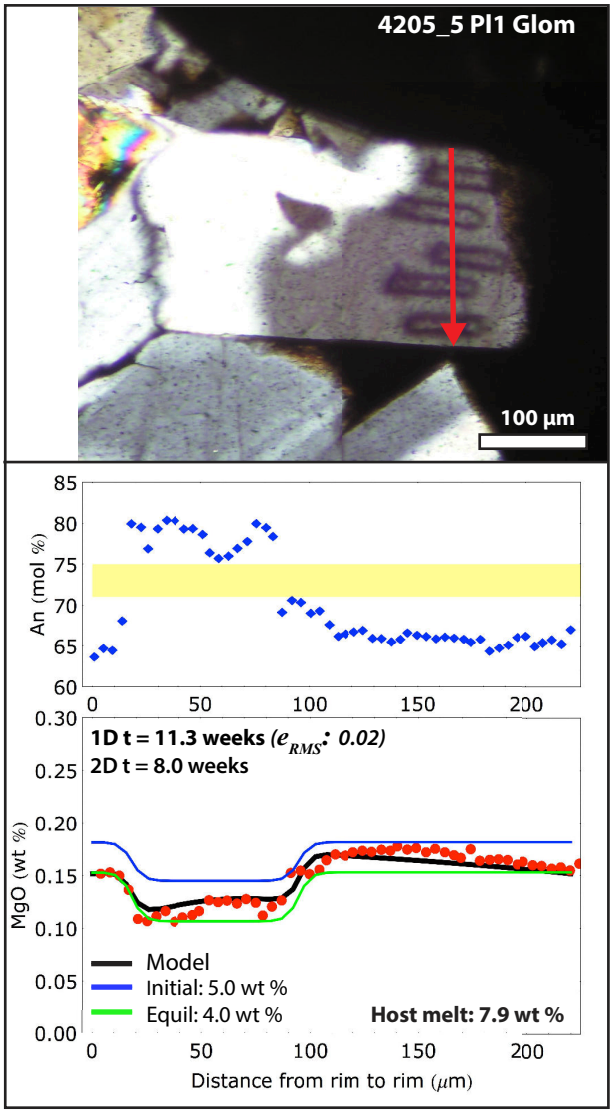

A. The crystal rims have open boundary conditions. This diffusion model is from a 2D model.

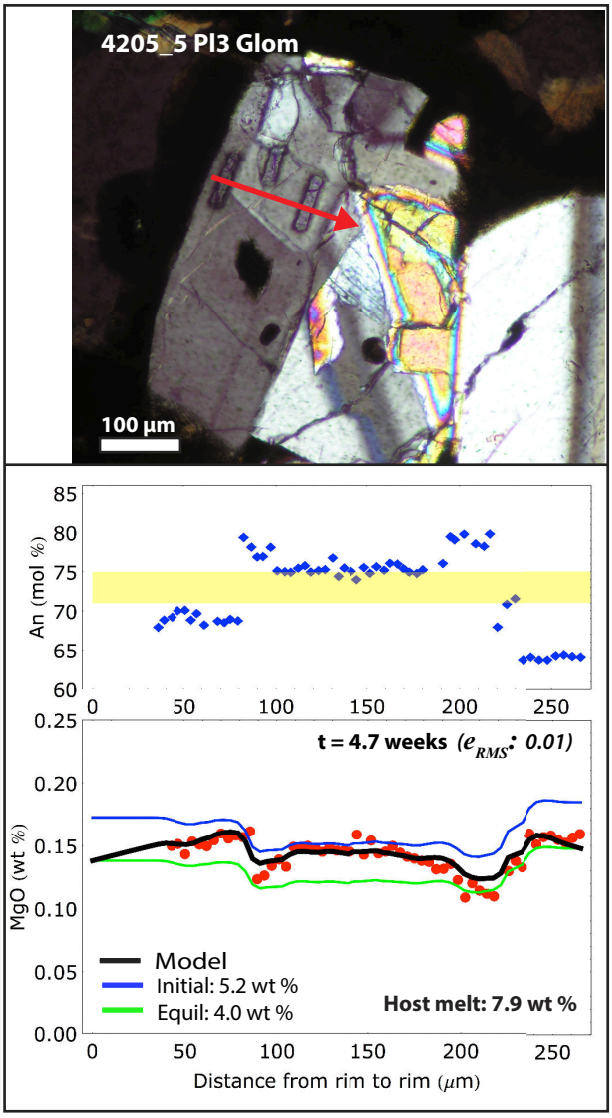

B. The boundary conditions at both rims are set as open. This assumes that the Mg diffusion rate at the crystal-crystal interface (right of profile) is the same as the crystal-melt interface (left of profile).

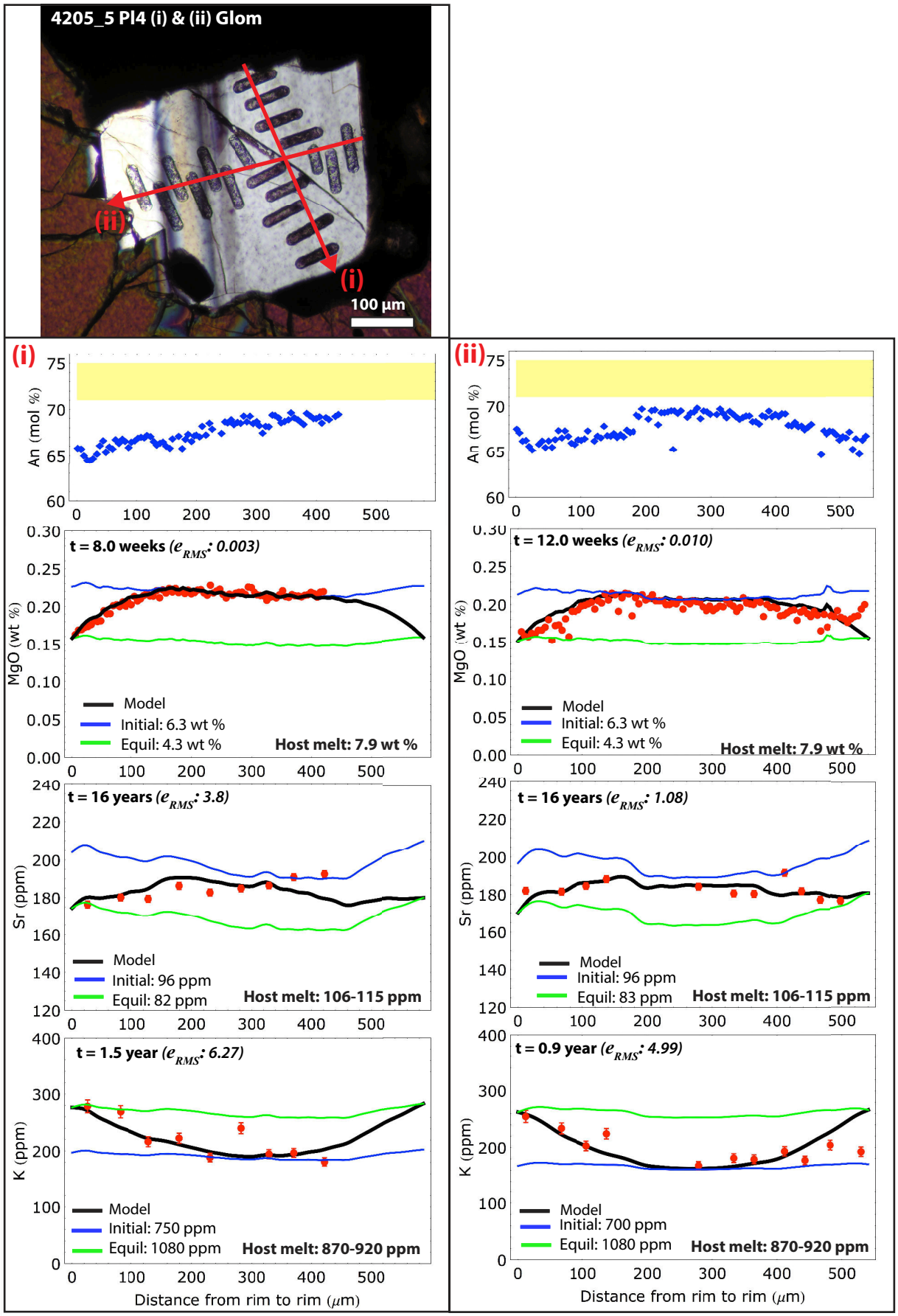

C. Boundary conditions for both profiles **(i)** and **(ii)** are open. This model assumes that after the zoning was produced, ~100 µm of rim 2 (right of profile **(i)**) was dissolved in order to account for its asymmetric shape. This is unlike profile **(ii)** where a roughly symmetrical shape is observed. The anorthite contents outside the profile range in **(i)** were estimated from the An profile of transect **(ii)**.

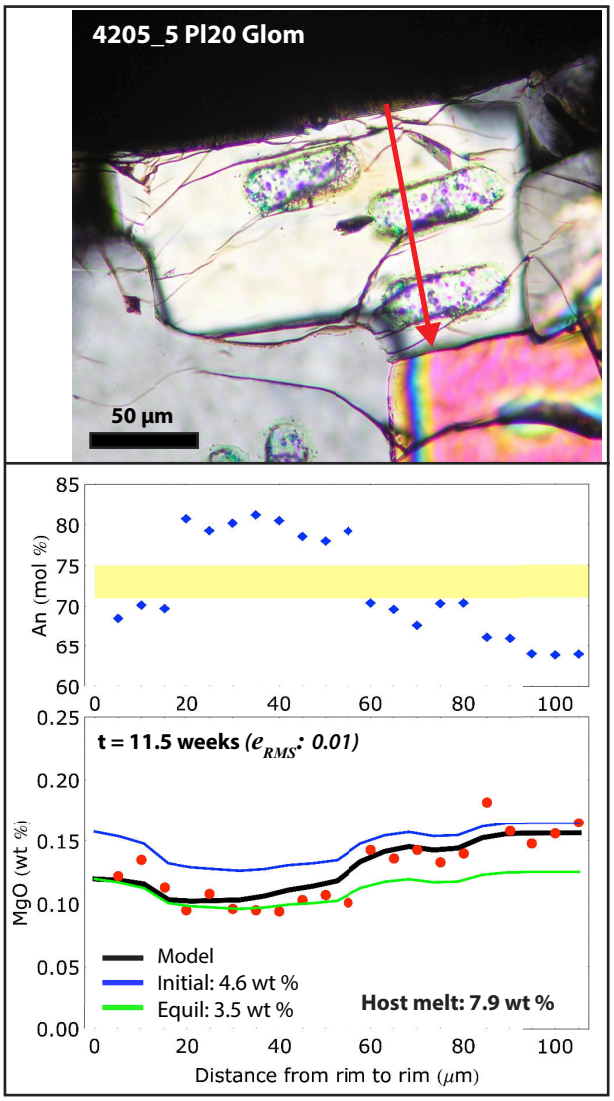

D. The plagioclase-melt interface has an open boundary, and the plagioclase-olivine interface has a closed boundary.

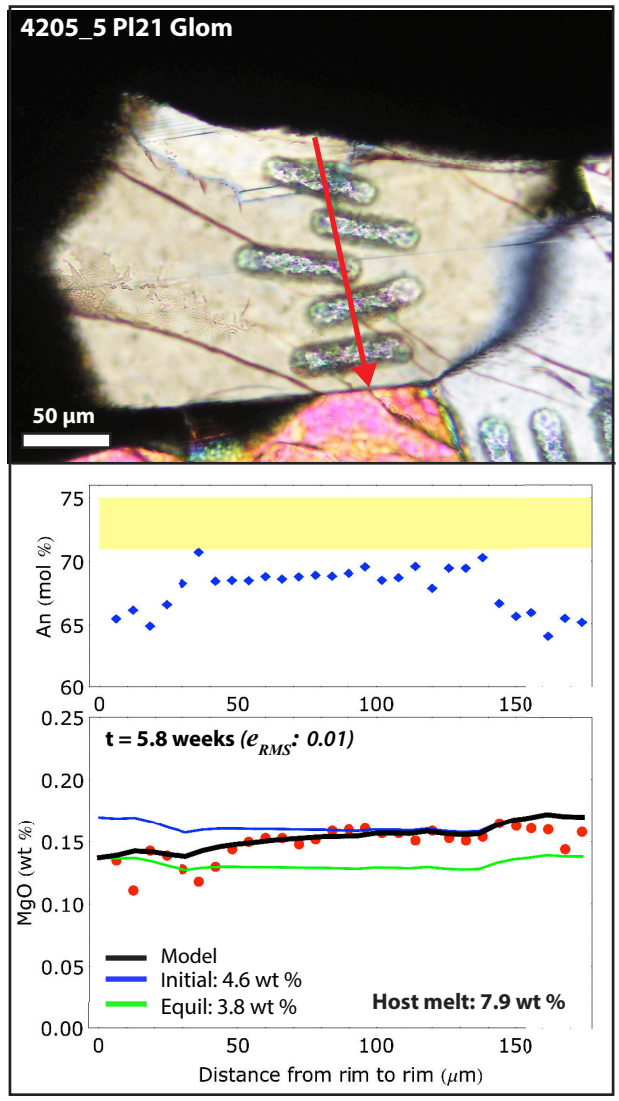

E. The plagioclase-melt interface has an open boundary, and the plagioclase-olivine interface has a closed boundary.

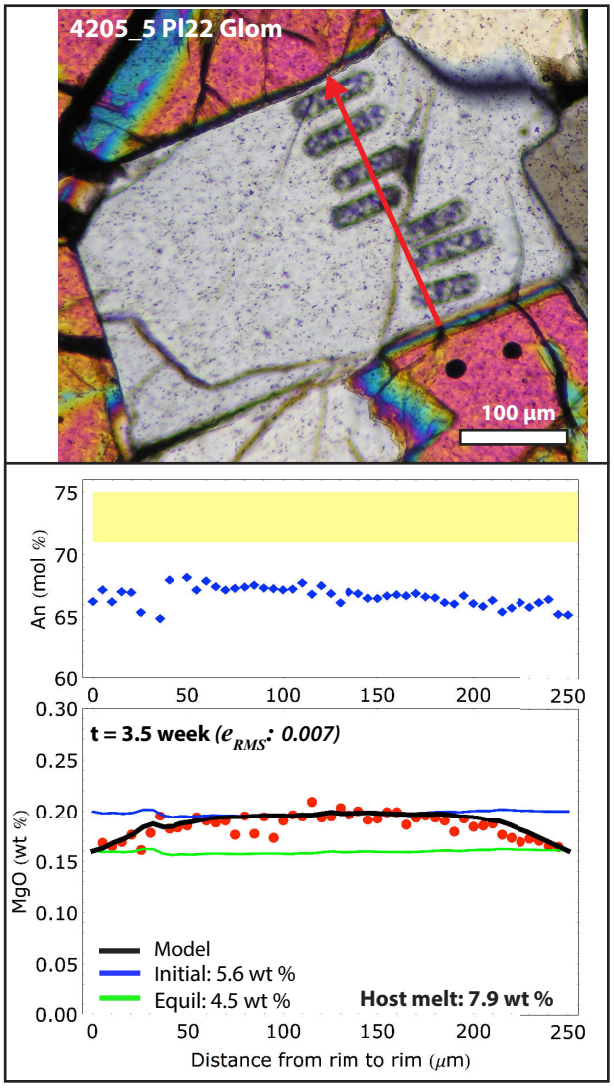

F. Boundary conditions at the rims are open and it is assumed they are in contact with melt.

Figure 21. **A** through to **E**: Olivine Fo, Mn, Ni and Cr chemical zoning profiles (red), and results of diffusion models (black). For the location of the olivine profiles completed on the glomerocryst refer to Figure 18. The arrow direction on the transect is always left to right in relation to the x-axis on the plots. The errors associated with MnO, NiO and Cr LA-ICP-MS analyses are based on the precision found in the corresponding analytical session (Appendix 1.2). Note, the errors associated with Cr analysis are smaller than the size of the symbol used. Two initial profiles (blue) are used, the first (ini 1) is an initial homogeneous profile at the maximum/minimum concentrations found in the core. The second (ini 2) is a zoned initial profile at the maximum and minimum concentrations found at the rim and core. The equilibrium profile is shown in green. The boundary conditions at crystal rims in contact with the surrounding melt are open and set at the corresponding value of the rim. The diffusion model represents the best fit model which was determined by minimizing the square root of the misfit between the model and data (e_{RMS}; shown in the parentheses; Equation A.3 in Appendix A.4.2). The diffusion models shown are from an initially zoned profile (ini 2). For further details on the exact initial conditions and boundary conditions used for each model see their corresponding caption. Reported modelled times (t) are retrieved from the diffusion coefficients parallel to the *c*-axis.

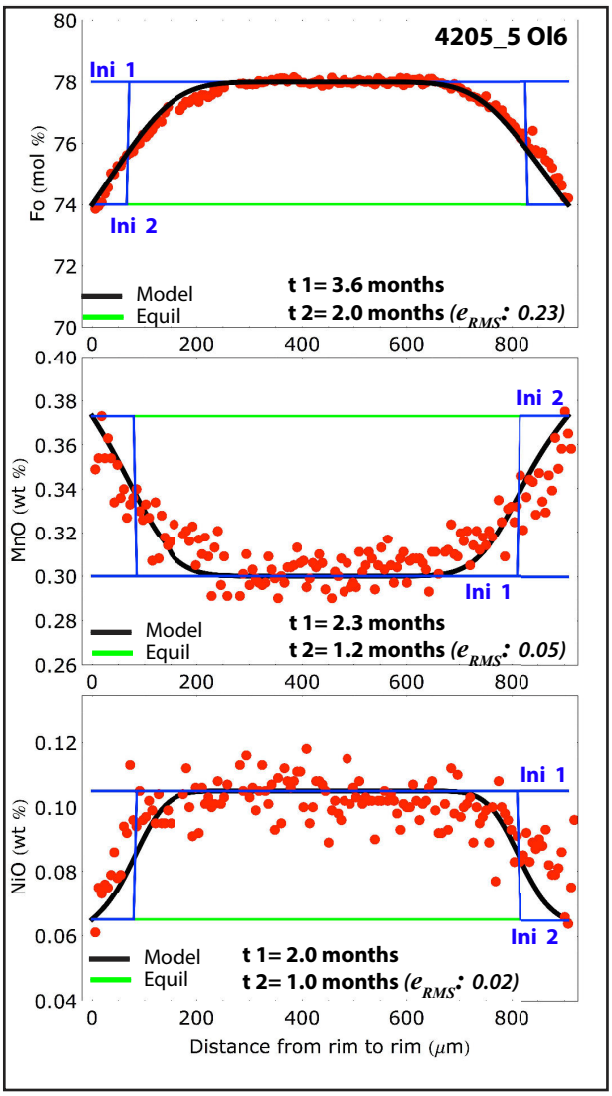

A. The boundary conditions at the crystal rims are open.

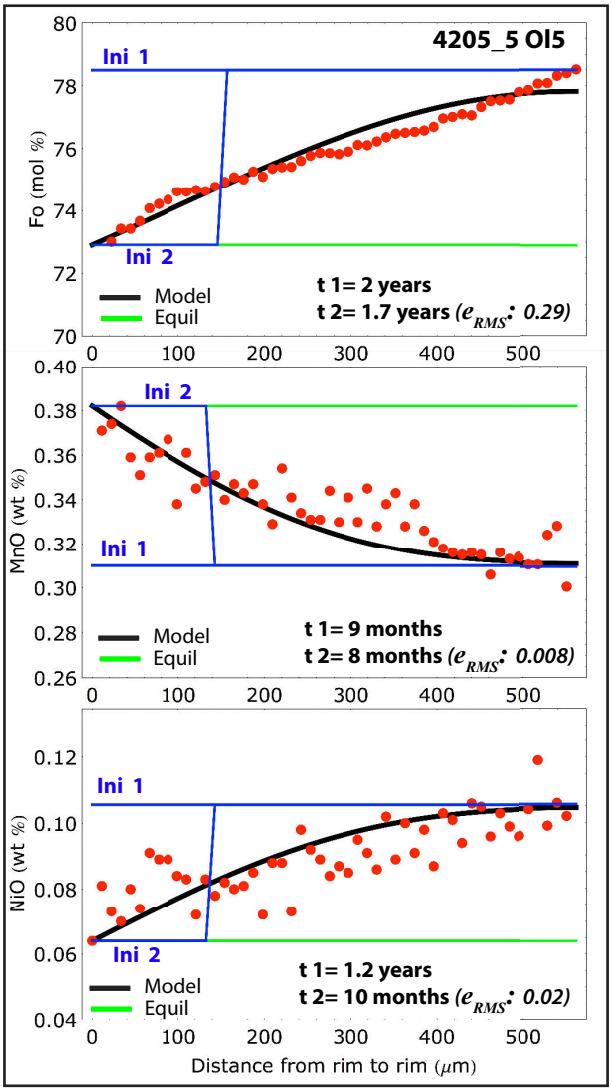

B. The olivine-plagioclase interface (right side of profile) has a closed boundary and the olivine-melt interface has an open boundary.

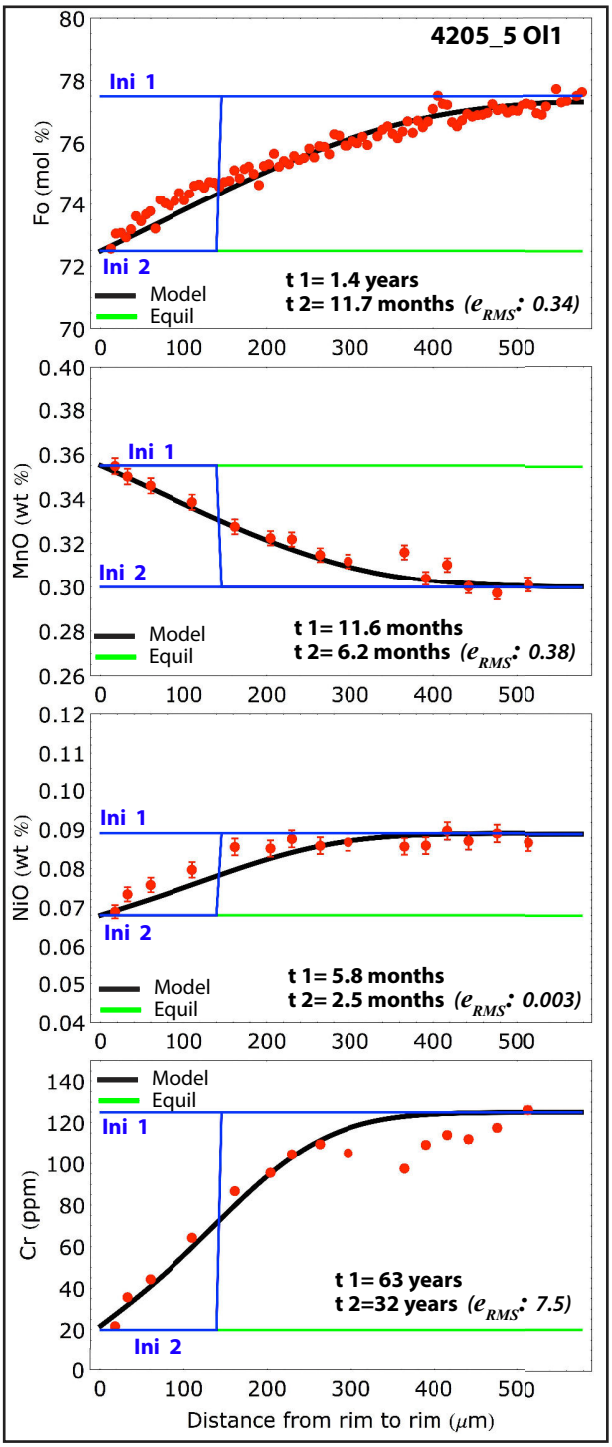

C. The olivine-melt interface (left of profile) has an open boundary and the olivine-plagioclase interface (right of profile) has a closed boundary.

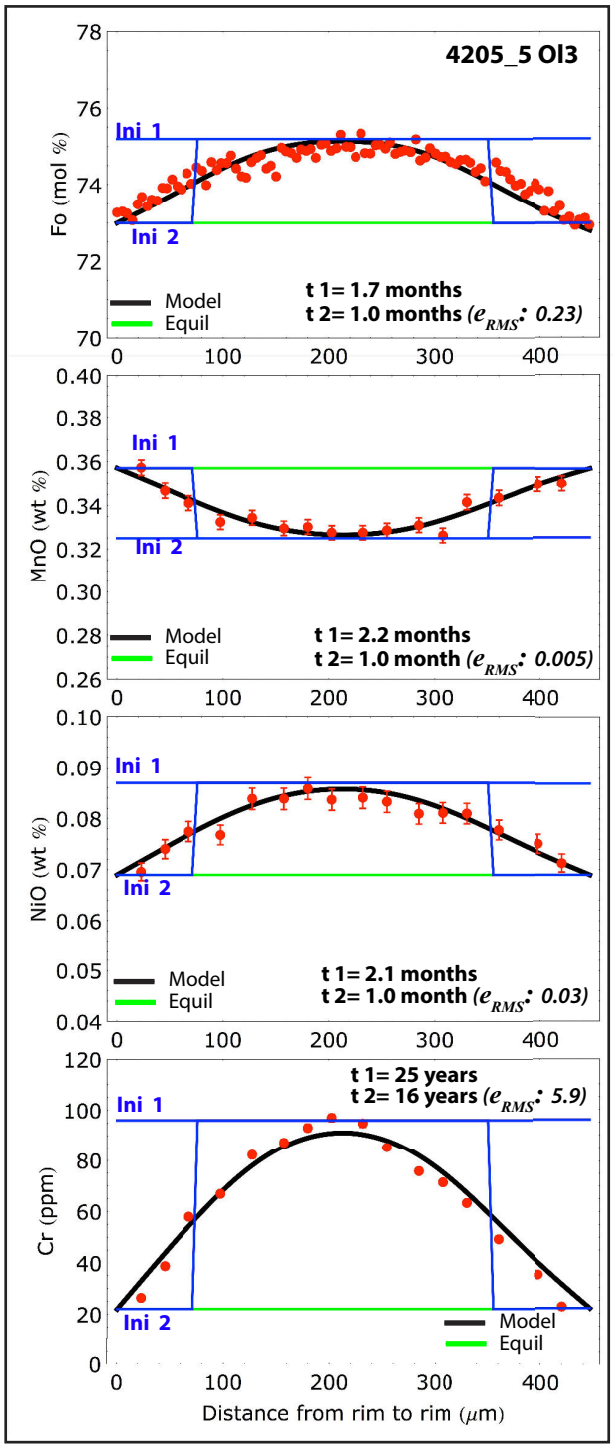

D. The crystal rims have open boundaries.

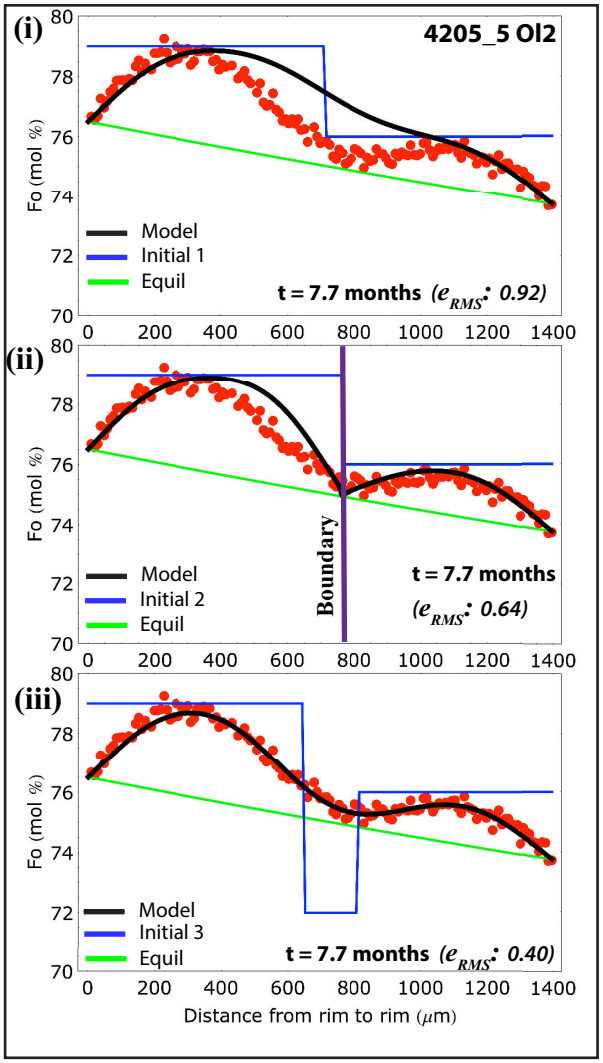

E. This profile is modelled using three initial conditions. In all three cases the crystal rims have an open boundary. **(i)**: an initial zoned profile at the two maximum Fo concentrations. In this model the olivine grew from two different melt compositions. **(ii)**: a similar initial profile to (i), with the addition of diffusion along a grain boundary (purple line). This assumes diffusion along the grain boundary is occurring at the same rate as diffusion at the rims. The olivine is optically continuous (i.e. no evidence of multiple grains), suggesting the absence of a grain boundary, although it may have annealed.

The third model **(iii)** gives a better fit to the data than **(i)** or **(ii),** although has a more complex initial profile with three zoning steps. In this model the olivine grows from three melt compi-sitions. All three initial profile provides a similar time of ~ 7.7 months.

transects (Figure 21) were modelled. The initial and boundary conditions used for plagioclase and olivine diffusion models are the same as for euhedral crystals (Section 2.6.1 & 2.6.3). A temperature of 1200°C is used for all diffusion models. However as noted above, these crystals are in equilibrium with more evolved melts than their host suggesting lower temperatures than the 1200°C predicted for the melt compositions of 2005-06 lavas. Decreasing the temperature by ~ 50°C will decrease diffusion rates within crystals and increase the reported modelled timescales by a factor of ~ 2.

The time of initial crystallisation of dendritic olivine and high An plagioclase cores (An_{80}) cannot be constrained due to a lack of geochemical data from this early stage. The time of initial crystallisation from a ~ 6.5 wt % MgO melt can be constrained from modelling the observed profiles in plagioclase and olivine. Results of diffusion modelling of Mg profiles in plagioclase provides timescales between 3.5 and 11.6 weeks (Figure 20). In plagioclase, one crystal shows pronounced internal disequilibrium in both Sr and K, with a core in equilibrium with a 97 ± 2 ppm Sr and 750 ppm K melt, and a rim in equilibrium with a 83 ± 2 ppm Sr and 1080 ppm K melt. Modelling this crystal's Sr profile gives a time of ~ 16 years, and for K a time of ~ 1 year (Figure 20C). These times are significantly longer than the weeks retrieved from Mg in plagioclase. Modelling the Fo, Mn, Ni and Mn profiles from five olivine transects in the glomerocryst provide times between 1 month and 2 years (Figure 21). The Cr profiles from two olivine crystals in the glomerocryst have cores of 100-120 ppm decreasing to ~ 20 ppm at their rims (Figure 21 B & D). Modelling of these Cr profiles provides times between 16 and 63 years, which are substantially longer than those retrieved from the divalent cations. The difference in modelled times between the slower and faster diffusing elements in olivine and plagioclase can be explained by the Sr, K and Cr profiles representing crystal growth and differentiation. Their initially zoned profiles have not been significantly modified by diffusion due to their slower diffusion rates (Ito and Ganguly, 2006; Giletti and Casserly, 1994; Giletti and Shanahan, 1997). The times retrieved from plagioclase MgO profiles are shorter than those determined from Fo, Mn or Ni in olivine which could be due to: (i) uncertainty in their initial profile. Diffusion rates of Mg in plagioclase are faster than divalent cations in olivine (LaTourrette and Wasserburg, 1998) which will lead to the rapid eradication of the initial profile; (ii) the majority of plagioclase crystals being

surrounded by olivine. This will result in Mg diffusion at the olivine and plagioclase boundary being controlled by grain-boundary diffusion and/or exchange with olivine. These are likely to be slower processes than Mg exchange at plagioclase-melt contacts. The modelled timescales retrieved from plagioclase and olivine suggests crystal growth began from a 6.5 wt % melt no longer than a few years prior to eruption.

In the final stage of the model, fragments of the crystal mush zone are disrupted and mixed into its host melt where it is dissolved. The *maximum* time interval between entrainment of the glomerocryst into its host melt, and eruption on the sea floor is calculated from the time it would take for the MgO disequilibria at plagioclase rims to be erased. Rates of Mg diffusion in plagioclase are used due to it being the fastest diffusing elements in plagioclase, and faster than Fo, Mn or Ni diffusion in olivine and therefore will be the first to show signs of re-equilibration with its host. A maximum time of ~ 2 days is calculated, assuming no dissolution. The proposed model for the glomerocryst involves dissolution occurring once the glomerocryst has been entrained in to its host melt. Therefore, this maximum time will increase depending on the area being dissolved and the dissolution rate of both plagioclase and olivine. In the proposed model, plagioclase crystals are surrounded by olivine, therefore dissolution of olivine is required in order for plagioclase crystals to be exposed to its host melt. Plagioclase dissolution rates have been explored in Section 2.6.2, where it was concluded that dissolution will not substantially alter the calculated *maximum* time the crystals spent in its host melt due to rapid dissolution rates of plagioclase. Olivine dissolution rates were determined using the same methods as plagioclase (Section 2.6.2). A dissolution rate of 7.4×10^{-8} cm s^{-1} at 1200°C is calculated from a plot of olivine dissolution rates against temperature. Rates of dissolution are taken from experiments completed on $Fo_{88.5}$ olivine spheres in basalt by Donaldson (1985). Using this rate, the time taken to dissolve 0.02 cm of olivine is ~ 74 hours. (There are no known experiments performed on olivine dissolution with Fo contents lower than $Fo_{88.5}$). Dissolution rates for olivine were also determined using the expression in Edwards and Russell (1996a,b; 1998) using the same method and parameters explained in Section 2.6.2. This gave a dissolution rate of 2.88×10^{-7} cm s^{-1} which would dissolve 0.02 cm of olivine in ~ 19 hours. These dissolution rates indicate

that olivine dissolution will alter the calculated maximum time the glomerocryst spent in its host melt by no more than a few days.

In summary, olivine and plagioclase zoning profiles from the glomerocryst in the Southern Fissure represent crystal growth from a progressively more evolved melt in a mush zone at the roof of the AMC, after an initial stage of rapid growth. The olivine and plagioclase began to grow from a ~ 6.5 wt % MgO melt no longer than a few years prior to being erupted. Better constrained timescales cannot be retrieved from these crystals due to the uncertainty in determining how much of the observed zoning is from growth, and how much is from diffusion. The glomerocryst was then mixed into its host melt and began to dissolve. It resided in its host for no longer than a few days before it was erupted on to the sea floor.

2.7 Discussion

2.7.1 Petrogenetic Model

A five stage petrogenetic model is used to explain the observed melt compositions, crystal abundances, and chemical zoning profiles in plagioclase and olivine, along with their retrieved modelled timescales (Sections 2.1 to 2.6). The model systematically outlines the events occurring in the magma chamber leading up to the 2005-06 eruption (Figure 22). Accompanying Figure 22 is a list of the observations made throughout this study that support the interpretations (Int) described here (Figure 22B). This list can be referred to throughout this section by matching the stage reference number in the text with the corresponding number in Figure 22B (e.g. Int 1*a* = interpretation *a* made during stage 1).

Prior to the 1991-92 eruption, the magma chamber crystallized plagioclase (An_{75-80}) from a melt containing between 90 and 105 ppm Sr (MELT 1; Figure 22; Int 1*a*). A second melt containing over 130 ppm Sr, with an equilibrium plagioclase An content of ~ An_{75-77}, was injected and mixed into the melt lens no more than ~ 30 years prior to the 2005-06 eruption (Figure 22; Int 1*b*). Portions of the lower mush zone were disrupted and incorporated into the melt lens where they begin to dissolve (Figure 22; Int 2*a*). This

Figure 22. **A**: Petrogenetic model illustrating the five major stages occurring in the AMC leading up to the 2005-06 eruption. Rectangles represent plagioclase, and hexagons represent olivine within the AMC. Colours increasing in gradient from white to blue represent increasing Sr contents, and from orange to red represent increasing MgO, in both crystals and melts. When known, the melt composition and the equilibrium An contents of plagioclase are shown at each stage. For additional details see main text. Pre 1991-92, plagioclase (An_{75-80}) crystallised from MELT 1 which contained between 90 and 105 ppm Sr. A higher Sr melt (>130 ppm) is injected into the AMC and mixes with MELT 1 to produce the host for the crystals that are subsequently erupted in 1991-92. In the repose period between 1991-92 and 2005-06, the residual melt in the melt lens undergoes crystallisation and differentiation to a composition of 7.7-8.3 wt % MgO. Some crystals accumulate in a mush zone on the roof and floor of the AMC. Approximately 1-2 years prior to the 2005-06 eruption growth of olivine and plagioclase continues in a roof mush zone from an evolved interstitial melt (see Figure 17 & 18 for details). A maximum time of ~7 weeks prior to the 2005-06 eruption, a small volume of primitive melt containing few crystals (~ 9 wt % MgO; MELT 4) is injected into the AMC. Mixing occurs and fragments of the crystal-mush zone are incorporated into the melt lens and begin to dissolve. This melt becomes the host for the crystals erupted in 2005-06. Note, the majority of euhedral crystals have MgO, Sr and K contents in equilibrium with their host melt but are not represented in these figures. **B**: A list of observations from known melt compositions, crystal zoning profiles, modeled timescales and crystal abundances from Sections 2.3 to 2.6. These observations support the corresponding interpretation (Int) made at that particular stage of the model and in the main text (Section 2.7.1). Note, SF is short for Southern Fissure, BE for the Bull's eye, and S refers to a particular Section (i.e. S.2.3 is Section 2.3).

A: Petrogenetic Model	B: Observations
Stage 1 **t = pre 1991-92** 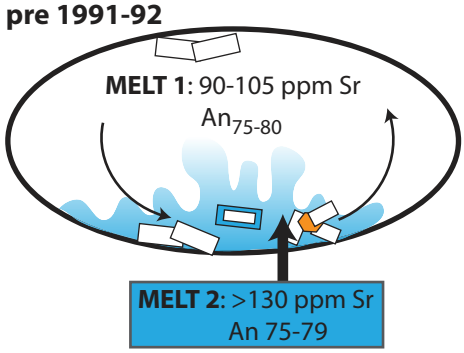 	**1a** • Crystals in equilibrium with a 90-105 ppm Sr melt and with An contents between An_{75-80} (S.2.5.1). **1b** • Sr contents of 1991-92 lavas are 118-127 ppm Sr (Sims et al., 2002), which requires an input of a higher Sr melt to mix with the 90-105 ppm melt in the AMC. • Five crystals with rims in equilibrium with a higher Sr melt than their cores. Modelling of these profiles provides times of between 4 and 30 years prior to the 2005-06 eruption (S.2.6.2.1). • Euhedral plagioclase with An contents of An_{75-77} (S.2.5.1.1)
Stage 2 **t =1991-92** 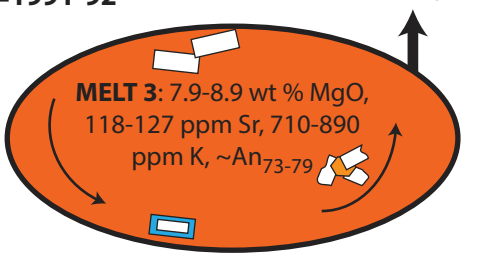 	**2a** • A xenolith from 1991 lavas containing plagioclase and olivine. Crystals display corroded margins and signs of internal re-melting and is interpreted to be derived from a lower crystal mush zone (Ridley et al., 2006). **2b** • Range of melt compositions reported in 1991-92 lavas by Sims et al. (2002).
Stage 3 **t = between 1991-92 and 2005-06** 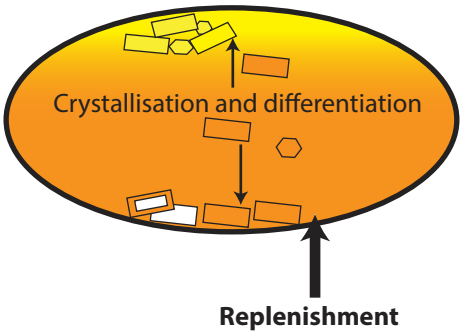 	**3a** • The presence of euhedral plagioclase (An_{75-77}; S.2.5.1.1) and olivine (Fo_{85}; S.2.5.2) • The 2005-06 lavas are more differentiated than those from the 1991-92 eruption (Goss et al., 2010; S.2.4.1). **3b** • Plagioclase and olivine within glomerocrysts from the BE and SF (S.2.5 & S.2.6.4). **3c** • Crystals in the glomerocryst from the SF are in equilibrium with a progressively more evolved melts from core (6.5 wt % MgO) to rim (3.5 wt % MgO). Such evolved melts indicate cool temperatures which suggests a location in a roof mush zone (S.2.6.4) **3d** • Diffusion modelling of the zoning profiles in the SF glomerocryst provide a maximum time of 1-2 years between growth and eruption (S.2.6.4.2).
Stage 4 **t = weeks - months before 2005-06 eruption** 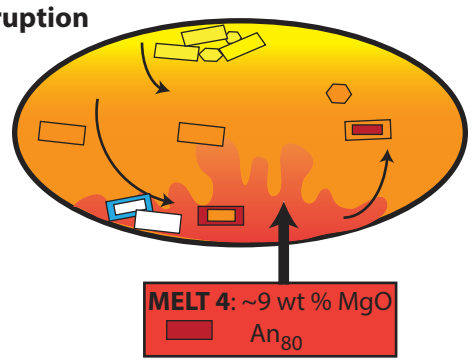 	**4a** • Six crystals from the BE region have cores or rims in equilibrium with a higher MgO melt (> 8.8 wt % MgO) than their host melt (S.2.5.1.2). Diffusion modeling of the MgO profiles of these crystals provides times of between 1-6 weeks (S.2.6.2.1). **4b** • The majority of euhedral crystals are in equilibrium with their host melts (S.2.5) **4c** • Rare resorbed plagioclase are found within all regions (S.2.3) • The texture of the glomerocryst from the SF provides evidence of dissolution occurring along grain boundaries (S.2.3).
Stage 5 **t = 2005-06** 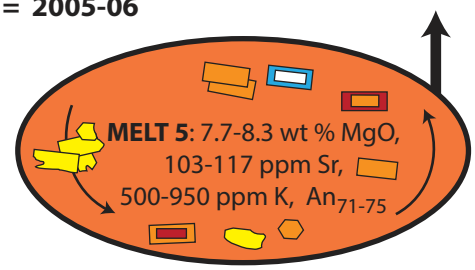 	**5a** • Lavas from the 2005-06 eruption contain 7.7-8.3 wt % MgO (Goss et al., 2010). **5b** • Crystal rims have MgO, Sr and K contents out of equilibrium with their host melts, requiring a minimum time of ~ 2 days in their host melt before eruption (S.2.6).

mixing resulted in a third melt with MgO, Sr and K contents between 8.4-8.7 wt %, 118-127 ppm, and 710-890 ppm respectively (Sims et al., 2002), and equilibrium plagioclase An contents of An_{73-79} (anorthite equilibrium contents are maximum and minimum values calculated using the same three methods described in Section 2.4.2.2; Int 2*a*). Between 1991 and 1992 this mixed melt was erupted onto the seafloor (Stage 2; Figure 22). During the ~ 13 year repose period between the 1991-92 and 2005-06 eruption, the residual melt crystallised plagioclase (An_{75-77}) and olivine (Fo_{85}), leaving the remaining melt within the AMC more differentiated (Figure 22; Int 3*a*). Replenishment of the melt lens is required within these ~13 years in order to prevent the melt lens from freezing (e.g. Liu and Lowell, 2009), and to prevent the melt from evolving to low MgO contents (< 7.7 wt % MgO; Goss et al., 2010). Goss et al. (2010) calculated that the AMC would completely crystallize in the repose period between the 1991-92 and 2006-06 eruptions in ~ 4.6 years without magma replenishment. During this repose period, a number of crystals are caught up within mush zones surrounding the AMC (Figure 22; Int 3b). Within a roof mush zone, crystallisation of plagioclase and olivine occurred from a progressively more evolved interstitial melt (Figure 22; Int 3*c*). This crystallization began a maximum time of 1-2 years prior to the 2005-06 eruption (Figure 22B; Int 3*d*; Section 2.6.4.2).

In the weeks to months leading up to the 2005-06 eruption a small volume of primitive melt, containing ~ 9 wt % MgO and a small number of phenocrysts, is injected into the melt lens (Figure 22; Int 4*a*). This input of more primitive melt occurred primarily in the AMC beneath the central Bull's eye region (Int 4*a*). This supports the suggestion that the Bull's eye (9º50’N) region may have a higher magmatic budget than regions to the north or south (Section 1.2). The small volume of primitive melt ensures that once mixed sufficiently the overall composition of the melt within the AMC is not substantially altered. Subsequently, the vast majority of phenocrysts remain close to being in equilibrium with the melt residing in the melt lens (Figure 22; Int 4*b*). In rare cases, there is insufficient time for the MgO content within some crystals to completely equilibrate with the melt it is brought into contact with. This is seen in euhedral crystals with MgO contents at rims in equilibrium with a higher or lower MgO melt than their cores (Figure 22; Int 4*a*). This mixing event disrupts and incorporates fragments of the

crystal mush zone from both the roof and floor of the AMC into the melt lens. An injection of hotter, more primitive magma into the AMC is thought to induce upwards migration of the melt lens, which is consistent with inducing disruption and assimilation of portions of the roof zone (e.g. Gillis and Coogan, 2002; Gillis et al., 2003; France et al., 2009). The low Cl contents (~50 ppm) found in the 2005-06 lavas by Soule et al. (2010) suggest the assimilated roof zone portions were not hydrothermally altered. Dissolution of these mush fragments progressed along grain boundaries, releasing some crystals into the melt lens. In rare cases these released crystals did not completely dissolve and now appear as resorbed phenocrysts (Int 4*c*). In the final stage, mixing occurred resulting in the melt compositions observed in the the 2005-06 lavas (Int 5*a*). A final mixing event must have occurred less than 2 days prior to eruption (Int 5*b*). This mixing may have occurred in the AMC, and/or in dykes, and/or within lava flows on the seabed.

2.7.2 Comparison of modelled timescales to previous work

2.7.2.1 Comparison of timescales with seismic data from Tolstoy et al. (2006)

The number timescales modelled from 2005-06 phenocrysts can be compared to the increase in number of earthquakes recorded per day (Tolstoy et al., 2006) to determine if there is a link between processes occurring in the magma chamber and seismic activity (Figure 23). Increasing numbers of seismic events were observed in the ~ 2 years leading up to the 2005-06 eruption, from October 2003 to Jan 2006 (Tolstoy et al., 2006; Figure 23). These seismic events likely reflects crustal inflation, tectonic cracking and hydrothermal activity prior to the eruption (Tolstoy et al., 2006). There is a clear increase in the number of modelled timescale representing mixing events within the AMC, which follows the trend of increased seismic activity (Figure 23). This suggests a link exists between the input of melt and magma mixing within the AMC, and seismic activity prior to a MOR eruption.

The only other location where two submarine eruptions have been observed in situ is the Axial Seamount on the Juan de Fuca ridge. An eruption in 1998 was recorded with geodetic sensors (Fox et al., 2001; Dziak et al., 1999), and more recently a second

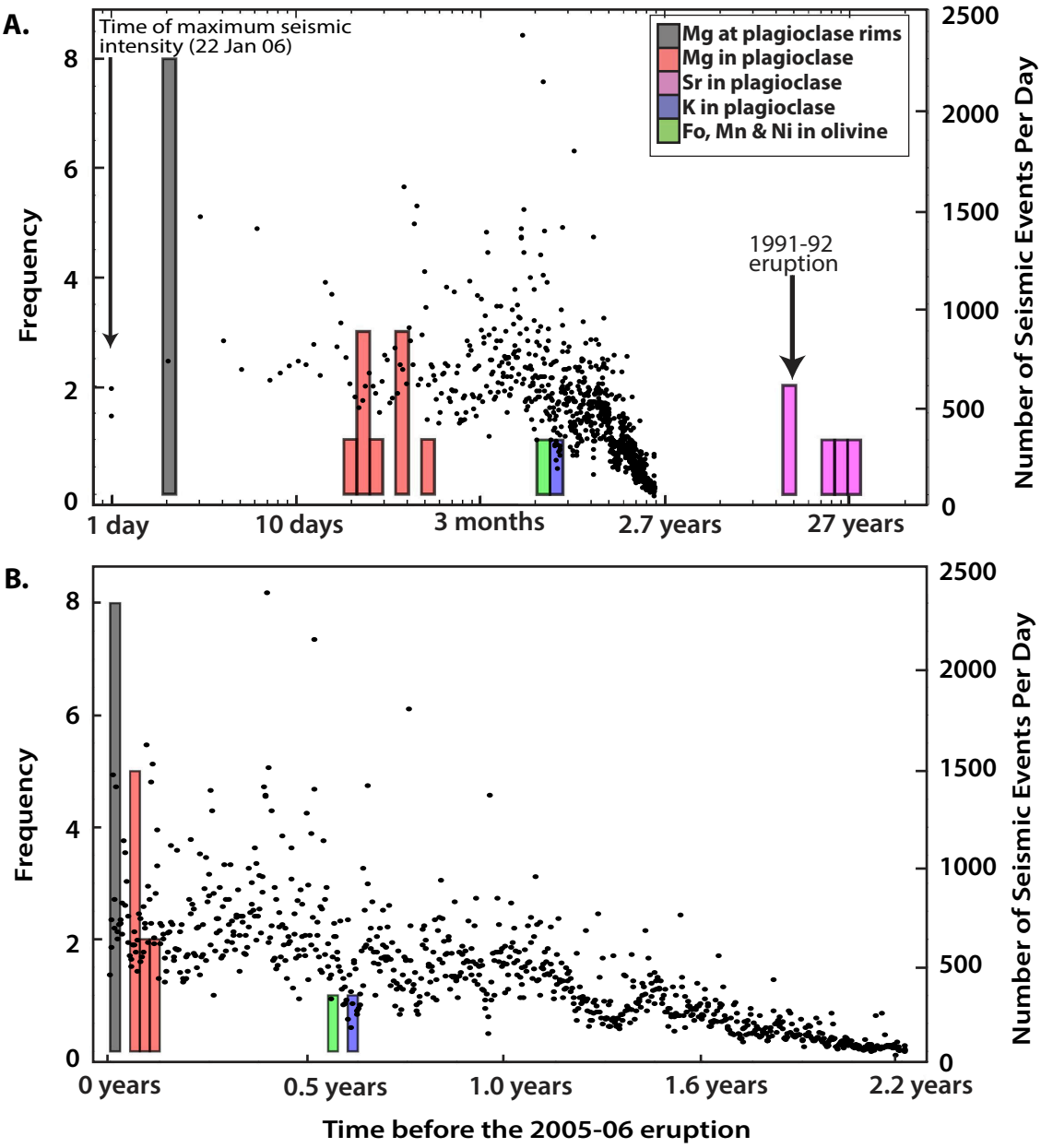

Figure 23. Histograms of the number of modelled timescales retrieved from plagioclase and olivine crystals from 2005-06 lavas that represent mixing events. The x-axis represents time before the 2005-06 eruption, and is on a logarithmic scale in plot **A**. Plot **B** displays the same data (minus the longer times retrieved from Sr in plagioclase) and is plotted on a linear scale. The grey bar represents the number of crystals with MgO, Sr and K contents at rims that are out of equilibrium with their host melt, and have been mixed into their host less than ~2 days prior to eruption (Note, here the timescales retrieved from plagioclase and olivine crystals within the Southern Fissure glomerocryst are counted as one time). The red, pink, and blue bars represent the number of modelled times retrieved from MgO, Sr, and K in plagioclase (using times retrieved from 1D diffusion models). The green bar represent the number of modeled times from Fo, Mn and Ni in olivine crystals. Overlain on this histogram are data from the number of seismic events per day recorded from October 2003 up to what is taken as the culmination of the eruption on the 22 Jan 2006 (taken from Tolstoy et al., 2006; black dots). The increase in the number of modelled timescales follows the increase in the number of seismic events recorded prior to the eruption.

eruption was recorded in April 2011 using ocean bottom hydrophones (OBHs; Dziak et al., 2012; Chadwick et al., 2012). OBHs were deployed around the caldera of Axial Seamount from late 2006 until 2011 due to evidence of re-inflation of the caldera measured from bottom pressure recorders (BPRs). The OBHs recorded a steady increase in seismic activity up to 5 years prior to the April 2011 eruption (Dziak et al., 2012). Bottom pressure recorder measurements showed the volcano inflation rate gradually increased over 3-4 months due to magma intrusion prior to eruption (Chadwick et al., 2012). This data is consistent with the interpretations made from this study that a relationship exists between seismicity and magma intrusion in submarine volcanic activity.

2.7.2.2 Comparisons between the timescales derived from previous diffusion modelling studies in oceanic basalts

Costa et al. (2009) used a similar methodology as described here to study An, Mg, and Sr zoning profiles within plagioclase from both the Costa Rica Rift and the Mid-Atlantic Ridge. Diffusion modelling of crystals from the Mid-Atlantic Ridge gave residence times within a mush zone of <140 years, followed by disaggregation of the mush zone less than 1.5 years before eruption (Costa et al., 2009). This idea of a crystal mush zone being disrupted prior to an eruption concurs with the short timescales determined from the glomerocryst and resorbed crystals erupted in 2005-06. Modelling of plagioclase from the Costa Rica Ridge indicates mixing with a primitive melt occurred between 1 and 10 years before eruption, followed by mixing with an evolved melt a maximum of a few days prior to eruption (Costa et al., 2009). These times are similar to those retrieved from this study. Pan and Batiza (2002) present results from diffusion modelling of olivine zoning profiles from the 9˚30'N and 10˚30'N portion of the EPR. They modelled zoning profiles assuming a continuously fed AMC, using a three-dimensional spherical diffusion equation, and using $D_{Fe\text{-}Mg}$ based on data from Chakraborty (1997) for the direction along the faster *c*-crystallographic axis. From this method, they calculated timescales on the order of months to years, with shorter timescales being more abundant than longer (Pan and Batiza, 2002). These complement

the magma mixing times determined from this study. The conclusions drawn from Costa et al. (2009) and Pan and Batiza (2002) are similar to those detailed here, in that a mixing event commonly occurs less than a year prior to a MOR eruption.

Zellmer et al. (2011, 2012) examined Sr and Ba zoning within plagioclase from the EPR, Juan de Fuca ridge, North Gorda ridge and the Gakkel Ridge. The modelling approach used by Zellmer et al. (1999, 2003, 2010, 2011, 2012) is different to the method used in this study. Zellmer's approach involves modelling the diffusive disequilibria that is retained between two parts of a plagioclase, using a model that assumes a closed boundary at the crystal rim. They therefore retrieve very short timescales by modelling local disequilibria that exists between closely spaced zones in many parts of a crystal. Crystal residence times varied between days to a few months. These times are similar to those retrieved from Mg in plagioclase here; however they are up to four orders of magnitude shorter than those determined from modelling Sr in this study. This discrepancy in the timescales modelled from Sr profiles is due to the different models used. The method used in this study is preferred as disequilibria between two closely spaces zones in a crystal may often be within the error of the analyses.

2.7.3 Broader implications

Lavas erupted from mid ocean ridges provide direct evidence of the magmatic processes that are occurring in the underlying magma reservoir. The chemical evidence from crystals erupted in the 2005-06 lavas indicate an influx of more primitive melt into the AMC occurred weeks prior to eruption. These short timescales support the idea of eruptions at MOR being initiated by an input of more magma into the AMC. This mechanism for driving eruptions has been proposed both at slow and fast spreading ridges (e.g. Sinton and Detrick, 1992; Costa et al., 2009), as well as in convergent and intraplate margins (e.g. Wright, 1973; Sparks et al., 1977). The petrogenic model described above contradicts that put forward by Goss et al. (2010) who state that there is no chemical evidence to suggest that the 2005-06 eruption was induced by an injection of more primitive melt into the AMC. Instead, Goss et al. (2010) proposes that the eruption

was triggered by fractionated melt being expelled into the overlying AMC from the mush zone.

The chemical zoning profiles of resorbed crystals and crystals within the glomerocryst from 2005-06 lavas supports the idea of disaggregation of a crystal mush zone occurring shortly before eruption (e.g. Sinton et al., 1993; Ridley et al., 2006; Costa et al., 2009). The evolved melts calculated to be in equilibrium with the glomerocryst and resorbed crystals suggests growth occurred within a roof mush zone, where hydrothermal circulation can facilitate cooling of melt temperatures on short timescales. Disruption of a roof mush zone is consistent with an influx of hotter, more primitive melt, inducing upwards migration of the melt lens and disrupting portions of the roof (e.g. Gillis and Coogan, 2002; Gillis et al., 2003; France et al., 2009). Assimilation of the AMC roof material has been documented in ophiolites, and at Pito and Hess Deep (e.g. Pedersen, 1986; Gillis and Roberts, 1999; Gillis, 2002; Gillis and Coogan, 2002; Gillis et al., 2003). The low Cl contents (~ 50 ppm) in 2005-06 lavas (Soule et al. 2012) indicate little to no hydrothermally altered roof material was assimilated prior to the eruption. The evidence of dissolved mush zone fragments indicate evolved interstitial melts and crystals will both play a role in the evolution of MORB geochemistry (e.g. Sinton et al., 1993; Ridley et al., 2006; Costa et al., 2009).

Chapter 3.0 Conclusions and Future Work

3.1 Conclusions

The phenocrysts and lavas from the 2005-06 eruption along the EPR, ~ 9°50, provide a unique opportunity to examine the magmatic processes occurring beneath the ridge and which can be related to the current magmatic system. The primary conclusions of this study are as follows:

1. The composition of melts calculated to be in equilibrium with plagioclase and olivine crystals provide evidence of melts both more evolved, and more primitive, than those compositions found within the host melts. This requires mixing to erase this large scale heterogeneity.
2. Glomerocrysts and resorbed crystals in equilibrium with very evolved melts (3.5 -6.5 wt % MgO) suggest that disruption and assimilation of a roof-mush zone may occur within the melt lens. This disruption may be initiated by an injection of hotter, more primitive melt. Disaggregation of mush zones implies that evolved, interstitial melt will play a role in the evolution of MORB's.
3. Chemical evidence from the 2005-06 lavas suggests the eruption was likely triggered by an injection of hotter, more primitive melt (~ 9 wt % MgO) into the melt lens weeks to months prior to eruption onto the seafloor.
4. The number of modelled timescales from 2005-06 phenocrysts representing mixing events correlates with the increase in seismic events recorded prior to the 2005-06 eruption (Tolstoy et al., 2006). This suggests a possible link exists between magma mixing and seismic activity at fast spreading ridges.

3.2 Future Work

To learn more about the timescales of magmatic processes at 9°50'N along the EPR, future work may involve analysing additional samples from the 2005-06 lavas using the same approach described here. Ideally this would include analysing more resorbed crystals from lavas which may provide information on equilibrium melt

concentrations, and timescales of magma-mush zone interactions within the AMC. A similar course of study could also be performed on phenocrysts in lavas collected from the 1991-92 eruption. This would provide further insight into replenishing rates and the possible triggers of eruptions at fast spreading ridges. Suggestions for improvements and additions to this study include:

- Isolating the crystallographic axes of the EMP transect in olivine. This would lead to a more accurate determination of the Fe-Mg, Mn, Ni, and Cr diffusion coefficients in order to obtain better constrained timescales from diffusion modelling.
- The interpretation of P zoning observed in the olivine EMP maps could be supplemented with analysis of P in the crystals. Quantifying P contents could provide further insight into the melt compositions in the early stages of olivine growth.
- The geochemical history of olivine and plagioclase crystals could be linked together by analysing Sr in olivine. This approach would allow for a more robust indication of the Sr contents found in the melt within the melt lens and mush zone. Timescales retrieved from diffusion modelling of Sr zoning profiles in olivine could test those retrieved from plagioclase Sr profiles. Potential problems include the Kd_{Sr} in olivine being poorly constrained due to few experimental studies being completed on the partitioning of Sr between olivine and basaltic melt (Beattie 1993; 1994). Those determined by Beattie (1993, 1994) have large standard errors associated with their absolute values. Another major difficulty is the diffusion coefficient of Sr in olivine not being known. To date, the only published Sr diffusion rates have been determined for Mn-olivine (Morioka, 1983).
- Throughout this study the reported Mg contents in equilibrium with crystals are derived from a Kd_{Mg} that is based on the Mg content of euhedral plagioclase from the 2005-06 lavas (Equation 1; Section 2.4.2.3). The absolute values of the Kd_{Mg} in plagioclase and its controls should be investigated by designing and performing high temperature experiments. In order to look at the effects of anorthite content

on the partitioning of Mg in plagioclase over time, a synthetic melt containing MgO can be used to grow plagioclase that is zoned in anorthite. Experimental runs can be left at a certain hold temperature for long enough for Mg to internally equilibrate with regards to its An content. Comparisons between the initial and equilibrium Mg zoning profiles should provide clues as to whether Mg preferentially partitions into more albitic or more anorthitic plagioclase. Experiments using natural basalt starting compositions from the 2005-06 lavas can be used to grow and equilibrate plagioclase to calculate absolute values of the Kd_{Mg}. The results of this experiment could be compared to the Kd_{Mg} calculated from the Mg contents of 2005-06 euhedral crystals (Section 2.4.2.3). This partition coefficient value would be specific to the mineral and melt compositions, and liquidus temperatures found in the lavas from the 2005-06 eruption.

References

Adams, D.T., Nielsen, R.L., Kent, A.J.R., and Tepley, F.J., 2011, Origin of minor and trace element compositional diversity in anorthitic feldspar phenocrysts and melt inclusions from the Juan de Fuca Ridge: Geochemistry, Geophysics, Geosystems, v. 12, no. 12,

Aigner-Torres, M., Blundy, J., Ulmer, P., and Pettke, T., 2007, Laser Ablation ICPMS study of trace element partitioning between plagioclase and basaltic melts: an experimental approach: Contributions to Mineralogy and Petrology, v. 153, no. 6, p. 647–667.

Allan, J.F., Batiza, R., Perfit, M.R., Fornari, D.J., and Sack, R.O., 1989, Petrology of lavas from the Lamont seamount chain and adjacent East Pacific Rise, 10 N: Journal of Petrology, v. 30, no. 5, p. 1245–1298.

Angel, R.J., Carpenter, M.A., and Finger, L.W., 1990, Structural variation associated with compositional variation and order-disorder behavior in anorthite-rich feldspars: American Mineralogist, v. 7, no. 5, p. 150–162.

Ariskin, A.A., Frenkel, M.Y., Barmina, G.S., and Nielsen, R.L., 1993, COMAGMAT: a Fortran program to model magma differentiation processes: Computers & Geosciences, v. 19, no. 8, p. 1155–1170.

Arndt, N.T., 1977, Partitioning of nickel between olivine and ultrabasic and basic komatiite liquids: Year Book—Carnegie Institution of Washington, v. 76, p. 553–557.

Babcock, J.M., Harding, A.J., Kent, G.M., and Orcutt, J.A., 1998, An examination of along-axis variation of magma chamber width and crustal structure on the East Pacific Rise between 13 30'N and 12 20'N: Journal of Geophysical Research, v. 103, no. B12, P. 30451-30.

Baker, E.T., Feely, R.A., Mottl, M.J., Sansone, F.T., Wheat, C.G., Resing, J.A., and Lupton, J.E., 1994, Hydrothermal plumes along the East Pacific Rise, 8 40′ to 11 50′ N: Plume distribution and relationship to the apparent magmatic budget: Earth and Planetary Science Letters, v. 128, no. 1, p. 1–17.

Baker, E.T., and Urabe, T., 1996, Extensive distribution of hydrothermal plumes along the superfast spreading East Pacific Rise, 13 30′--18 40′ S: Journal of geophysical research, v. 101, no. B4, p. 8685–8695.

Barnes, S.J., 1986, The effect of trapped liquid crystallization on cumulus mineral compositions in layered intrusions: Contributions to Mineralogy and Petrology, v. 93, no. 4, p. 524–531.

Batiza, R., and Niu, Y., 1992, Petrology and Magma Chamber Processes at the East Pacific Rise ∾ 9°30′N: Journal of Geophysical Research, v. 97, no. B5, p. 6779–6797.

Beattie, P., 1993, Olivine-melt and orthopyroxene-melt equilibria: Contributions to Mineralogy and Petrology, v. 115, no. 1, p. 103–111.

Beattie, P., 1994, Systematics and energetics of trace-element partitioning between olivine and silicate melts: Implications for the nature of mineral/melt partitioning: Chemical Geology, v. 117, no. 1-4, p. 57–71.

Beattie, P., Ford, C., Russell, D.., 1991, Partition coefficients for olivine-melt and orthopyroxene-melt systems: Contributions to Mineralogy and Petrology 109, no. 2, p. 212–224.

Bindeman, I.N., Davis, A.M., and Drake, M.J., 1998, Ion microprobe study of plagioclase-basalt partition experiments at natural concentration levels of trace elements: Geochimica et Cosmochimica Acta, v. 62, no. 7, p. 1175–1193.

Blundy, J.D., and Wood, B.J., 1991, Crystal-chemical controls on the partitioning of Sr and Ba between plagioclase feldspar, silicate melts, and hydrothermal solutions: Geochimica et Cosmochimica Acta, v. 55, no. 1, p. 193–209.

Boudier, F., Nicolas, A., and Ildefonse, B., 1996, Magma chambers in the Oman ophiolite: Fed from the top and the bottom. Earth and Planetary Science Letters, 144: 239-250.

Brearley, M., and Scarfe, C.M., 1986, Dissolution Rates of Upper Mantle Minerals in an Alkali Basalt Melt at High Pressure: An Experimental Study and Implications for Ultramafic Xenolith Survival: Journal of Petrology, v. 27, no. 5, p. 1157–1182.

Brewer, T.S., and Bach, W, Furnes, H. 1996. Geochemistry of lavas from Hole 896A. In: Alt JC, Kinoshita H, Stokking LB, Michael PJ (eds) Proceedings ocean drilling program scientific results, vol 148, pp 9-17.

Butterfield, D.A., Jonasson, I.R., Massoth, G.J., Feely, R.A., Roe, K.K., Embley, R.E., Holden, J.F., McDuff, R.E., Lilley, M.D., Delaney, J.R., and others, 1997, Seafloor eruptions and evolution of hydrothermal fluid chemistry [and discussion]: Philosophical Transactions: Mathematical, Physical and Engineering Sciences, p. 369–386.

Cann, J.R., 1974, A Model for Oceanic Crustal Structure Developed: Geophysical Journal of the Royal Astronomical Society, 39:169–187.

Carbotte, S., and Macdonald, K., 1992, East Pacific Rise 8--10 30′ N: Evolution of ridge segments and discontinuities from SeaMARC II and three-dimensional magnetic studies: Journal of Geophysical Research, v. 97, no. B5, p. 6959–6982.

Carpenter, M. A., 1992, Equilibrium thermodynamics of Al/Si ordering in anorthite: Physics and Chemistry of Minerals, v. 19, no. 1, p. 1–24.

Carpenter, M. A., 1991, Mechanisms and kinetics of Al-Si ordering in anorthite; I, Incommensurate structure and domain coarsening: American Mineralogist, v. 76, no. Ic.

Carpenter, M. A., Angel, R.J., and Finger, L.W., 1990, Calibration of Al/Si order variations in anorthite: Contributions to Mineralogy and Petrology, v. 104, no. 4, p. 471–480.

Carpenter, M.A., and McConnell, J.D.C., 1984, Experimental delineation of the Cl<--> Il transformation in intermediate plagioclase feldspars: American Mineralogist, v. 69, no. 1-2, p. 112–121.

Cashman, K. V., 1993, Relationship between plagioclase crystallization and cooling rate in basaltic melts: Contributions to Mineralogy and Petrology, v. 113, no. 1, p. 126–142.

Cashman, K. V, 1990, Textural constraints on the kinetics of crystallization of igneous rocks: Reviews in Mineralogy and Geochemistry, v. 24, no. 1, p. 259–314.

Chadwick, W.W., Dziak, R.P., Haxel, J.H., Embley, R.W., and Matsumoto, H., 2012, Submarine landslide triggered by volcanic eruption recorded by in situ hydrophone: Geology , v. 40 , no. 1 , p. 51–54.

Chakraborty, S., 1997, Rates and mechanisms of Fe-Mg interdiffusion in olivine at 980°–1300°C: Journal of Geophysical Research, v. 102, no. B6, p. 12317.

Collier, J.S., and Singh, S.C., 1997, Detailed structure of the top of the melt body beneath the East Pacific Rise at 9 40’N from Waveform: Journal of Geophysical Research, v. 102, no. B9, p. 20–287.

Coogan, L. A., 2003, Roof assimilation at fast spreading ridges: An investigation combining geophysical, geochemical, and field evidence: Journal of Geophysical Research, v. 108, no. B1, p. 2002.

Costa, F., Chakraborty, S., and Dohmen, R., 2003, Diffusion coupling between trace and major elements and a model for calculation of magma residence times using plagioclase: Geochimica et Cosmochimica Acta, v. 67, no. 12, p. 2189–2200.

Costa, F., Coogan, L. A., and Chakraborty, S., 2009, The time scales of magma mixing and mingling involving primitive melts and melt–mush interaction at mid-ocean ridges: Contributions to Mineralogy and Petrology, v. 159, no. 3, p. 371–387.

Cottrell, E., and Kelley, K. A, 2011, The oxidation state of Fe in MORB glasses and the oxygen fugacity of the upper mantle: Earth and Planetary Science Letters, v. 305, no. 3-4, p. 270–282.

Crawford, W.C., and Webb, S.C., 2002, Variations in the distribution of magma in the lower crust and at the Moho beneath the East Pacific Rise at 9°–10°N: Earth and Planetary Science Letters, v. 203, no. 1, p. 117–130.

Crisp, J.A., 1984, Rates of magma emplacement and volcanic output: Journal of Volcanology and Geothermal Research, v. 20, no. 3, p. 177–211.

Dalton, J.A., and Lane, A.J., 1996, Electron microprobe analysis of Ca in olivine close to grain boundaries : The problem of secondary X-ray fluorescence: American Mineralogist, v. 81, p. 194–201.

Von Damm, K.L., Oosting, S.E., and Buttermore, L.G., 1994, Chemical evolution of hydrothermal fluids at 9-10'N EPR since the 1991 eruption: 1994 results: EOS, Transactions American Geophysical Union, v. 75, p. 44.

Danyushevsky, L. V, 2001, The effect of small amounts of H2O on crystallisation of mid-ocean ridge and backarc basin magmas: Journal of Volcanology and Geothermal Research, v. 110, no. 3-4, p. 265–280.

Danyushevsky, L. V, and Plechov, P., 2011, Petrolog3: Integrated software for modeling crystallization processes: Geochemistry Geophysics Geosystems, v. 12, no. 7, p. Q07021.

Davis, A.S., and Clague, D. A., 1990, Gabbroic xenoliths from the Northern Gorda Ridge: Implications for magma chamber processes under slow spreading centers: Journal of Geophysical Research, v. 95, no. B7, p. 10885.

Detrick, R.S., Buhl, P., Vera, E., Mutter, J., Orcutt, J., Madsen, J., and Brocher, T., 1987, Multi-channel seismic imaging of a crustal magma chamber along the East Pacific Rise: Nature, v. 326, no. 6108, p. 35–41.

Detrick, R.S., Harding, A.J., Kent, G.M., Orcutt, J.A., Mutter, J.C., and Buhl, P., 1993, Seismic structure of the southern East Pacific Rise: Science, v. 259, p. 499–503.

Dixon, J.E., Clague, D.A., and Eissen, J.-P., 1986, Gabbroic xenoliths and host ferrobasalt from the southern Juan de Fuca Ridge: Journal of Geophysical Research: Solid Earth, v. 91, no. B3, p. 3795–3820.

Dohmen, R., Becker, H.-W., and Chakraborty, S., 2007a, Fe–Mg diffusion in olivine I: experimental determination between 700 and 1,200°C as a function of composition, crystal orientation and oxygen fugacity: Physics and Chemistry of Minerals, v. 34, no. 6, p. 389–407.

Dohmen, R., and Chakraborty, S., 2007b, Fe–Mg diffusion in olivine II: point defect chemistry, change of diffusion mechanisms and a model for calculation of diffusion coefficients in natural olivine: Physics and Chemistry of Minerals, v. 34, no. 6, p. 409–430.

Dohmen, R., Chakraborty, S., Palme, H., and Rammensee, W., 2003, Role of element solubility on the kinetics of element partitioning: In situ observations and a thermodynamic kinetic model: Journal of Geophysical Research-Solid Earth, v. 108, no. B3.

Donaldson, C.H., 1976, An experimental investigation of olivine morphology: Contributions to Mineralogy and Petrology, v. 57, no. 2, p. 187–213.

Donaldson, C.H., 1990, Forsterite dissolution in superheated basaltic, andesitic and rhyolitic melts, Mineralogical Magazine, v. 54, no. March, p. 67–74.

Donaldson, C.H., 1985, The Rates of Dissolution of Olivine, Plagioclase, and Quartz in a Basalt Melt: Mineralogical Magazine, v. 49, no. 354, p. 683–693.

Druitt, T.H., Costa, F., Deloule, E., Dungan, M., and Scaillet, B., 2012, Decadal to monthly timescales of magma transfer and reservoir growth at a caldera volcano.: Nature, v. 482, no. 7383, p. 77–80.

Dungan, M.A., and Rhodes, J.M., 1978, Residual glasses and melt inclusions in basalts from DSDP Legs 45 and 46: evidence for magma mixing: Contributions to Mineralogy and Petrology, v. 67, no. 4, p. 417–431.

Dunn, R. A., Toomey, D.R., and Solomon, S.C., 2000, Three-dimensional seismic structure and physical properties of the crust and shallow mantle beneath the East Pacific Rise at 9°30’N: Journal of Geophysical Research, v. 105, no. B10, p. 23537–23555.

Dziak, R.P., and Fox, C.G., 1999, Long-term seismicity and ground deformation at Axial Volcano, Juan de Fuca Ridge: Geophysical Research Letters, v. 26, no. 24, p. 3641–3644.

Dziak, R.P., Haxel, J.H., Bohnenstiehl, D.R., Chadwick, W.W., Nooner, S.L., Fowler, M.J., Matsumoto, H., and Butterfield, D. A., 2012, Seismic precursors and magma ascent before the April 2011 eruption at Axial Seamount: Nature Geoscience, v. 5, no. 7, p. 478–482.

Edwards, B.R., and Russell, J.K., 1996a, A review and analysis of silicate mineral dissolution experiments in natural silicate melts: Chemical Geology, v. 130, no. 3-4, p. 233–245.

Edwards, B.R., and Russell, J.K., 1996b, Influence of magmatic assimilation on mineral growth and zoning, The Canadian Mineralogist, v. 34, pp 1149-1162.

Edwards, B.R., Russell, J.K., 1998, Time scales of magmatic processes : New insights from dynamic models for magmatic assimilation: Chemical Geology, v. 26, no.12, p. 1103-1106.

Elkins, L.T., and Grove, T.L., 1990, Ternary feldspar experiments and thermodynamic models: American Mineralogist, v. 75, no. 5-6, p. 544–559.

Faure, F., Schiano, P., Trolliard, G., Nicollet, C., and Soulestin, B., 2006, Textural evolution of polyhedral olivine experiencing rapid cooling rates: Contributions to Mineralogy and Petrology, v. 153, no. 4, p. 405–416.

Fisk, M.R., 1984, Depths and temperatures of mid-ocean-ridge magma chambers and the composition of their source magmas: Geological Society, London, Special Publications, v. 13, no. 1, p. 17–23.

Fontaine, F.J., Olive, J.A., Cannat, M., Escartin, J., and Perol, T., 2011, Hydrothermally - induced melt lens cooling and segmentation along the axis of fast - and intermediate - spreading centers: Geophysical Research Letters, v. 38, no. 14, p. 1–7.

Fornari, D.J., Shank, T., Von Damm, K.L., Gregg, T.K.P., Lilley, M., Levai, G., Bray, A., Haymon, R.M., Perfit, M.R., and Lutz, R., 1998, Time-series temperature measurements at high-temperature hydrothermal vents, East Pacific Rise 9 49′--51′ N: Evidence for monitoring a crustal cracking event: Earth and Planetary Science Letters, v. 160, no. 3, p. 419–431.

Fornari, D., Tivey, M., Schouten, H., Perfit, M., Yoerger, D., Bradley, A., Edwards, M., Haymon, R., Scheirer, D., Damm, K. Von, Shank, T., and Soule, A., 2004, Submarine Lava Flow Emplacement at the East Pacific Rise 9 ° 50 ′ N :

Implications for Uppermost Ocean Crust Stratigraphy and Hydrothermal Fluid Circulation: Mid-Ocean Ridges: Hydrothermal Interactions Between the Lithosphere and Oceans, Geophysical Monograph Series 148 p, 187-218.

Fox, C.G., Chadwick, W.W., and Embley, R.W., 2001, Direct observation of a submarine volcanic eruption from a sea-floor instrument caught in a lava flow.: Nature, v. 412, no. 6848, p. 727–9.

France, L., Ildefonse, B., and Koepke, J., 2009, Interactions between magma and hydrothermal system in Oman ophiolite and in IODP Hole 1256D: Fossilization of a dynamic melt lens at fast spreading ridges: Geochemistry Geophysics Geosystems, v. 10, no. 10.

Fundis, A.T., Soule, S.A., Fornari, D.J., and Perfit, M.R., 2010, Paving the seafloor: Volcanic emplacement processes during the 2005-2006 eruptions at the fast spreading East Pacific Rise, 9 50′ N: Geochemistry Geophysics Geosystems, v. 11, no. 8.

Gaetani, G.A., and Grove, T.L., 1997, Partitioning of moderately siderophile elements among olivine, silicate melt, and sulfide melt: Constraints on core formation in the Earth and Mars: Geochimica et Cosmochimica Acta, v. 61, no. 9, p. 1829–1846.

Gee, L.L., and Sack, R.O., 1988, Experimental petrology of melilite nephelinites: Journal of Petrology, v. 29, no. 6, p. 1233–1255.

Gente, P., Auzende, J.M., Renard, V., Fouquet, Y., and Bideau, D., 1986, Detailed geological mapping by submersible of the East Pacific Rise axial graben near 13 N: Earth and planetary science letters, v. 78, no. 2, p. 224–236.

Geotimes conference, 1972, Penrose field conference on ophiolites: Geotimes, v. 17, p. 24–25.

Ghiorso, M.S., and Sack, R.O., 1995, Chemical mass transfer in magmatic processes IV. A revised and internally consistent thermodynamic model for the interpolation and extrapolation of liquid-solid equilibria in magmatic systems at elevated temperatures and pressures: Contributions to Mineralogy and Petrology, v. 119, no. 2, p. 197–212.

Giletti, B., and Casserly, J.E., 1994, Strontium diffusion kinetics in plagioclase feldspars: Geochimica et Cosmochimica Acta, v. 58, no. 18, p. 3785–3793.

Giletti, B.J., and Shanahan, T.M., 1997, Alkali diffusion in plagioclase feldspar: Chemical Geology, v. 1, no. 1975, 3-20.

Gillis, K.M., 2002, The Rootzone of an Ancient Hydrothermal System Exposed in the Troodos Ophiolite, Cyprus: The Journal of Geology, v. 110, no. 1, p. 57–74.

Gillis, K.M., and Coogan, L.A., 2002, Anatectic Migmatites from the Roof of an Ocean Ridge Magma Chamber: Journal of Petrology, v. 43, no. 11, p. 2075–2095.

Gillis, K.M., Coogan, L.A., and Chaussidon, M., 2003, Volatile element (B, Cl, F) behaviour in the roof of an axial magma chamber from the East Pacific Rise: Earth and Planetary Science Letters, v. 213, no. 3–4, p. 447–462.

Gillis, K.M., and Roberts, M.D., 1999, Cracking at the magma–hydrothermal transition: evidence from the Troodos Ophiolite, Cyprus: Earth and Planetary Science Letters, v. 169, no. 3–4, p. 227–244.

Goss, a. R., Perfit, M.R., Ridley, W.I., Rubin, K.H., Kamenov, G.D., Soule, S. a., Fundis, a., and Fornari, D.J., 2010, Geochemistry of lavas from the 2005–2006 eruption at the East Pacific Rise, 9°46′N–9°56′N: Implications for ridge crest plumbing and decadal changes in magma chamber compositions: Geochemistry Geophysics Geosystems, v. 11, no. 5, p. 1–35.

Gregg, T.K.P., Fornari, D.J., Perfit, M.R., Haymon, R.M., and Fink, J.H., 1996, Rapid emplacement of a mid-ocean ridge lava flow on the East Pacific Rise at 9 46′--51′ N: Earth and Planetary Science Letters, v. 144, no. 3, p. E1–E7.

Grove, T.L., Baker, M.B., and Kinzler, R.J., 1984, Coupled CaAl-NaSi diffusion in plagioclase feldspar: Experiments and applications to cooling rate speedometry: Geochimica et Cosmochimica Acta, v. 48, no. 10, p. 2113–2121.

Grove, T.L., Kinzler, R.J., and Bryan, W.B., 1992, Fractionation of mid-ocean ridge basalt (MORB): Geophysical Monograph Series, v. 71, p. 281–310.

Hall, J.M., 1979, The oceanic crust : Investigations by Canadian groups on the Mid-Atlantic Ridge crest and other areas. Canadian Journal of Earth Sciences, v. 16, no. 3, p. 695-711.

Hanson, B., and Jones, J.H., 1998, The systematics of Cr^{3+} and Cr^{2+} partitioning between olivine and liquid in the presence of spinel: American Mineralogist, v. 83, no. 7-8, p. 669–684.

Harding, A.J., Kent, G.M., and Orcutt, J. a., 1993, A Multichannel Seismic Investigation of Upper Crustal Structure at 9°N on the East Pacific Rise: Implications for Crustal Accretion: Journal of Geophysical Research, v. 98, no. B8, p. 13925–13944.

Harp, K.S., 1995, Geochemical variations in a single basaltic flow at 9°30'N on the East Pacific Rise, In Proceedings of the Ocean Drilling Program - Scientific Results, v. 142, p. 9–22.

Hart, S.R., and Davis, K.E., 1978, Nickel partitioning between olivine and silicate melt: Earth and Planetary Science Letters, v. 40, no. 2, p. 203–219.

Haymon, R.M., Fornari, D.J., Von Damm, K.L., Lilley, M.D., Perfit, M.R., Edmond, J.M., Shanks, W.C., Lutz, R.A., Grebmeier, J.M., Carbotte, S., and others, 1993, Volcanic eruption of the mid-ocean ridge along the East Pacific Rise crest at 9 45--52′ N: direct submersible observations of seafloor phenomena associated with an eruption event in April, 1991: Earth and Planetary Science Letters, v. 119, no. 1, p. 85–101.

Haymon, R.M., Fornari, D.J., Edwards, M.H., Carbotte, S., Wright, D., and Macdonald, K.C., 1991, Hydrothermal vent distribution along the East Pacific Rise crest (9 09′--54′ N) and its relationship to magmatic and tectonic processes on fast-spreading mid-ocean ridges: Earth and Planetary Science Letters, v. 104, no. 2, p. 513–534.

Hekinian, R., Auzende, J.M., Francheteau, J., Gente, P., Ryan, W.B.F., and Kappel, E.S., 1985, Offset spreading centers near 12 53′ N on the East Pacific Rise: Submersible observations and composition of the volcanics: Marine Geophysical Researches, v. 7, no. 3, p. 359–377.

Holland, T., and Powell, R., 1998, An internally consistent thermodynamic data set for phases of petrological interest: Journal of Metamorphic Geology, p. 309–343.

Hooft, E.E.E., Detrick, R.S., and Kent, G.M., 1997, Seismic structure and indicators of magma budget along the southern East Pacific Rise: Journal of Geophysical Research, v. 102, no. B12, p. 27319–27327.

Horn, I., Hinton, R.W., Jackson, S.E., and Longerich, H.P., 1997, Ultra-Trace Element Analysis of NIST SRM 616 and 614 using Laser Ablation Microprobe-Inductively Coupled Plasma-Mass Spectrometry (LAM-ICP-MS): a Comparison with Secondary Ion Mass Spectrometry (SIMS): Geostandards Newsletter, v. 21, no. 2, p. 191–203.

Irving, A.J., 1978, A review of experimental studies of crystal/liquid trace element partitioning: Geochimica et Cosmochimica Acta, v. 42, no. 6, p. 743–770.

Ito, M., and Ganguly, J., 2006, Diffusion kinetics of Cr in olivine and 53Mn–53Cr thermochronology of early solar system objects: Geochimica et Cosmochimica Acta, v. 70, no. 3, p. 799–809.

Jones, J.H., 1988, Partitioning of Mg and Fe between olivine and liquids of lunar compositions: the roles of composition, pressure and Ti speciation, *in* Lunar and Planetary Institute Science Conference Abstracts, p. 561.

Karson, J. A., 2002, Geologic Structure of the Uppermost Oceanic Crust Created At Fast-To Intermediate- Rate Spreading Centers: Annual Review of Earth and Planetary Sciences, v. 30, no. 1, p. 347–384.

Karson, J.A., 1998, Internal structure of oceanic lithosphere: A perspective from tectonic windows: Geophysical Monograph Series, v. 106, p. 177–218.

Kelemen, P.B., Koga, K., and Shimizu, N., 1997, Geochemistry of gabbro sills in the crust-mantle transition zone of the Oman ophiolite : Implications for the origin of the oceanic lower crust: Earth and Planetary Science Letters, v. 146, no. 3, p. 475–488.

Kennedy, A.K., Lofgren, G.E., and Wasserburg, G.J., 1993, An experimental study of trace element partitioning between olivine, orthopyroxene and melt in chondrules: equilibrium values and kinetic effects: Earth and Planetary Science Letters, v. 115, no. 1, p. 177–195.

Kent, G.M., Harding, A.J., and Orcutt, J.A., 1993a, Distribution of magma beneath the East Pacific Rise between the Clipperton transform and the 9 17′ N Deval from forward modeling of common depth point data: Journal of Geophysical Research, v. 98, no. B8, p. 13913–13945.

Kent, G.M., Harding, A.J., and Orcutt, J. A., 1993b, Distribution of Magma Beneath the East Pacific Rise Near the 9°03′N Overlapping Spreading Center From Forward Modeling of Common Depth Point Data: Journal of Geophysical Research, v. 98, no. B8, p. 13971–13995.

Kent, G.M., Singh, S.C., Harding, A.J., Sinha, M.C., Orcutt, J.A., Barton, P.J., White, R.S., Bazin, S., Hobbs, R.W., Tong, C.H., and others, 2000, Evidence from three-dimensional seismic reflectivity images for enhanced melt supply beneath mid-ocean-ridge discontinuities: Nature, v. 406, no. 6796, p. 614–618.

Kinzler, R.J., Grove, T.L., and Recca, S.I., 1990, An experimental study on the effect of temperature and melt composition on the partitioning of nickel between olivine and silicate melt: Geochimica et Cosmochimica Acta, v. 54, no. 5, p. 1255–1265.

Kohut, E.J., and Nielsen, R.L., 2003, Low-pressure phase equilibria of anhydrous anorthite-bearing mafic magmas: Geochemistry, Geophysics, Geosystems, v. 4, no. 7, p.

Kushiro, I., and Mysen, B.O., 2002, A possible effect of melt structure on the Mg-Fe^{2+} partitioning between olivine and melt: Geochimica et Cosmochimica Acta, v. 66, no. 12, p. 2267–2272.

Kushiro, I., and Walter, M.J., 1998, Mg-Fe partitioning between olivine and mafic-ultramafic melts: Geophysical Research Letters, v. 25, no. 13, p. 2337–2340.

Langmuir, C.H., Bender, J.F., and Batiza, R., 1986, Petrological and tectonic segmentation of the East Pacific Rise, 5 30′--14 30′ N: Nature, v. 322, no. 6078, p. 422–429.

Langmuir, C.H., Klein, E.M., and Plank, T., 1992, Petrological systematics of mid-ocean ridge basalts: Constraints on melt generation beneath ocean ridges: Geophysical Monograph Series, v. 71, p. 183–280.

LaTourrette, T., and Wasserburg, G.J., 1998, Mg diffusion in anorthite: implications for the formation of early solar system planetesimals: Earth and Planetary Science Letters, v. 158, no. 3-4, p. 91–108.

Liu, L., and Lowell, R.P., 2009, Models of hydrothermal heat output from a convecting, crystallizing, replenished magma chamber beneath an oceanic spreading center: Journal of Geophysical Research, v. 114, no. B2, B012102.

Loewenstein, W., 1954, The distribution of aluminum in the tetrahedra of silicates and aluminates: American Mineralogist, v. 39, no. 1-2, p. 92–96.

Longhi, J., Walker, D., and Hays, J.F., 1978, The distribution of Fe and Mg between olivine and lunar basaltic liquids: Geochimica et Cosmochimica Acta, v. 42, no. 10, p. 1545–1558.

Lonsdale, P., 1977, Regional shape and tectonics of the equatorial East Pacific Rise: Marine Geophysical Researches, v. 3, no. 3, p. 295–315.

Macdonald, K.C., and Fox, P.J., 1988, The axial summit graben and cross-sectional shape of the East Pacific Rise as indicators of axial magma chambers and recent volcanic eruptions: Earth and Planetary Science Letters, v. 88, no. 1-2, p. 119–131.

Macdonald, K.C., Fox, P.J., Miller, S., Edwards, M.H., Eisen, M., Fornari, D.J., Perram, L.J, Pockalny, R., Scheirer, D., Tighe, S., Weiland, C., and Wilson, D., 1992, History of Segmentation, Propagation and Spreading Direction based on SeaMARCH II and Sea Beam studies: Marine geophysical researches, v. 14, no. 4, p. 299–344.

Macdonald, K.C., Fox, P.J., Perram, L.J., Eisen, M.F., Haymon, R.M., Miller, S.P., Carbotte, S.M., Cormier, M.-H., and Shor, A.N., 1988, A new view of the mid-ocean

ridge from the behaviour of ridge-axis discontinuities: Nature, v. 335, no. 6187, p. 217–225.

Mallmann, G., & O'Neill, H. S. C. (2009). The crystal/melt partitioning of V during mantle melting as a function of oxygen fugacity compared with some other elements (Al, P, Ca, Sc, Ti, Cr, Fe, Ga, Y, Zr and Nb). Journal of Petrology, v. 50, no. 9, 1765-1794.

Michael, P.J., and Cornell, W.C., 1998, Influence of spreading rate and magma supply on crystallization and assimilation beneath mid-ocean ridges: Evidence from chlorine and major element chemistry of mid-ocean ridge basalts: Journal of Geophysical Research, v. 103, no. B8, p. 18325-18.

Michael, P.J., and Schilling, J.-G., 1989, Chlorine in mid-ocean ridge magmas: Evidence for assimilation of seawater-influenced components: Geochimica et Cosmochimica Acta, v. 53, no. 12, p. 3131–3143.

Miller, S.A., Asimow, P.D., and Burnett, D.S., 2006, Determination of melt influence on divalent element partitioning between anorthite and CMAS melts: Geochimica et Cosmochimica Acta, v. 70, no. 16, p. 4258–4274.

Milman-Barris, M.S., Beckett, J.R., Baker, M.B., Hofmann, A.E., Morgan, Z., Crowley, M.R., Vielzeuf, D., and Stolper, E., 2008, Zoning of phosphorus in igneous olivine: Contributions to Mineralogy and Petrology, v. 155, no. 6, p. 739–765.

Morioka, M., 1983, Cation diffusion in olivine III. Mn2SiO4 system: Geochimica et Cosmochimica Acta, v. 47, no. 12, p. 2275–2279.

Muir, I.D., Tilley, C.E., and Scoon, J.H., 1964, Basalts from the northern part of the rift zone of the Mid-Atlantic Ridge: Journal of petrology, v. 5, no. 3, p. 409–434.

Mutter, J.C., Buck, W.R., and Zehnder, C.M., 1988, Convective partial melting 1. A model for the formation of thick basaltic sequences during the initiation of spreading: Journal of Geophysical Research, v. 93, no. B2, p. 1031–1048.

Myers, E.R., Heine, V., and Dove, M.T., 1998, Thermodynamics of Al/Al avoidance in the ordering of Al/Si tetrahedral framework structures: Physics and Chemistry of Minerals, v. 25, no. 6, p. 457–464.

Myers, J. T., and Eugster, H. P, 1983, The system Fe-Si-O: Oxygen buffer calibrations to 1,500 K: Contributions to Mineralogy and Petrology, v. 82, no. 1, p. 75-90.

Natland, J.H., 1989, Partial melting of a lithologically heterogeneous mantle: inferences from crystallization histories of magnesian abyssal tholeiites from the Siqueiros

Fracture Zone: Geological Society, London, Special Publications, v. 42, no. 1, p. 41–70.

Nicolas, A., Reuber, I., and Benn, K., 1988, A new magma chamber model based on structural studies in the Oman ophiolite: Tectonophysics, v. 151, no. 1-4, p. 87–105.

Nielsen, R.L., 1985, EQUIL: a program for the modeling of low-pressure differentiation processes in natural mafic magma bodies: Computers & Geosciences, v. 11, no. 5, p. 531–546.

Nielsen, R.L., Crum, J., Bourgeois, R., Hascall, K., Forsythe, L.M., Fisk, M.R., and Christie, D.M., 1995, Melt inclusions in high-An plagioclase from the Gorda Ridge: an example of the local diversity of MORB parent magmas: Contributions to Mineralogy and Petrology, v. 122, no. 1, p. 34–50.

O'Hara, M.J., 1977, Geochemical evolution during fractional crystallisation of a periodically refilled magma chamber: Nature, v. 266, p. 503–507.

Pan, Y., and Batiza, R., 2003, Magmatic processes under mid-ocean ridges: A detailed mineralogic study of lavas from East Pacific Rise 9° 30′ N, 10° 30′ N, and 11° 20′ N: Geochemistry Geophysics Geosystems, v. 4, no. 11, p. 8623.

Pan, Y., and Batiza, R., 2002, Mid-ocean ridge magma chamber processes: Constraints from olivine zonation in lavas from the East Pacific Rise at 9°30′N and 10°30′N: Journal of Geophysical Research: Solid Earth, v. 107, no. B1, p. 2022

Panjasawatwong, Y., Danyushevsky, L. V, Crawford, A.J., and Harris, K.L., 1995, An experimental study of the effects of melt composition on plagioclase-melt equilibria at 5 and 10 kbar: implications for the origin of magmatic high-An plagioclase: Contributions to Mineralogy and Petrology, v. 118, no. 4, p. 420–432.

Pearce, N.J.G., Perkins, W.T., Westgate, J.A., Gorton, M.P., Jackson, S.E., Neal, C.R., and Chenery, S.P., 1997, A compilation of new and published major and trace element data for NIST SRM 610 and NIST SRM 612 glass reference materials: Geostandards Newsletter, v. 21, no. 1, p. 115–144.

Pedersen, R.B., 1986, The nature and significance of magma chamber margins in ophiolites: examples from the Norwegian Caledonides: Earth and Planetary Science Letters, v. 77, no. 1, p. 100–112.

Perfit, M.R., and Chadwick Jr., W.W., 1998, Magmatism at mid-ocean ridges: Constraints from volcanological and geochemical investigations, In: Faulting and Magmatism at Mid Ocean Ridges, AGU, Washington, DC, p. 59–115.

Perfit, M.R., Fornari, D.J., Smith, M.C., Bender, J.F., Langmuir, C.H., and Haymon, R.M., 1994, Small-scale spatial and temporal variations in mid-ocean ridge crest magmatic processes: Geology, v. 22, no. 4, p. 375–379.

Peters, M.T., Shaffer, E.E., Burnett, D.S., and Kim, S.S.A.M., 1995, Magnesium and titanium partitioning between anorthite and Type B CAI liquid : Dependence on oxygen fugacity and liquid composition: Geochimica et Cosmochimica Acta, v. 59, no. 13, p. 2785–2796.

Petry, C., Chakraborty, S., and Palme, H., 2004, Experimental determination of Ni diffusion coefficients in olivine and their dependence on temperature, composition, oxygen fugacity, and crystallographic orientation: Geochimica et Cosmochimica Acta, v. 68, no. 20, p. 4179–4188

Presnall, D.C., and Hoover, J.D., 1987, High pressure phase equilibrium constraints on the origin of mid-ocean ridge basalts: Magmatic processes: physicochemical principles, p. 75–89.

Quick, J.E., and Denlinger, R.P., 1993, Ductile deformation and the origin of layered gabbro in ophiolites: Journal of Geophysical Research: Solid Earth, v. 98, p. 14015-140278.

Raitt, M., 1963, The crustal rocks: The sea, v. 3, p. 85–102.

Renard, V., Hekinian, R., Francheteau, J., Ballard, R.D., and Backer, H., 1985, Submersible observations at the axis of the ultra-fast-spreading East Pacific Rise (17 30′ to 21 30′ S): Earth and Planetary Science Letters, v. 75, no. 4, p. 339–353.

Rhodes, J.M., Dungan, M.A., Blanchard, D.P., and Long, P.E., 1979, Magma mixing at mid-ocean ridges: evidence from basalts drilled near 22 N on the Mid-Atlantic Ridge: Tectonophysics, v. 55, no. 1, p. 35–61.

Ribbe, P.H., 1975, The chemistry, structure and nomenclature of feldspars. In: Ribbe, P.H., Ed., Reviews in Mineralogy, v. 2, p. 1–19, Mineralogical Society of America Washington D.C.

Ridley, W.I., Perfit, M.R., Smith, M.C., and Fornari, D.J., 2006, Magmatic processes in developing oceanic crust revealed in a cumulate xenolith collected at the East Pacific Rise, 9°50′N: Geochemistry Geophysics Geosystems, v. 7, no. 12, p. 1–25.

Roeder, P.L., and Emslie, RF., 1970, Olivine-liquid equilibrium: Contributions to mineralogy and petrology, v. 29, no. 4, p. 275–289.

Le Roux, P., Shirey, S., Hauri, E., Perfit, M., and Bender, J., 2006, The effects of variable sources, processes and contaminants on the composition of northern EPR MORB (8–10°N and 12–14°N): Evidence from volatiles (H2O, CO2, S) and halogens (F, Cl): Earth and Planetary Science Letters, v. 251, no. 3-4, p. 209–231.

Rubin, K.H., Macdougall, J.D., and Perfit, M.R., 1994, 210Po-210Pb dating of recent volcanic eruptions on the sea floor: Nature, v. 368, no. 6474, p. 841–844.

Rubin, K.H., Perfit, M.R., Fornari, D.J., Soule, S.A., Tolstoy, M., Waldhauser, F., 2006, Geochronology and composition of the 2005-06 volcanic eruptions of the East Pacific Rise, 9 46′-56′ N: Eos (Transactions, American Geophysical Union), AGU, v. 87, no. 52..

Rubin, K.H., Smith, M.C., Bergmanis, E.C., Perfit, M.R., Sinton, J.M., and Batiza, R., 2001, Geochemical heterogeneity within mid-ocean ridge lava flows: insights into eruption, emplacement and global variations in magma generation: Earth and Planetary Science Letters, v. 188, no. 3, p. 349–367.

Rubin, K.H., Tolstoy, M., Fornari, D.J., Dziak, R.P., Soule, S.A., Waldhauser, F., and Von Damm, K.L., 2008, Integrating Radiometric, Geophysical and Thermal Signals of Volcanic Unrest and Eruption in 2005-06 at 9 deg 50’N EPR, *in* AGU Fall Meeting Abstracts, p. 7.

Sack, R.O., Walker, D., and Carmichael, I.S.E., 1987, Experimental petrology of alkalic lavas: constraints on cotectics of multiple saturation in natural basic liquids: Contributions to Mineralogy and Petrology, v. 96, no. 1, p. 1–23.

Shipboard Scientific Party, 1988, HOLE 648A. In: Detrick, R., Honnorez. J., Bryan., W. B., Juteau, T., et al. (eds). Proceeding of ODP, initial reports, vol. 106/109. College Station, TX (Ocean Drilling Program).

Shor Jr, G.G., Menard, H.W., and Raitt, R.W., 1970, Structure of the Pacific basin: The sea, v. 4, no. Part 2, p. 3–27.

Sims, K.W.W., Goldstein, S.J., Blichert-Toft, J., Perfit, M.R., Kelemen, P., Fornari, D.J., Michael, P., Murrell, M.T., Hart, S.R., DePaolo, D.J., and others, 2002, Chemical and isotopic constraints on the generation and transport of magma beneath the East Pacific Rise: Geochimica et Cosmochimica Acta, v. 66, no. 19, p. 3481–3504.

Singh, S.C., Collier, J.S., Harding, A.J., Kent, G.M., and Orcutt, J.A., 1999, Seismic evidence for a hydrothermal layer above the solid roof of the axial magma chamber at the southern East Pacific Rise: Geology, v. 27, no. 3, p. 219-222.

Singh, S. C., Kent, G. M., Collier, J. S., Harding, A. J., & Orcutt, J. A. 1998. Melt to mush variations in crustal magma properties along the ridge crest at the southern East Pacific Rise. Nature, v. 394, no. 6696, 874-878.

Sinton, C.W., Christie, D.M., Coombs, V.L., Nielsen, R.L., and Fisk, M.R., 1993, Near-primary melt inclusions in anorthite phenocrysts from the Galapagos Platform: Earth and Planetary Science Letters, v. 119, no. 4, p. 527–537.

Sinton, J.M., and Detrick, R.S., 1992, Mid-ocean ridge magma chambers: Journal of Geophysical Research, v. 97, no. B1, p. 197.

Sisson, T.W., and Grove, T.L., 1993, Temperatures and H_2O contents of low-MgO high-alumina basalts: Contributions to Mineralogy and Petrology, v. 113, no. 2, p. 167–184.

Smith, V.C., Blundy, J.D., and Arce, J.L., 2009, A Temporal Record of Magma Accumulation and Evolution beneath Nevado de Toluca, Mexico, Preserved in Plagioclase Phenocrysts: Journal of Petrology, v. 50, no. 3, p. 405–426.

Smith, M.C., Perfit, M.R., Fornari, D.J., Ridley, W.I., Edwards, M.H., Kurras, G.J., and Von Damm, K.L., 2001, Magmatic processes and segmentation at a fast spreading mid-ocean ridge: detailed investigation of an axial discontinuity on the East Pacific Rise crest at 9 37′ N: Geochemistry Geophysics Geosystems, v. 2, no. 10, p. 1034–1040.

Soule, S.A., Fornari, D.J., Perfit, M.R., and Rubin, K.H., 2007, New insights into mid-ocean ridge volcanic processes from the 2005–2006 eruption of the East Pacific Rise, 9°46′N–9°56′N: Geology, v. 35, no. 12, p. 1079.

Soule, S.A., Nakata, D.S., Fornari, D.J., Fundis, A.T., Perfit, M.R., and Kurz, M.D., 2012, CO_2 variability in mid-ocean ridge basalts from syn-emplacement degassing: Constraints on eruption dynamics: Earth and Planetary Science Letters, v. 327, p. 39–49.

Spandler, C., and O'Neill, H, St. C, 2010, Diffusion and partition coefficients of minor and trace elements in San Carlos olivine at 1,300 ° C with some geochemical implications: Contributions to Mineralogy and Petrology, v. 159, no. 6, p. 791–818.

Sparks, S.R.J., Sigurdsson, H., and Wilson, L., 1977, Magma mixing: a mechanism for triggering acid explosive eruptions: Nature, v. 267, no. 5609, p. 315–318.

Taylor, J.R., 1982, Propagation of uncertainties: An introduction to error analysis: the study of uncertainties in physical measurements, University science books, v. 2, p. 61.

Thornber, C.R., and Huebner, J.S., 1985, Dissolution of olivine in basaltic liquids; experimental observations and applications: American Mineralogist, v. 70, no. 9-10, p. 934–945.

Tolstoy, M., Cowen, J.P., Baker, E.T., Fornari, D.J., Rubin, K.H., Shank, T.M., Waldhauser, F., Bohnenstiehl, D.R., Forsyth, D.W., Holmes, R.C., Love, B., Perfit, M.R., Weekly, R.T., Soule, S. a, et al., 2006, A sea-floor spreading event captured by seismometers.: Science (New York, N.Y.), v. 314, no. 5807, p. 1920–2.

Toomey, D.R., Purdy, G.M., Solomon, S.C., and Wilcock, W.S.D., 1990, The three-dimensional seismic velocity structure of the East Pacific Rise near latitude 9 30′ N: Nature, v. 347, no. 6294, p. 639–645.

Toplis, M.J., 2005, The thermodynamics of iron and magnesium partitioning between olivine and liquid : criteria for assessing and predicting equilibrium in natural and experimental systems: Contributions to Mineralogy and Petrology, v 149, no. 1, p. 22–39.

Urabe, T., Baker, E.T., Ishibashi, J., Feely, R.A., Marumo, K., Massoth, G.J., Maruyama, A., Shitashima, K., Okamura, K., Lupton, J.E., and others, 1995, The effect of magmatic activity on hydrothermal venting along the superfast-spreading East Pacific Rise: Science, p. 1092-1095.

VanTongeren, J. a., Kelemen, P.B., and Hanghøj, K., 2008, Cooling rates in the lower crust of the Oman ophiolite: Ca in olivine, revisited: Earth and Planetary Science Letters, v. 267, no. 1-2, p. 69–82.

Wagner, T.P., and Grove, T.L., 1997, Experimental constraints on the origin of lunar high-Ti ultramafic glasses: Geochimica et Cosmochimica Acta, v. 61, no. 6, p. 1315–1327.

Watson, E.B., 1977, Partitioning of manganese between forsterite and silicate liquid: Geochimica et Cosmochimica Acta v. 4, no. 9, p. 1363-1374..

Weaver, S.J., and Langmuir, C.H., 1990, Calculation of phase equilibrium in mineral-melt systems: Computers & Geosciences, v. 16, no. 1, p. 1–19.

Welsch, B., Faure, F., Famin, V., Baronnet, A., and Bachèlery, P., 2013, Dendritic Crystallization: A Single Process for all the Textures of Olivine in Basalts?: Journal of Petrology, v. 54, no. 3, p. 539–574.

Wilson, D.S., Clague, D.A., Sleep, N.H., and Morton, J.L., 1988, Implications of magma convection for the size and temperature of magma chambers at fast spreading ridges: Journal of Geophysical Research: Solid Earth, v. 93, no. B10, p. 11974–11984.

Wright, T.L., 1973, Magma Mixing as Illustrated by the 1959 Eruption, Kilauea Volcano, Hawaii: Geological Society of America Bulletin, v. 84, no. 3, p. 849–858.

Yund, R.A., and Tullis, J., 1980, The Effect of Water, Pressure, and Strain on Ai/Si Order-Disorder Kinetics in Feldspar: Contributions to Mineralogy and Petrology v. 72, no. 3, p. 297-302.

Zellmer, G.F., Blake, S., Vance, D., Hawkesworth, C., and Turner, S., 1999, Plagioclase residence times at two island arc volcanoes (Kameni Islands, Santorini, and Soufriere, St. Vincent) determined by Sr diffusion systematics: Contributions to Mineralogy and Petrology, v. 136, no. 4, p. 345–357.

Zellmer, G.F., Dulski, P., Iizuka, Y., and Perfit, M.R., 2012, Rates and processes of crystallization in on-axis and off-axis MOR basaltic melts: Lithos, v. 154, p. 1–15.

Zellmer, G.F., Rubin, K.H., Dulski, P., Iizuka, Y., Goldstein, S.L., and Perfit, M.R., 2011, Crystal growth during dike injection of MOR basaltic melts: evidence from preservation of local Sr disequilibria in plagioclase: Contributions to Mineralogy and Petrology, v. 161, no. 1, p. 153–173.

Zellmer, G.F., Rubin, K.H., Dulski, P., Iizuka, Y., Goldstein, S.L., and Perfit, M.R., 2010, Crystal growth during dike injection of MOR basaltic melts: evidence from preservation of local Sr disequilibria in plagioclase: Contributions to Mineralogy and Petrology, v. 161, no. 1, p. 153–173.

Zellmer, G.F., Sparks, R.S.J., Hawkesworth, C.J., and Wiedenbeck, M., 2003, Magma emplacement and remobilization timescales beneath Montserrat: insights from Sr and Ba zonation in plagioclase phenocrysts: Journal of Petrology, v. 44, no. 8, p. 1413–1431.

Zhang, Y., Walker, D., and Lesher, C.E., 1989, Diffusive crystal dissolution: Contributions to Mineralogy and Petrology, v. 102, no. 4, p. 492–513.

Appendix

Appendix A.1: Analytical Techniques, Precision and Accuracy

A.1.1: Electron microprobe analysis (EMP)

The details of the analytical conditions for transects through plagioclase and olivine crystals at (a) the University of Barcelona (Cameca SX-50), (b) the Earth Observatory of Singapore (Nanyang Technological University; JOEL JXA-8530F), and (c) for the University of British Columbia (Cameca SX-50) are shown in Table A.1. Full details of the analytical conditions used for EMP elemental maps of olivine and plagioclase obtained at the Earth Observatory of Singapore are shown in Table A.2. Due to a software problem, the MgO data from plagioclase analysed in the Northern Fissure and from seven profiles in the Southern Fissure (4205_5 Pl11, Pl8, Pl9; 4205_3 Pl3b, Pl1, Pl5, Pl14) are rounded to two decimal places.

Table A.1. Details of analytical conditions for plagioclase and olivine analysed at (a) the University of Barcelona, (b) the Earth Observatory of Singapore, and (c) the University of British Columbia.

EMP	Mineral	Element	Accelerating Voltage (kV)	Counting time (s)	Beam current (nA)
(a) Barcelona	Plagioclase	Na, Ca, Al, Si, K	20	10	15
		Fe	20	20	15
		Mg, Ti	20	60	100
	Olivine	Si, Mg, Fe, Mn	20	20	15
		Ni, Ca	20	30	100
(b) Singapore	Plagioclase	Na, Ca,Al, Si, Ti, Mg, K, Fe	15	60	60
	Olivine: *Samples 4205_5 Ol7a,b,c, Ol6, Ol5 and 4203_2 Ol3-2a*	Si, Mg, Fe	15	20	100
		Mn	15	30	100
		Ca, Ni	15	60	100
		Al	15	100	100

	Olivine: *Sample 4203_2 Ol302b*	Si, Mg, Al	15	40	100
		Fe	15	50	100
		Cr, P	15	100	100
(c) British Columbia	Plagioclase	Na, Mg, Al, Si, K, Ca, Fe	15	20	20

Table A.2. Details of analytical conditions used for elemental maps of olivine and plagioclase obtained on the EMP at the Earth Observatory of Singapore.

Mineral	**Sample**	**Elements analysed**	**Resolution (µm/step)**	**Current (nA)**	**Dwell time (msec/point)**
Olivine	4203_2 Ol3	Mg, Cr, Al, P, Ca	1	300	30
	4203_2 Ol3-2	Fe, Co, F, V, Ti	1	300	70
	4205_5 Ol2	Mg, Cr, Al, P, Ca	1	300	10
	4205_5 Ol1	Mg, Fe, Al, P, Ni	1	100	13
Plagioclase	4205_5 Pl20, Pl21, Pl22, Pl4	Al, Ca, Mg, Fe, Ti	1	100	10
	4205_3 Pl3	Al, Ca, Mg, Fe, Ti	1	100	13

A.1.2: Accuracy and precision of data

A.1.2.1: Precision of LA-ICP-MS data

A.1.2.1.1: Precision within an analytical session

Precision within an analytical session was based on the standard deviation of NIST glass standards (Table A.3). Reported errors are based on the NIST glass analyses which contain the concentrations closest to those found in the sample. These errors are shown as error bars on elemental profiles in Section 2.6. Precision calculated from NIST 613 are used for Sr, and NIST 611 for K, Cr, Mn and Ni. The NIST glass containing Ba concentrations closest to those found in the sample is NIST 615. The calculated precision for Ba in NIST 615 is worse than the other analysed elements (up to 29.8 %). Therefore, Ba analyses are not included in the results or interpretation of this thesis.

Table A.3. Precision of analysed elements for NIST 611, 613, and 615 within each analytical session. Highlighted in red are the percentage errors used on elemental profiles in Section 2.6 ('-' corresponds to an unknown elemental concentrations within the NIST glass).

Analytical session	No. of NIST analysis	Element	Precision (% Error)		
			NIST 611	NIST 613	NIST 615
10-Jan-11	12	**^{88}Sr**	2.1	4.0	6.6
		^{39}K	8.3	17.6	-
		^{137}Ba	3	8.8	29.8
25-Jan-11	18	**^{88}Sr**	1.4	3.9	3.6
		^{39}K	13.3	17.5	-
		^{137}Ba	2.2	7.5	11.8
14-Jul-11	24	**^{88}Sr**	3.4	3.2	3.6
		^{39}K	10.6	15.2	-
		^{137}Ba	4.1	5	10.6
18-Jul-11	23	**^{88}Sr**	1.0	0.7	0.9
		^{39}K	4.1	29.2	-
		^{137}Ba	1.3	2	6.4
24-Aug-11	20	**^{88}Sr**	2.3	2.8	3.8
		^{39}K	13.9	23.0	-
		^{137}Ba	3.6	5.1	16.7
11-Apr-12	19	**^{88}Sr**	1.0	0.8	1.1
		^{39}K	2.2	6.7	-
		^{137}Ba	1	2.4	7.8
06-Jun-12	19	**^{52}Cr**	1.3	1.5	-
		^{53}Cr	1.4	2.0	-
		^{55}Mn	0.8	1.0	20.5
		^{60}Ni	0.9	3.7	-
		^{61}Ni	3.7	10.6	-
		^{62}Ni	2.4	7.3	-

A.1.2.1.2: Precision between analytical sessions

The precision between days was based on the standard deviation of synthetic plagioclase glasses and natural plagioclase crystals analysed at the beginning and end of each analytical session (Table A.4). The precision for each element was based on the plagioclase glass and natural plagioclase analyses with concentrations closest to those found in the sample. A precision of 6.5 % was used for Sr and 9.2 % for K. A worse precision is calculated for Ba analysis (~ 30 %) and therefore Ba is not included in the results section.

Table A.4. Precision of Sr, K, and Ba within synthetic plagioclase glasses and natural plagioclase crystals. The average concentration of Sr, K and Ba within each glass and crystal are shown in parentheses.

Plagioclase Glass	Sr	K	Ba	Natural Plagioclase	Sr	K	Ba
Glass 1: An0*	37.3 % (150 ppm)	30.00 % (7 ppm)	122.7 % (0.04 ppm)	**Plag 2: Oligoclase**	6.0 % (225 ppm)	9.2 % (2755 ppm)	23.10 % (13.4 ppm)
Glass 2: An25	4.8 % (1275 ppm)	37.30 % (80 ppm)	30.90 % (0.4 ppm)	**Plag 3: Andesine**	3.9 % (476 ppm)	8.3 % (672 ppm)	4.10 % (50 ppm)
Glass 3: An50	3.9 % (1350 ppm)	42.10 % (44 ppm)	27.70 % (0.4 ppm)	**Plag 4: Labradorite**	4.8 % (980 ppm)	10.4 % (2310 ppm)	4.30 % (87 ppm)
Glass 4: An75	3.5 % (1225 ppm)	27.8 % (44 ppm)	34.20 % (0.3 ppm)	**Plag 5: Bytownite**	6.5 % (350 ppm)	9.0 % (390 ppm)	25.50 % (30 ppm)
Glass 5: An100	2.9 % (1500 ppm)	34.70 % (24 ppm)	31.10 % (0.2 ppm)				

**Analyses showed variation within each analytical session due to poor ablation.*

A.1.2.2: Comparison of data from different sources

A.1.2.2.1: EMP versus LA-ICP-MS

Concentrations of Mn and Ni in olivine were analysed by both EMP and LA-ICP-MS. The results from each analytical technique are plotted against each other, and a regression line obtained, to check for data quality (Figure A.1). The discrepancy between this regression line and the 1:1 ratio is ~ 24 % for Mn analyses (Figure A.1.A). The maximum difference between the regression line and Mn analysed by EMP is ± 0.08 wt %, and Mn analysed by LA-ICP-MS is ± 0.06 wt % (Figure A.1. A). The Mn analysed by LA-ICP-MS are therefore used in the results sections due to its better precision. The discrepancy between the 1:1 ratio and the regression line between Ni analysed by EMP and Ni analysed by LA-ICP MS is 5 % for ^{60}Ni, 11 % for ^{61}Ni, and 4 % for ^{62}Ni (Figure A.1. B, C, D). The maximum difference between the regression line in Figure A.1.B and Ni analysed by EMP is ± 0.023 wt %, and ^{60}Ni analysed by LA-ICP-MS is ± 0.020 wt %.

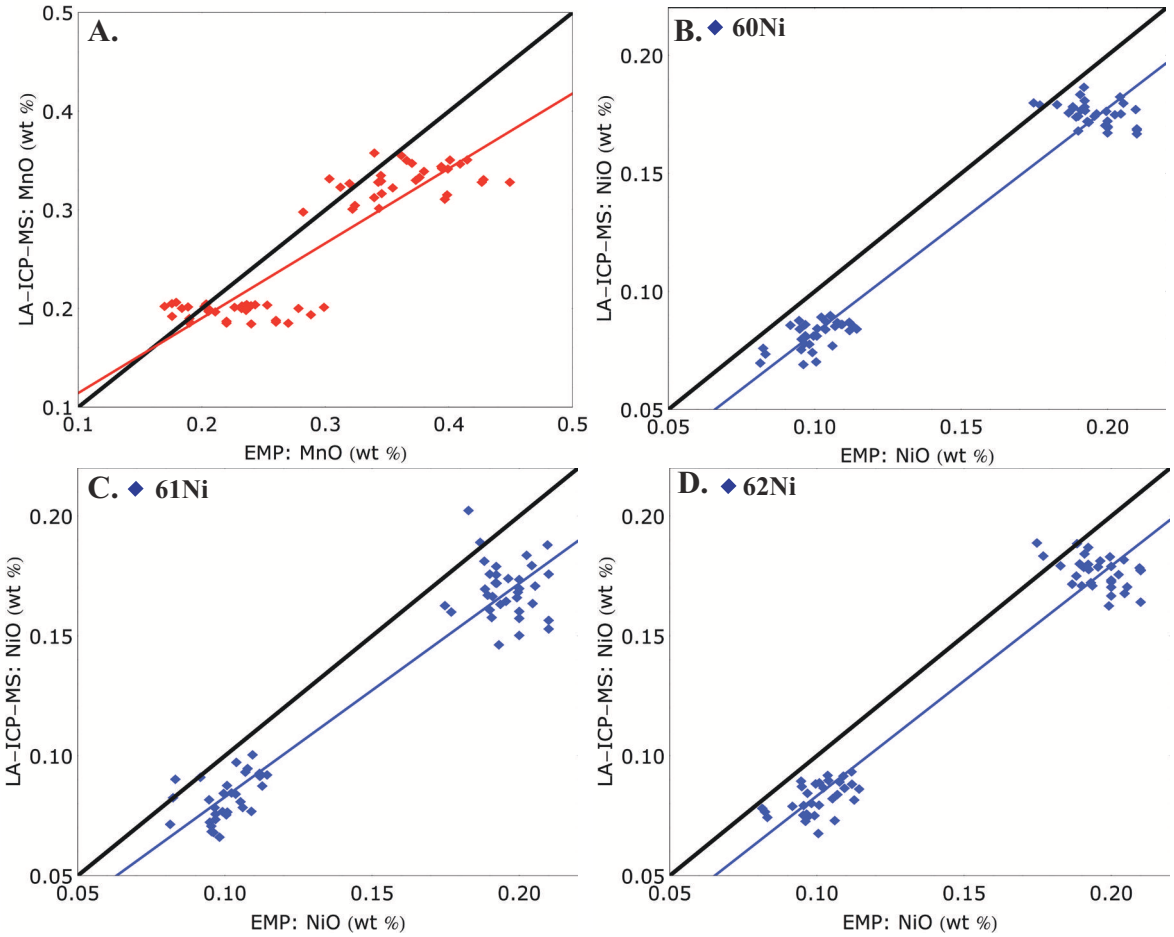

Figure A.1. **A**: Mn (red), **B**: ^{60}Ni, **C**: ^{61}Ni, and **D**: ^{62}Ni (blue) concentrations in olivine analysed by EMP against those analysed by LA-ICP-MS. The black line represents a 1:1 correlation, and the coloured lines represent a best fit between the two techniques.

The maximum difference between the regression line in Figure A.1.C and Ni analysed by EMP is ± 0.029 wt %, and ^{61}Ni analysed by LA-ICP-MS is ± 0.040 wt %. The maximum difference between the regression line in Figure A.1.D and Ni analysed by EMP is ± 0.021 wt %, and ^{62}Ni analysed by LA-ICP-MS is ± 0.010 wt %. An average between ^{60}Ni and ^{62}Ni analysed by LA-ICP-MS are used in the results due their better precision in comparison to both ^{61}Ni, and Ni analysed by EMP.

A.1.2.2.2: Singapore EMP data compared to Barcelona EMP data

A poor correlation was found between the stoichiometric values of Si, Al, Na and Ca in plagioclase analysed from (a) Barcelona and from (b) Singapore. To ensure both data sets are internally consistent selected points along each plagioclase transect from (a) and (b) were re-analysed using the EMP at (c) the University of British Columbia. Points chosen to be re-analysed extended from the highest (An_{94}) to the lowest (An_{50}) anorthite contents. The data from (a) and (b) were then normalised to the data analysed at (c). This involved plotting each element analysed in an analytical session at (a) and (b) against the corresponding element analysed at (c). The equation of the linear regression between the two data sets (forced to pass through the origin) was used to calculate the normalised value for each element. The corrected plagioclase analyses have stoichiometry totals within ± 1.5 % of the ideal total number of cations (5 cations per 8 oxygens). The normalised stoichiometric values of Si, Al, Na, and Ca analysed in each analytical session from both (a) and (b) are plotted against each other and follow the trend predicted by a stoichiometric plagioclase (black line; Figure A.2). The maximum difference in mol % An between the corrected values and raw analyses from (a) Barcelona is ~ 1 mol %. The maximum difference in mol % An between the corrected values and raw analyses from (b) Singapore is ~ 1.5 mol %. An increase in An content of 1.5 mol % will decrease the Kd_{Mg} by ~ 2.5 % using Equation (1), the Kd_{Sr} by ~ 3.2 % using the equation from Blundy and Wood (1991), and the Kd_K by ~ 3 % using Equation (2). The maximum difference between the corrected MgO plagioclase data and the raw MgO analyses from (a) Barcelona is 0.85 %. The maximum difference between the corrected MgO plagioclase analyses and the raw MgO analyses from (b) Singapore is 6.6 %. A 6.6 % change in the

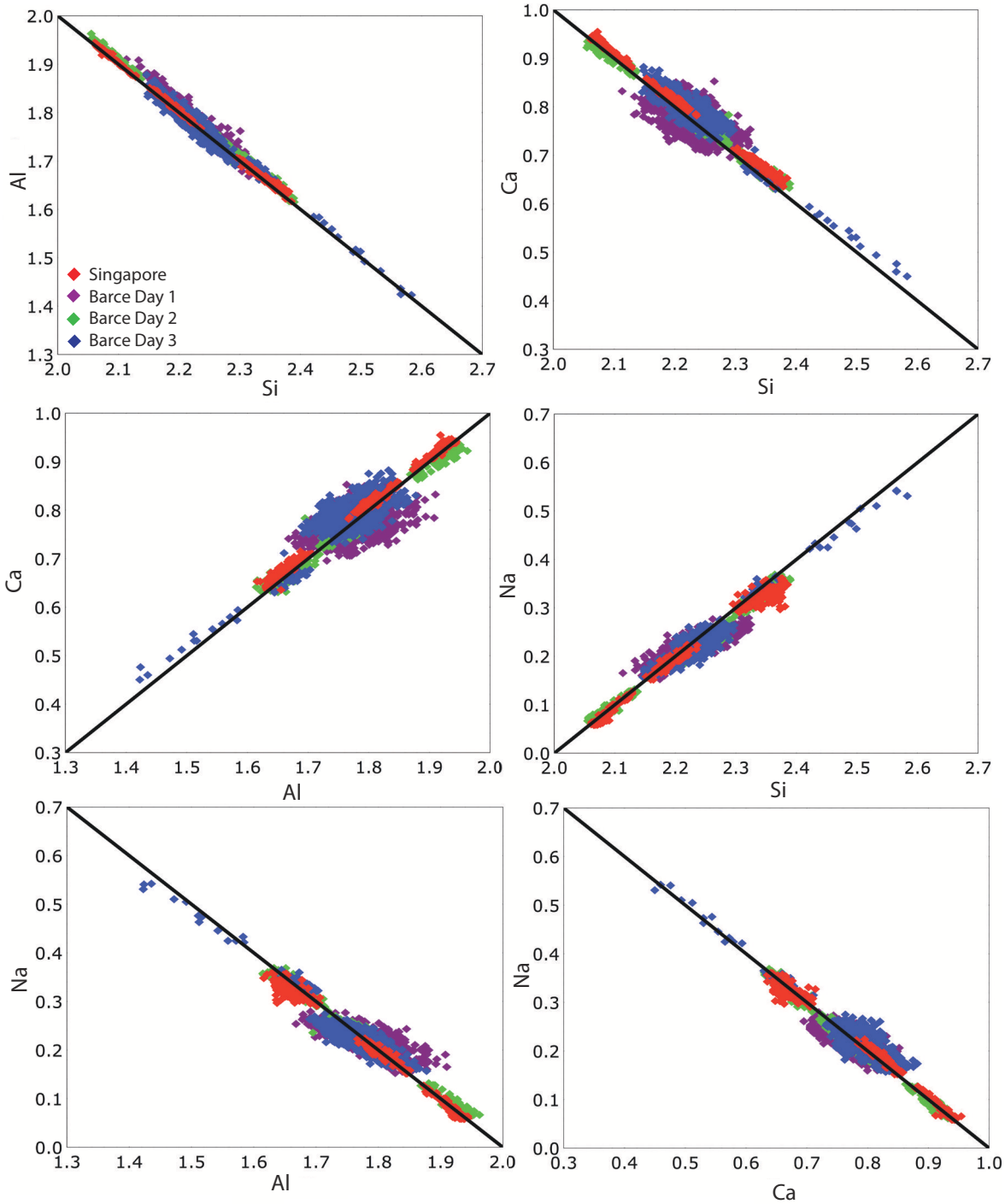

Figure A.2. The normalised stoichiometric values of Si, Al, Na, and Ca in plagioclase analysed by EMP for each analytical session (Singapore, Barcelona Day 1, Barcelona Day 2, and Barcelona Day 3). The black line represents a pure stoichiometric plagioclase.

MgO content in plagioclase will change the equilibrium MgO melt content by ~ 6 % using Equation (1). Therefore, the results of this thesis would not change significantly if either the MgO and An contents from the corrected values are used, or the data from the raw analyses.

A.1.2.2.3: LA-ICP-MS multiple isotope comparison in olivine

Multiple isotopes of Ni and Cr were analysed by LA-ICP-MS in olivine as a check for isobaric interferences during analysis, and are plotted against each other to check the data quality (Figure A.3). The discrepancy between the 1:1 ratio and the regression between ^{53}Cr and ^{52}Cr is ~ 1 %. The maximum difference between the regression line and ^{53}Cr is ± 3 ppm, and for ^{52}Cr is ± 20 ppm. The concentrations used in the results are an average between ^{53}Cr and ^{52}Cr. A smaller discrepancy is seen between the 1:1 ratio and the regression between ^{60}Ni and ^{62}Ni (~ 0.8 %), in comparison to the regression between ^{60}Ni and ^{61}Ni (~ 7 %). The maximum difference between the regression line between ^{60}Cr and ^{61}Cr, and the data is ± 0.006 wt % for ^{60}Cr, and ± 0.008 wt % for ^{61}Cr. The maximum difference between the regression line between ^{60}Cr and ^{62}Cr, and the data is ± 0.003 wt % for ^{60}Cr, and ± 0.001 wt % for ^{61}Cr. The concentrations used in the results are an average between ^{60}Ni and ^{62}Ni due their better precision.

A.1.2.2.4: Analysed glass data compared to values published in Goss et al. (2010)

The average concentrations of Sr, K, Mn, Ni and Cr within glass analysed by LA-ICP-MS are compared to published bulk glass analysis in Goss et al. (2010; Figure A.4). Note, the elements Mn, Ni and Cr were only analysed in the glass of two samples by LA-ICP-MS here. The maximum and minimum melt concentrations for each region from LA-ICP-MS analysis and bulk glass data from Goss et al. (2010) are shown in Table A.5. Goss et al. (2010) analysed K and Mn using EMP and trace elements Sr, Ni, and Cr using solution ICP MS. Concentrations of Sr and K within 5 samples gave a maximum percentage difference between LA-ICP-MS data and data from Goss et al. (2010) of 7 % for Sr and 63 % for K. Concentrations of Ni and Mn analysed within two samples gave a

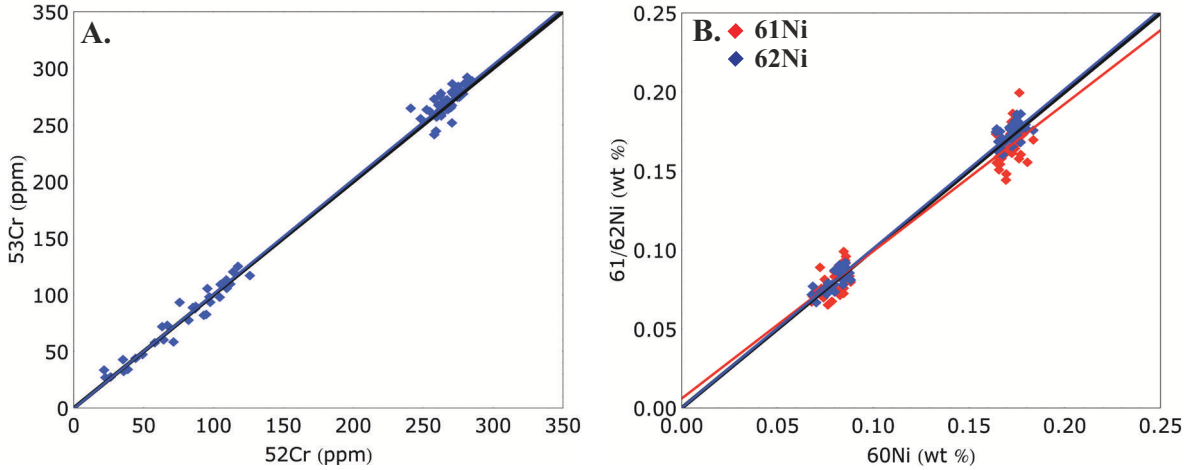

Figure A.3. Plots of **A**: ^{53}Cr against ^{52}Cr (blue), and **B**: ^{61}Ni (red), and ^{62}Ni (blue), against ^{60}Ni from olivine analyses. The black line represents a 1:1 correlation, and the coloured lines represent a best fit between the two isotopes.

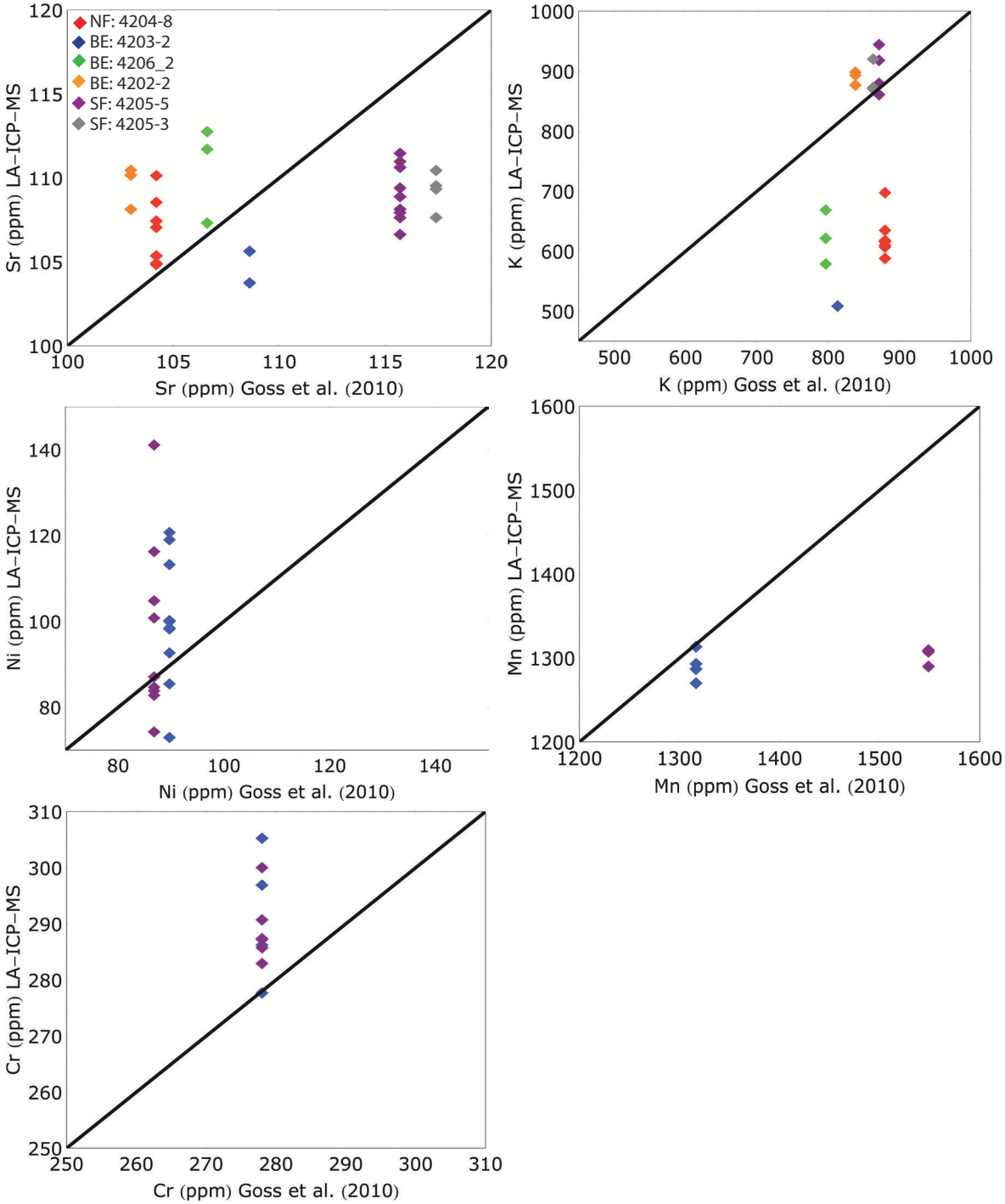

Figure A.4. Plots of Sr, K, Mn, Ni, and Cr analysed in glass using LA-ICP-MS against bulk glass data from Goss et al. (2010). The black line represents a 1:1 correlation between the two data sets. The different coloured symbols represent glass data in samples from the Northern Fissure (NF), the Southern Fissure (SF) and the Bull's eye (BE).

maximum difference between LA-ICP-MS data and data from Goss et al. (2010) of 16 % for Mn, and 7.3% for Ni. Analysis of Cr by LA-ICP-MS within two samples gave a range of between 285-318 ppm, whereas Goss et al. (2010) published concentrations of 278 ppm in both samples, giving a maximum difference of 12.5 %. The Mn values analysed by EMP reported by Goss et al. (2010) are likely within error of those analysed by LA-ICP-MS here. The variations seen within the Sr, K, Ni, and Cr analyses likely reflect variations found within the glass. The maximum and minimum values from both glass analysed by LA-ICP-MS, and those reported in Goss et al. (2010), are used for the range of melt compositions in the results sections (Sections 2.3-2.7; Table A.5).

Table A.5. Concentrations of MgO, Sr, K, MnO, NiO, and Cr in the lavas from the 2005-06 eruption analysed by LA-ICP-MS and taken from bulk glass data in Goss et al. (2010). The last column shows the compositional range used in this thesis for each region and are the maximum and minimum values taken from both LA-ICP-MS data and bulk glass data in Goss et al. (2010). Note, there is no reported error associated with the K analyses in Goss et al. (2010)

Element	Region	LA-ICP-MS glass analysis	Goss et al. (2010)	Range used
MgO (wt %)	Northern Fissure	-	7.76 to 7.78	7.76 to 7.78
	Bull's eye	-	8.02 to 8.28	8.02 to 8.28
	Southern Fissure	-	7.76 to 8.28	7.76 to 8.28
Sr (ppm)	Northern Fissure	104 ± 6.7 to 110 ± 7.1	104 ± 3.1 to 107 ± 3.3	104 ± 6.7 to 110 ± 7.1
	Bull's eye	103 ± 6.7 to 113 ± 7.4	103 ± 3.1 to 109 ± 3.3	103 ± 6.7 t o 113 ± 7.3
	Southern Fissure	106 ± 6.9 to 111 ± 7.2	115 ± 3.4 to 117 ± 3.5	106 ± 6.9 to 117 ± 3.5
K (ppm)	Northern Fissure	590 ± 82 to 700 ± 65	860 to 880	590 ± 82 to 880
	Bull's eye	500 ± 70 to 900 ± 126	800 to 840	500 ± 70 to 900 ± 126
	Southern Fissure	870 ± 122 to 950 ± 133	860 to 870	870 ± 122 to 950 ± 133
MnO (wt %)	Bull's eye	0.163 ± 0.001 to 0.169 ± 0.001	0.17 to 0.19	0.163 ± 0.001 to 0.169 ± 0.001
	Southern Fissure	0.166 ± 0.001 to 0.169 ± 0.001	0.19 to 0.20	0.166 ± 0.001 to 0.169 ± 0.001
NiO (wt %)	Bull's eye	0.009 ± 0.0003 to 0.015 ± 0.0003	0.011 ± 0.0003 to 0.012 ± 0.0004	0.009 ± 0.0003 to 0.015 ± 0.0003
	Southern Fissure	0.009 ± 0.0003 to	0.011 ± 0.0003 to	0.009 ± 0.0003 to

		0.015 ± 0.0003	0.013 ± 0.0004	0.015 ± 0.0003
Cr (ppm)	Bull's eye	278 ± 4.2 to 318 ± 4.8	266 ± 9.3 to 292 ± 10.2	266 ± 9.3 to 318 ± 4.8
	Southern Fissure	286 ± 4.3 to 312 ± 4.7	278 ± 9.7 to 320 ± 11.2	278 ± 9.7 to 320 ± 11.2

A.1.3: Differences in calculated melt temperatures

Melt temperatures have been calculated using the methods described by Sinton and Detrick (1992), Wilson et al., (1988), and the MELTs (Ghiorso and Sack, 1995) and PetroLog (Danyushevsky and Plechov, 2011) algorithms (Section 2.4.2.1). Figure A.5 illustrates the variation in the calculated melt temperatures using the above four methods for the melt compositions found in the 2005-06 lavas.

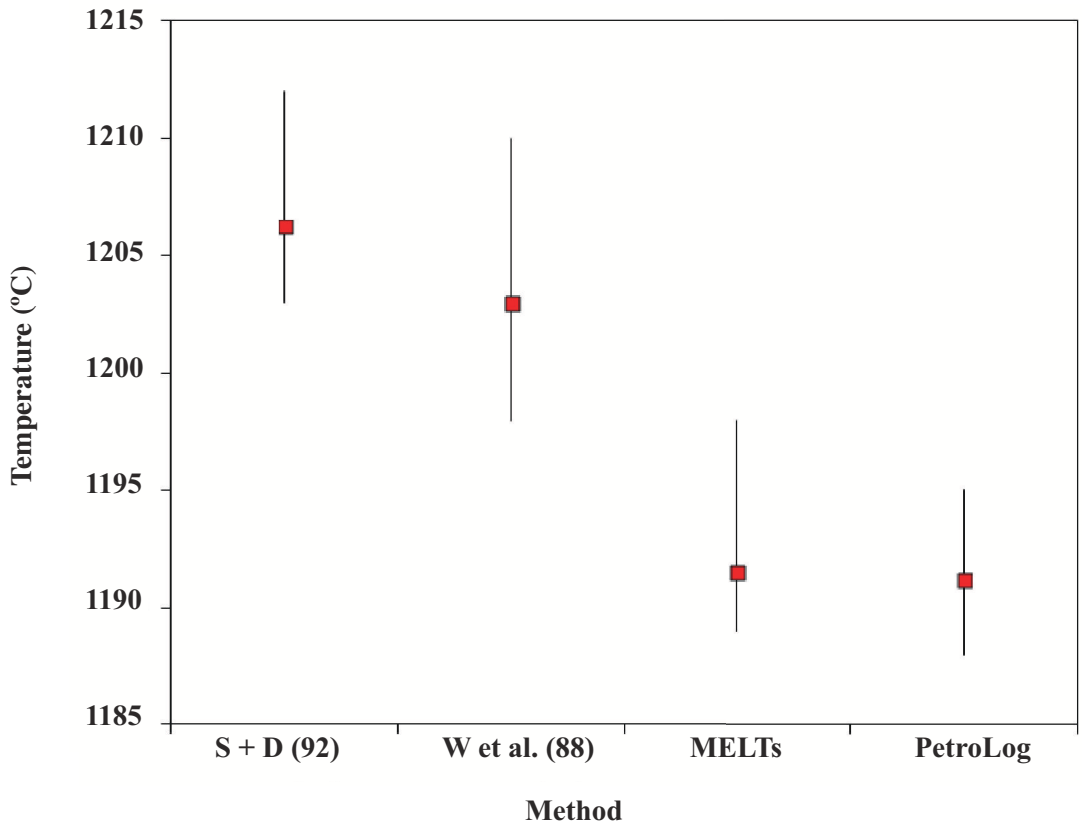

Figure A.5. Plot illustrating the range of melt temperatures calculated using the methods described by Sinton and Detrick (1992; S+D [92]), Wilson et al., (1988; W et al. [88]]), and the MELTs (Ghiorso and Sack, 1995) and PetroLog (Danyushevsky and Plechov, 2011) algorithms. Further details on the methods are given in Section 2.4.2.1. The line represents the range of melt temperatures calculated using each method for the different melt compositions found in the 2005-06 lavas (from Goss et al., 2010). The red square represents the average melt temperature calculated using each method.

Appendix A.2: Major and trace element data

The attached C.D. contains the major and trace element contents analysed in olivine and the corrected concentrations in plagioclase analysed by EMP. It also contains trace element data analysed by LA-ICP-MS in plagioclase, olivine and the surrounding glass.

Appendix A.3: Sample locations, petrography and techniques used on each sample.

Table A.6 provides information on the locations of each sample studied, along with their petrography, (details of the number of phases found in each samples), and what analytical method was used on each sample.

Table.A.6. Locations of each sample from the 2005-06 eruption, petrographic phase abundances in each sample, and analytical techniques performed.

Sample	**Location**		**Petrology**					**Analytical techniques**	
	Longitude (West)	Latitude (North)	**Plagioclase**		**Olivine**	**Glomerocryst**		EMP	LA-ICP-MS
			Euhedral	Resorbed	Sub-Euhedral	Plagioclase	Olivine		
Northern Fissure									
4204-8	104º17.529'	9º53.078'	38	0	0	0	0	√	√
4204-9	104º17.525'	9º52.965'	74	2	0	0	0	√	√
4204-6	104º17.502'	9º53.095'	33	1	0	0	0	√	
4202-5	104º17.586'	9º53.060'	20	0	0	0	0		
4204-4a	104º17.689'	9º53.028'	57	2	0	0	0		
4204-4b	104º17.689'	9º53.028'	31	0	0	0	0		
4204-2	104º17.855'	9º52.998'	89	0	0	0	0		
4204_1	104º18.135'	9º52.954'	41	1	0	0	0		
		TOTAL	***383***	***6***	***0***	***0***	***0***		
Bull's Eye									
4203-2	104º17.568'	9º50.328'	79	1	2	21	2	√	√
4206-2	104º17.480'	9º50.105'	46	2	0	0	0	√	√
4202-1	104º17.743'	9º50.803'	17	1	1	0	0	√	√
4202-6	104º17.568'	9º50.328'	23	0	0	0	0	√	√
4203-1	104º17.588'	9º50.793'	14	2	0	0	0		
4202-4	104º17.582'	9º50.737'	7	1	0	0	0		

4202-2a	104º17.590'	9º50.793'	18	0	0	0	0		
		TOTAL	***204***	***7***	***3***	***21***	***2***		
Southern Fissure									
4205-5	104º16.828'	9º46.525'	63	2	0	15	3	√	√
4205-3	104º16.793'	9º46.257'	57	12	0	0	0	√	√
4205-6	104º17.011'	9º47.169'	23	2	0	0	0	√	
		TOTAL	***143***	***16***	***0***	***15***	***3***		

Appendix A.4: Errors in partition coefficients and diffusion models

A.4.1: Error of the plagioclase-melt partition coefficients

Plagioclase partition coefficients (Kd) are taken from Equation (1) and (2), and equations in Bindeman et al. (1998) and Blundy and Wood (1991; Section 2.4.2.3). Each equation takes the similar form of (e.g. Bindeman et al., 1998);

$$RT\ln(Kd) = \mathrm{m}\ (\pm\ a)\ XAn + \mathrm{c}\ (\pm\ \mathrm{b}) \qquad \text{(A.1)}$$

where R is the gas constant, T is temperature in Kelvin, and a and b are the standard error associated with the regressed parameters (m and c). The absolute error associated with the partition coefficients (E_{Kd}) is derived through error propagation of the uncertainties in their regressed parameters (assuming independent errors; Taylor, 1982). The error propagation was calculated at a temperature of 1200°C for anorthite contents between An_{50} and $An_{100,}$ and does not take into account the error associated with temperature estimates or with the analysed An or trace elements contents. The equation used is;

$$E_{Kd} = \{\{[[XAn\ \exp((\mathrm{m}\ XAn + \mathrm{c})/RT)]/RT]\ \mathrm{a}\ \}^2 + \{[[\exp((\mathrm{m}\ XAn + \mathrm{c})/RT)]/RT]\ \mathrm{b}\ \}^2\}^{0.5} \qquad \text{(A.2)}$$

which uses the same parameters as in Equation A.1.

A.4.2: Calculating the misfit between a diffusion model and analysed data

The best fit diffusion model for each profile in olivine and plagioclase (Section 2.6) was calculated by minimising the square root of the difference (e_{RMS}) between the model (*model*) and the data (*data*) via the equation;

$$e_{RMS} = \sqrt{\{\sum[(data\text{-}model)^2/(n\text{-}2)]\}} \qquad (A.3)$$

where n is the number of data points in the profile.

Appendix A.5: Photomicrographs of plagioclase and olivine, and elemental zoning profiles.

The following sections contain photomicrographs and zoning profiles for plagioclase and olivine transects from: samples 4204_9 (A.5.1.1) and 4204_8 (A.5.1.2) from the Northern Fissure (A.5.1); samples 4206_2 (A.5.2.1), 4202_1 (A.5.2.2), 4203_2 (A.5.2.3), and 4202_6 (A.5.2.4) from the Bull's eye (A.5.2); and samples 4205_5 (A.5.3.1), and 4205_3 (A.5.3.2) from the Southern Fissure (A.5.3). These zoning profiles are from every analysed transect, including those that have been modelled in Section 2.6. The red or green arrow on the photomicrograph shows the location of the EMP traverse, and the pits from LA-ICP-MS analyses are visible. The arrow direction is always left to right in relation to the x-axis on the underlying profiles, and the x-axis reflects the distance along the profile. The yellow band on the anorthite profile (blue) represents the range of calculated anorthite contents in equilibrium with their host melts ($An_{70\text{-}75}$; Section 2.4.2.2). The green line on the plagioclase MgO, Sr, and K profiles (red) represents the calculated concentrations in equilibrium with their host melts. In some plagioclase transects, the LA-ICP-MS transect extends outside the EMP traverse, in this case the An content used to calculate the equilibrium profile was estimated using the SEM image. The MgO host melt concentrations are taken from bulk glass data from Goss et al. (2010; Table A.5). The Sr and K host melt concentration are an average taken from LA-ICP-MS data and bulk glass data from Goss et al, (2010; values written on each profile).

A.5.1: Northern Fissure

A.5.1.1: Sample 4204_9

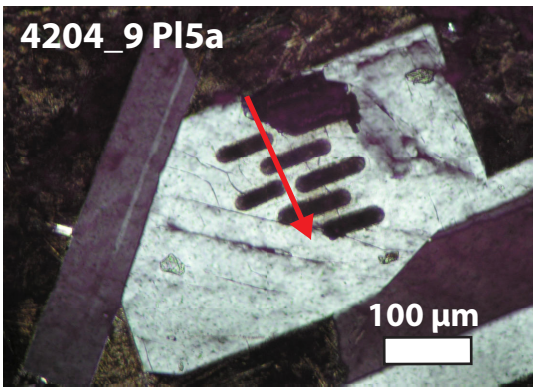

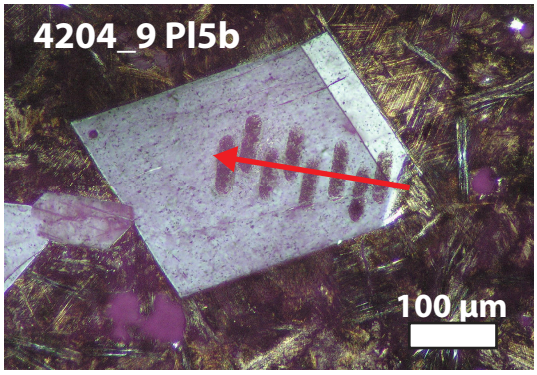

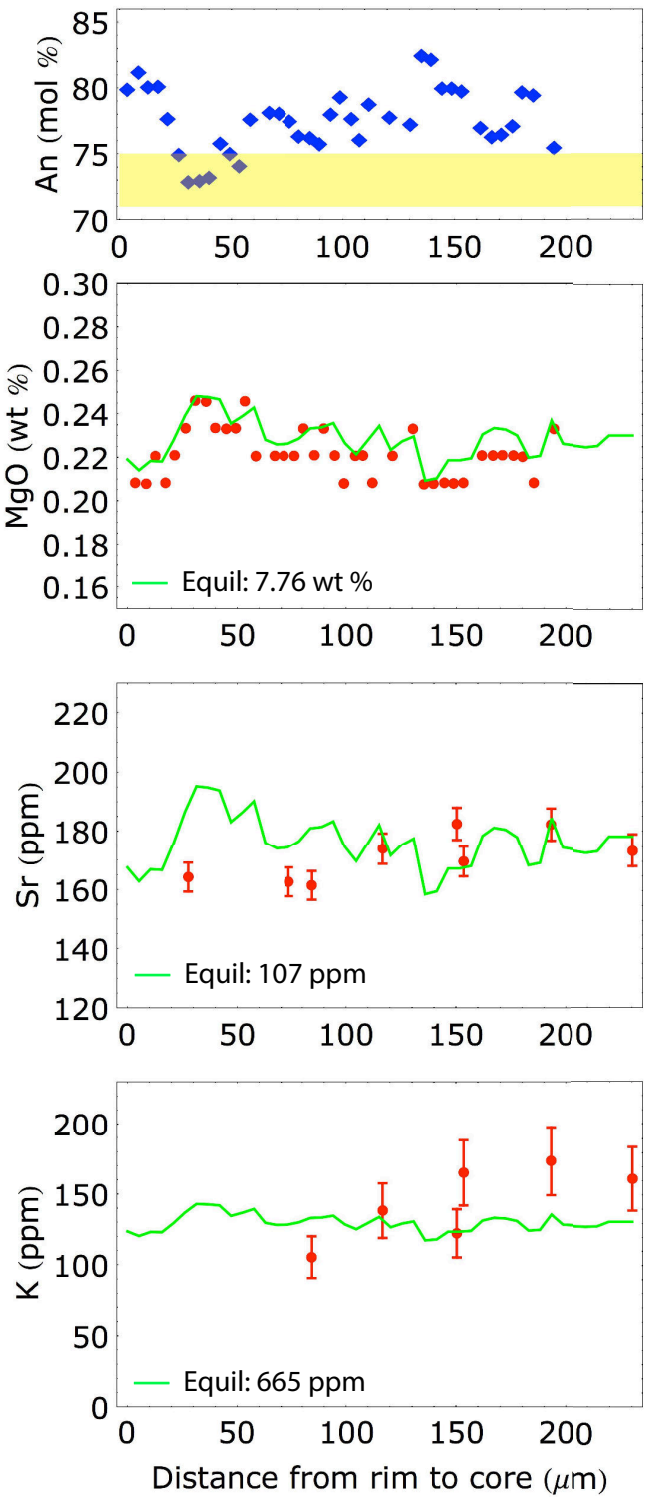

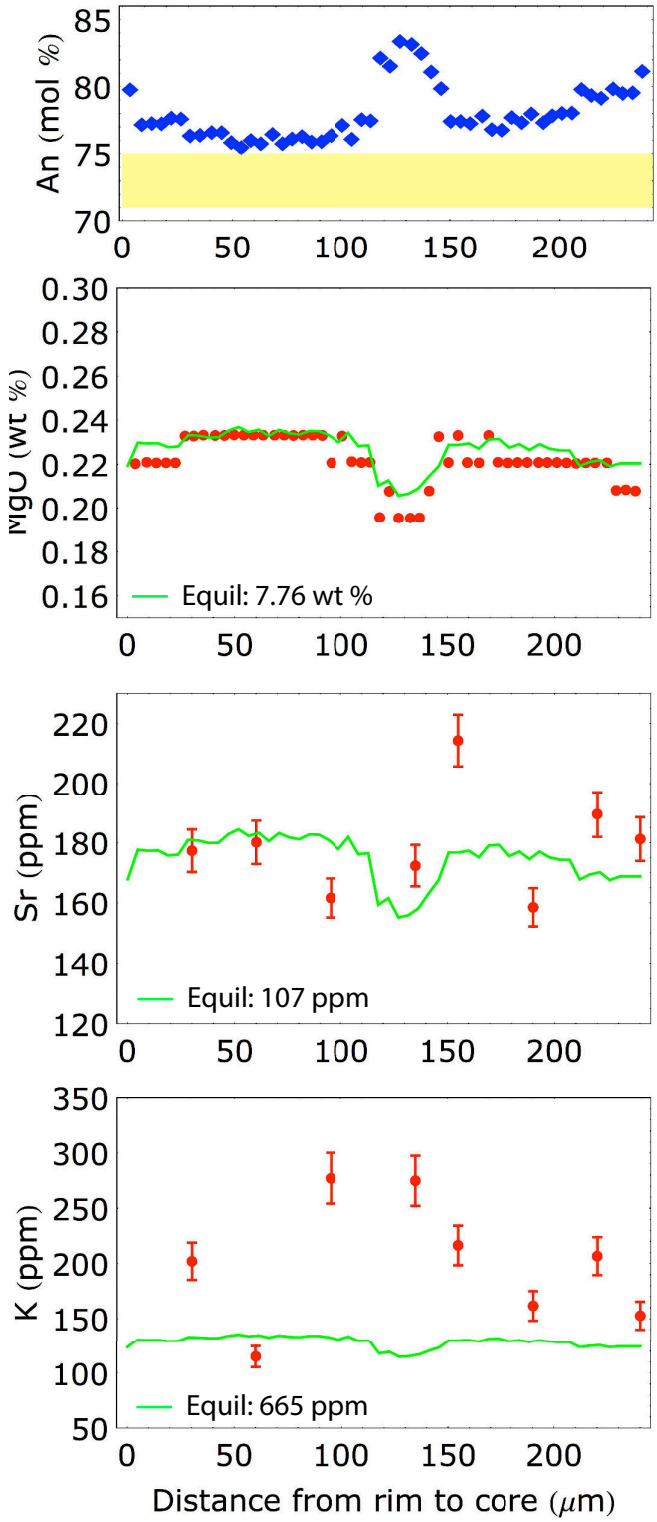

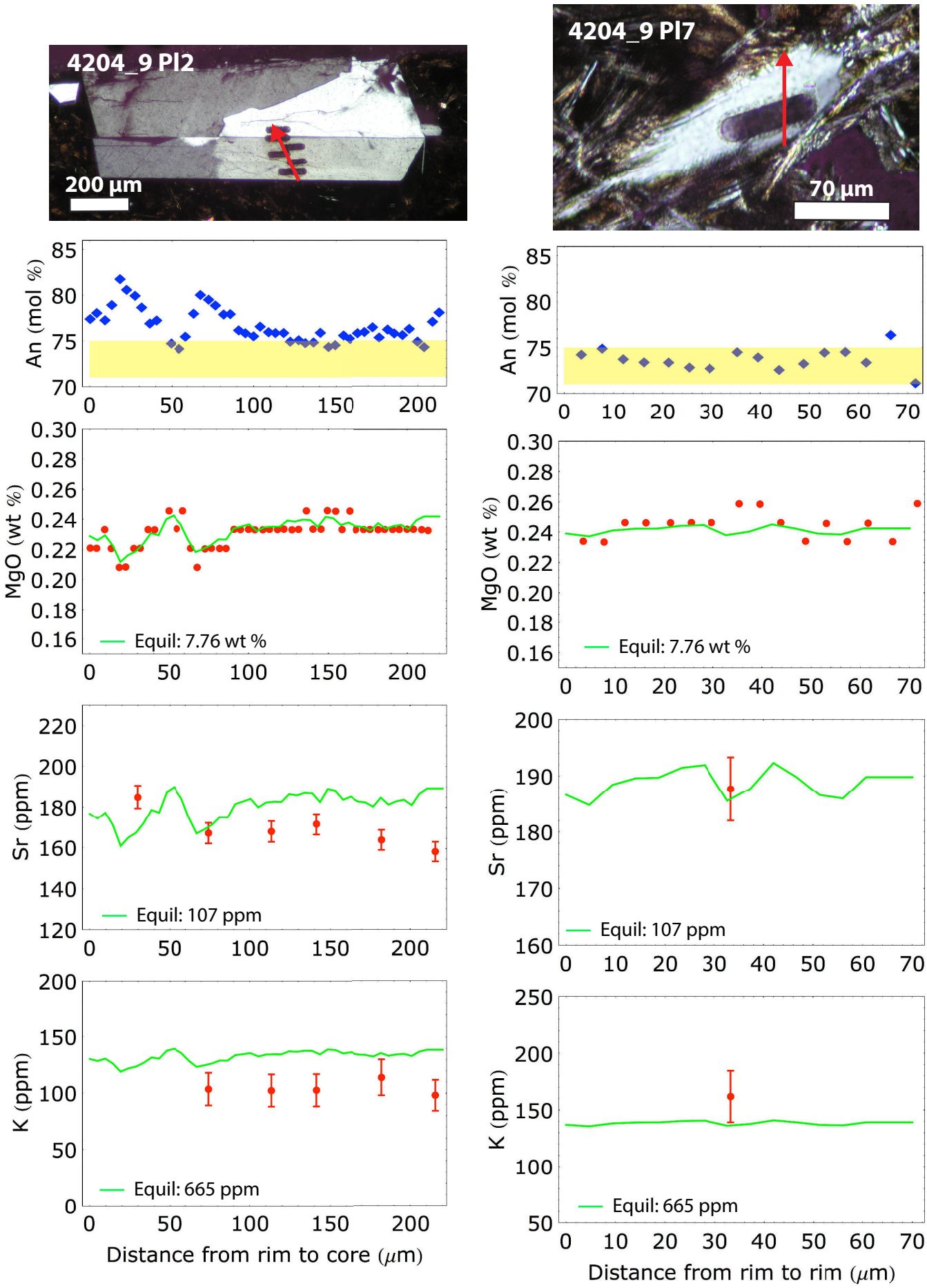
4204_9 Pl2
200 µm
4204_9 Pl7
70 µm
An (mol %)
MgO (wt %)
Equil: 7.76 wt %
Sr (ppm)
Equil: 107 ppm
K (ppm)
Equil: 665 ppm
Distance from rim to core (µm)
Distance from rim to rim (µm)

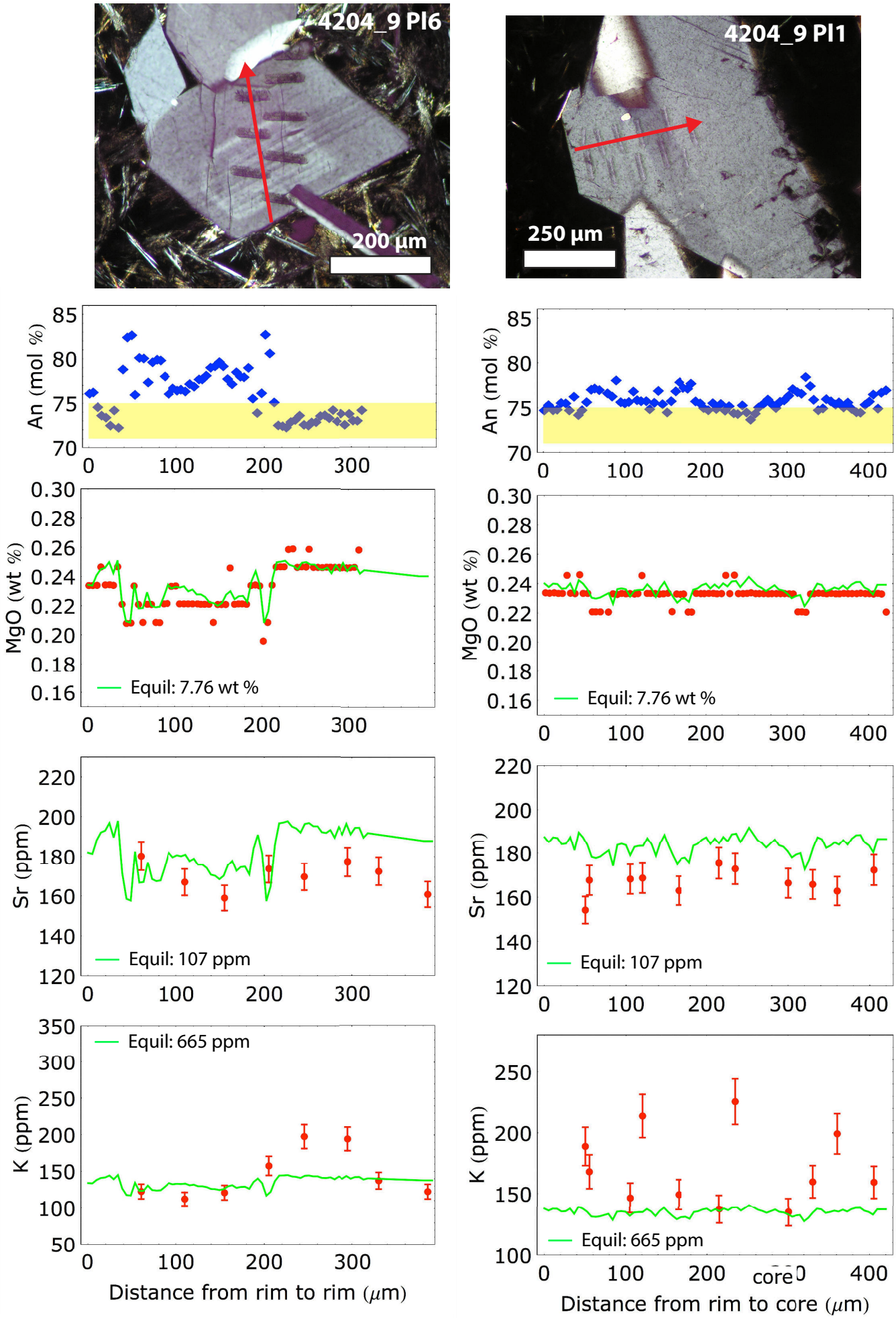
4204_9 Pl6
200 µm
4204_9 Pl1
250 µm
An (mol %)
MgO (wt %)
Equil: 7.76 wt %
Sr (ppm)
Equil: 107 ppm
K (ppm)
Equil: 665 ppm
Distance from rim to rim (µm)
core
Distance from rim to core (µm)

A.5.1.2: Sample 4204_8

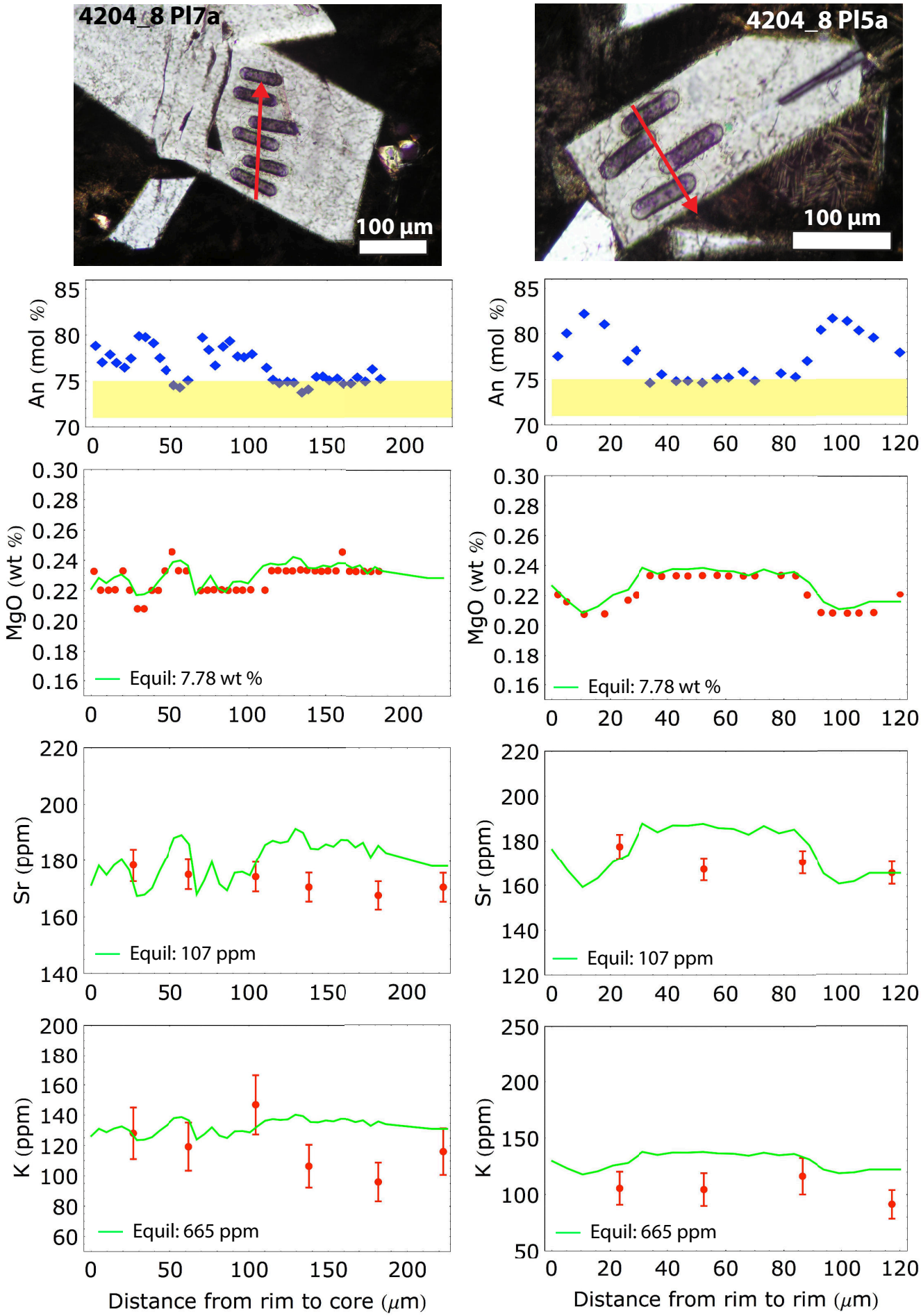

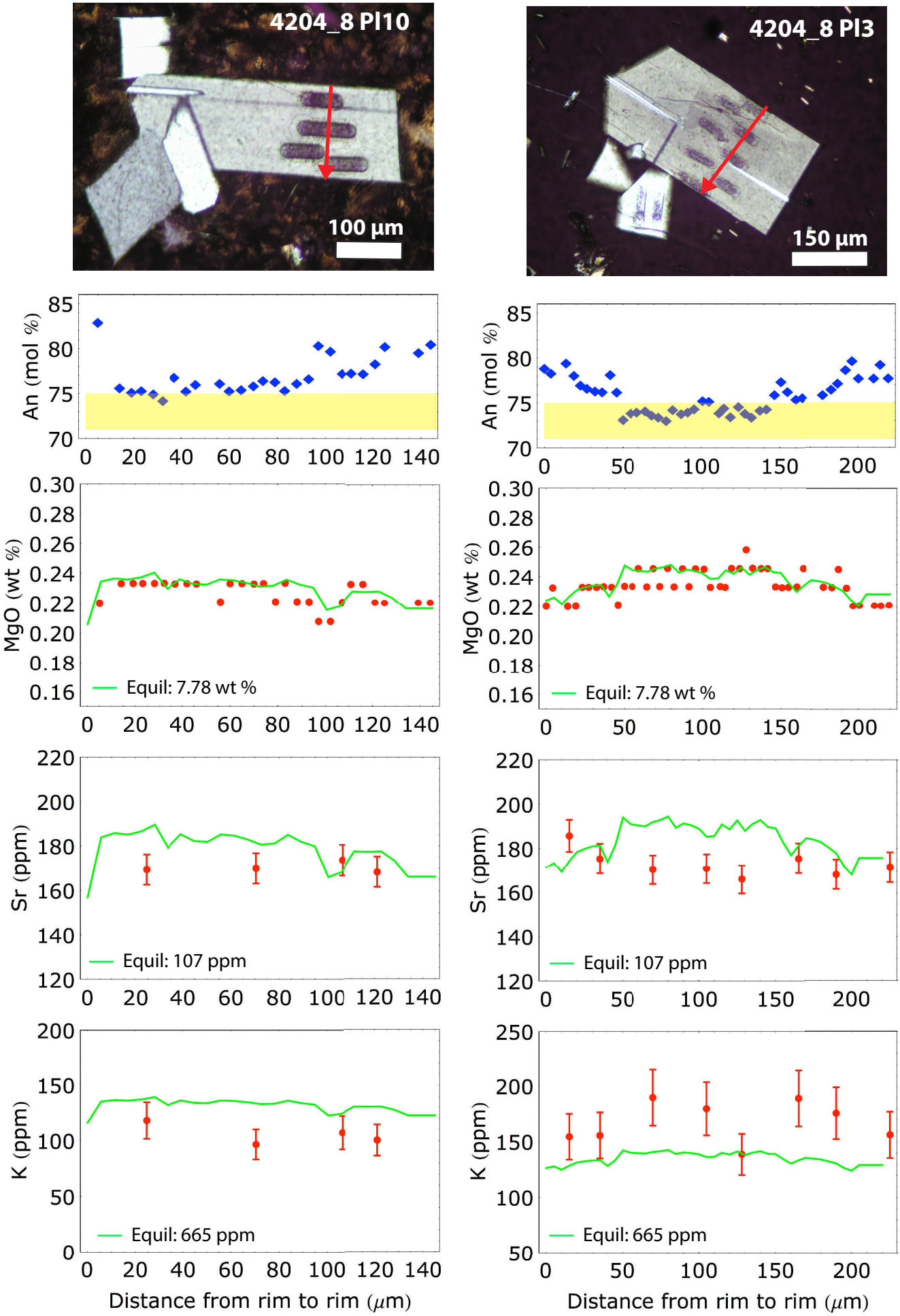
4204_8 Pl10
100 µm
4204_8 Pl3
150 µm
An (mol %)
MgO (wt %)
Equil: 7.78 wt %
Sr (ppm)
Equil: 107 ppm
K (ppm)
Equil: 665 ppm
Distance from rim to rim (µm)

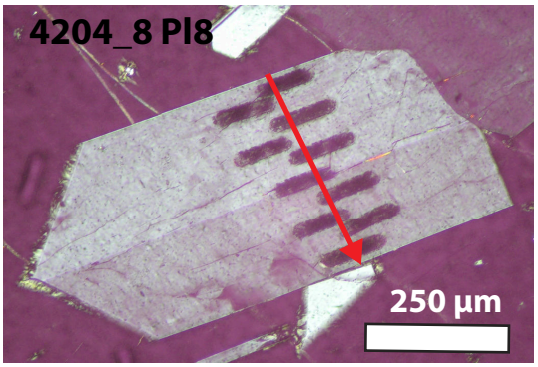
4204_8 Pl8
250 µm

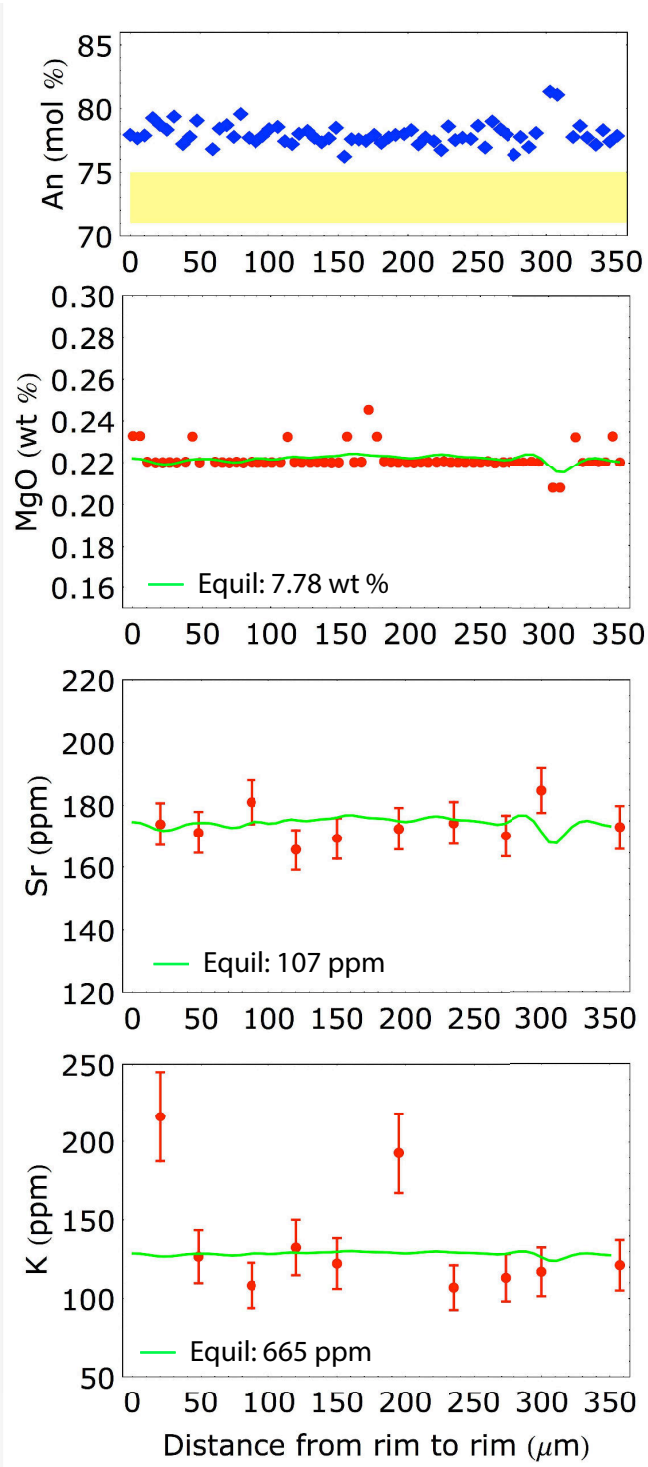
An (mol %)
85
80
75
70
0 50 100 150 200 250 300 350
MgO (wt %)
0.30
0.28
0.26
0.24
0.22
0.20
0.18
0.16
Equil: 7.78 wt %
0 50 100 150 200 250 300 350
Sr (ppm)
220
200
180
160
140
120
Equil: 107 ppm
0 50 100 150 200 250 300 350
K (ppm)
250
200
150
100
50
Equil: 665 ppm
0 50 100 150 200 250 300 350
Distance from rim to rim (µm)

A.5.2: Bull's eye

A.5.2.1: Sample 4206_2

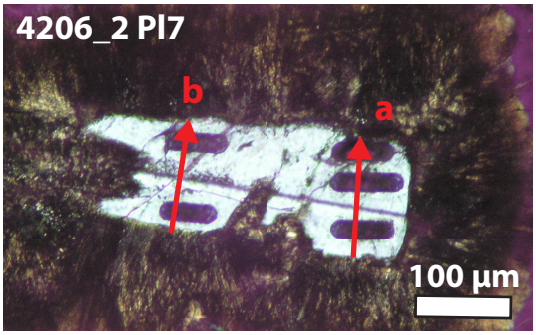

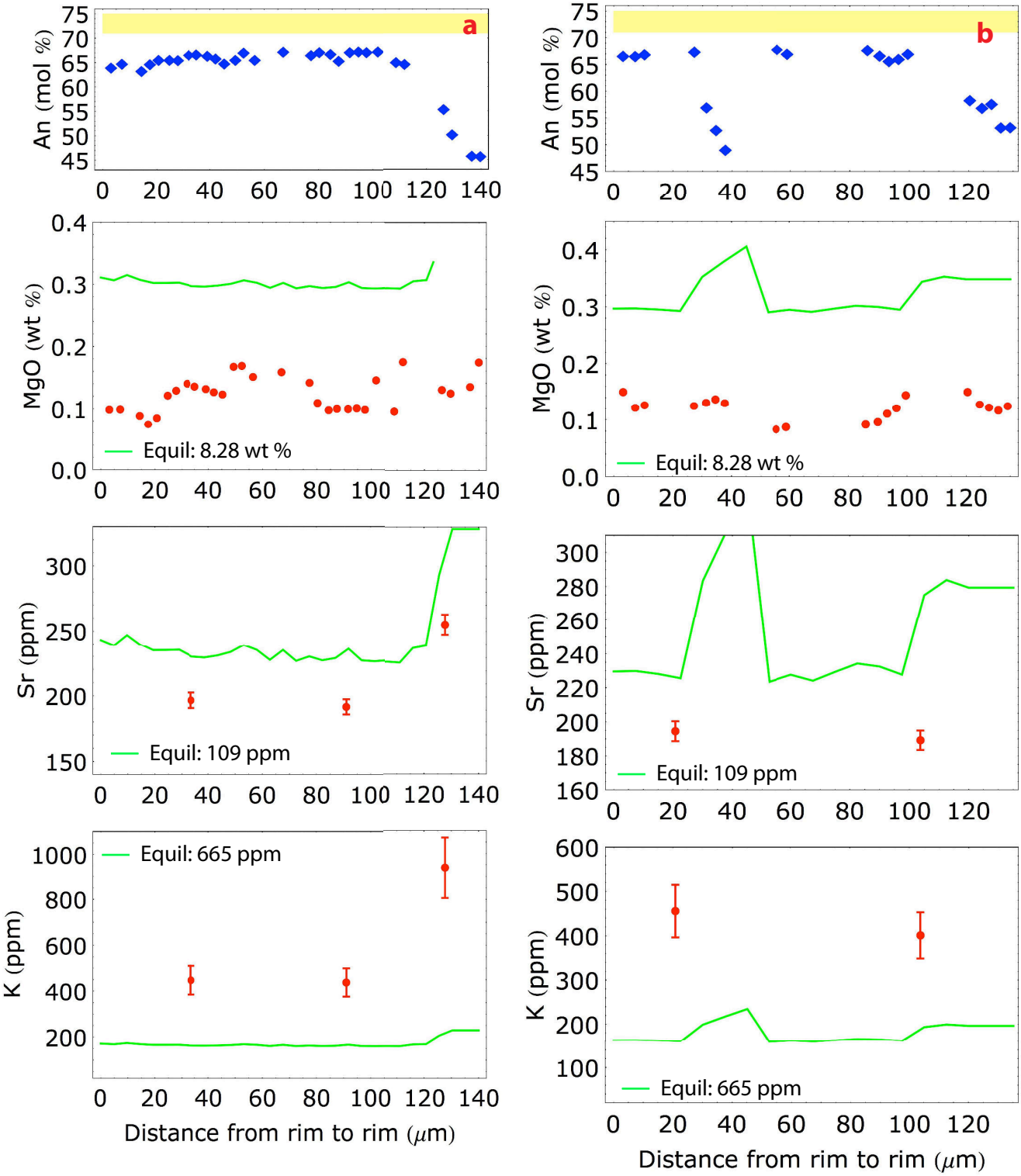

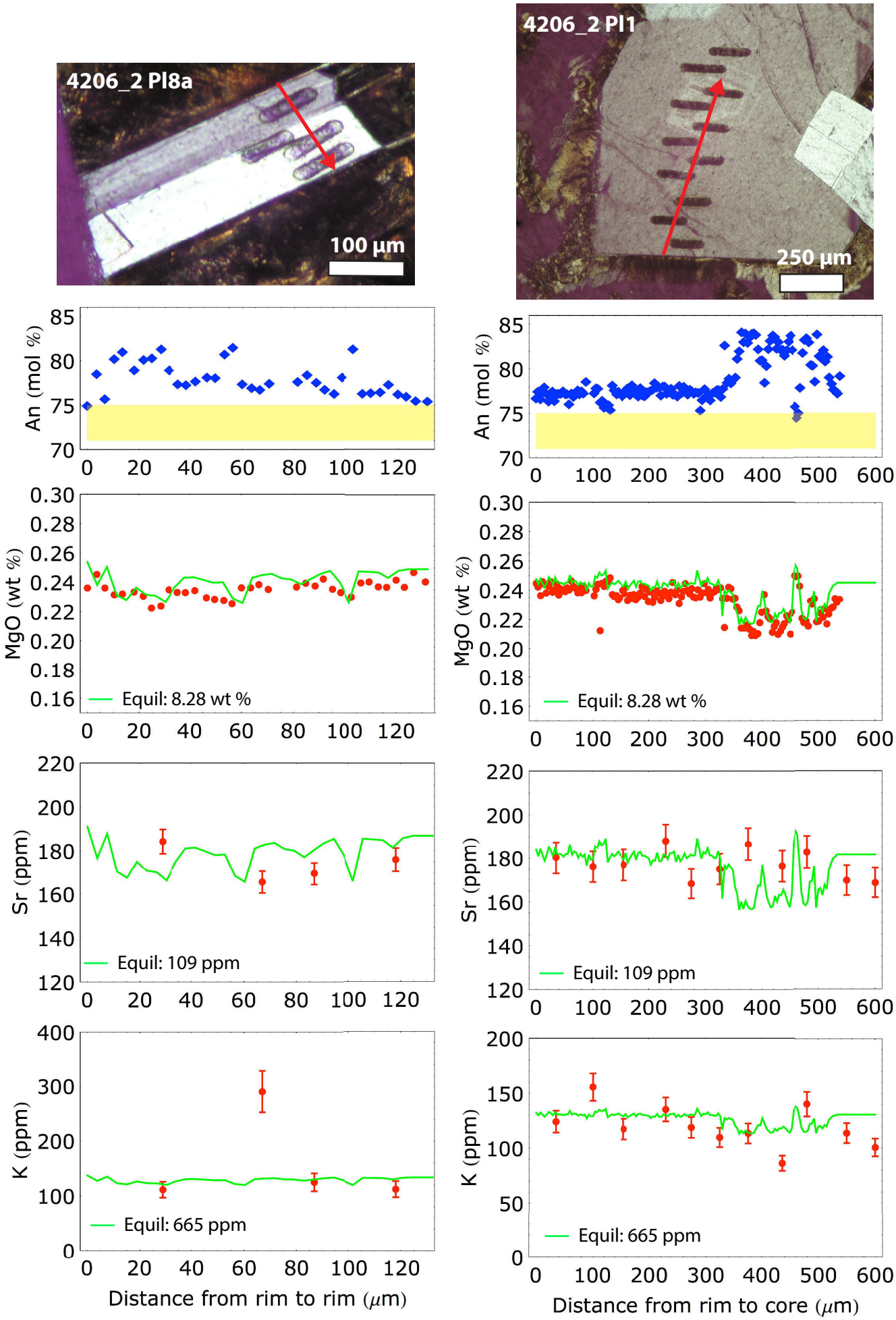
4206_2 Pl8a
100 µm
4206_2 Pl1
250 µm
An (mol %)
MgO (wt %)
Equil: 8.28 wt %
Sr (ppm)
Equil: 109 ppm
K (ppm)
Equil: 665 ppm
Distance from rim to rim (µm)
Distance from rim to core (µm)

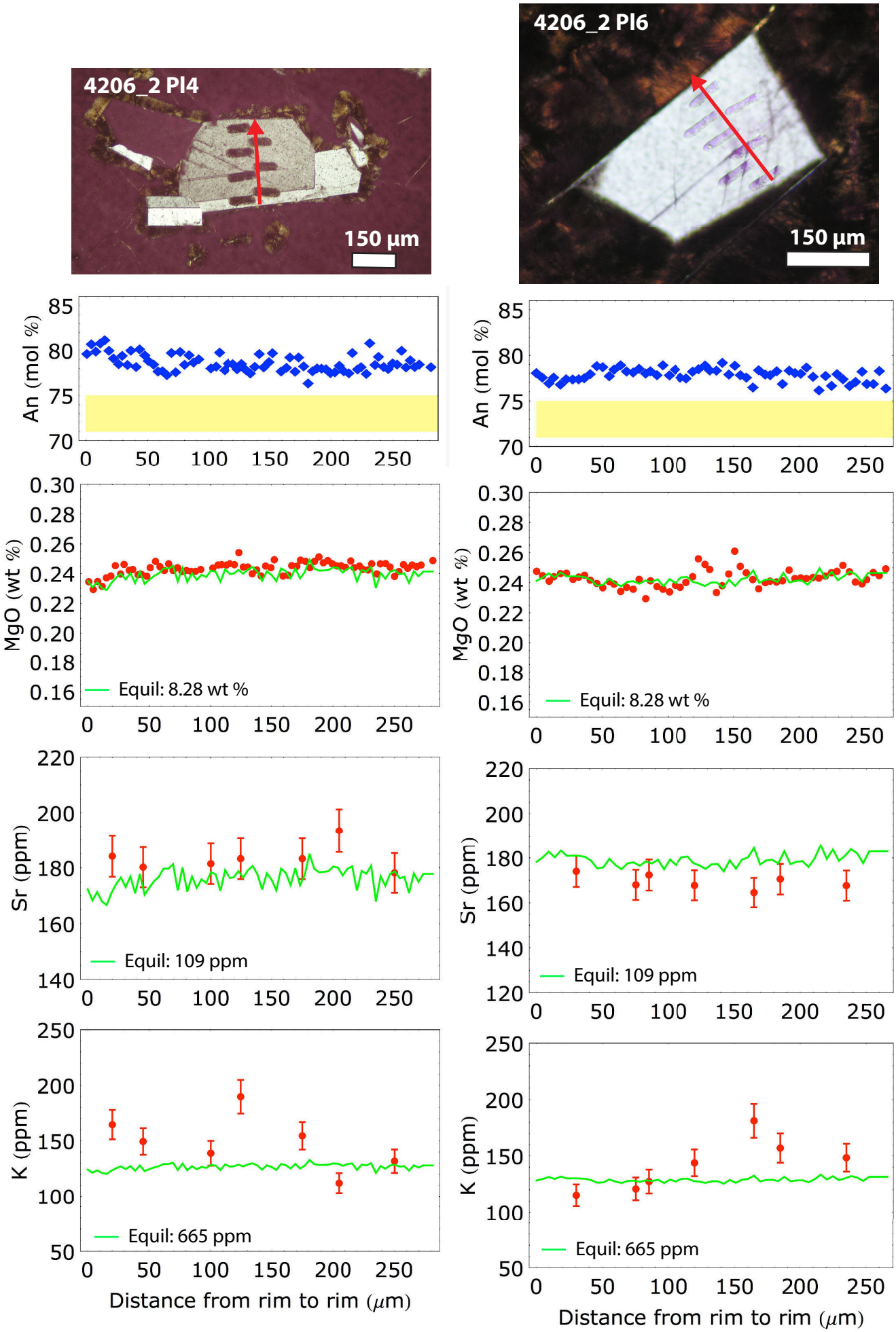
4206_2 Pl4
150 µm
4206_2 Pl6
150 µm
An (mol %)
MgO (wt %)
Equil: 8.28 wt %
Sr (ppm)
Equil: 109 ppm
K (ppm)
Equil: 665 ppm
Distance from rim to rim (µm)

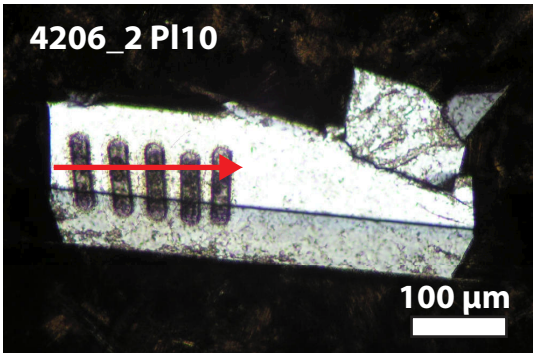
4206_2 Pl10
100 µm

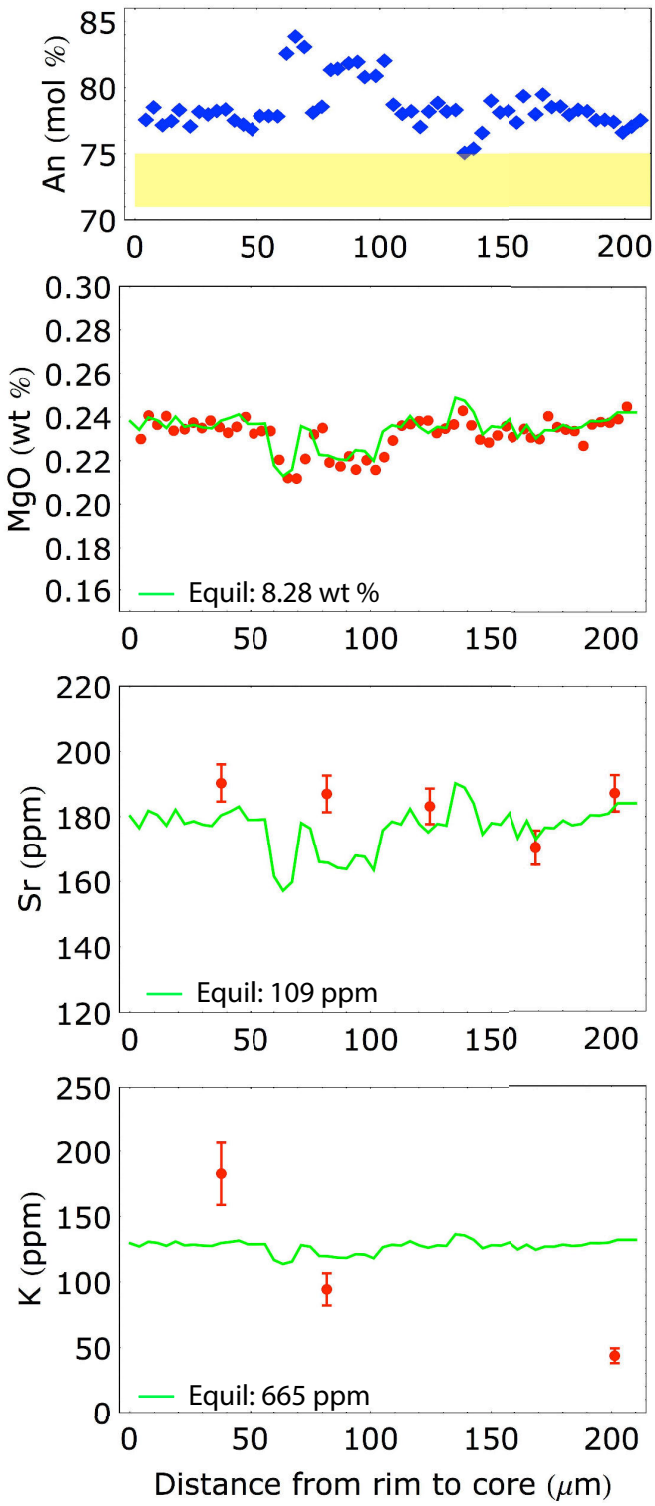
An (mol %)
85
80
75
70
0
50
100
150
200
MgO (wt %)
0.30
0.28
0.26
0.24
0.22
0.20
0.18
0.16
Equil: 8.28 wt %
Sr (ppm)
220
200
180
160
140
120
Equil: 109 ppm
K (ppm)
250
200
150
100
50
0
Equil: 665 ppm
Distance from rim to core (µm)

A.5.2.2: Sample 4202_1

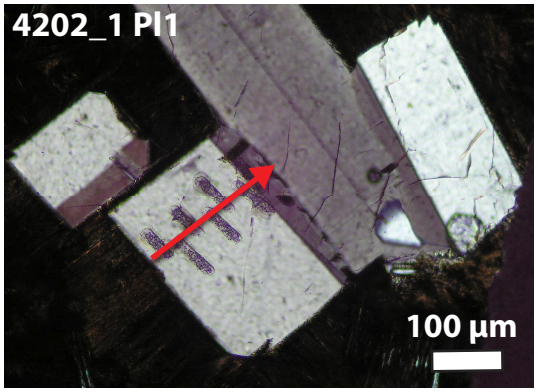

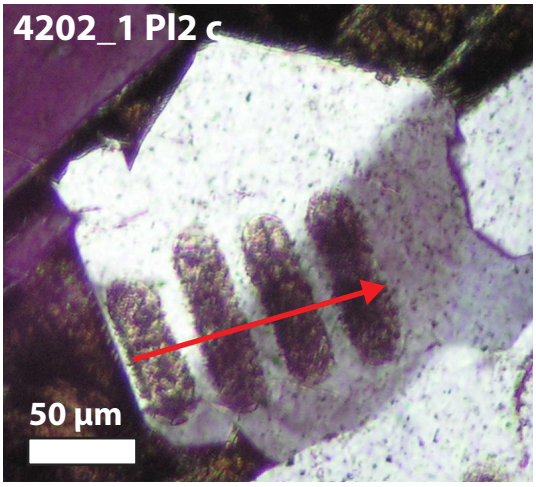

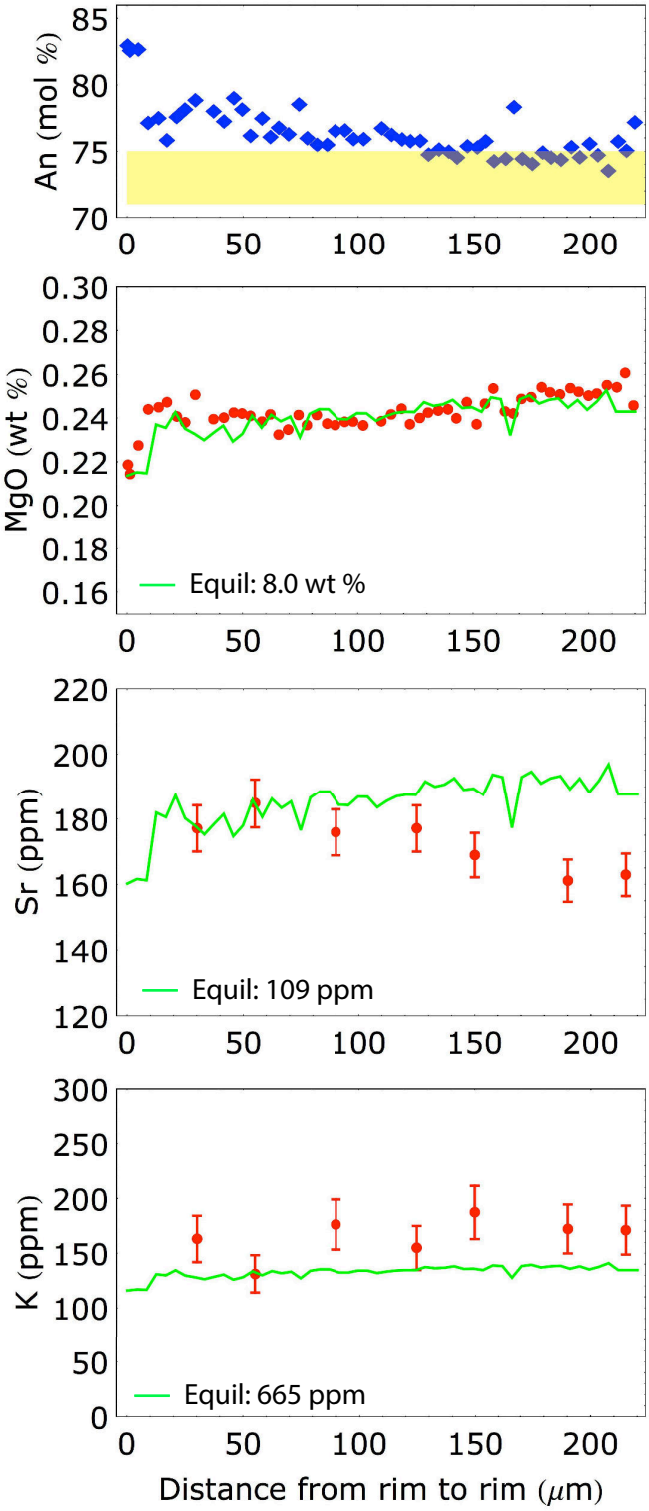

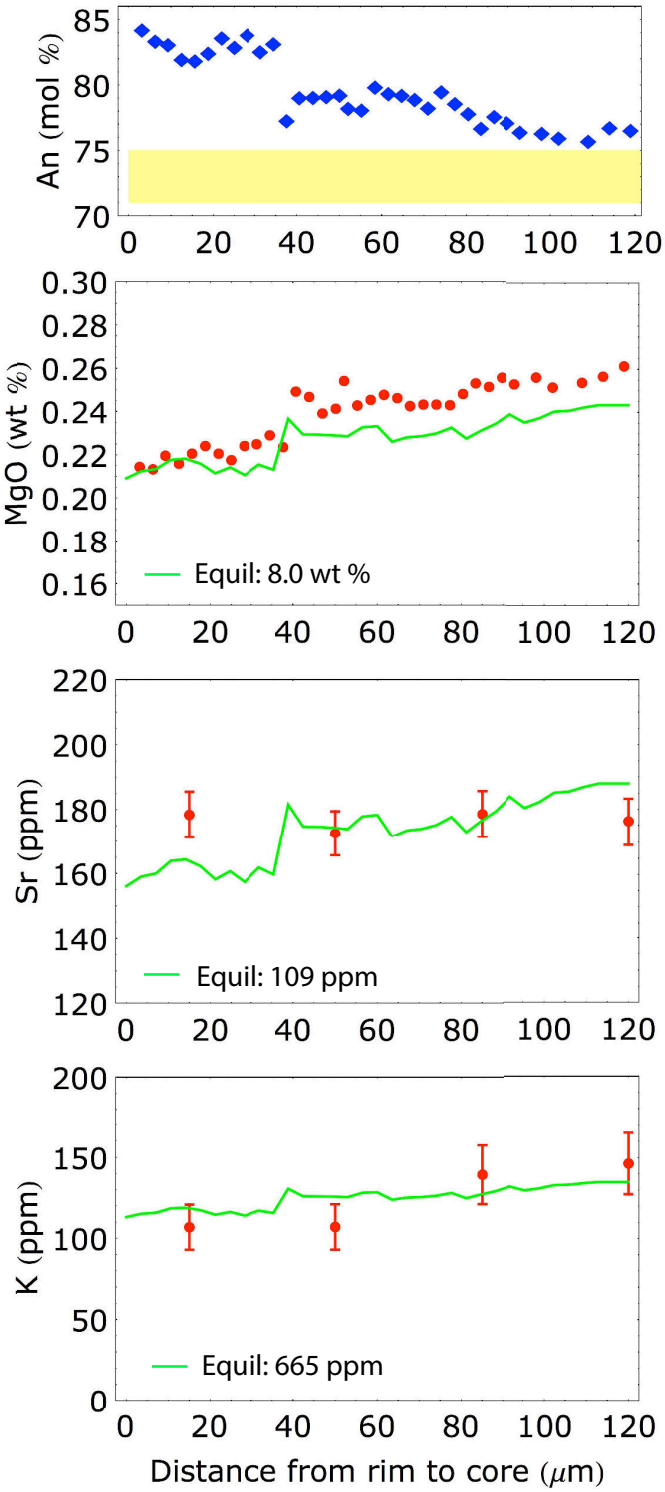

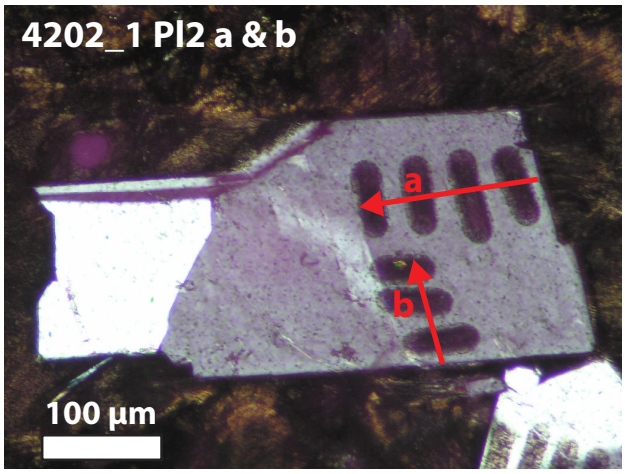
4202_1 Pl2 a & b
a
b
100 µm

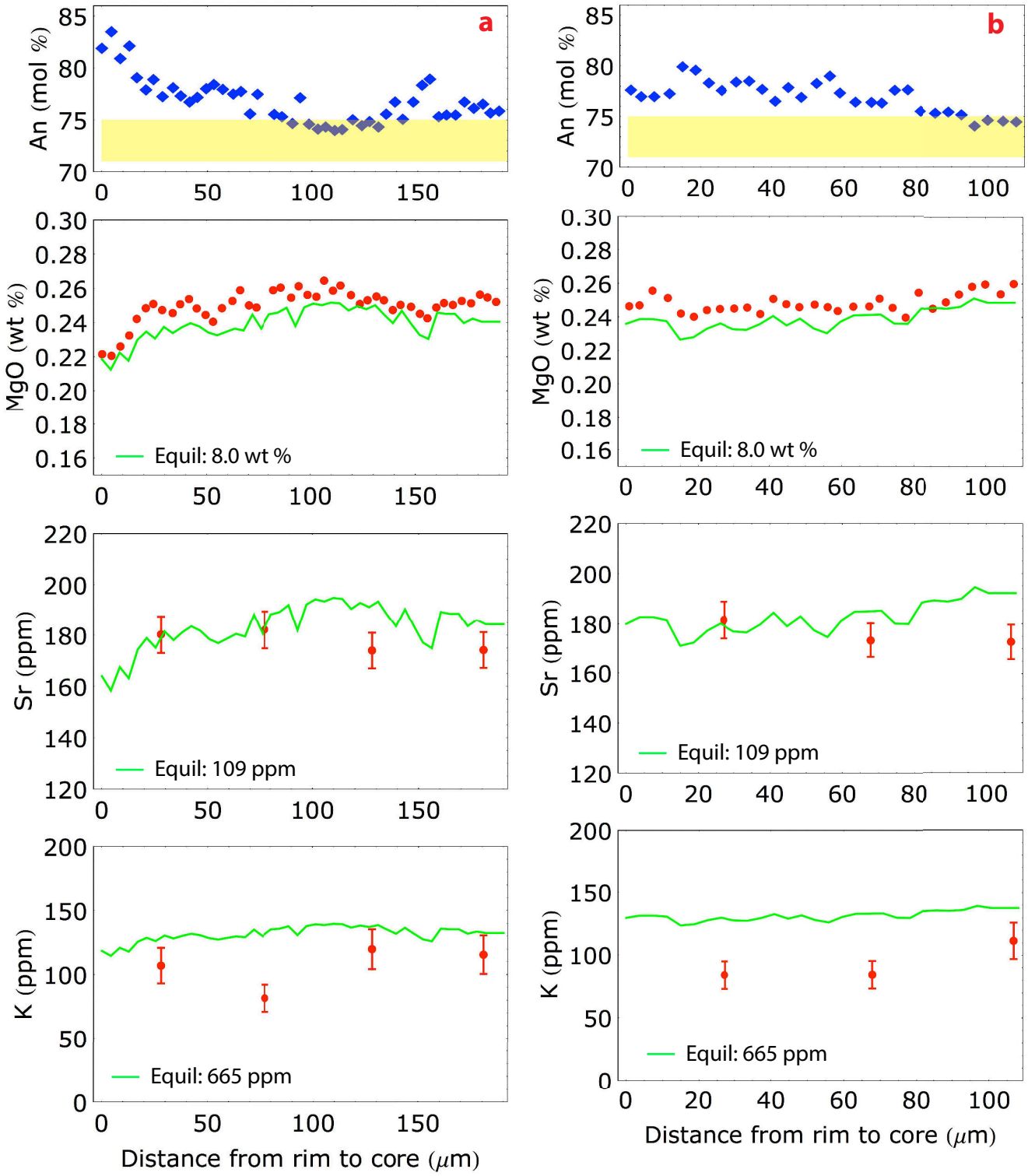
a
b
An (mol %)
MgO (wt %)
Sr (ppm)
K (ppm)
Equil: 8.0 wt %
Equil: 109 ppm
Equil: 665 ppm
Distance from rim to core (µm)

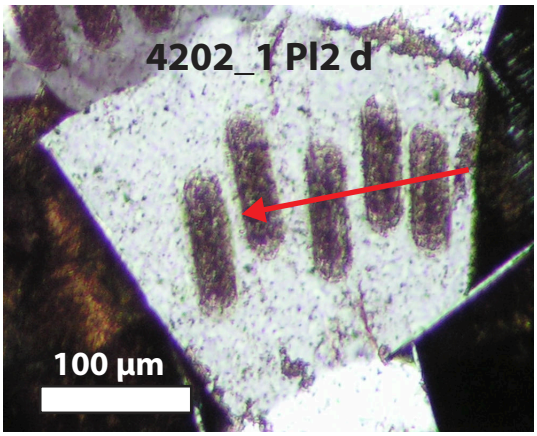
4202_1 Pl2 d
100 µm

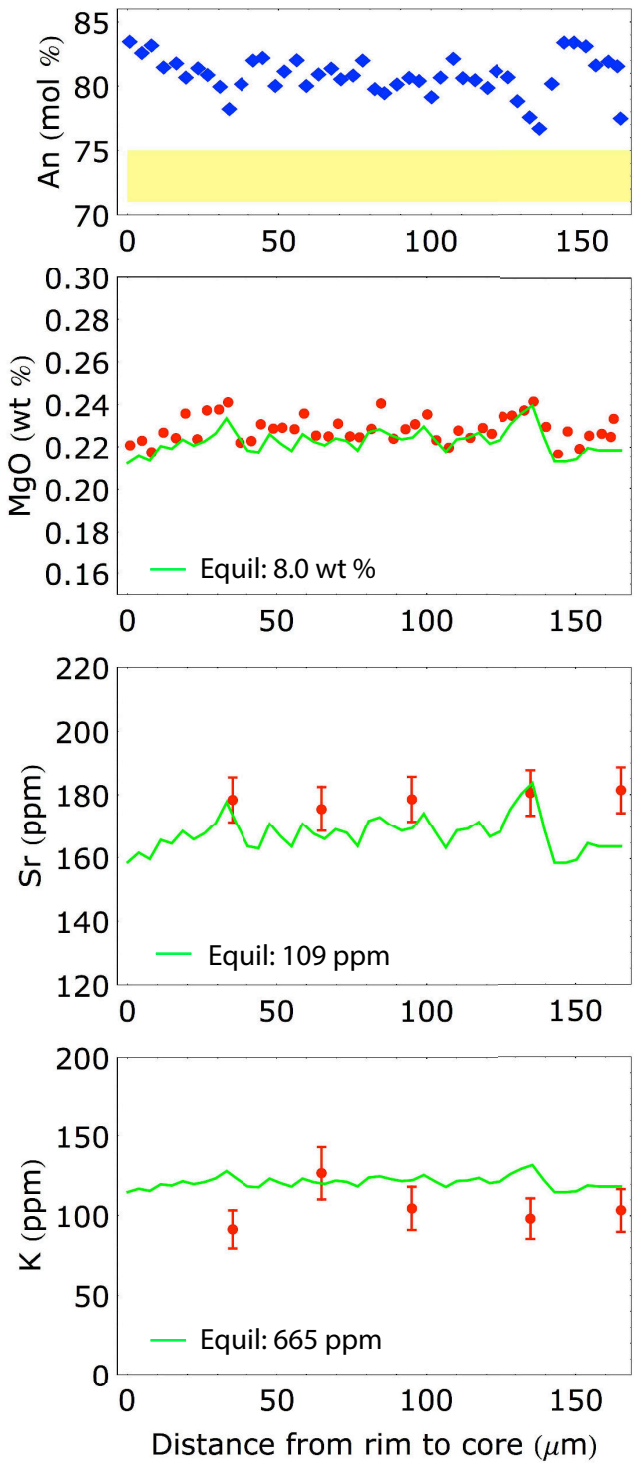
An (mol %)
85
80
75
70
0
50
100
150
MgO (wt %)
0.30
0.28
0.26
0.24
0.22
0.20
0.18
0.16
Equil: 8.0 wt %
Sr (ppm)
220
200
180
160
140
120
Equil: 109 ppm
K (ppm)
200
150
100
50
0
Equil: 665 ppm
Distance from rim to core (µm)

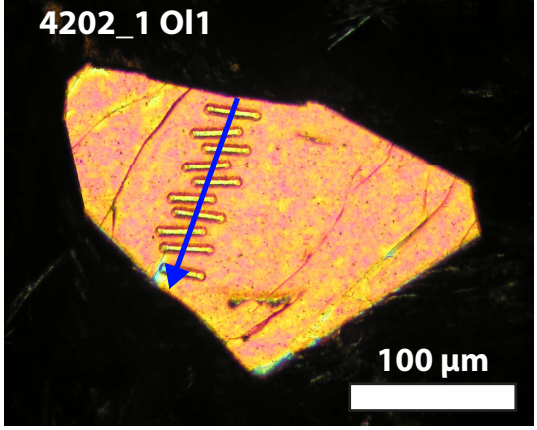
4202_1 Ol1
100 µm

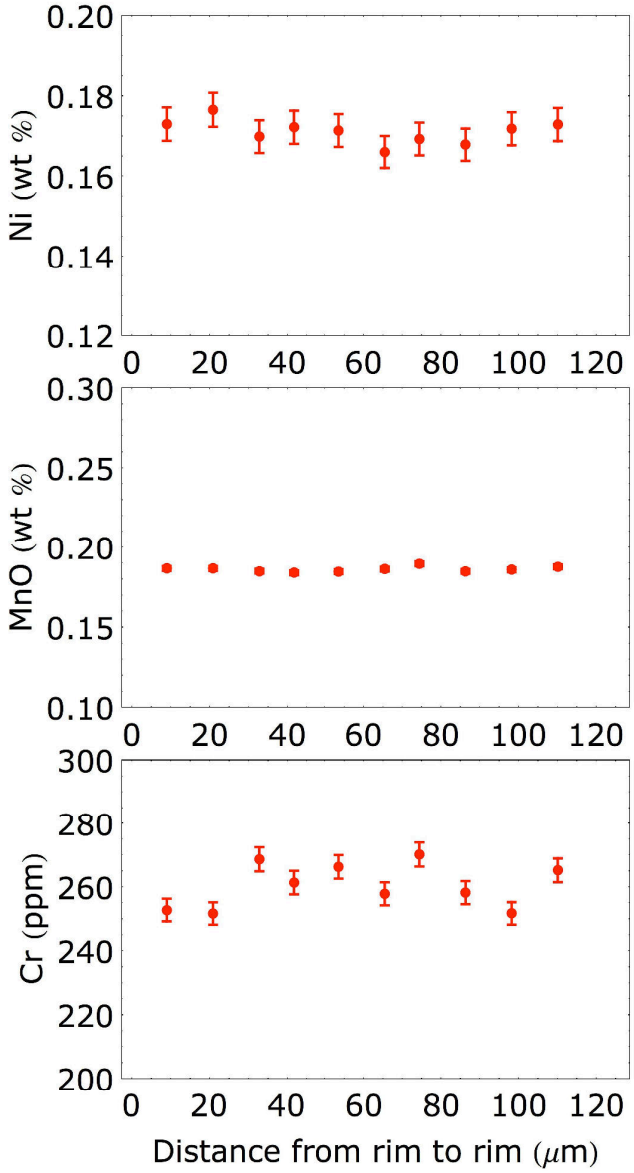
Ni (wt %)
0.20
0.18
0.16
0.14
0.12
MnO (wt %)
0.30
0.25
0.20
0.15
0.10
Cr (ppm)
300
280
260
240
220
200
0 20 40 60 80 100 120
Distance from rim to rim (µm)

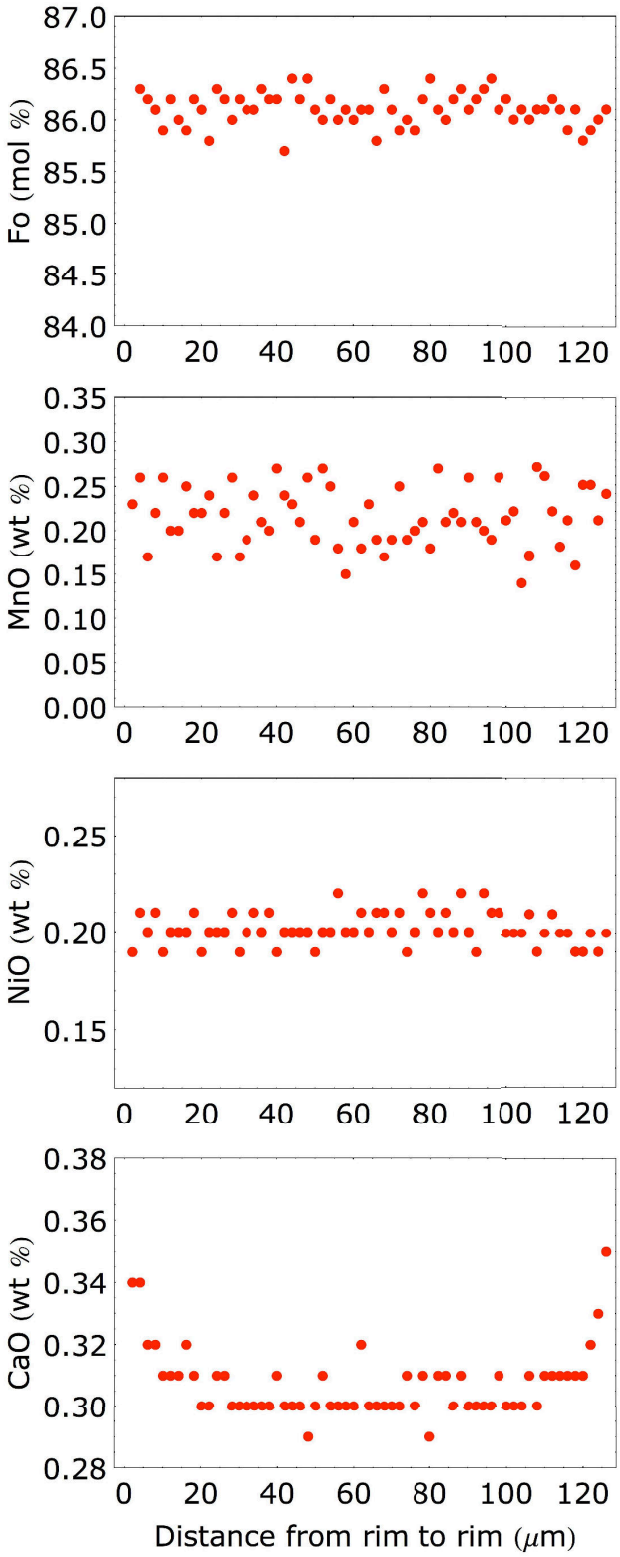
Fo (mol %)
87.0
86.5
86.0
85.5
85.0
84.5
84.0
MnO (wt %)
0.35
0.30
0.25
0.20
0.15
0.10
0.05
0.00
NiO (wt %)
0.25
0.20
0.15
CaO (wt %)
0.38
0.36
0.34
0.32
0.30
0.28
0 20 40 60 80 100 120
Distance from rim to rim (µm)

A.5.2.3: Sample 4203_2

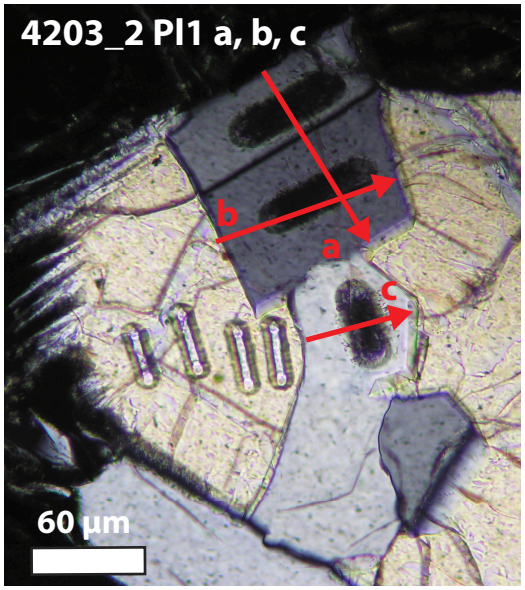

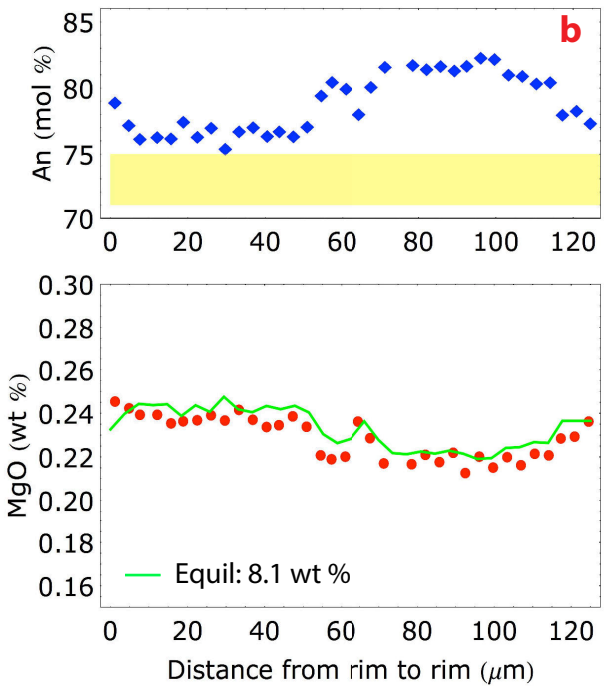

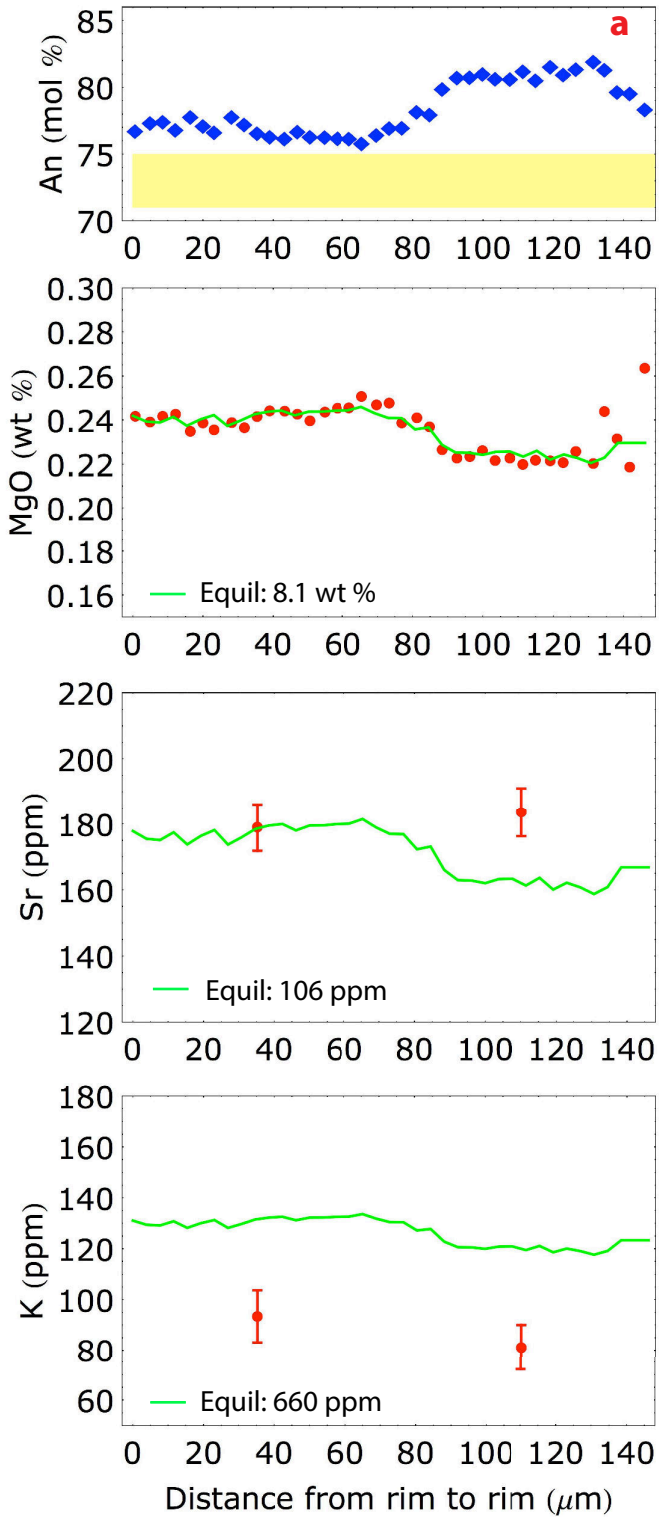

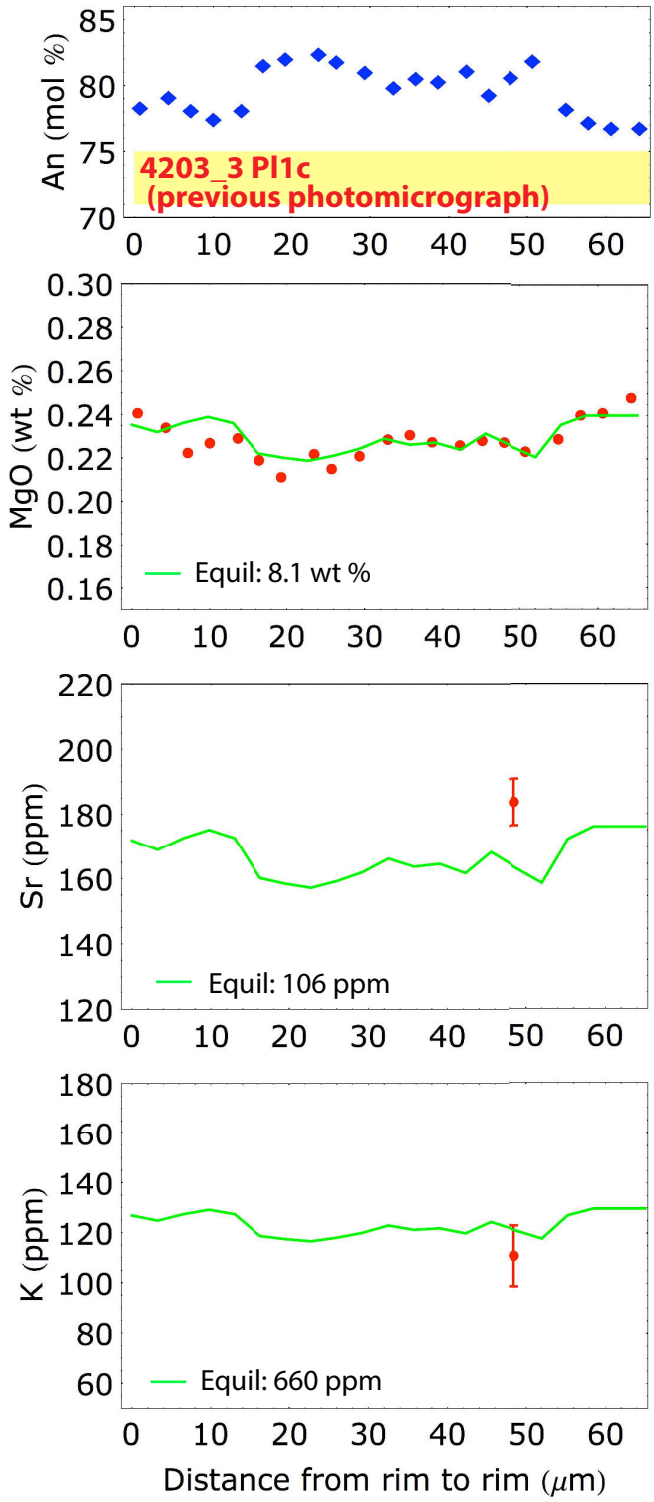
4203_3 Pl1c
(previous photomicrograph)
An (mol %)
MgO (wt %)
Equil: 8.1 wt %
Sr (ppm)
Equil: 106 ppm
K (ppm)
Equil: 660 ppm
Distance from rim to rim (μm)

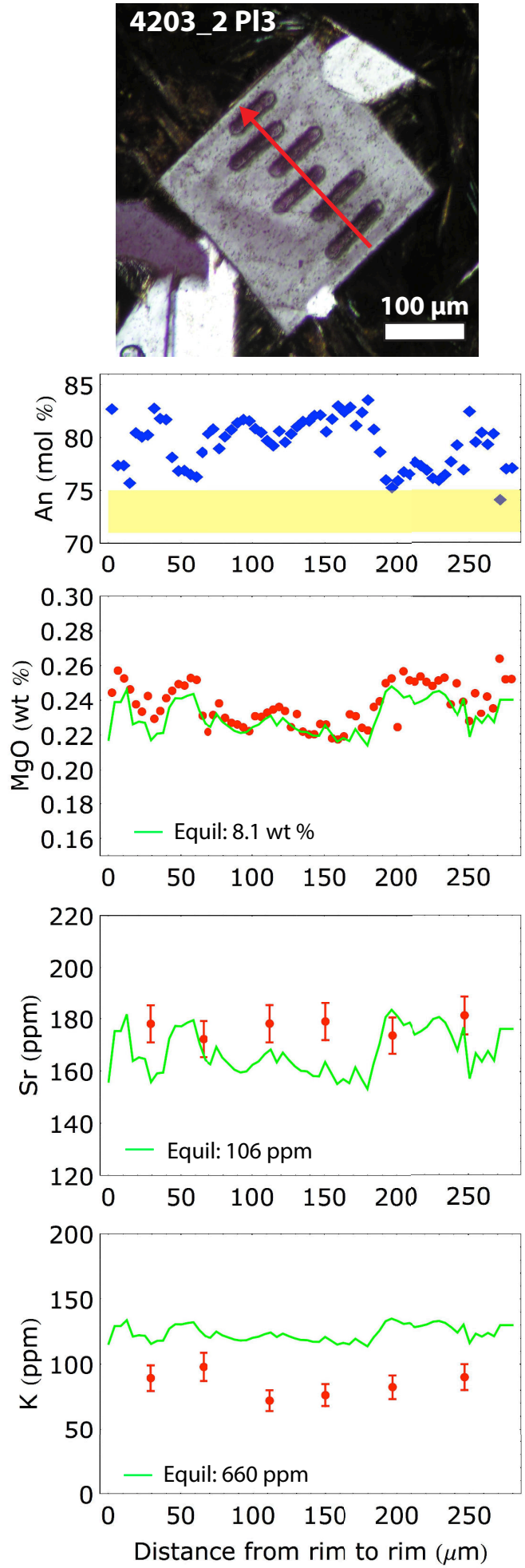
4203_2 Pl3
100 μm
An (mol %)
MgO (wt %)
Equil: 8.1 wt %
Sr (ppm)
Equil: 106 ppm
K (ppm)
Equil: 660 ppm
Distance from rim to rim (μm)

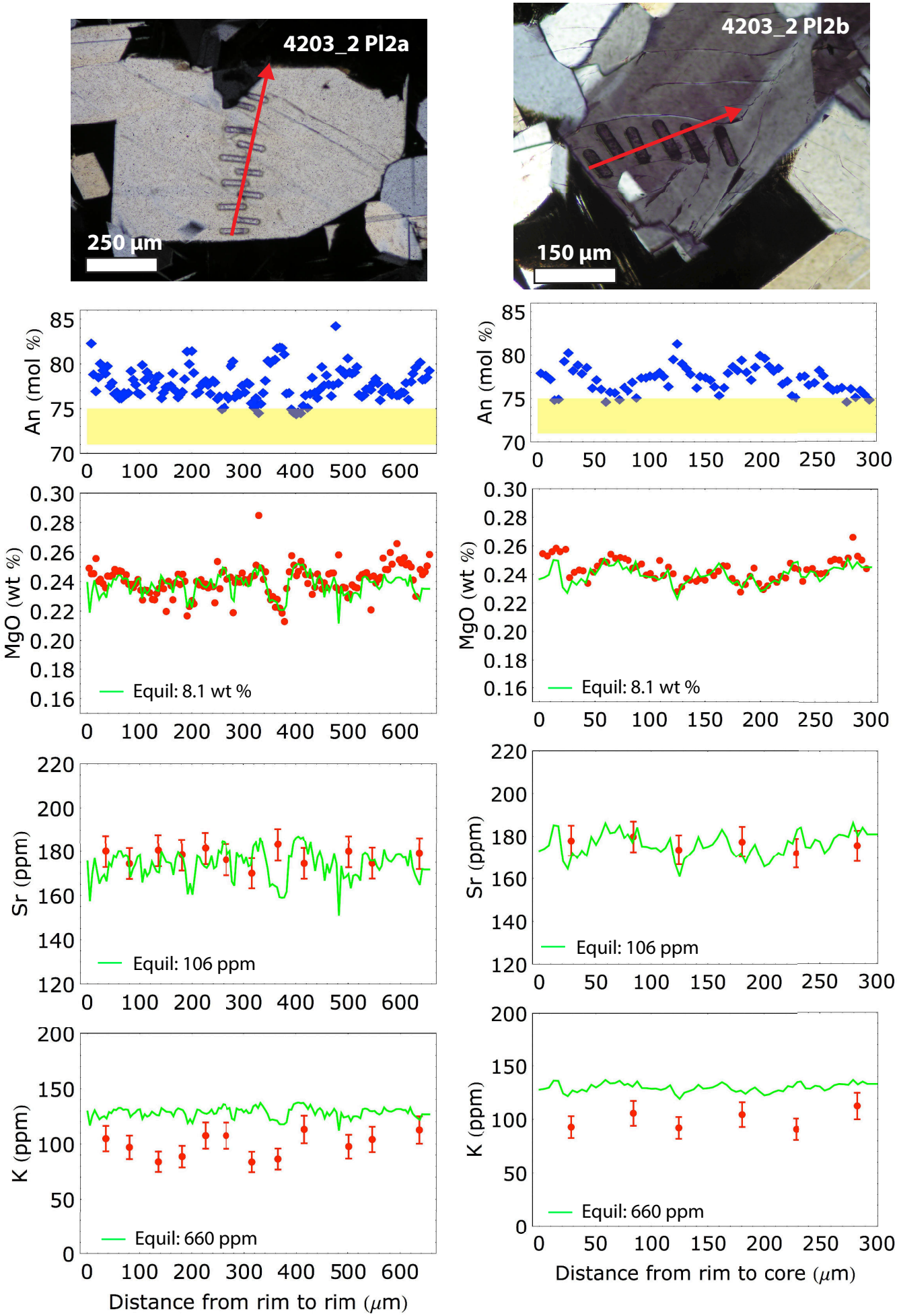
4203_2 Pl2a
250 µm
4203_2 Pl2b
150 µm
An (mol %)
MgO (wt %)
Equil: 8.1 wt %
Sr (ppm)
Equil: 106 ppm
K (ppm)
Equil: 660 ppm
Distance from rim to rim (µm)
Distance from rim to core (µm)

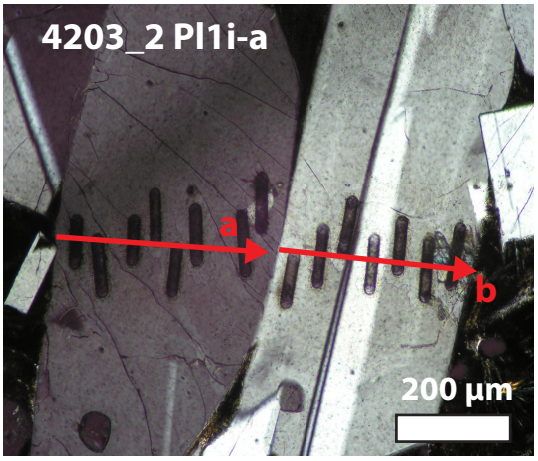
4203_2 Pl1i-a
a
b
200 µm

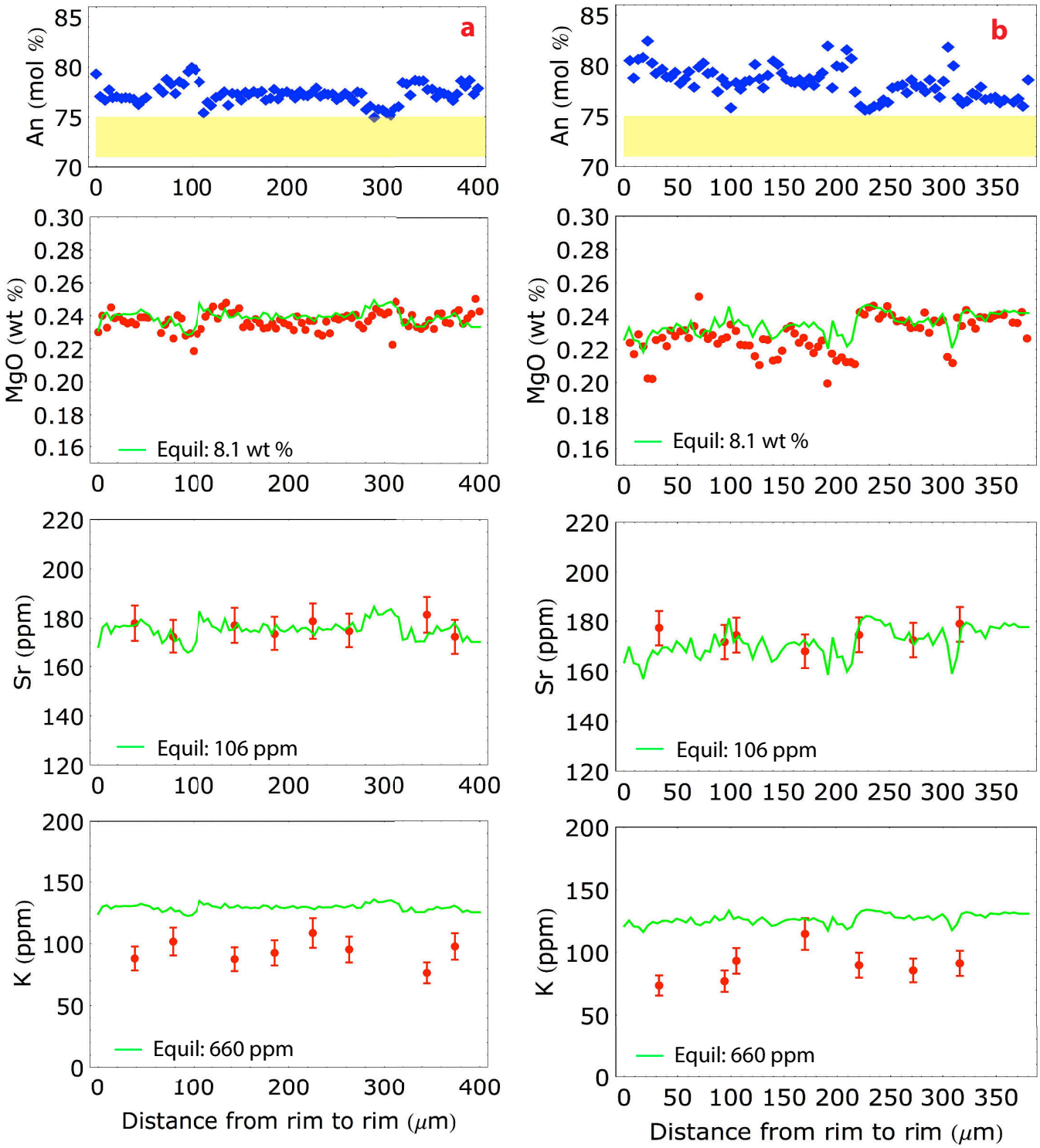
a
b
An (mol %)
MgO (wt %)
Equil: 8.1 wt %
Sr (ppm)
Equil: 106 ppm
K (ppm)
Equil: 660 ppm
Distance from rim to rim (µm)

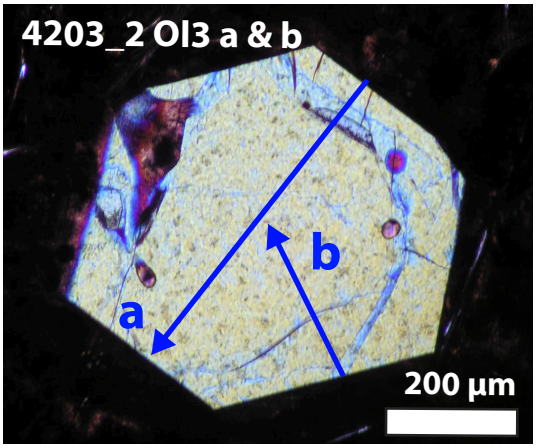
4203_2 Ol3 a & b
a
b
200 µm

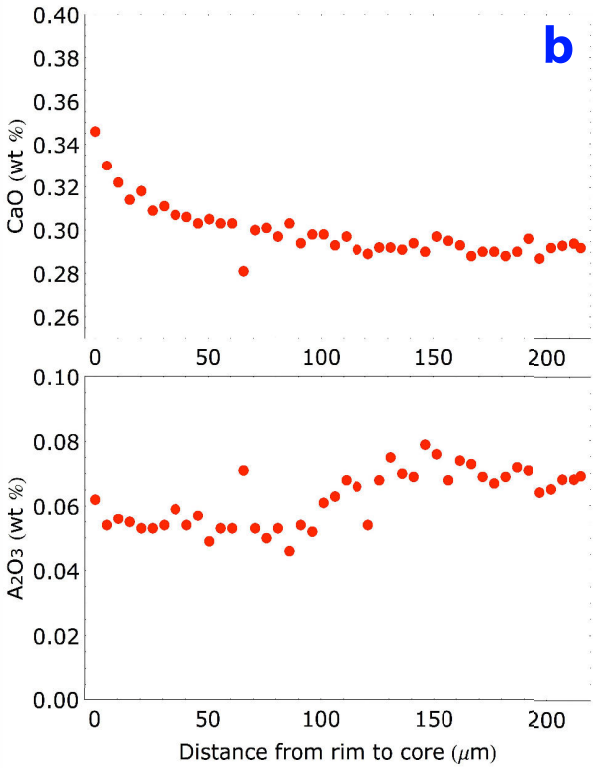
b
CaO (wt %)
0.40
0.38
0.36
0.34
0.32
0.30
0.28
0.26
0
50
100
150
200
A2O3 (wt %)
0.10
0.08
0.06
0.04
0.02
0.00
Distance from rim to core (µm)

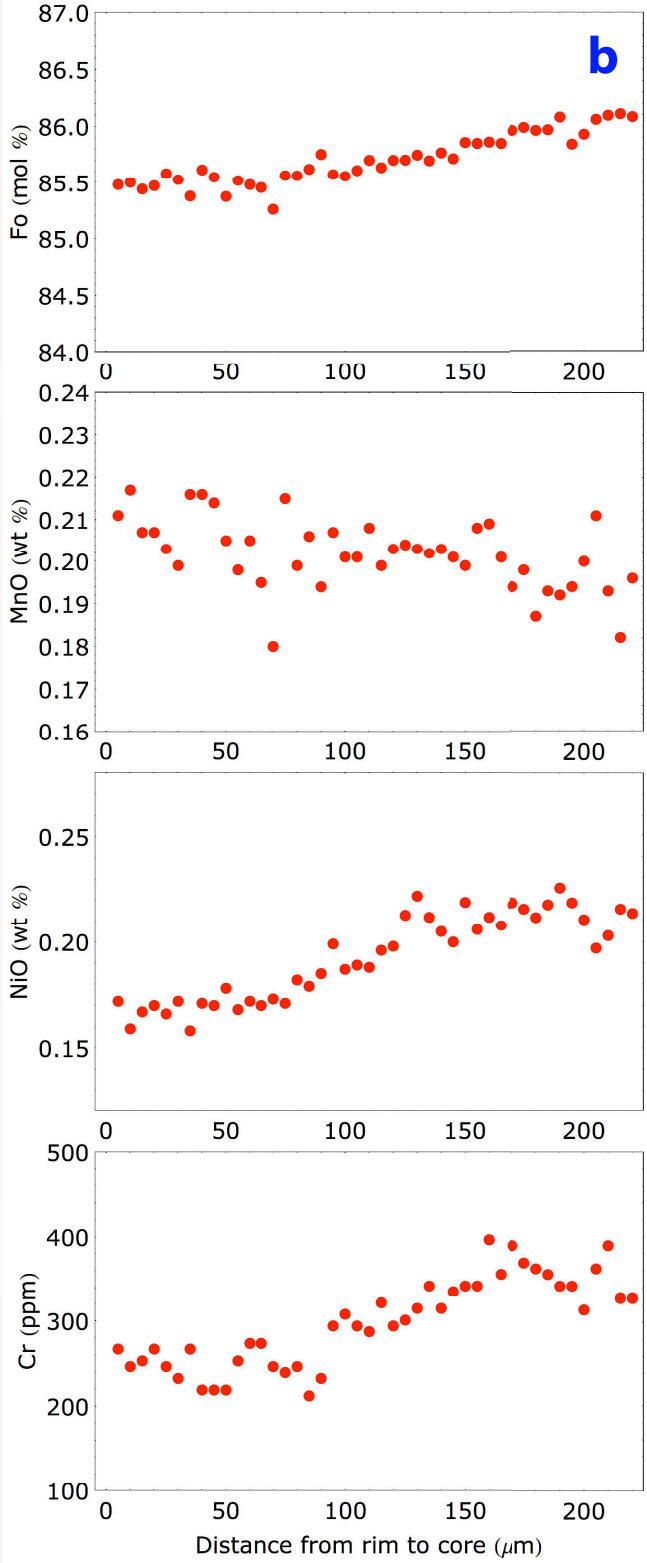
b
Fo (mol %)
87.0
86.5
86.0
85.5
85.0
84.5
84.0
MnO (wt %)
0.24
0.23
0.22
0.21
0.20
0.19
0.18
0.17
0.16
NiO (wt %)
0.25
0.20
0.15
Cr (ppm)
500
400
300
200
100
0
50
100
150
200
Distance from rim to core (µm)

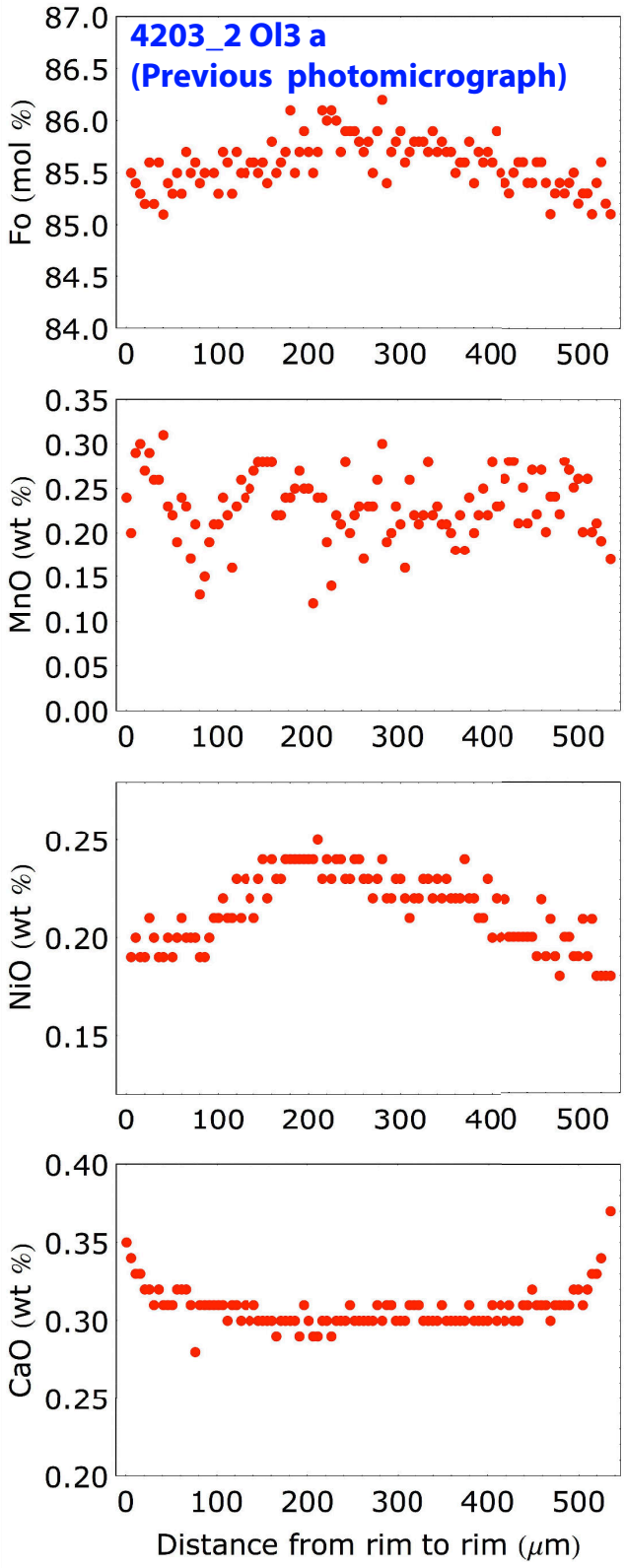
4203_2 Ol3 a
(Previous photomicrograph)
Fo (mol %)
87.0
86.5
86.0
85.5
85.0
84.5
84.0
MnO (wt %)
0.35
0.30
0.25
0.20
0.15
0.10
0.05
0.00
NiO (wt %)
0.25
0.20
0.15
CaO (wt %)
0.40
0.35
0.30
0.25
0.20
0
100
200
300
400
500
Distance from rim to rim (μm)

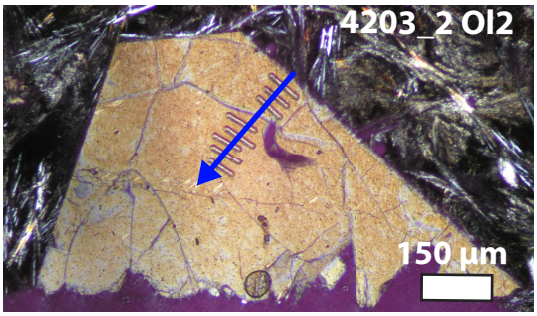
4203_2 Ol2
150 µm

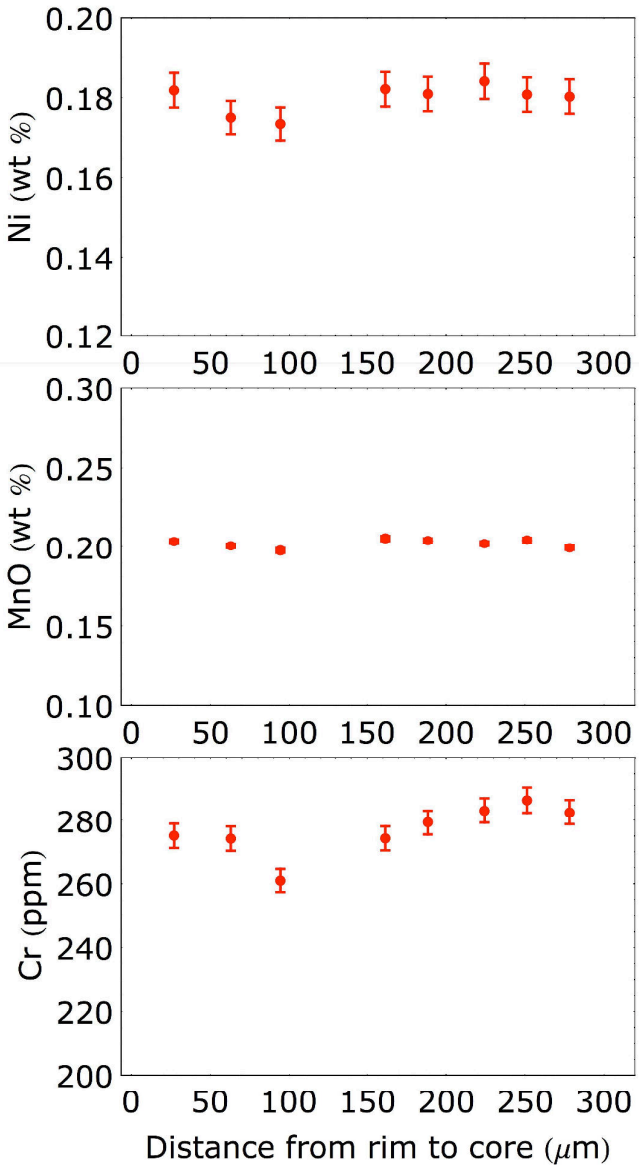
Ni (wt %)
MnO (wt %)
Cr (ppm)
Distance from rim to core (µm)

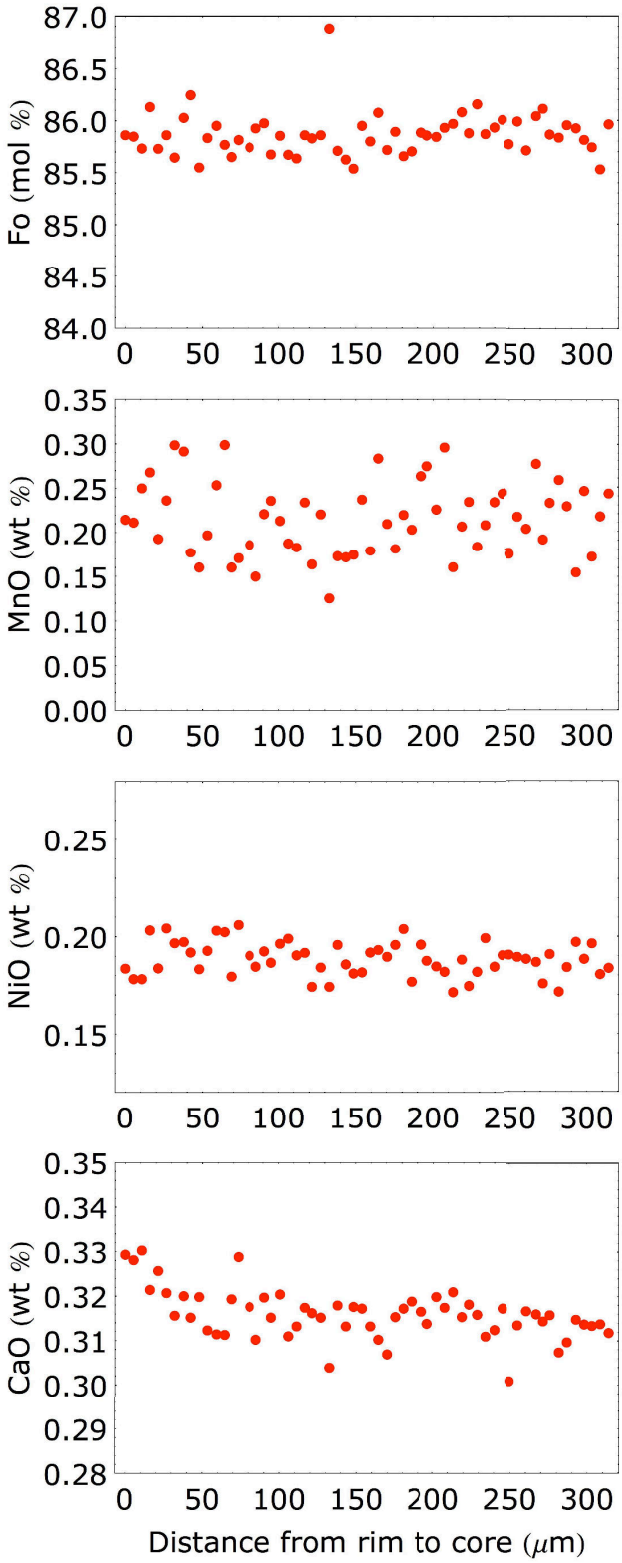
Fo (mol %)
MnO (wt %)
NiO (wt %)
CaO (wt %)
Distance from rim to core (µm)

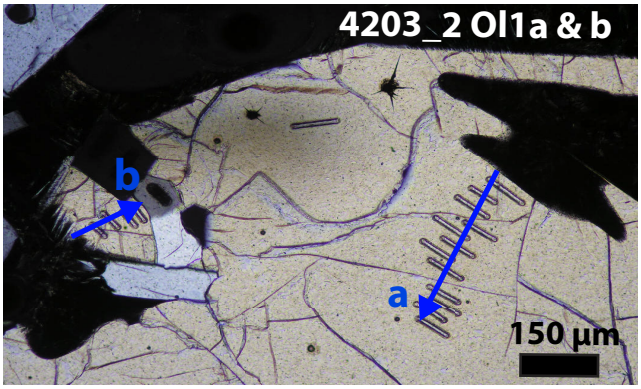
4203_2 Ol1a & b
b
a
150 µm

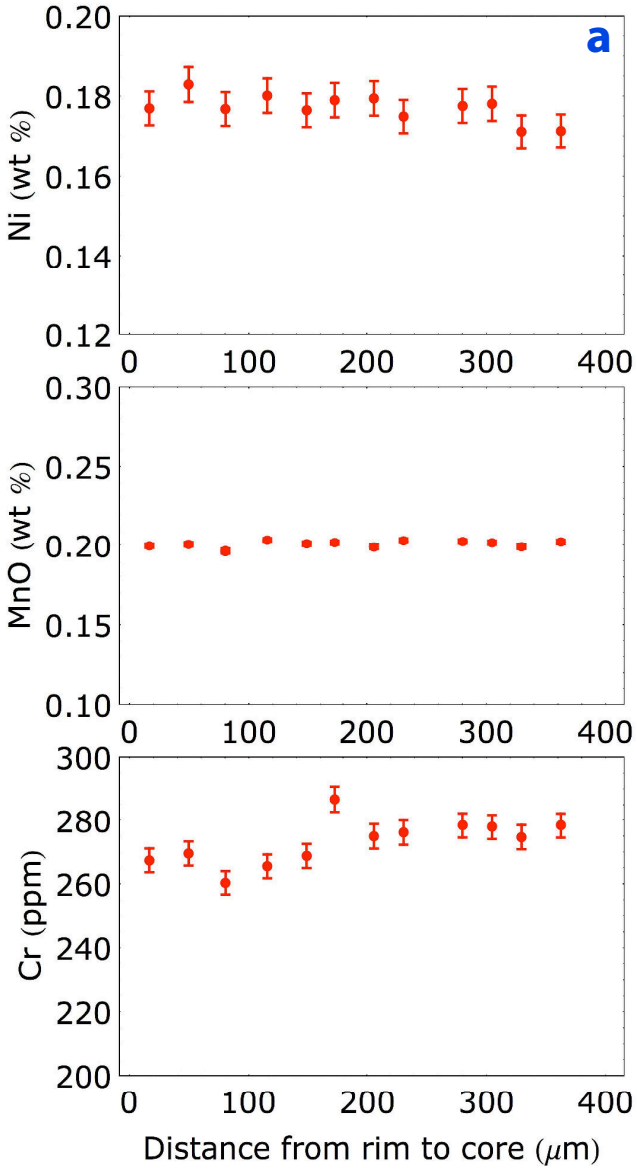
a
Ni (wt %)
MnO (wt %)
Cr (ppm)
Distance from rim to core (µm)

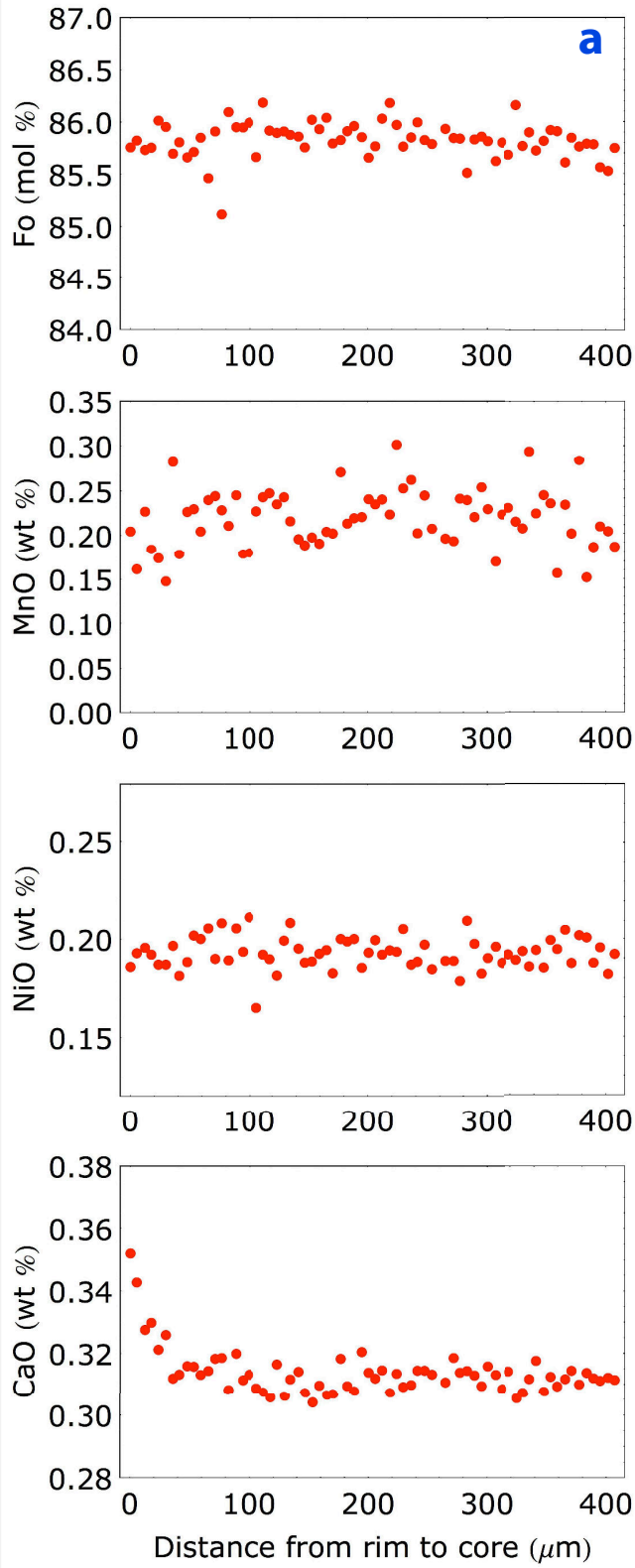
a
Fo (mol %)
MnO (wt %)
NiO (wt %)
CaO (wt %)
Distance from rim to core (µm)

4203_2 Ol1 b
(Previous photomicrograph)

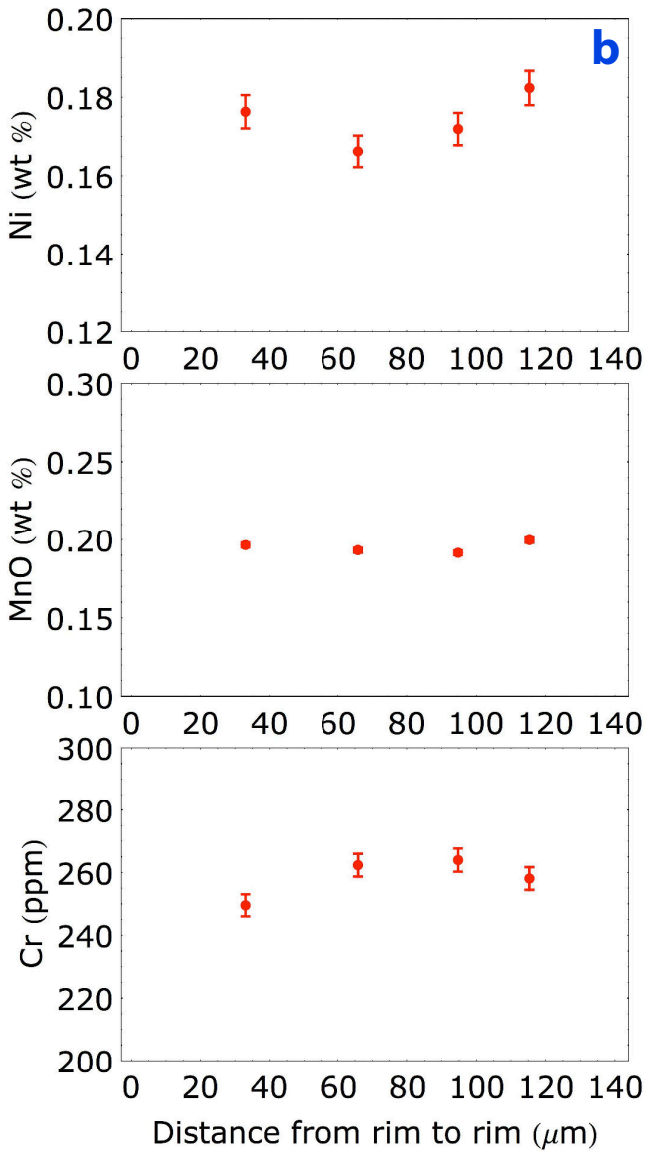

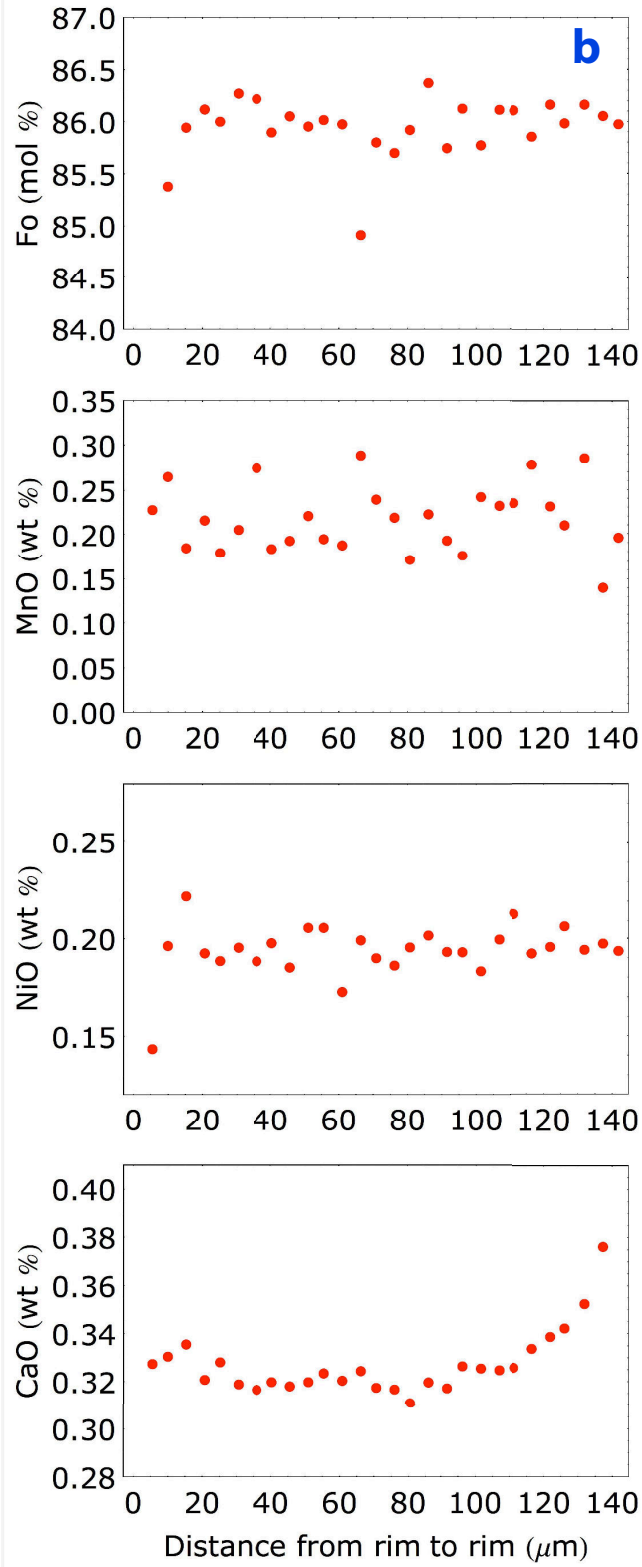

A.5.2.4: Sample 4202_6

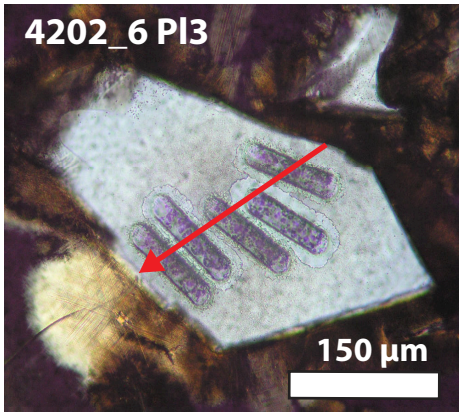

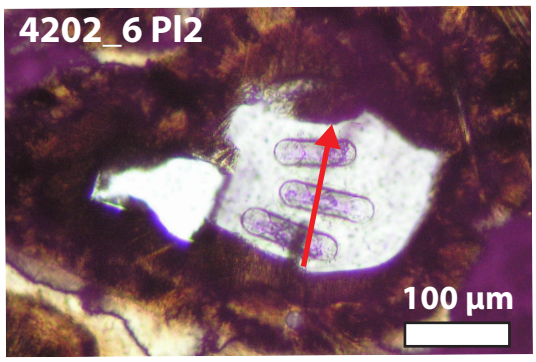

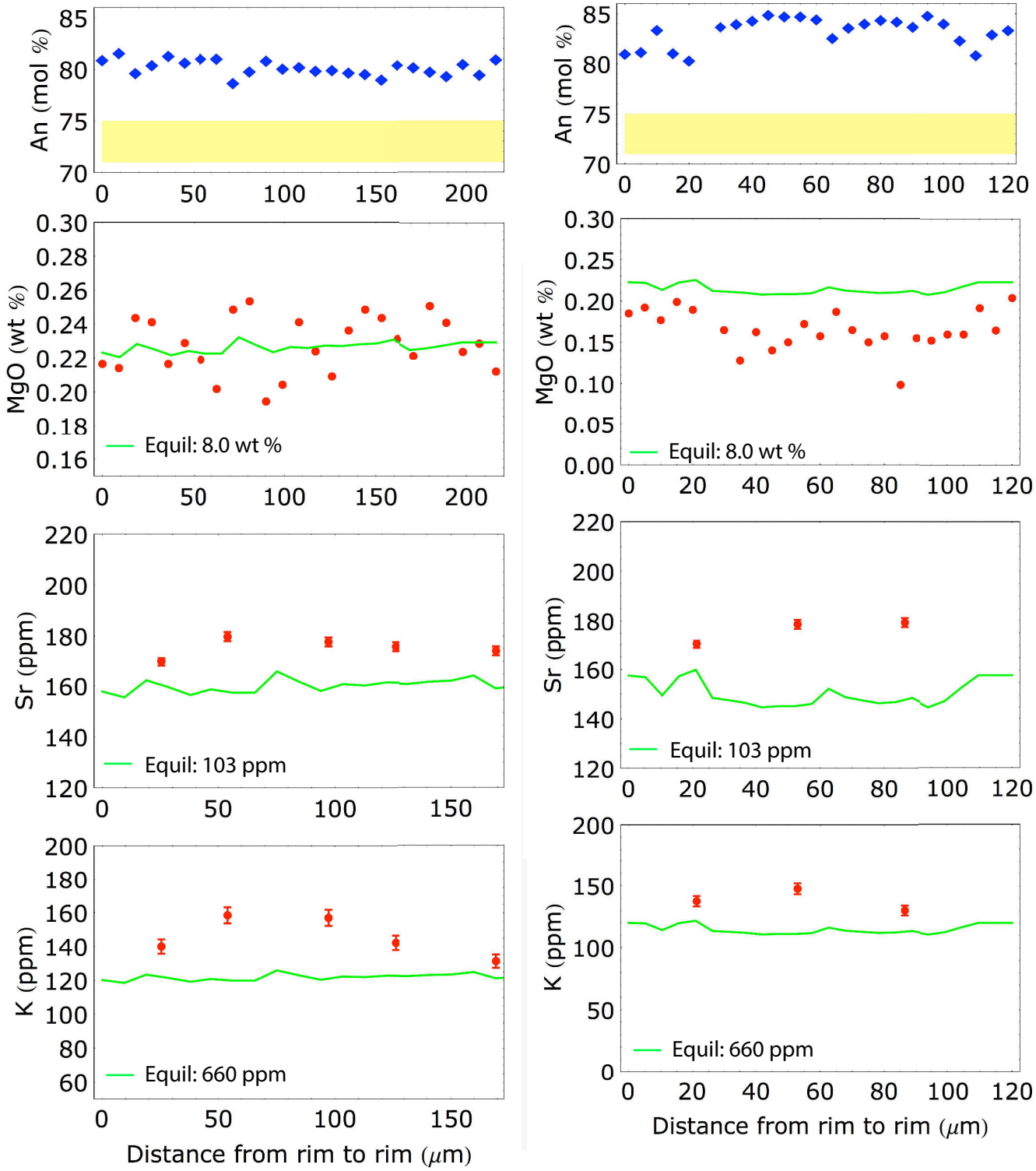

A.5.3: Southern Fissure

A.5.3.1: Sample 4205_5

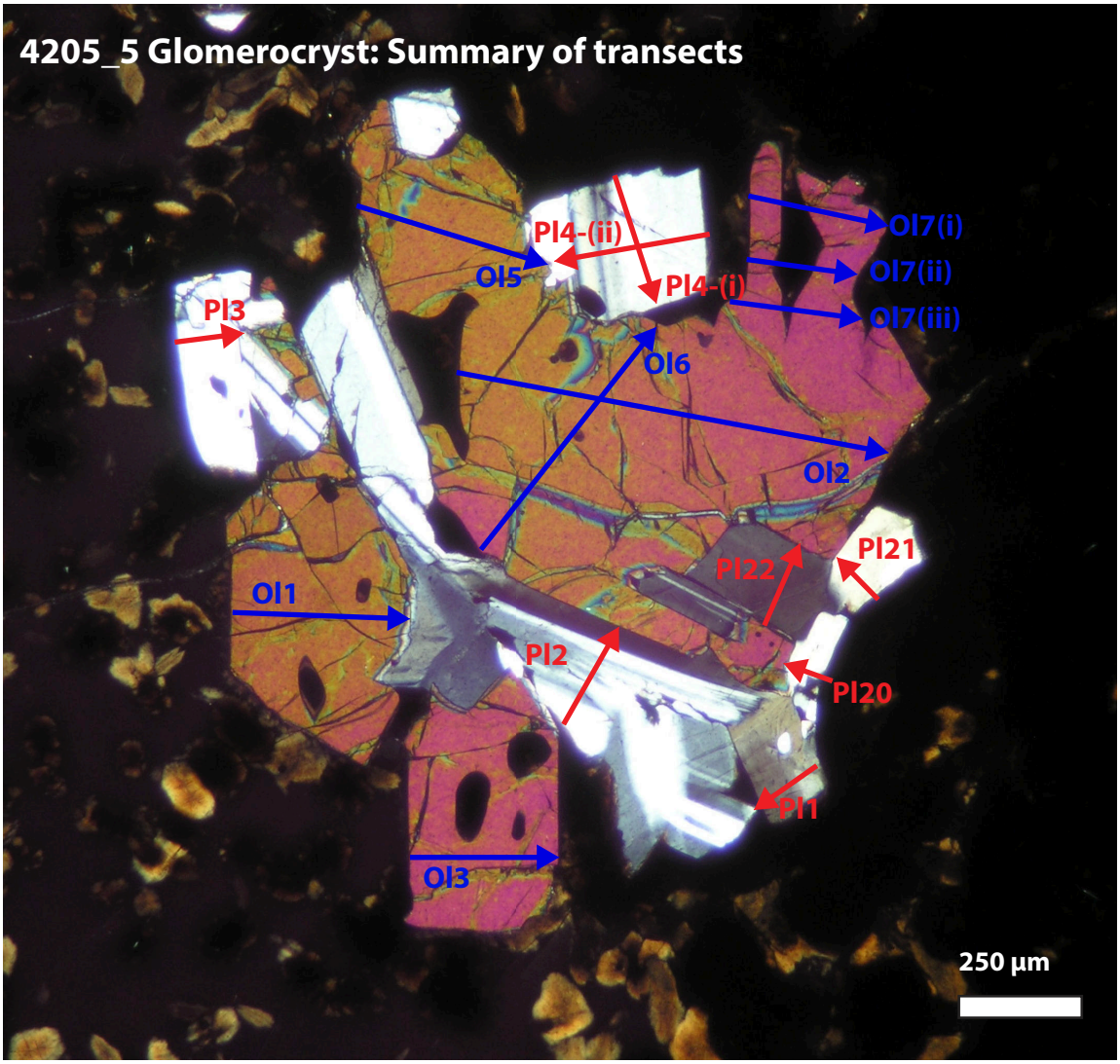

The above photomicrograph shows the glomerocryst from the Southern Fissure. The red and blue arrows represent the transects through plagioclase and olivine. The following twelve photomicrographs (A to L) show a close up of the individual transects with their underlying major and trace element profiles.

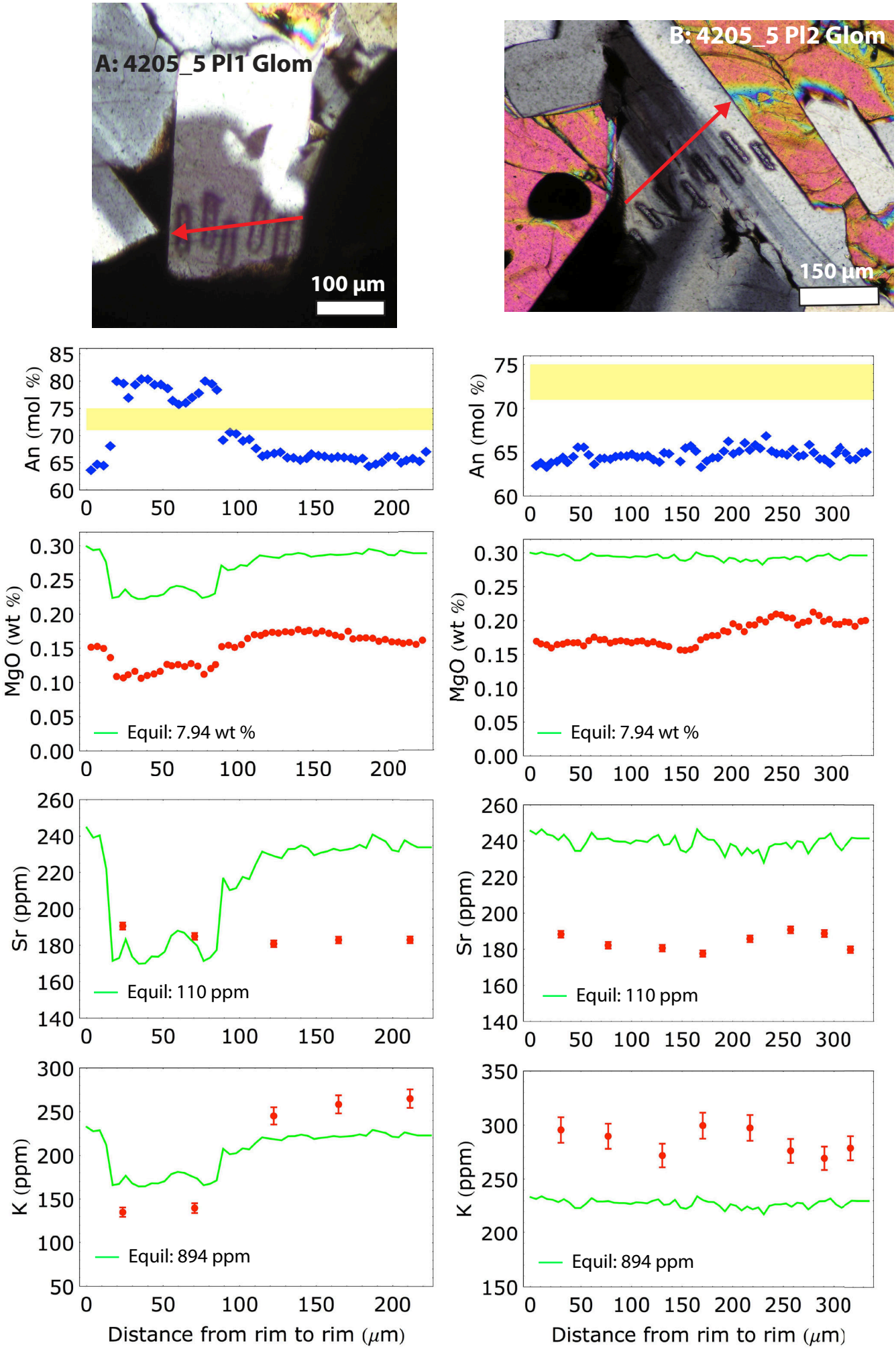
A: 4205_5 Pl1 Glom
100 µm
B: 4205_5 Pl2 Glom
150 µm
An (mol %)
MgO (wt %)
Equil: 7.94 wt %
Sr (ppm)
Equil: 110 ppm
K (ppm)
Equil: 894 ppm
Distance from rim to rim (µm)

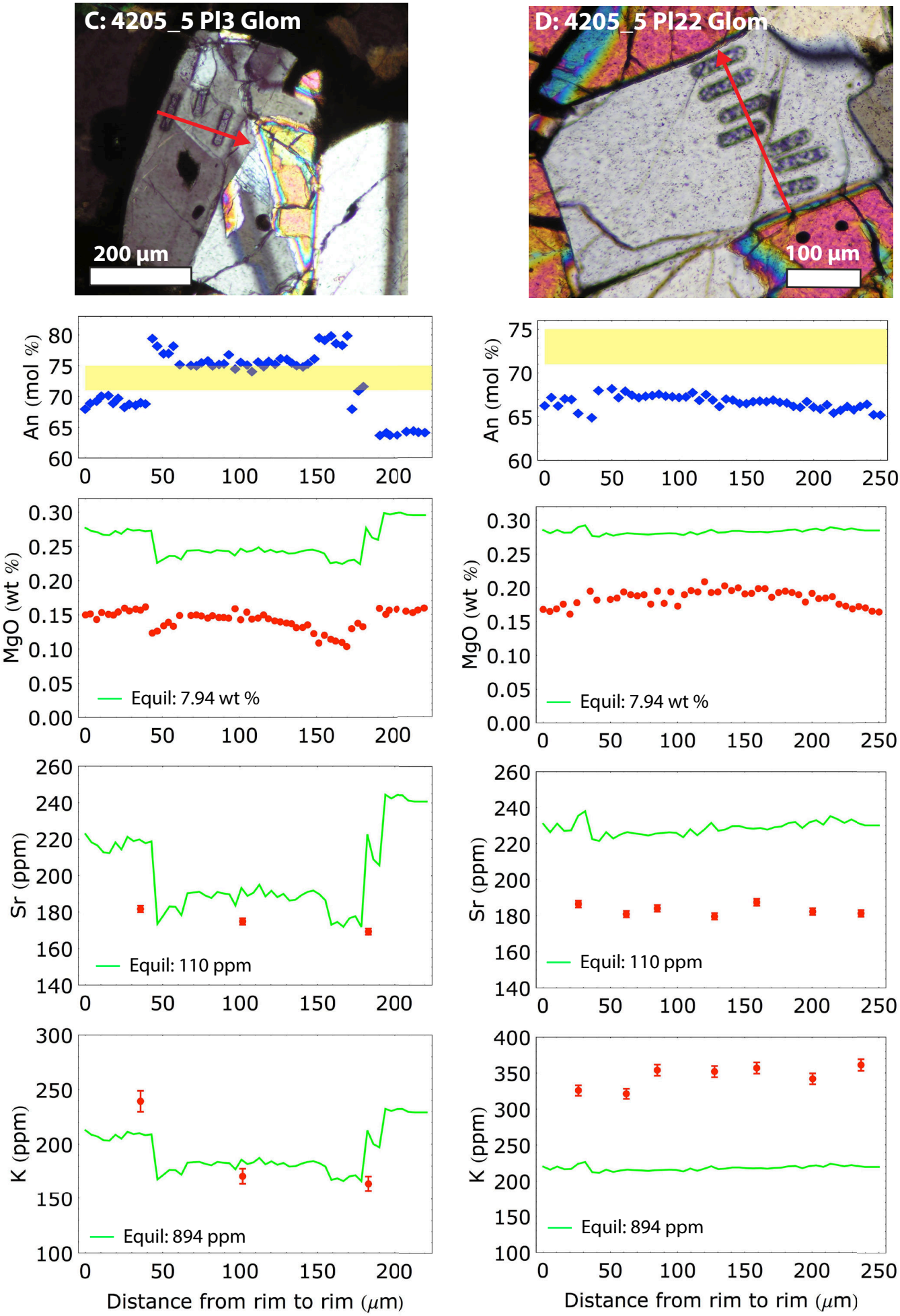
C: 4205_5 Pl3 Glom
200 µm
D: 4205_5 Pl22 Glom
100 µm
An (mol %)
MgO (wt %)
Equil: 7.94 wt %
Sr (ppm)
Equil: 110 ppm
K (ppm)
Equil: 894 ppm
Distance from rim to rim (µm)

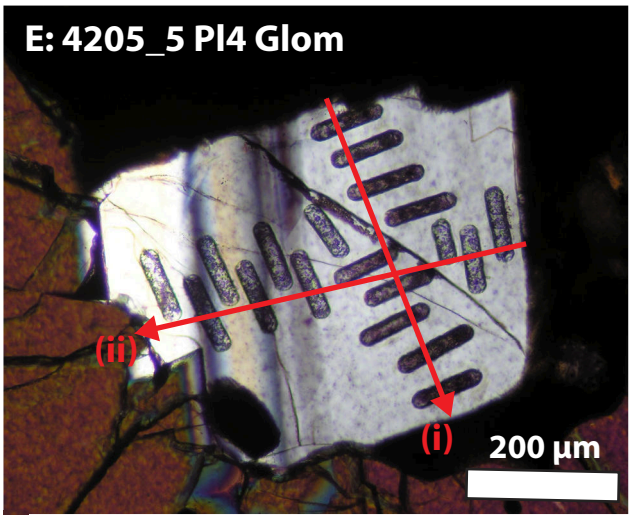
E: 4205_5 Pl4 Glom
(ii)
(i)
200 µm

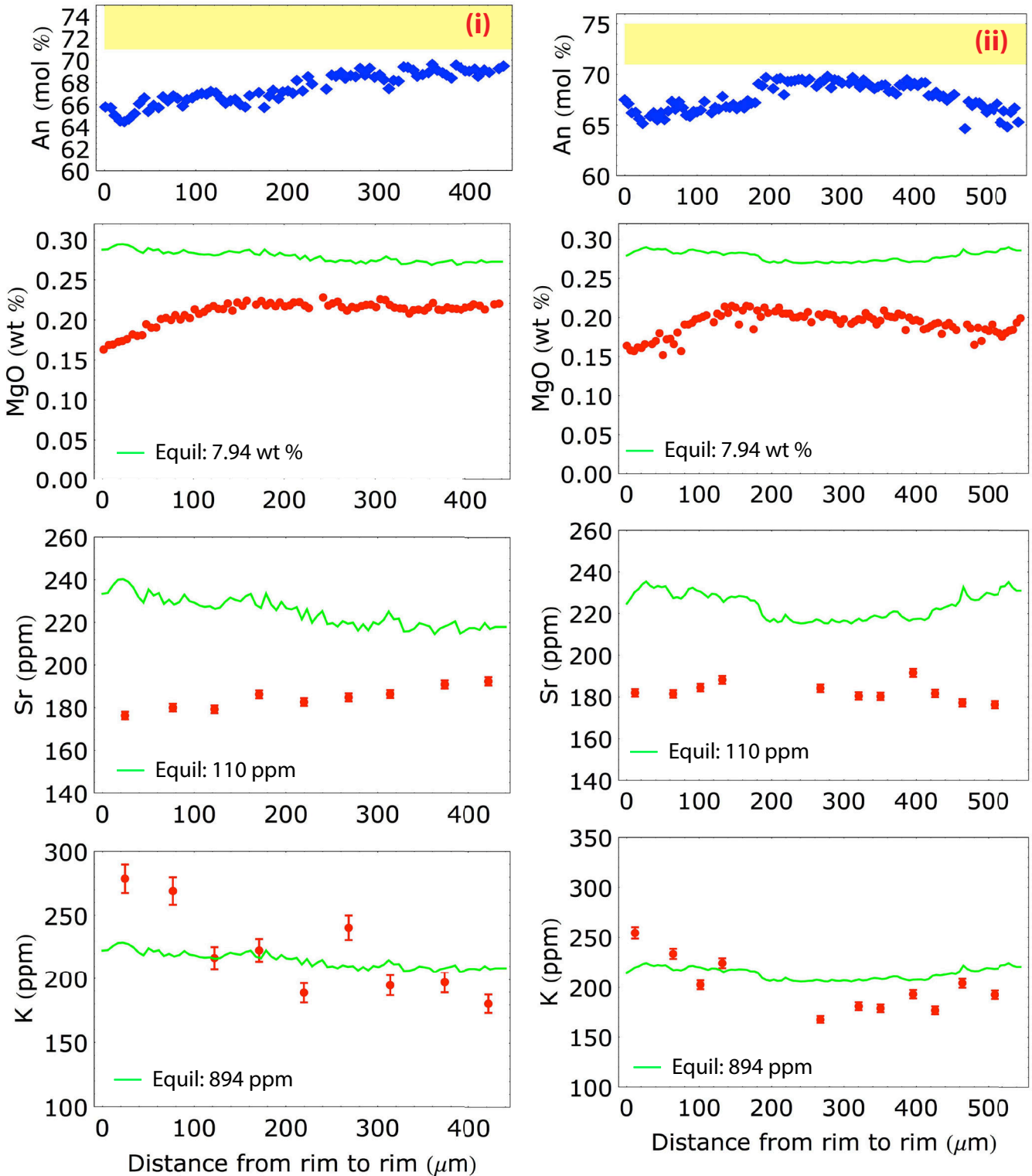
(i)
(ii)
An (mol %)
MgO (wt %)
Sr (ppm)
K (ppm)
Equil: 7.94 wt %
Equil: 110 ppm
Equil: 894 ppm
Distance from rim to rim (µm)

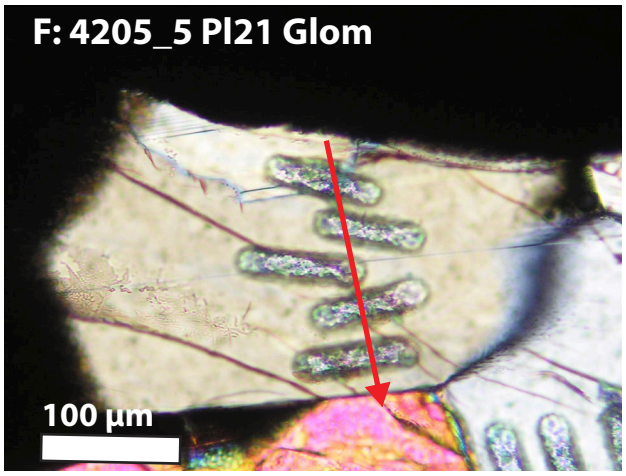
F: 4205_5 Pl21 Glom
100 µm

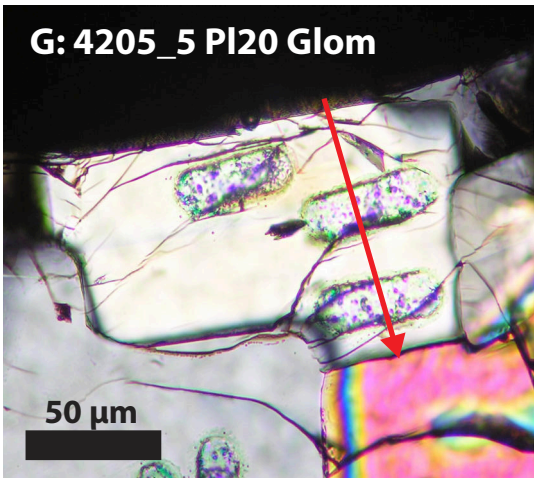
G: 4205_5 Pl20 Glom
50 µm

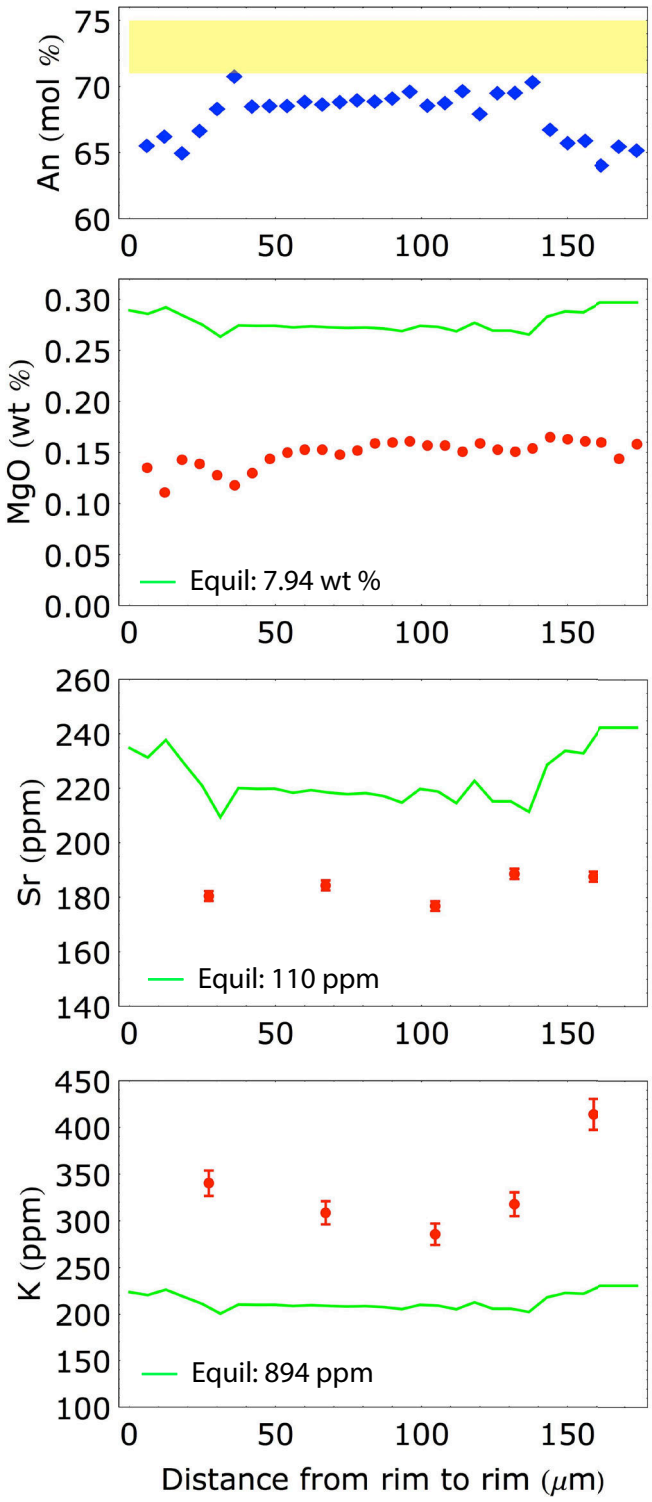
An (mol %)
MgO (wt %)
Equil: 7.94 wt %
Sr (ppm)
Equil: 110 ppm
K (ppm)
Equil: 894 ppm
Distance from rim to rim (µm)

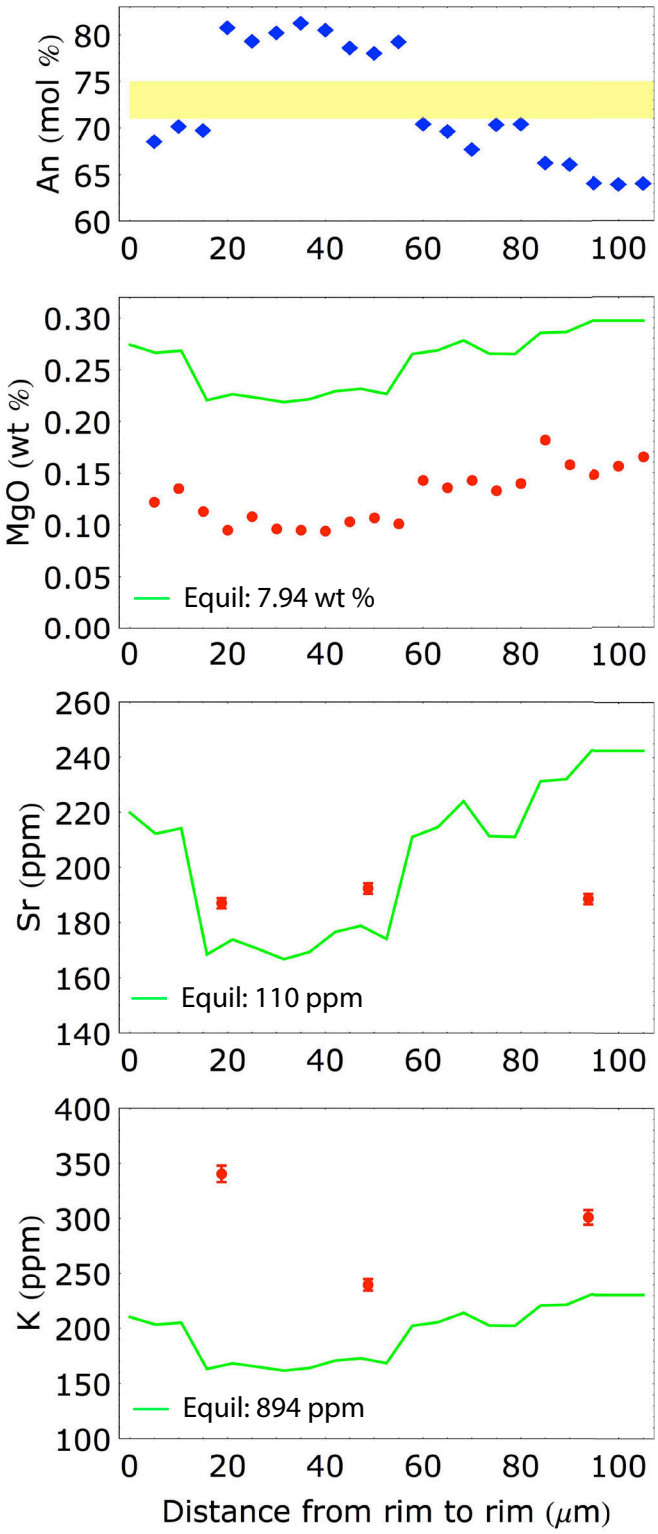
An (mol %)
MgO (wt %)
Equil: 7.94 wt %
Sr (ppm)
Equil: 110 ppm
K (ppm)
Equil: 894 ppm
Distance from rim to rim (µm)

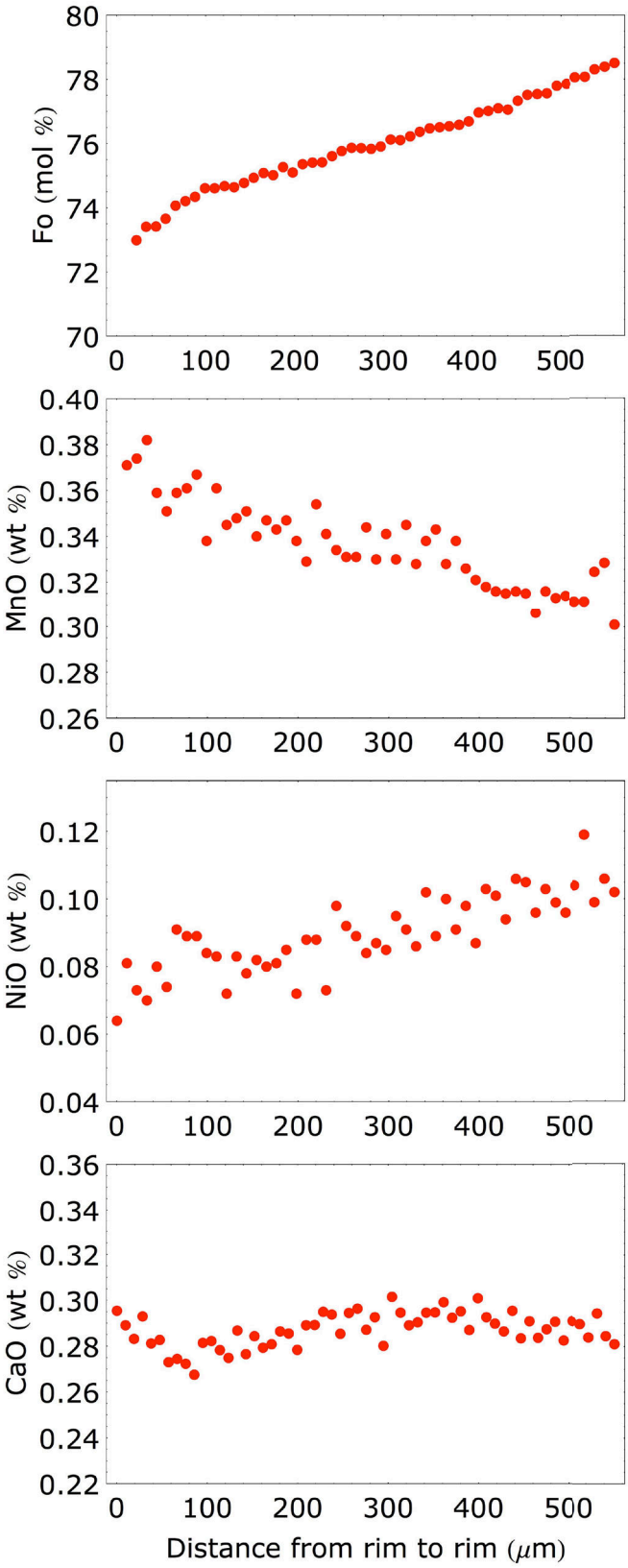
Fo (mol %)
80
78
76
74
72
70
0
100
200
300
400
500
MnO (wt %)
0.40
0.38
0.36
0.34
0.32
0.30
0.28
0.26
NiO (wt %)
0.12
0.10
0.08
0.06
0.04
CaO (wt %)
0.36
0.34
0.32
0.30
0.28
0.26
0.24
0.22
Distance from rim to rim (μm)

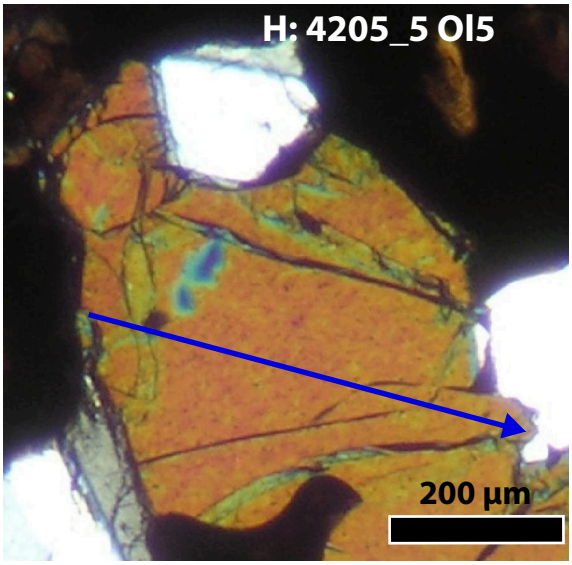
H: 4205_5 Ol5
200 µm

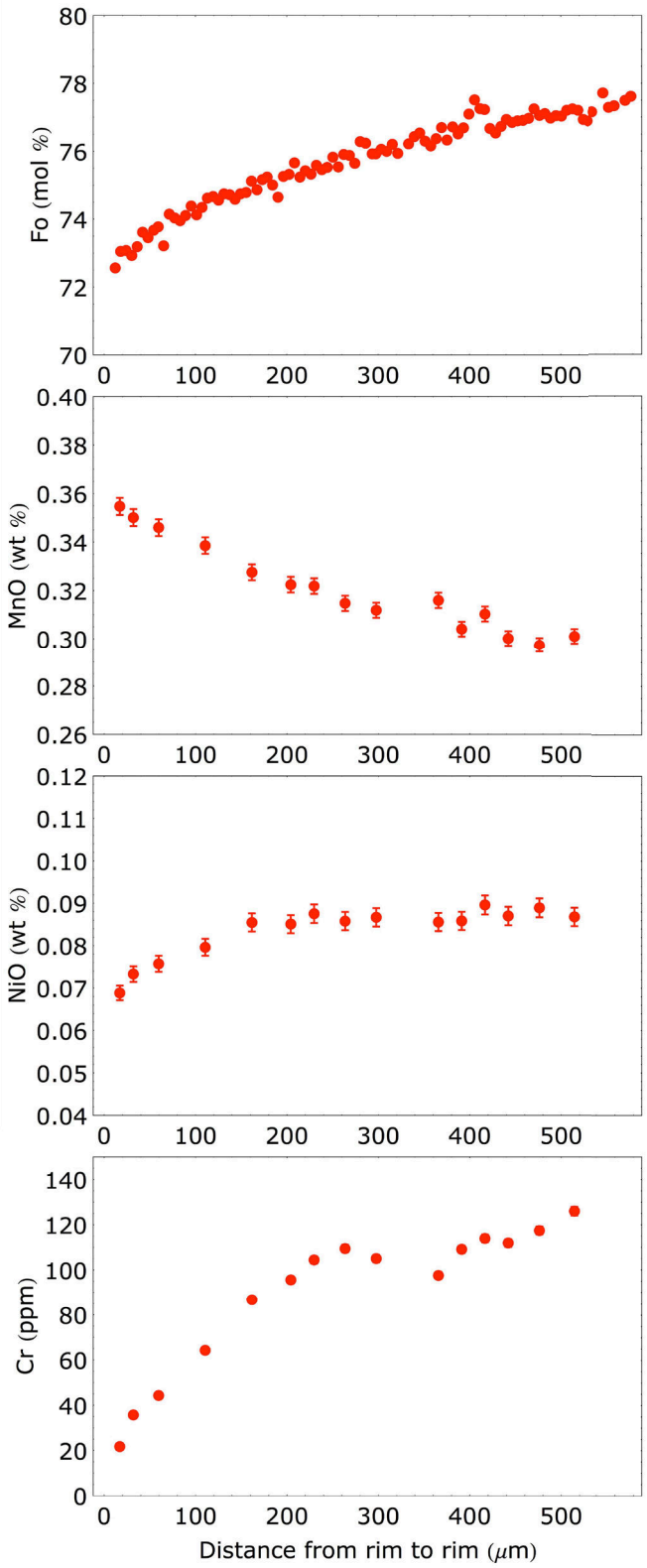
Fo (mol %)
MnO (wt %)
NiO (wt %)
Cr (ppm)
Distance from rim to rim (μm)

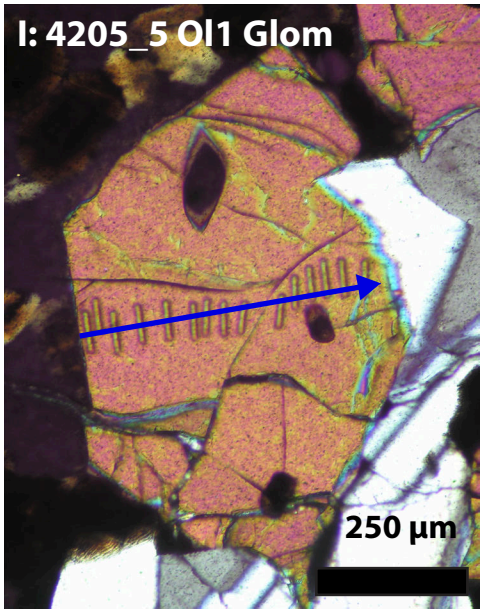
I: 4205_5 Ol1 Glom
250 μm

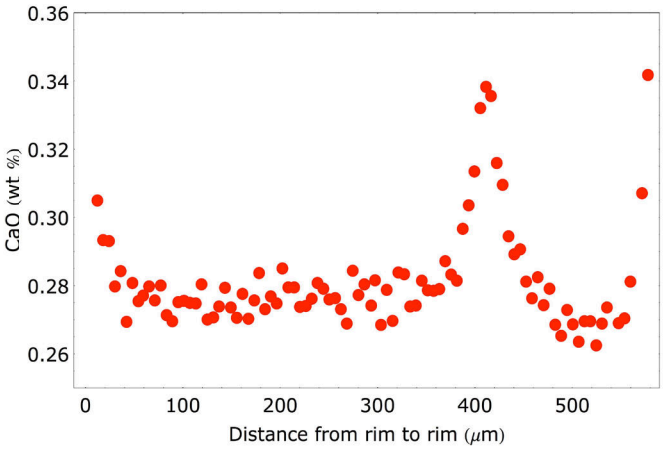
CaO (wt %)
Distance from rim to rim (μm)

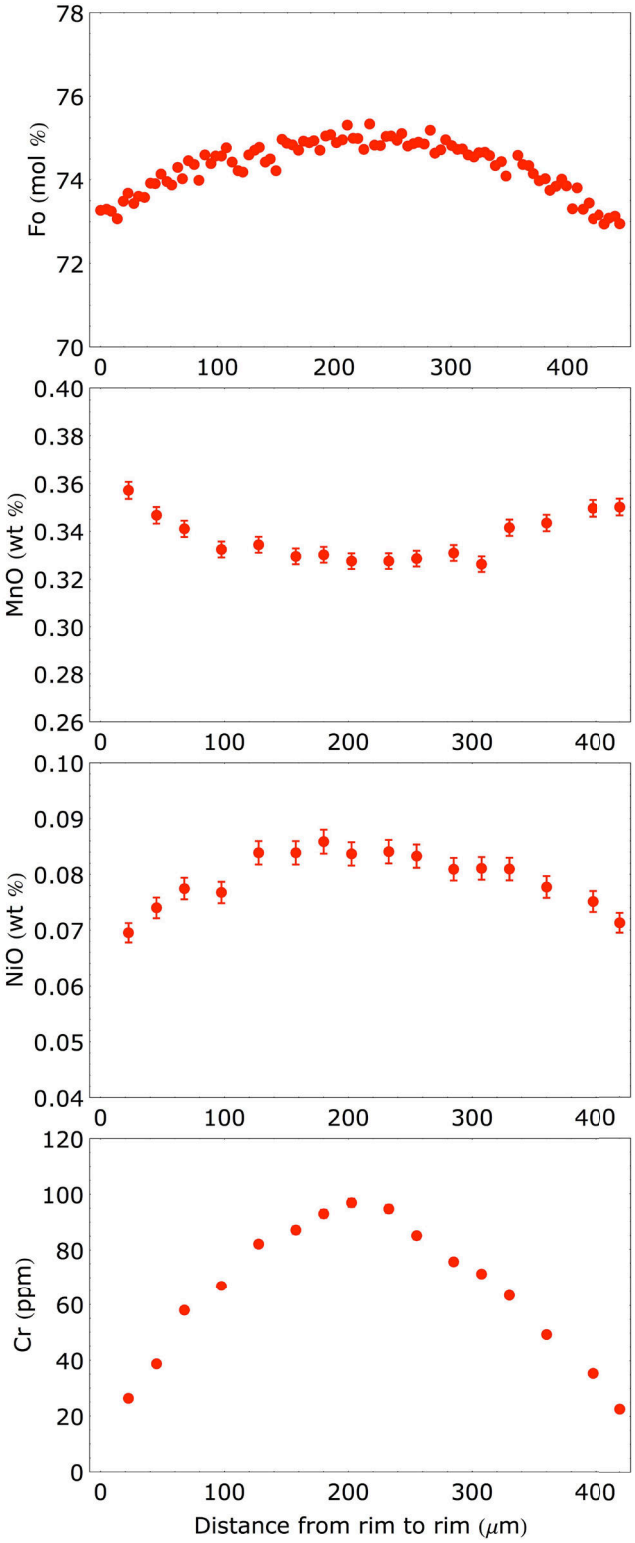
Fo (mol %)
MnO (wt %)
NiO (wt %)
Cr (ppm)
Distance from rim to rim (μm)

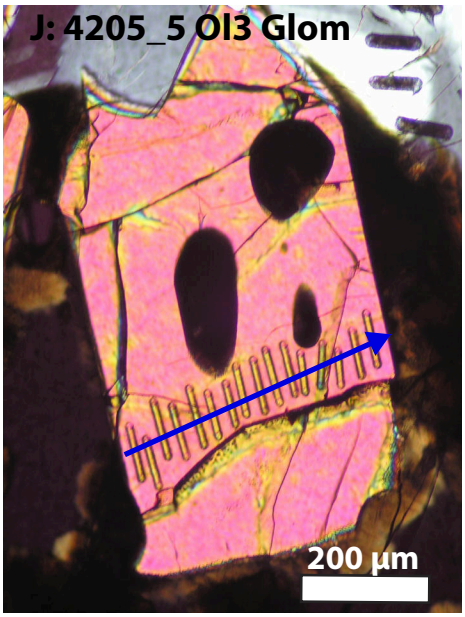
J: 4205_5 Ol3 Glom
200 μm

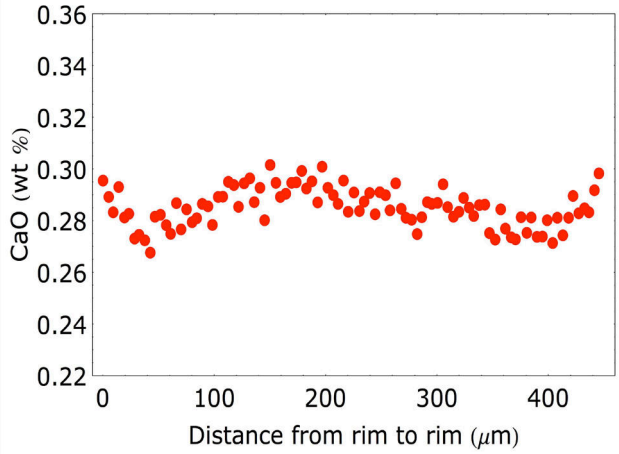
CaO (wt %)
Distance from rim to rim (μm)

K: 4205_5 Ol 5 & 6 Glom

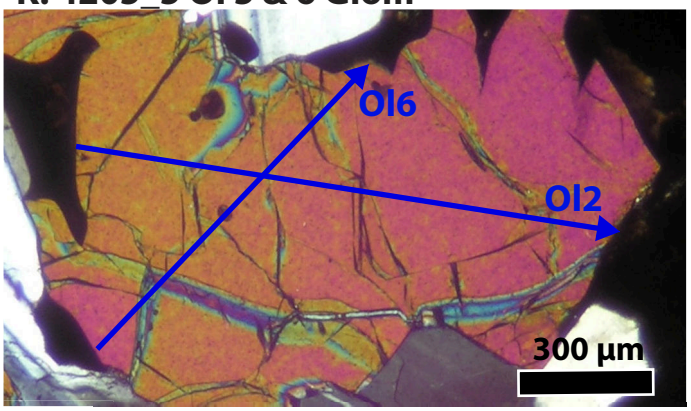

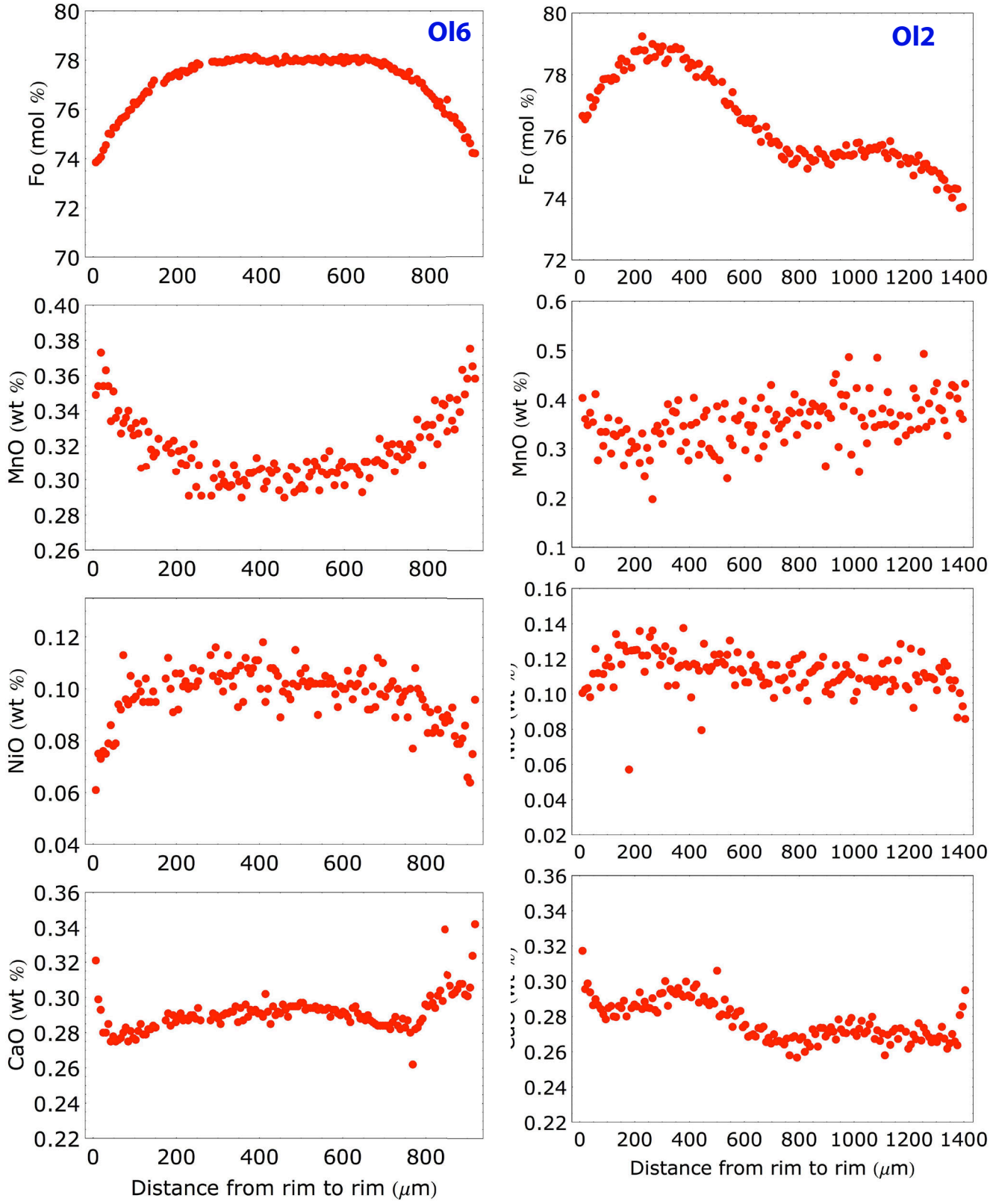

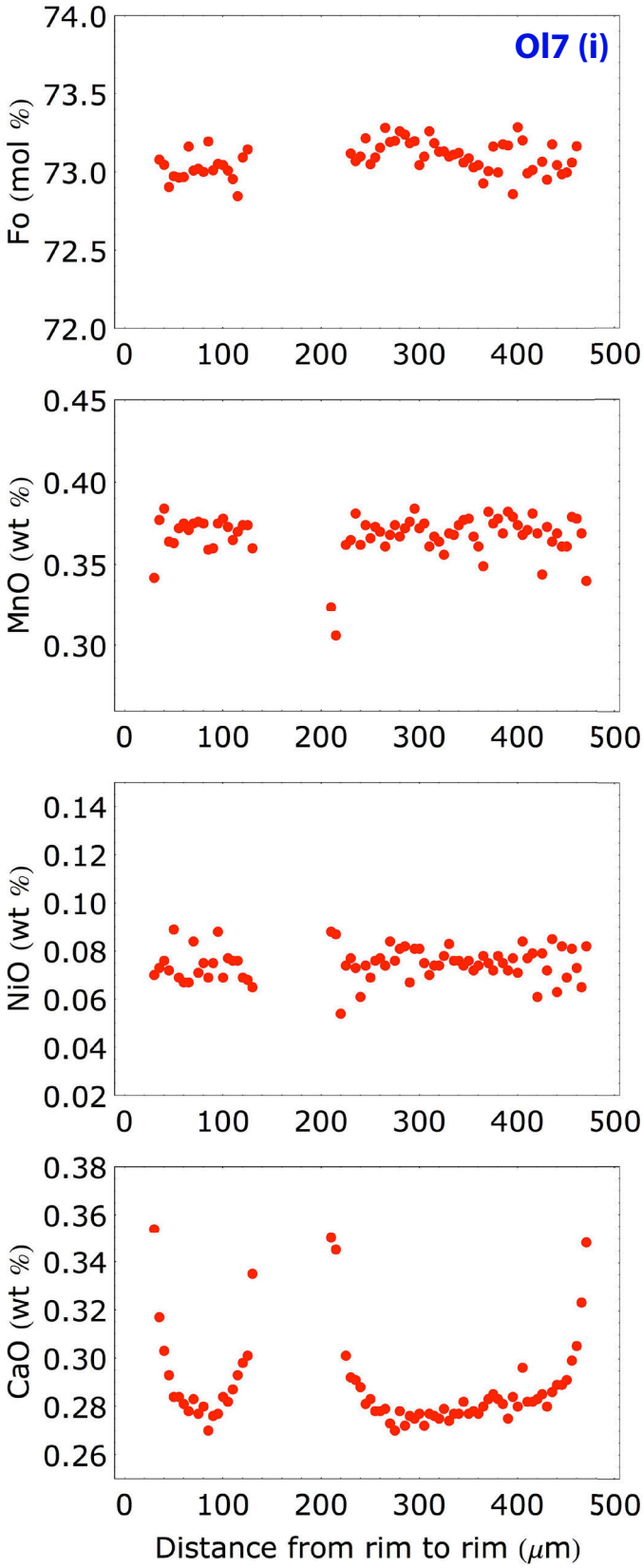
Ol7 (i)
Fo (mol %)
74.0
73.5
73.0
72.5
72.0
MnO (wt %)
0.45
0.40
0.35
0.30
NiO (wt %)
0.14
0.12
0.10
0.08
0.06
0.04
0.02
CaO (wt %)
0.38
0.36
0.34
0.32
0.30
0.28
0.26
0
100
200
300
400
500
Distance from rim to rim (μm)

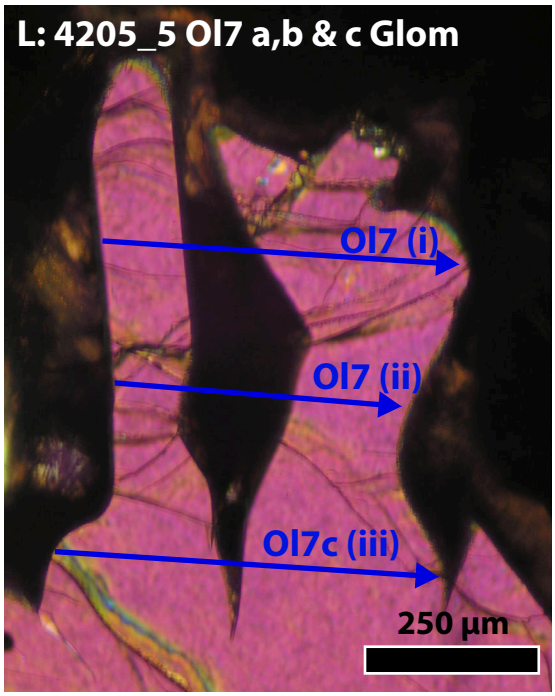
L: 4205_5 Ol7 a,b & c Glom
Ol7 (i)
Ol7 (ii)
Ol7c (iii)
250 µm

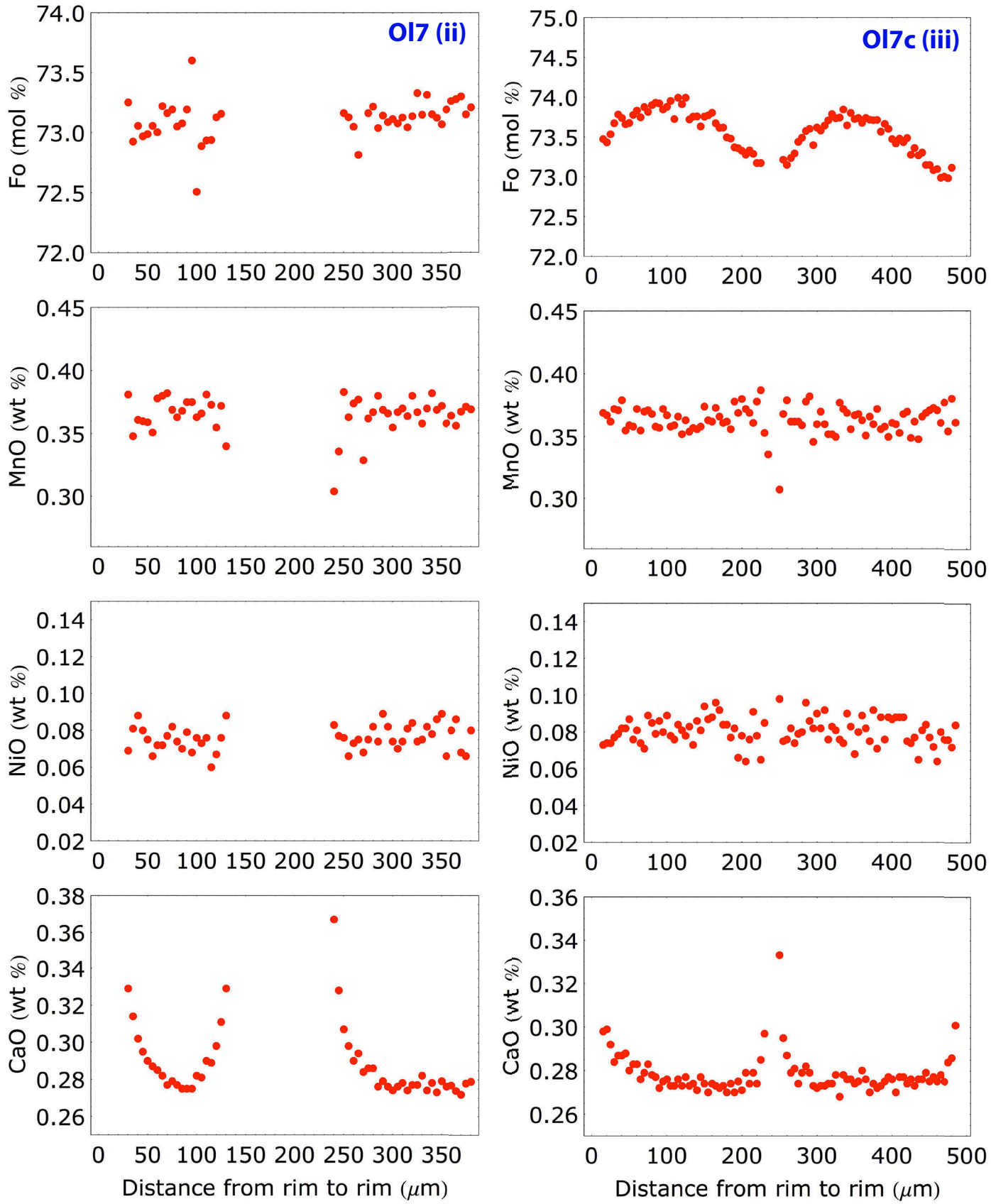
Ol7 (ii)
Ol7c (iii)
Fo (mol %)
MnO (wt %)
NiO (wt %)
CaO (wt %)
Distance from rim to rim (μm)
Distance from rim to rim (μm)

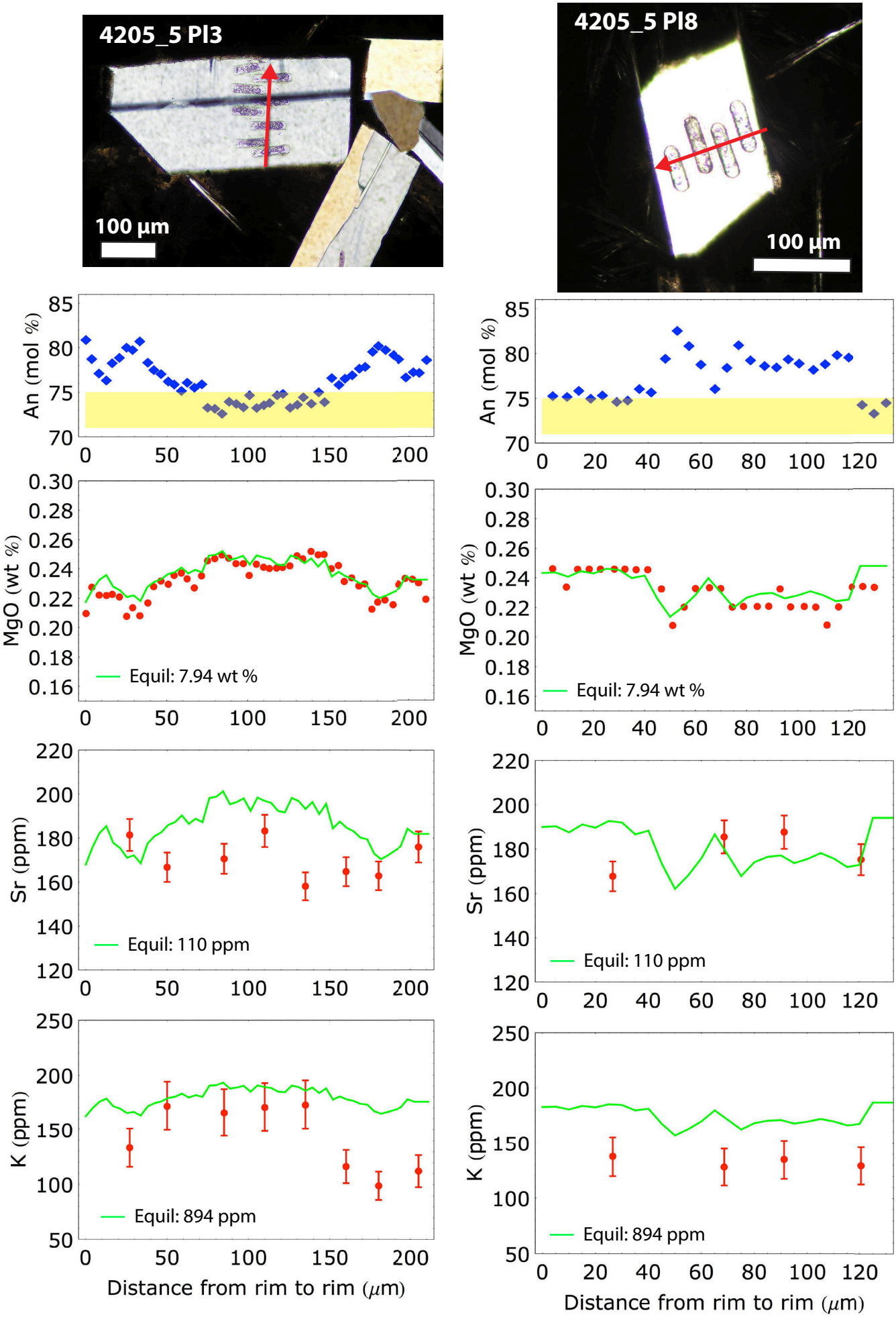
4205_5 Pl3
100 µm
4205_5 Pl8
100 µm
An (mol %)
MgO (wt %)
Equil: 7.94 wt %
Sr (ppm)
Equil: 110 ppm
K (ppm)
Equil: 894 ppm
Distance from rim to rim (µm)

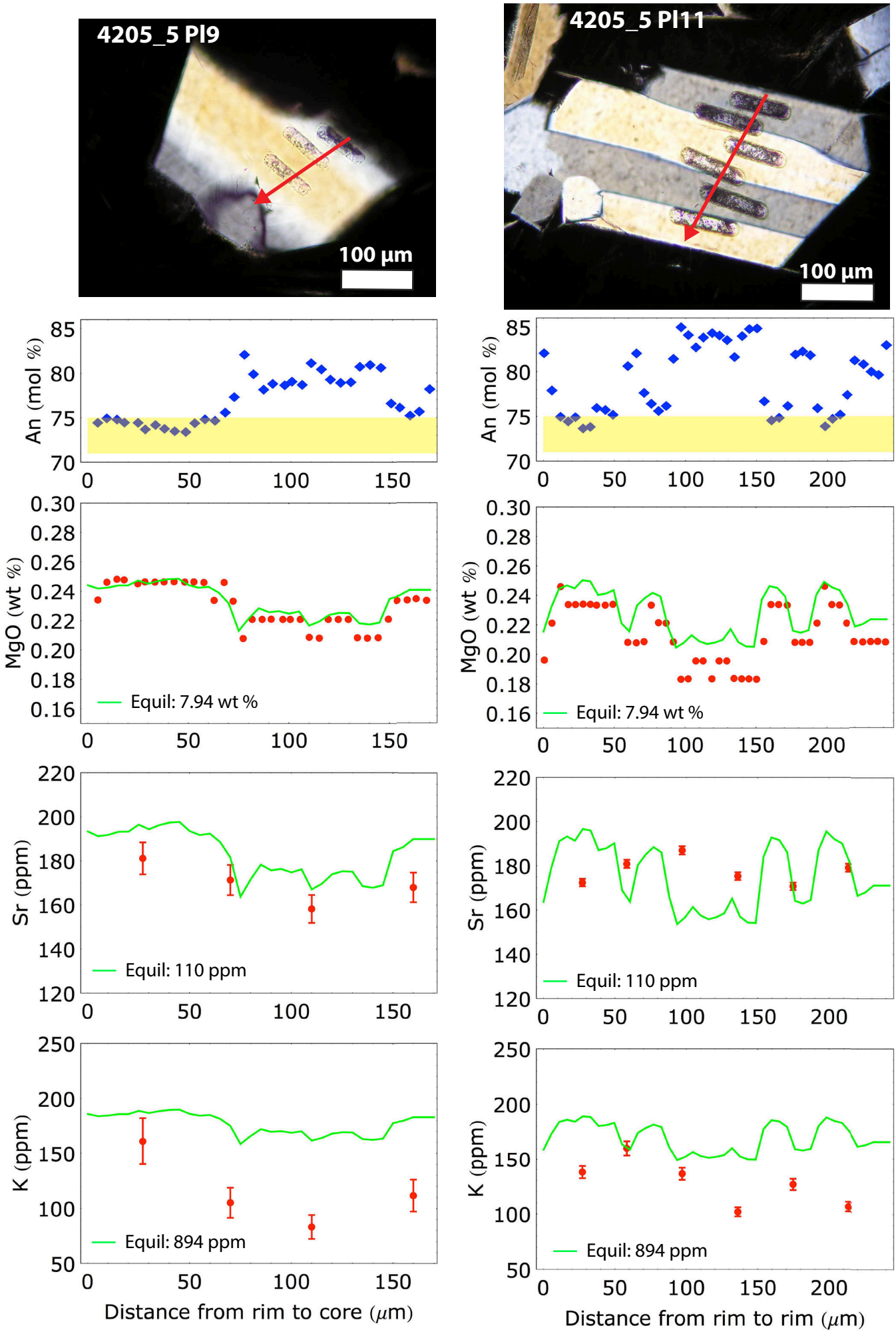
4205_5 Pl9
100 µm
4205_5 Pl11
100 µm
An (mol %)
MgO (wt %)
Equil: 7.94 wt %
Sr (ppm)
Equil: 110 ppm
K (ppm)
Equil: 894 ppm
Distance from rim to core (µm)
Distance from rim to rim (µm)

A.5.3.2: Sample 4205_3

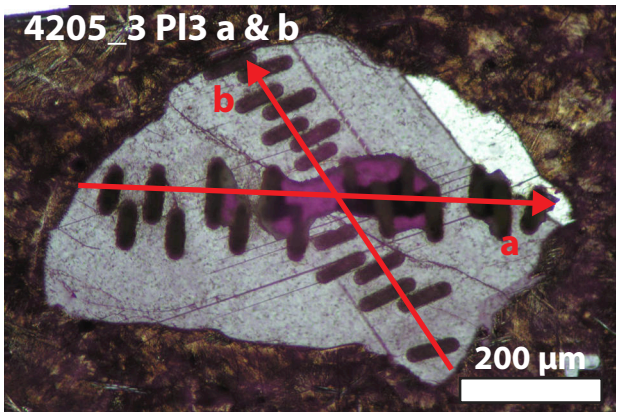

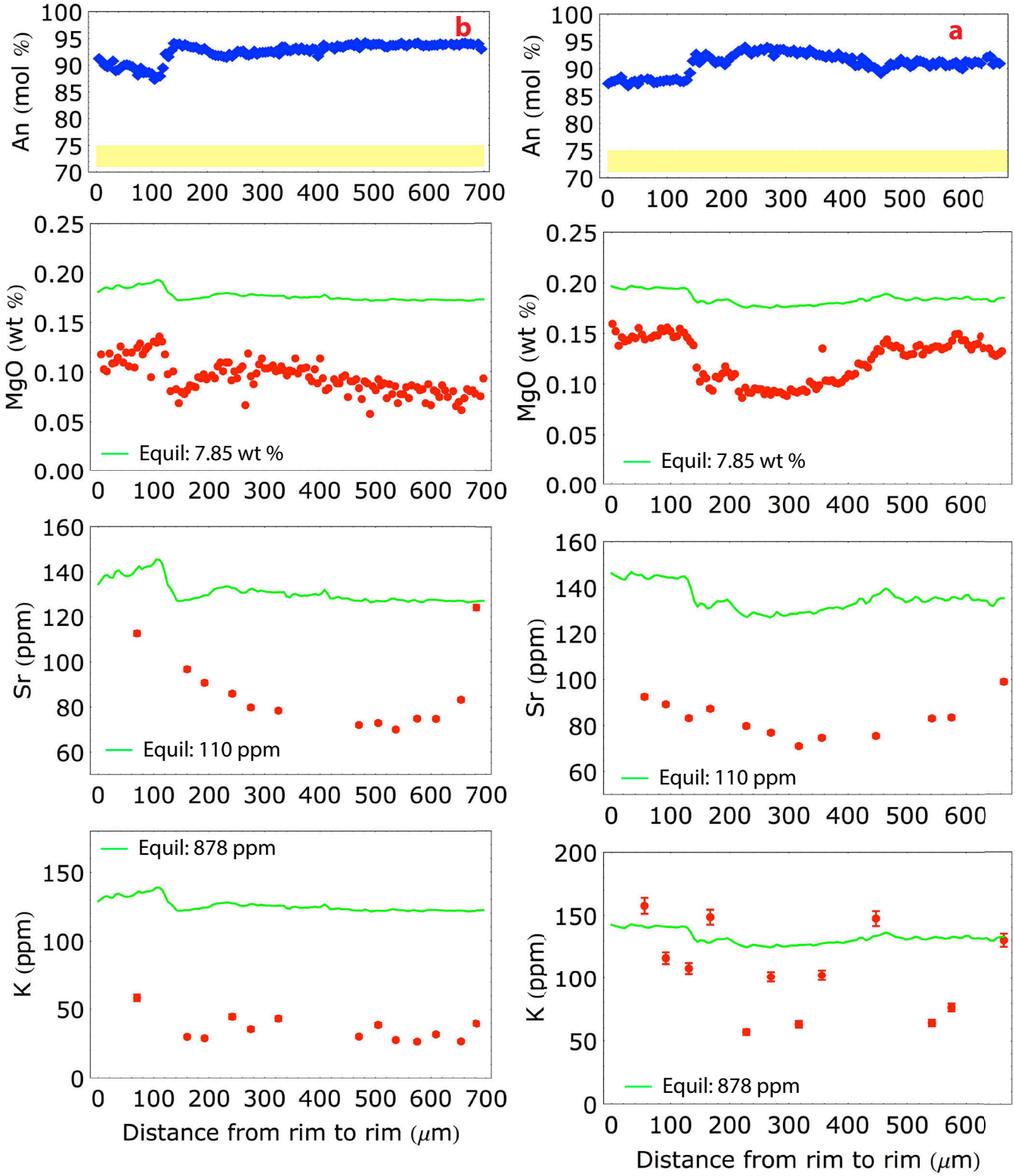

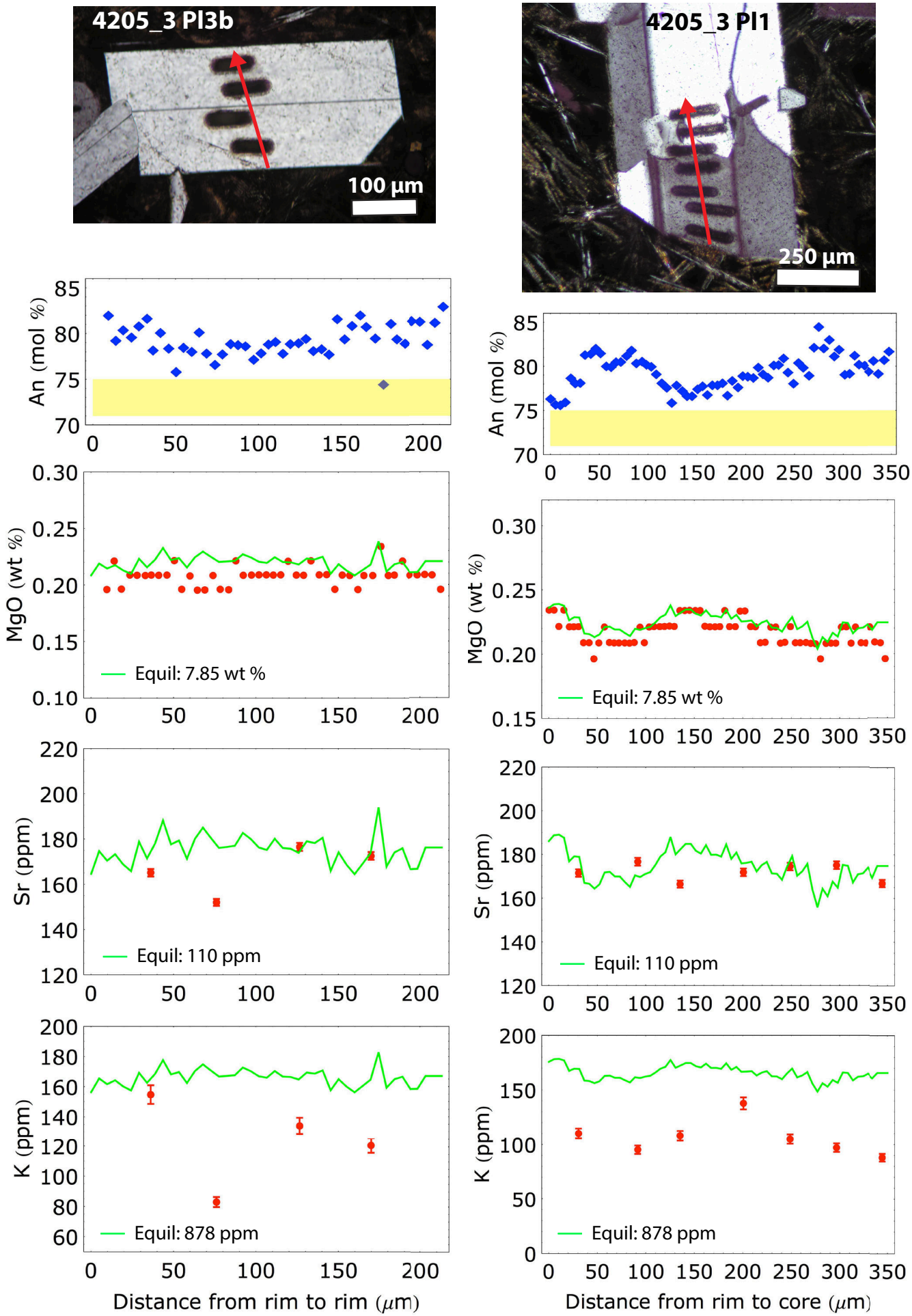
4205_3 Pl3b
100 µm
4205_3 Pl1
250 µm
An (mol %)
MgO (wt %)
Equil: 7.85 wt %
Sr (ppm)
Equil: 110 ppm
K (ppm)
Equil: 878 ppm
Distance from rim to rim (µm)
Distance from rim to core (µm)

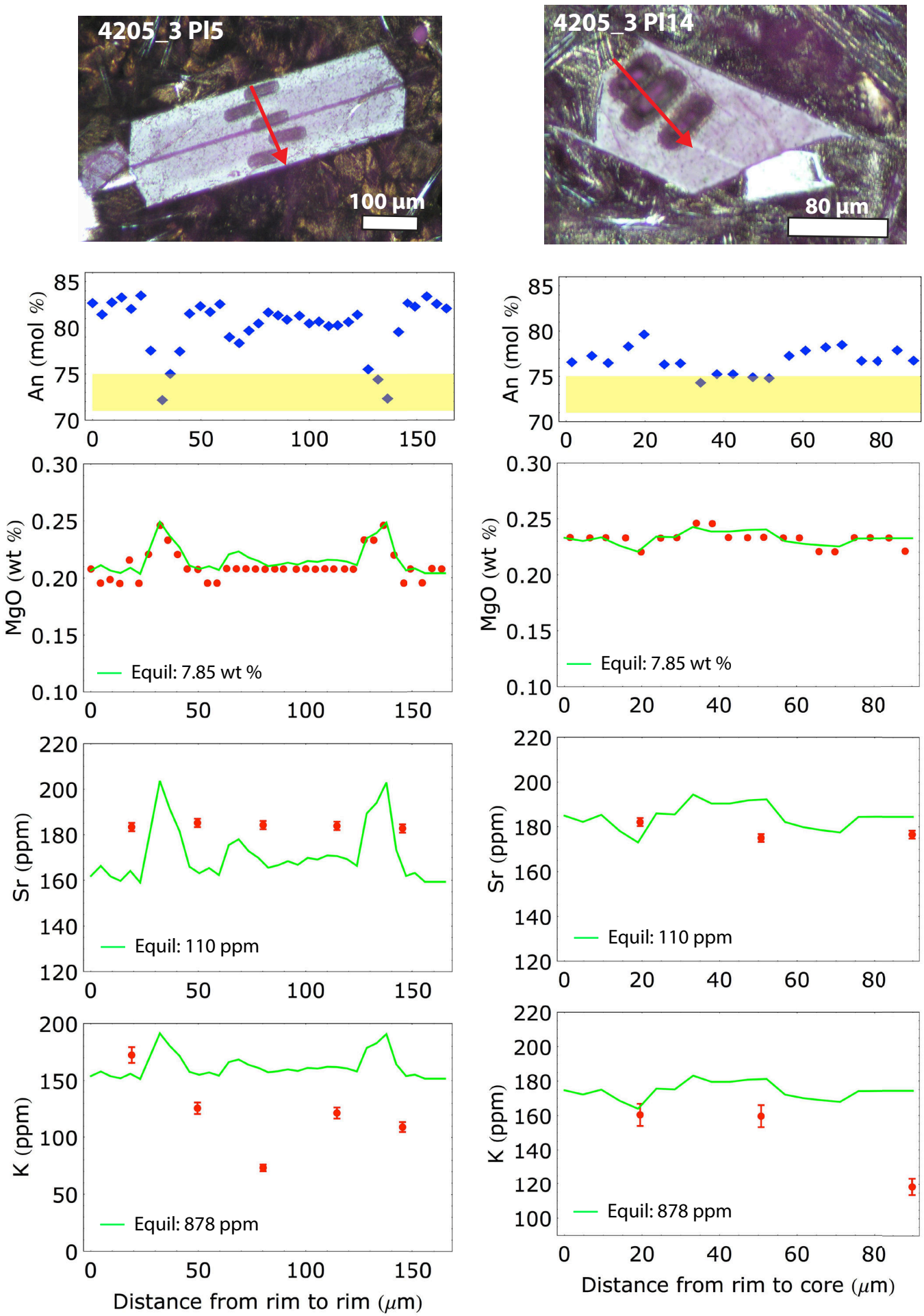
4205_3 Pl5
100 µm
4205_3 Pl14
80 µm
An (mol %)
MgO (wt %)
Equil: 7.85 wt %
Sr (ppm)
Equil: 110 ppm
K (ppm)
Equil: 878 ppm
Distance from rim to rim (µm)
Distance from rim to core (µm)

Appendix A.6: Explanations and examples of diffusion models.

The attached C.D. contains four examples of the different diffusion models used in Section 2.6, along with an explanation of each model. Each diffusion model was completed in Mathematica 8.0 and saved in a notebook format. A pdf copy of each Mathematica file is also shown below. The four examples of diffusion models are; a 1D diffusion model for both plagioclase (A.6.1.1) and olivine (A.6.1.2), a 2D diffusion model for plagioclase (A.6.2), and a 1D diffusion plus growth model for plagioclase (A.6.3). The details of each model are discussed in each file.

A.6.1: A 1D diffusion model

A 1D diffusion model was used to retrieve timescales from plagioclase and olivine crystals that are in disequilibria with their host melts (Section 2.6). An example of a 1D diffusion model for Mg is shown for a euhedral plagioclase from the Bull's eye (A.6.1.1), along with an example of a 1D model for Fo in an olivine from the glomerocryst in the Southern Fissure (A.6.1.2).

****

Appendix A.6.1.1: Example of a 1D diffusion model in plagioclase
A program to model Mg diffusion in one dimension in crystal 4202_1 Pl1 from the Bull's eye. The model assumes the crystal was intially in equilibrium with a 7.8 wt % MgO prior to being instantaneously mixed into a 8.4 wt % MgO melt. This induces diffusive gain of Mg at the crystal rims as it attempts to re-equilibrate. The retrieved time is ~ 3.5 weeks.
The model uses a finite difference explicit method (e.g. Crank, 1979)

****

The variables below are 'cleared' to avoid complications from previous values and definitions being associated with them.

```
Clear[An1, An2, C10, C20, D1, D2, s, c, R, g, mgc, tf, D1,
 h, r, δx, δt, T, t, equi2, k, AN, ANx, Anplot1, Anplot]
```

Temperature (T) is in celsius. The diffusion coefficient for Mg (D1) is in $\mu m^2 s^{-1}$ and is taken from LaTourette and Wasserburg (1998).

A distance step (δx) in microns and a time step (δt) in seconds is chosen. Note, the stability criteria for the explicit method is R*D1 < 0.5. The variable "tf" is the number of points in the plagioclase transect and so the total length of the transect (s) will equal δx * tf. The total time for the diffusion model will be δt * ttiter, where ttiter is the number of time iterations used in the model, see below.
A and r are parameters used in the diffusion model below.

```
T = 1200.;
```

$$D1 = \left(1.2 * 10^{-6} * \mathrm{Exp}\left[\frac{-266.}{(T + 273.) * 8.3144 * 10^{-3.}}\right]\right) * 10^{12};$$

$$\delta x = 5.5;\ \delta t = 0.9 * 10\hat{}4;\ R1 = \frac{\delta t}{\delta x^2} D1$$

```
0.13185
```

$$A = 26.1;\ r = 8.314 * 10^{-3.} * (T + 273.);$$

$$R = \frac{\delta t}{\delta x^2};$$

```
tf = 52;  s = 217;
```

Import the MgO profile in a text file. Assign the profile to "mgc"

```
Import["/Users/kathryngillis/Desktop/Aerona./Desktop/mathmatica/
    Plagioclase/Mg/Be/4202_1 Pl1-Mg.txt", "Table"];
```

```
mgc = {{1, 0.2275`}, {2, 0.244`}, {3, 0.245`}, {4, 0.2473`}, {5, 0.2408`}, {6, 0.238`},
   {7, 0.2508`}, {8, 0.2396`}, {9, 0.2403`}, {10, 0.2425`}, {11, 0.2421`}, {12, 0.2411`},
   {13, 0.2385`}, {14, 0.2418`}, {15, 0.2325`}, {16, 0.2348`}, {17, 0.2415`}, {18, 0.2368`},
   {19, 0.2415`}, {20, 0.2375`}, {21, 0.2368`}, {22, 0.2383`}, {23, 0.2385`}, {24, 0.2367`},
   {25, 0.2386`}, {26, 0.2418`}, {27, 0.2443`}, {28, 0.2372`}, {29, 0.2401`}, {30, 0.2425`},
   {31, 0.2435`}, {32, 0.244`}, {33, 0.24`}, {34, 0.2473`}, {35, 0.2372`}, {36, 0.2466`},
   {37, 0.2536`}, {38, 0.2431`}, {39, 0.2421`}, {40, 0.2489`}, {41, 0.2496`}, {42, 0.2542`},
   {43, 0.2519`}, {44, 0.2509`}, {45, 0.2537`}, {46, 0.2521`}, {47, 0.2504`},
   {48, 0.2513`}, {49, 0.2551`}, {50, 0.2541`}, {51, 0.2607`}, {52, 0.2459`}};
```

Plot the MgO data

```
data = ListPlot[mgc, PlotRange → {0.001, 0.35},
  PlotStyle → {RGBColor[1, 0, 0], PointSize[0.02]}]
```

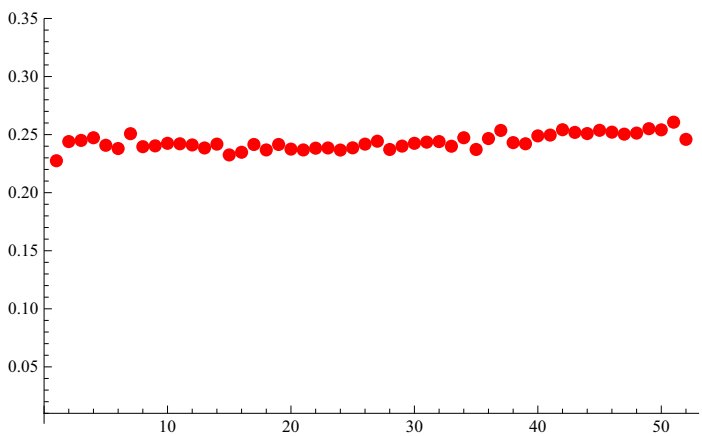

Import the anorthite (An) profile in a text file. Assign the profile to “An”

```
An = Import[
   "/Users/kathryngillis/Desktop/Aerona./Desktop/mathmatica/
     Plagioclase/Mg/Be/4202_1 Pl1-An.txt", "Table"];
```

```
An = {{1, 82.62`}, {2, 77.08`}, {3, 77.43`}, {4, 75.76`}, {5, 77.52`}, {6, 78.09`},
   {7, 78.79`}, {8, 77.96`}, {9, 77.19`}, {10, 78.94`}, {11, 78.09`}, {12, 76.11`},
   {13, 77.41`}, {14, 76.02`}, {15, 76.72`}, {16, 76.23`}, {17, 78.46`},
   {18, 75.93`}, {19, 75.43`}, {20, 75.44`}, {21, 76.47`}, {22, 76.51`}, {23, 75.86`},
   {24, 75.87`}, {25, 76.67`}, {26, 76.18`}, {27, 75.83`}, {28, 75.71`}, {29, 75.73`},
   {30, 74.7`}, {31, 75.08`}, {32, 74.92`}, {33, 74.46`}, {34, 75.31`}, {35, 75.22`},
   {36, 75.7`}, {37, 74.2`}, {38, 74.38`}, {39, 78.26`}, {40, 74.38`}, {41, 73.99`},
   {42, 74.84`}, {43, 74.46`}, {44, 74.3`}, {45, 75.26`}, {46, 74.48`}, {47, 75.49`},
   {48, 74.64`}, {49, 73.47`}, {50, 75.68`}, {51, 74.98`}, {52, 77.12`}};
```

Plot the An data.

```
ListPlot[An, PlotRange → {70, 85}]
```

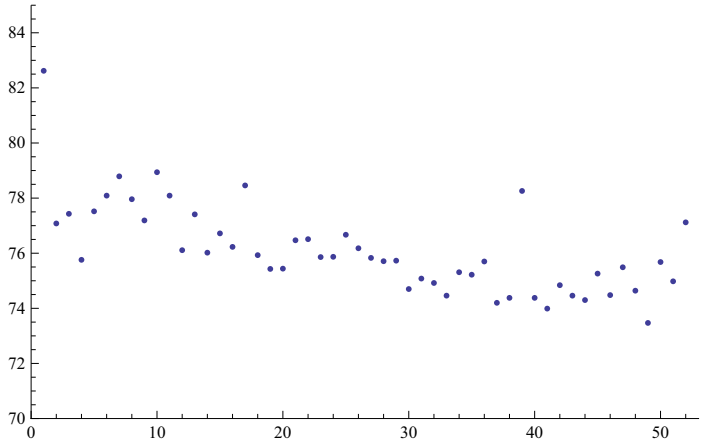

Convert the anorthite data to mole fraction.
Determine the diffusion coefficient (DIF) at each point.
The An profile is them smoothed slightly using the diffusion model to remove sharp concentration changes.
This will reduce any artifical aritifacts from the spacial resolution of the EMP analyses.

```
AN = An[[All, 2]]; AN = An[[All, 2]] / 100.; An;
AN[[tf]] = AN[[tf - 1]] = AN[[tf - 2]];
DIF = Table[0.`, {tf}];
```

$$\text{Do}\left[\text{DIF}[[i]] = \frac{\left(1.2` \,\text{Exp}\left[-\frac{266.`}{\frac{(T+273.`)\,8.3144`}{10^{3.`}}}\right]\right) 10^{12}}{10^{6}}, \{i, 1, tf\}\right];$$

```
Do[ANx = AN; (Do[AN[[i]] =
    ANx[[i]] + R * DIF[[i]] * (ANx[[i + 1]] - 2 * ANx[[i]] + ANx[[i - 1]]),
   {i, 2, tf - 1}]), {3}]; ListPlot[AN, Joined → True]
```

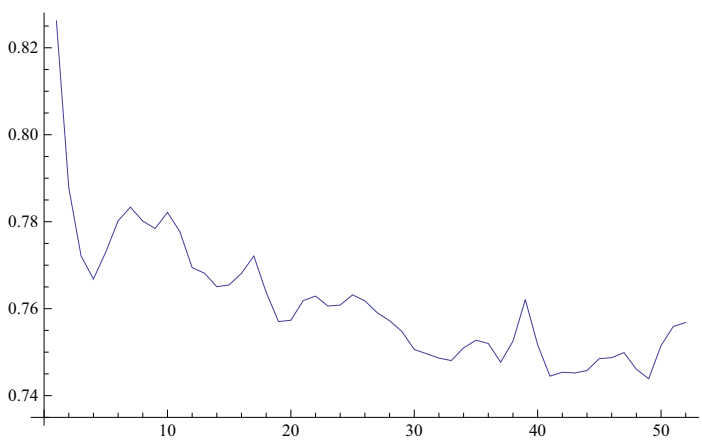

Define the partition coefficient (K). Here the partition coefficient of Mg in plagioclase is taken from Equation (1) in Section 2.4.2.3

```
K = Exp[(-21800 * AN - 26300)/(8.314 * (T + 273.))];
```

The equilibrium (ceq) and initial (ini) profiles are calculated using the partition coefficient of Mg and the plagioclase An profile. The initial profile is in equilibrium with a 7.8 wt % MgO melt, and the equilibrium profile is in equilibrium with a 8.4 wt % MgO melt.

```
ceq = Table[0, {tf}]; Do[ceq[[i]] = 8.4` K[[i]], {i, tf}];
equi = ListPlot[ceq, Joined → True,
  PlotStyle → {Thickness[0.005`], RGBColor[0, 1, 0]}];
c = Table[0, {tf}]; Do[c[[i]] = 7.8 * K[[i]], {i, tf}];
ini = ListPlot[c, Joined → True, PlotStyle →
   { Thickness [0.005], RGBColor[0, 0, 1]}]; Show[equi, ini, data]
```

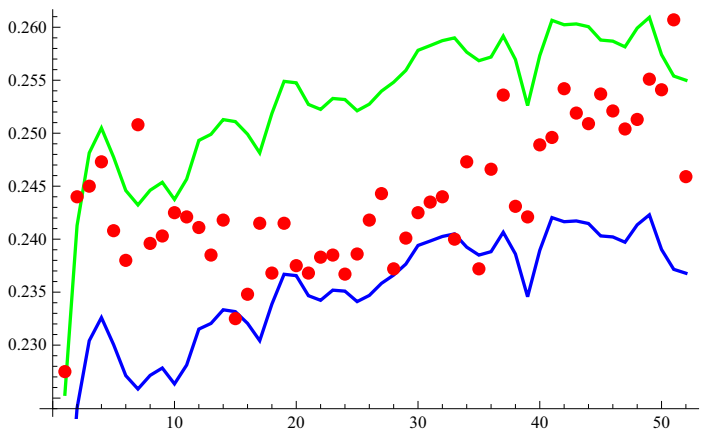


```
inidata = c; equidata = ceq;
```

The following parameters are required for the diffusion model.
ANA and ANO takes into account Mg diffusion driven by the change in An content, and DIFO takes into account Mg diffusion driven by the change in MgO content.

```
ANO = Table[0, {tf}];
Do[ANO[[i]] = AN[[i + 1]] - 2 * AN[[i]] + AN[[i - 1]], {i, 2, tf - 1}]; ANO;
DIFO = Table[0, {tf}];
Do[DIFO[[i]] = ((DIF[[i + 1]] - DIF[[i - 1]]) / 2), {i, 2, tf - 1}]; DIFO;
ANA = Table[0, {tf}];
Do[ANA[[i]] = ((AN[[i + 1]] - AN[[i - 1]])) / 2, {i, 2, tf - 1}]; ANA;
```

ttiter is the number of time iterations used in the model

```
titer = 329;
```

The diffusion algorithm

The first Do loop excutes the number of iterations (titer) used in the model.
The boundary conditions at the crystal rims are set. In this case the concentration at rim 1 (‘c[[1]]’) and rim 2 (‘c[[tf]]’) are set as open and equal the equilibrium concentrations.

b=c is set which stores the concentration of MgO after every iteration.
The second Do loop contains the finite element formulation for the diffusion coefficient which depends on the gradients in the An profile, and the gradients in the MgO profile. This calculates the modelled profile and is based on Equation (7) in Costa et al. (2003).

```
Do[(c[[1]] = ceq[[1]]; c[[tf]] = ceq[[tf]]; b = c;
    Do[c[[i]] = b[[i]] + R * (((DIF[[i]] * b[[i]] * A / r) * ANO[[i]]) +
          (((1/r DIF[[i]] * A * ((b[[i + 1]] - b[[i - 1]]) / 2) +
              (b[[i]] * A * DIFO[[i]] / r)) * ANA[[i]]) +
          (DIFO[[i]] * ((b[[i + 1]] - b[[i - 1]]) / 2)) +
          DIF[[i]] * (b[[i + 1]] - 2 * b[[i]] + b[[i - 1]])),
     {i, 2, tf - 1}]), {titer}];
c;
```

Plot showing the model (mod; black) with the MgO data (red) and the initial (blue) and equilibrium (green) profile.

```
mod = ListPlot[c,
  FrameLabel → {"Distance from rim to rim (μm)", "MgO (wt %)"},
  LabelStyle → {FontFamily -> "Verdana", 12}, PlotRange → {0.15, 0.3},
  AxesOrigin → {0, 0}, Frame → True, Joined → True,
  PlotStyle → { Thickness [0.01], Black}]; Show[mod, equi, data, ini]
```

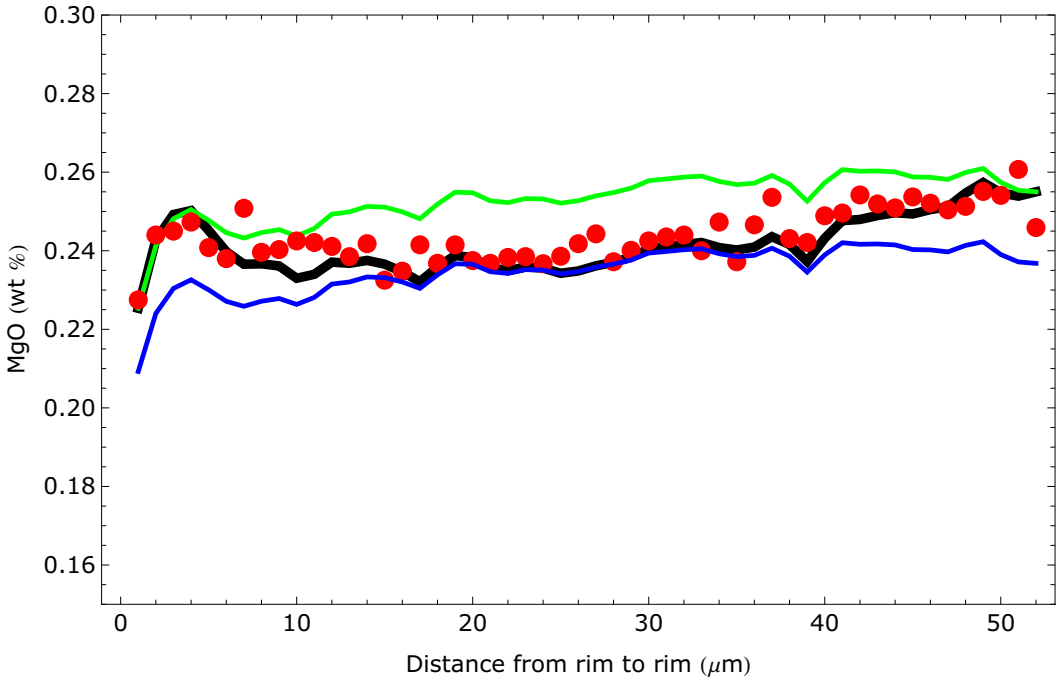

The retrieved time from the diffusion model

```
timeinsec = titer * δt
```

2.961×10^{6}

```
timeinweeks = (titer * δt) / 604 800.
```

4.89583

****

Appendix A.6.1.2: Example of a 1D diffusion model in olivine
A program to model Fe-Mg diffusion in one dimension in crystal 4205_5 Ol6 from the Southern Fissure. The model assumes the olivine has an initially homogenous forsterite content of 78 mol %, which corresponds to a MgO melt content of ~6.5 wt %. The crystal was than instantaneously mixed into a lower MgO melt of ~3.5 wt % MgO. This induces diffusive exchange of Fe-Mg at the crystal rims as it attempts to re-equilibrate. The retrieved time is ~ 3.6 months.

****

The variables below are 'cleared' to avoid complications from previous values and definitions being associated with them.

```
Clear[Fo, PRES, T, fO2, ax, bx, cx, NNO, deltaNNO, DFoc, DFox, DFoa,
 DFob, DFocd, DFoxd, DFoad, DFobd, R1, δt, δx, datafo, Fomin, Fomax, ttgrid,
 datanfo, cFo, bFo, DIFFo, datafop, iniFop, datanfop, eq1, timeinsec ]
```

Pressure (PRES) is in bars, temperature (T) is in celsius, the oxygen fugacoty (fO2) is in bars, and forsterite content (Fo) is in mol %. This Fo content is the lowest founf in the sample, and is used to check the stability of the model. The oxygen fugacity used is with respect to the QFM oxygen buffer calculated from Myers and Eugster (1983).

$$\text{PRES} = 800.;\ T = 1200.;\ fO2 = 10\hat{}-8.3;\ Fo = 73;\ QFM = \frac{-24\,441.}{(273. + T)} + 8.290$$

```
deltaQFM = Log[10, fO2] - QFM
```

```
-8.30267
```

```
0.00266802
```

The diffusion coefficient of Fe-Mg parallel to the c-axis (DFoc) in $\mu m^2 s^{-1}$ from Dohman and Chraborty (2007a,b).

$$DFoc = 10^{-9.21} * \left(\frac{fO2}{10^{-12}}\right)^{\frac{1}{6}} * 10^{3*(0.9-0.01*Fo)} * \text{Exp}\left[\frac{-\left(201\,000 + (PRES - 1) * 7 * 10^{-6} * 10^{5}\right)}{8.314 * (T + 273.15)}\right] * 10^{12};$$

The diffusion coefficient parallel to the c-axis without the Fo dependence. This is used in the diffusion model below.

$$DFoxc = 10^{-9.21} * \left(\frac{fO2}{10^{-12}}\right)^{\frac{1}{6}} * \text{Exp}\left[\frac{-\left(201\,000 + (PRES - 1) * 7 * 10^{-6} * 10^{5}\right)}{8.314 * (T + 273.15)}\right] * 10^{12};$$

The diffusion coefficient parallel to the a- and b-axis (DFoxab) which is approximately 6 times slower than in the c-direction.

```
DFoxab = DFoxc / 6;
```

DFox is the diffusion coefficient of Fe-Mg used in the diffusion model below. You can set it to equal the diffusion parallel to the c-axis (DFoxc), or the slower a/b- axis (DFoxab).

```
DFox = DFoxc;
```

Choose a distance step (δx) in μm and a time step (δt) in seconds. The total length of the profile will equal δx* the total number of grid points ('ttgrid', see below). The total time for the diffusion model will be δt * ttiter, where ttiter is the number of time iterations used in the model, see below.
Note, the stability criteria for the explicit method is R1*D1 < 0.5.

$$\delta x = 6.5;\ \delta t = 5.*10^3;\ R1 = \frac{\delta t}{\delta x^2};\ R1*DFoc$$

```
0.0696153
```

Import the Fo data in a text file. Assign the profile to "datafo". 'Fomin' is the minimum Fo concentration, and 'Fomax' is the maximum Fo concentration which are used when plotting the data.

```
Import["/Users/Laurencecoogan/Desktop/mathmatica/Olivine/Fo4205_5Ol6.txt", "Table"];
```

Import::nffil : File not found during Import. ≫

```
datafo = {{6, 73.57539728`}, {12, 73.76432594`}, {18, 74.06758313`},
   {24, 74.34868252`}, {30, 74.55048847`}, {36, 75.02066952`}, {42, 74.9903404`},
   {48, 75.26237272`}, {54, 75.26993279`}, {60, 75.46563093`}, {66, 75.61721531`},
   {72, 75.68144015`}, {78, 75.73589668`}, {84, 75.95240631`}, {90, 76.00252288`},
   {96, 76.28324352`}, {102, 76.2103615`}, {108, 76.32613702`}, {114, 76.44723934`},
   {120, 76.61811452`}, {126, 76.73444624`}, {132, 76.70516085`}, {138, 76.99874979`},
   {144, 77.17963247`}, {168, 77.07919007`}, {174, 77.22631301`}, {180, 77.35312962`},
   {186, 77.33079546`}, {192, 77.42631826`}, {198, 77.50391392`}, {204, 77.34741509`},
   {210, 77.57120527`}, {216, 77.5611505`}, {222, 77.50100445`}, {228, 77.57421459`},
   {234, 77.77021027`}, {240, 77.65601211`}, {246, 77.880191`}, {252, 77.81647474`},
   {282, 77.93994914`}, {288, 77.9463061`}, {294, 77.91077822`}, {300, 77.92854094`},
   {306, 77.91353638`}, {312, 77.9228947`}, {318, 78.02866613`}, {324, 77.97359493`},
   {330, 78.00678889`}, {336, 78.48874904`}, {342, 78.06361477`}, {348, 78.02814742`},
   {354, 78.10612135`}, {360, 78.1201625`}, {366, 78.10780989`}, {372, 78.00964588`},
   {378, 78.07032294`}, {384, 78.15635711`}, {390, 78.08000939`}, {396, 77.98001694`},
   {402, 77.97608001`}, {414, 77.93399465`}, {420, 77.96637734`}, {426, 78.00148817`},
   {432, 78.05635586`}, {438, 77.86520095`}, {444, 78.50772594`}, {450, 77.91019023`},
   {456, 78.14287489`}, {462, 78.01027922`}, {468, 77.96254057`}, {474, 77.96365153`},
   {480, 78.06262223`}, {486, 77.97395304`}, {492, 77.97390879`}, {498, 77.94739969`},
   {504, 78.01163189`}, {510, 78.05969034`}, {516, 78.026135`}, {522, 77.99672149`},
   {528, 78.05061153`}, {534, 77.97104737`}, {540, 77.91721094`}, {546, 78.12572161`},
   {552, 78.03921152`}, {558, 77.97537865`}, {564, 77.91981384`}, {570, 78.01555375`},
   {576, 78.01483623`}, {582, 77.9815985`}, {588, 78.13052032`}, {594, 77.88985027`},
   {600, 78.11831906`}, {606, 77.95968811`}, {612, 78.05909711`}, {618, 78.06844304`},
   {624, 78.09364594`}, {630, 77.91771955`}, {636, 77.97311324`}, {642, 78.09190555`},
   {648, 78.1008856`}, {654, 78.00832754`}, {666, 77.95703697`}, {672, 77.91078221`},
   {678, 77.88861657`}, {684, 77.77512657`}, {696, 77.842384`}, {702, 77.77450246`},
   {708, 77.64410233`}, {714, 77.6622006`}, {720, 77.51633938`}, {726, 77.51086178`},
   {732, 77.47367244`}, {738, 77.35994206`}, {744, 77.34591085`}, {756, 77.1728834`},
   {768, 77.23391935`}, {774, 77.07565755`}, {780, 77.07547623`}, {792, 76.71797328`},
   {798, 76.65415544`}, {804, 76.53959685`}, {810, 76.39830705`}, {816, 76.15848976`},
   {822, 76.30673055`}, {828, 76.05454373`}, {834, 75.8220873`}, {840, 76.39194091`},
   {846, 75.76229988`}, {852, 75.65003142`}, {858, 75.68709182`}, {864, 75.43227939`},
   {870, 75.35489166`}, {876, 75.18211965`}, {882, 74.82559491`}, {888, 74.85952083`},
   {894, 74.6213342`}, {900, 74.22727292`}, {906, 74.21072148`}};
Fomin =
 73;
Fomax =
 78;
```

Plot the Fo data

```
data = ListPlot[datafo, PlotRange → {Fomin - 3, Fomax + 3},
  PlotStyle → {RGBColor[1, 0, 0], PointSize[0.02]}]
```

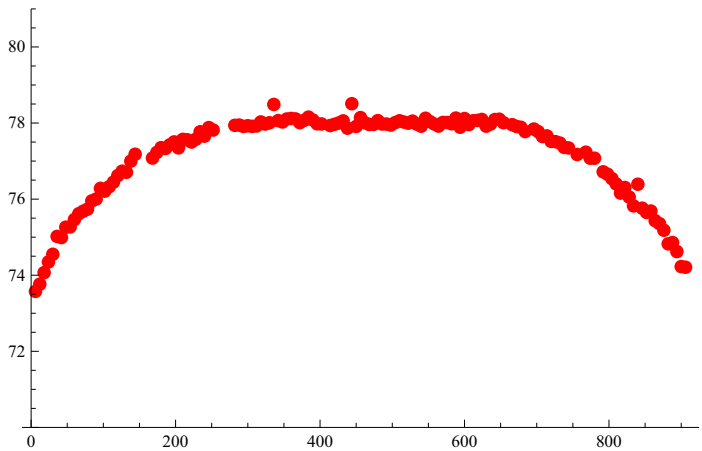

Define the total length of the profile in μm (ttlength). Determine the number of grid points in the model (ttgrid) by dividing the total length of the profile by the number of distance steps (δx).

```
ttlenght = 906; ttgrid = Round[ttlenght / δx]
```

```
139
```

Plot the Fo data (dataFo) to the number of gridpoints

```
datanfo = datafo; datanfo[[All, 1]] = datafo[[All, 1]] / δx ;
datanfop = ListPlot[datanfo, PlotRange → {Fomin - 3, Fomax + 3},
  PlotStyle → {RGBColor[1, 0, 0], PointSize[0.02]}]
```

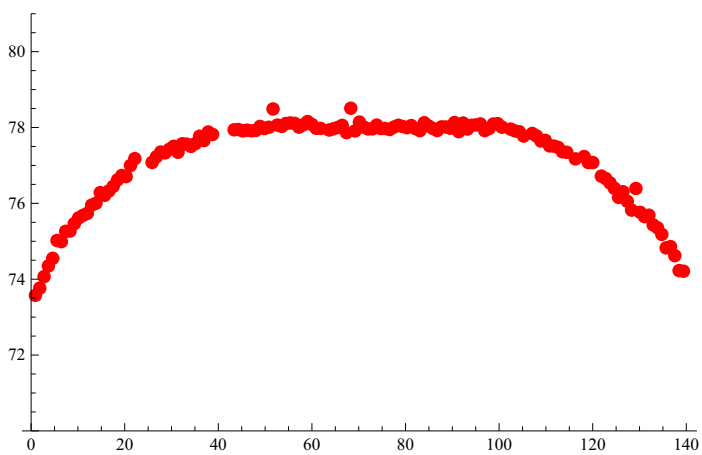

Determine the initial condition (Foini).
Here, an initial homogenous concentration is used at the maximum Fo content found in the profile (Fo78).

```
Foini = 78; cFo = Table[Foini, {ttgrid}];
iniFop = ListPlot[cFo, PlotRange → {Fomin - 3, Fomax + 3}, Joined → True,
  PlotStyle → { Thickness [0.005], RGBColor[0, 0, 1]}]; Show[iniFop, datanfop]
```

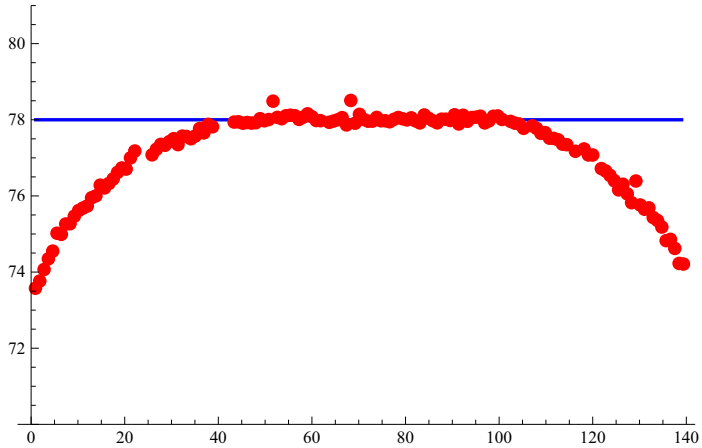


```
inidata = cFo;
```

Calculate the diffusion coefficient for Fe-Mg at each grid point using the initial Fo content.

```
DIFFo = Table[0., {ttgrid}];
Do[DIFFo[[i]] = DFox * 10^(3*(0.9-0.01*cFo[[i]])), {i, ttgrid}]; ListPlot[DIFFo]
```

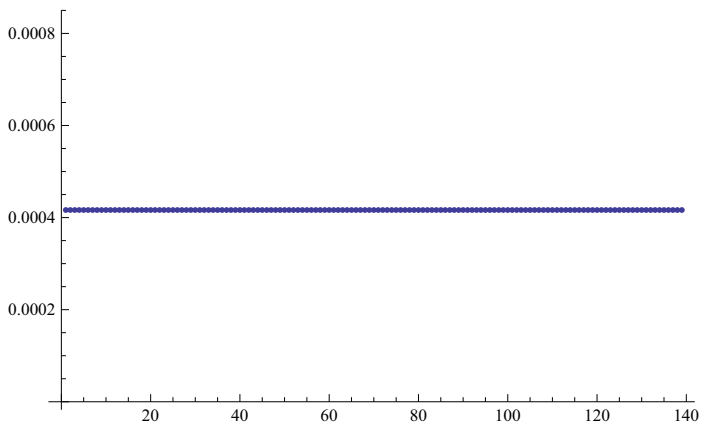

ttiter is the number of time iterations used in the model

```
ttiter = 1871;
```

The diffusion algorithm

The first Do loop excutes the number of iterations (titer) used in the model.
bFo=cFo is set which stores the concentration of Fo after every iteration.
The boundary conditions at the crystal rims are set. In this case the concentration at rim 1 (‘cFo[[1]]’) and rim 2 (‘cFo[[ttgrid]]’) are set as open and equal the Fo concentration at the rims.
The second Do loop calculates the diffusion coefficient. This is dependent on the Fo content and therefore needs to be calculated after each iteration.
The third Do loop contains the finite element formulation for the diffusion coefficient which depends on the the Fo concentration and calculates the modelled profile.

```
Do[bFo = cFo; cFo[[1]] = 73.5; cFo[[ttgrid]] = 74;
  Do[DIFFo[[i]] = DFox * 10^(3*(0.9-0.01*cFo[[i]])), {i, 1, ttgrid}]; Do[cFo[[i]] =
    bFo[[i]] + R1 * (((DIFFo[[i + 1]] - DIFFo[[i]]) * (bFo[[i + 1]] - bFo[[i]])) + (DIFFo[[i]] *
          (bFo[[i + 1]] - 2 * bFo[[i]] + bFo[[i - 1]]))), {i, 2, ttgrid - 1}], {ttiter}];
```

Plot showing the model (eq1; black) with the Fo data (red) and the initial (blue) profile.

```
eq1 = ListPlot[cFo, PlotRange → {70, 80},
  FrameLabel → {"Distance from rim to rim (μm)", "Fo (mol %)"},
  LabelStyle → {FontFamily -> "Verdana", 12}, AxesOrigin → {0, 0}, Frame → True,
  Joined → True, PlotStyle → { Thickness [0.01], Black}]; Ol6 = Show[eq1, datanfop, iniFop]
```

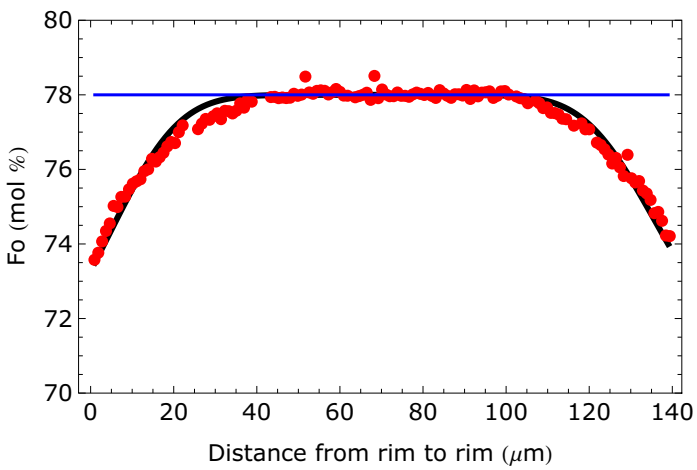

The retrieved time from the diffusion model

```
timeinsec = ttiter * δt
```

9.355×10^{6}

```
timeinyears = timeinsec / (3600 * 24 * 365)
```

0.296645

```
timeindays = timeinyears * 365
```

108.275

108.275

```
timeinmonths = timeindays / 30
```

3.60918

A.6.2: A 2D diffusion model: Plagioclase

A 2D diffusion model is used to model profiles in plagioclase where the analytical transect deviates from the centre line by a distance of one quarter of its width or less (Section 2.6.1). An example of a 2D diffusion model is shown for Mg from a plagioclase in the glomerocryst from the Southern Fissure.

****

Appendix A.6.2: Example of a 2D diffusion model
A program to model Mg diffusion in two dimensions in plagioclase 4205_5 Pl1glom from the Southern Fissure. The model assumes the crystal was intially in equilibrium with a 4.0 wt % MgO prior to being instantaneously mixed into a 5.0 wt % MgO melt. This induces diffusive gain of Mg at the crystal rims as it attempts to re-equilibrate.
The retrieved time is ~ 8.0 weeks.

****

The variables below are 'cleared' to avoid complications from previous values and definitions being associated with them.

```
Clear[x, y, z, w, dx, dy, dt, db, da, rx, ry]

Clear[D1, D2, s, c, f, g, h, δx, δy, δt, T, DIF, di, DIFF]
```

Temperature (T) is in celsius. The diffusion coefficient for Mg (D1) is in $\mu m^2 s^{-1}$ and is taken from LaTourette and Wasserburg (1998).

Choose a spacing for the gridpoints in the x direction (δx) and y direction (δy) in microns, and choose a time step (δt) in seconds. Note, the stability criteria for this method is $\frac{\delta t}{\delta x^2}$ D1 and $\frac{\delta t}{\delta y^2}$ D1 < 0.2.

The parameters 'A' and 'rat' and 'R1' and 'R2' are required for the diffusion model below.

```
T = 1200.;
```

$$D1 = \left(1.2 * 10^{-6} * \mathrm{Exp}\left[\frac{-266.}{(T + 273.) * 8.3144 * 10^{-3.}}\right]\right) * 10^{12};$$

$$\delta x = 5.;\ \delta y = 5.;\ \delta t = 0.03 * 10^{5};\ R = \frac{\delta t}{\delta y^2} D1$$

```
0.0531794
```

$$R1 = \frac{\delta t}{\delta x^2};\ R2 = \frac{\delta t}{\delta y^2}$$

```
120.
```

$$A = 26.1;\ rat = 8.314 * 10^{-3.} * (T + 273.);$$

Define the grid in the y-direction (tly, s, ss) and the x-direction (tlx, r, t).
Calculate the diffusion coefficient (DIF) at all grid points.

```
tly = 71; tlx = 44; s = 4; ss = 27; r = 4; t = 20;

di = Table[D1, {j, 1, tly}]; Do[di[[j]] = D1, {j, s, ss}]; di; DIF = Table[di, {i, 1, tlx}];
DIF; Do[DIF[[i, All]] = D1, {i, r}]; DIF; Do[DIF[[i, All]] = D1, {i, t, tlx}]; DIF;
```

Choose an equilibrium profile for the core and rim compositions. Here Mg (ppm) is 640 ppm in the core and 918 ppm in the rims. This initial profile is in equilibrium with a MgO melt content of 4 wt %. This is calculated using a Mg partition coefficient taken from Equation (1) in Section 2.4.2.3.

```
y = Table[918., {j, 1, tly}]; y; Do[y[[j]] = 640., {j, s, ss}]; y;

c = Table[y, {i, 1, tlx}]; c; Do[c[[i, All]] = 918., {i, r}];
c; Do[c[[i, All]] = 918., {i, t, tlx}]; c;

ListPlot3D[c]
```

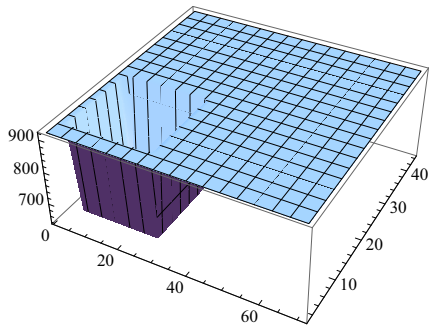

Smooth the equilibrium profile using the diffusion model

```
Do [b = c;
 Do[ Do[c[[i, j]] = b[[i, j]] + R2 * (DIF[[i, j]] * (b[[i, j + 1]] - 2 * b[[i, j]] + b[[i, j - 1]])) +
      R1 * (DIF[[i, j]] * (b[[i + 1, j]] - 2 * b[[i, j]] + b[[i - 1, j]])), {j, 2, tly - 1}] ,
   {i, 2, tlx - 1}], {5}]; c[[All, tly]] = c[[All, tly - 1]]; c[[1, All]] = c[[2, All]]; c;

ListPlot3D[c]

xequ = c[[All, 10]]; xequ1 = ListPlot[xequ, PlotRange → {{0, tlx}, {0, 1200}},
   Joined → True, PlotStyle → { Thickness [0.005], RGBColor[0, 0, 1]}] ;


equdata = xequ;
```

Choose an initial profile for the core and rim compositions. Here Mg (ppm) is 870 ppm in the core and 1090 ppm in the rims. This initial profile is in equilibrium with a MgO melt content of 5 wt %.

```
yy = Table[1090., {j, 1, tly}]; yy; Do[yy[[j]] = 870., {j, s, ss}]; yy;

c = Table[yy, {i, 1, tlx}]; c; Do[c[[i, All]] = 1090., {i, r}];
c; Do[c[[i, All]] = 1090., {i, t, tlx}]; c;

ListPlot3D[c]
```

Smooth the initial profile using the diffusion model

```
Do [b = c;
 Do[ Do[c[[i, j]] = b[[i, j]] + R2 * (DIF[[i, j]] * (b[[i, j + 1]] - 2 * b[[i, j]] + b[[i, j - 1]])) +
      R1 * (DIF[[i, j]] * (b[[i + 1, j]] - 2 * b[[i, j]] + b[[i - 1, j]])), {j, 2, tly - 1}] ,
   {i, 2, tlx - 1}], {5}]; c[[All, tly]] = c[[All, tly - 1]]; c[[1, All]] = c[[2, All]]; c;

xini = c[[All, 10]]; xini1 = ListPlot[xini, PlotRange → {{0, tlx}, {0, 1200}},
   Joined → True, PlotStyle → { Thickness [0.005], RGBColor[0, 1, 0]}] ;
inidata = xini;
```

Define the anorthite profile (Ani), here the An contents at the core are 80 mol % and at the rims are 65 mol %.

```
Any = Table[0.65, {j, 1, tly}]; Any; Do[Any[[j]] = 0.8, {j, s, ss}]; Any;

Ani = Table[Any, {i, 1, tlx}]; Ani; Do[Ani[[i, All]] = 0.65, {i, r}];
Ani; Do[Ani[[i, All]] = 0.65, {i, t, tlx}];

ListPlot3D[Ani]
```

Smooth the An profile using the diffusion model.

```
Do [Ana = Ani; Do[ Do[Ani[[i, j]] =
     Ana[[i, j]] + R2 * (DIF[[i, j]] * (Ana[[i, j + 1]] - 2 * Ana[[i, j]] + Ana[[i, j - 1]])) +
      R1 * (DIF[[i, j]] * (Ana[[i + 1, j]] - 2 * Ana[[i, j]] + Ana[[i - 1, j]])), {j, 2, tly - 1}] ,
   {i, 2, tlx - 1}], {5}]; Ani[[All, tly]] = Ani[[All, tly - 1]];
Ani[[1, All]] = Ani[[2, All]];
Ani;

ListPlot3D[Ani]
```

Calculate the diffusion coefficient (DIF) for all grid points

```
Do[Do[DIF[[i, j]] = (1.2 * 10^-6 * Exp[-266. / ((T + 273.) * 8.3144 * 10^-3.)]) * 10^12, {j, 2, tly - 1}],
 {i, 2, tlx - 1}]; DIF[[All, tly]] = DIF[[All, tly - 1]];
DIF[[1, All]] = DIF[[2, All]]; DIF; ListPlot3D[DIF]
```

The following parameters are required for the diffusion model.
ANA and ANO take into account Mg diffusion being driven by the change in An content in the x direction (ANO1 & ANA1) and the y direction (ANO2 & ANA2).
The parameters DIFO takes into account Mg diffusion being driven by the change in MgO content in the x direction (DIFO1) and the y direction (DIFO2).

```
ANO1 = Table[0, {tlx}, {tly}]; ANO2 = Table[0, {tlx}, {tly}];
Do[Do[ANO1[[i, j]] = Ani[[i, j + 1]] - 2 * Ani[[i, j]] + Ani[[i, j - 1]], {j, 2, tly - 1}],
 {i, 2, tlx - 1}];  ANO1[[All, tly]] = ANO1[[All, tly - 1]]; ANO1[[1, All]] = ANO1[[2, All]];
ANO1; Do[Do[ANO2[[i, j]] = Ani[[i + 1, j]] - 2 * Ani[[i, j]] + Ani[[i - 1, j]],
   {i, 2, tlx - 1}, {j, 2, tly - 1}]]; ANO2[[All, tly]] = ANO2[[All, tly - 1]];
ANO2[[1, All]] = ANO2[[2, All]]; ANO2; ListPlot3D[ANO2]

ANA1 = Table[0, {tlx}, {tly}]; ANA2 = Table[0, {tlx}, {tly}];
Do[Do[ANA1[[i, j]] = (Ani[[i, j + 1]] - Ani[[i, j - 1]]) / 2, {j, 2, tly - 1}], {i, 2, tlx - 1}];
ANA1[[All, tly]] = ANA1[[All, tly - 1]]; ANA1[[1, All]] = ANA1[[2, All]]; ANA1;
Do[Do[ANA2[[i, j]] = (Ani[[i + 1, j]] - Ani[[i - 1, j]]) / 2, {i, 2, tlx - 1}, {j, 2, tly - 1}]];
ANA2[[All, tly]] = ANA2[[All, tly - 1]];
ANA2[[1, All]] = ANA2[[2, All]]; ANA2; ListPlot3D[ANA2]

DIFO1 = Table[0, {tlx}, {tly}]; DIFO2 = Table[0, {tlx}, {tly}];
Do[Do[DIFO1[[i, j]] = (DIF[[i, j + 1]] - DIF[[i, j - 1]]) / 2, {j, 2, tly - 1}], {i, 2, tlx - 1}];
DIFO1[[All, tly]] = DIFO1[[All, tly - 1]]; DIFO1[[1, All]] = DIFO1[[2, All]]; DIFO1;
Do[Do[DIFO2[[i, j]] = (DIF[[i + 1, j]] - DIF[[i - 1, j]]) / 2, {i, 2, tlx - 1}, {j, 2, tly - 1}]];
DIFO2[[All, tly]] = DIFO2[[All, tly - 1]]; DIFO2[[1, All]] = DIFO2[[2, All]]; DIFO2;
```

titer is the number of time iterations used in the model

```
titer = 1597;
```

The diffusion algorithm

The first Do loop excutes the number of iterations (titer) used in the model.
b=c is set which stores the concentration of MgO after every iteration.
The boundary conditions at the crystal rims are set. In this case the concentration at all the rims are set as open and equal the equilibrium concentrations.
The second and third Do loops calculate the modelled profile in both the x and y directions. It contains the finite element formulation for the diffusion coefficient which depends on the gradients in the An profile, and the gradients in the MgO profile. This is based on Equation (7) in Costa et al. (2003).

```
Do [b = c; c[[1, All ]] = 910; c[[All, 1 ]] = 910.; c[[tlx, All]] = 910.; c[[All, tly ]] = 910;
  Do[ Do[c[[i, j]] = b[[i, j]] + (R2 * (DIF[[i, j]] * b[[i, j]] * A / rat * ANO1[[i, j]] +
          (((DIF[[i, j]] * A * (b[[i, j + 1]] - b[[i, j - 1]]) / 2 / rat +
              b[[i, j]] * A * DIFO1[[i, j]] / rat) * ANA1[[i, j]]) +
          DIFO1[[i, j]] * ((b[[i, j + 1]] - b[[i, j - 1]]) / 2) + DIF[[i, j]] *
           (b[[i, j + 1]] - 2 * b[[i, j]] + b[[i, j - 1]])) +
        R1 * (DIF[[i, j]] * b[[i, j]] * A / rat * ANO2[[i, j]] + (((1 / rat DIF[[i, j]] * A *
              ((b[[i + 1, j]] - b[[i - 1, j]]) / 2) + b[[i, j]] * A * (DIFO2[[i, j]]) / rat) *
            ANA2[[i, j]]) + DIFO2[[i, j]] * ((b[[i + 1, j]] - b[[i - 1, j]]) / 2) +
          DIF[[i, j]] * (b[[i + 1, j]] - 2 * b[[i, j]] + b[[i - 1, j]]))),
    {j, 2, tly - 1}] , {i, 2, tlx - 1}], {titer}];
c;
```

The retrieved time from the diffusion model

```
timeinweeks = (titer * δt) / 604 800.
```

```
7.92163
```

A cross section through the modelled profile (x1) at the same location as the EMP traverse.

```
x1 = c[[All, 12]]; x11 = ListPlot[x1,
  PlotRange → {{0, tlx}, {0, 1200}}, Joined → True, PlotStyle → RGBColor[1, 0, 0]]
```

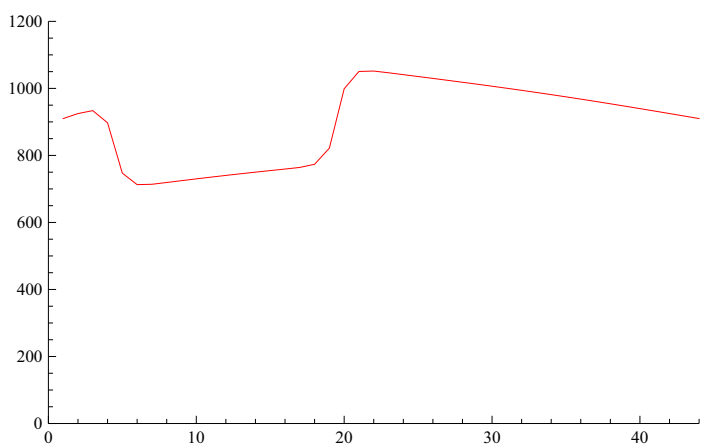

Convert the model (x1), equilibirum profile and inital profile into weight percent and import the plagioclase

MgO profile (mgc).

```
WT = 10 000 * (24 / 40);

cdata = x1; cdata[[All]] = x1[[All]] / WT;

inidata1 = inidata; inidata1[[All]] = inidata[[All]] / WT;

equdata1 = equdata; equdata1[[All]] = equdata[[All]] / WT;

cdatap = ListPlot[cdata, DataRange → {0, 220},
   FrameLabel → {"Distance from rim to rim (μm)", "MgO (wt %)"},
   LabelStyle → {FontFamily -> "Verdana", 12}, PlotRange → {0.0, 0.3}, AxesOrigin → {0, 0},
   Frame → True, Joined → True, PlotStyle → { Thickness [0.01], Black}];

Import[
  "/Users/Kathryngillis/Desktop/Aerona./Desktop/mathmatica/Plagioclase/Mg/SF/Mg4205_5
    poi1.txt", "Table"];

mgc = {{3.710260374`, 0.1517`}, {7.938075099`, 0.153`}, {12.16588982`, 0.1499`},
   {16.39370455`, 0.1366`}, {20.62151927`, 0.1089`}, {24.91914006`, 0.1069`},
   {29.04224569`, 0.1114`}, {33.16535131`, 0.1164`}, {37.63748727`, 0.1063`},
   {41.76059289`, 0.1103`}, {46.23272885`, 0.1126`}, {49.39500651`, 0.1164`},
   {53.86714246`, 0.1267`}, {57.99024809`, 0.1247`}, {62.11335372`, 0.1263`},
   {66.58548967`, 0.1235`}, {70.7085953`, 0.1278`}, {75.18073125`, 0.1242`},
   {78.34300891`, 0.1121`}, {82.46611454`, 0.1205`}, {86.93825049`, 0.1265`},
   {91.06135612`, 0.1525`}, {95.53349207`, 0.1547`}, {99.6565977`, 0.1514`},
   {104.1287337`, 0.1555`}, {107.2910113`, 0.1645`}, {111.4141169`, 0.1701`},
   {115.8862529`, 0.169`}, {120.0093585`, 0.1721`}, {124.4814945`, 0.1736`},
   {128.6046001`, 0.1724`}, {133.0767361`, 0.1744`}, {137.1998417`, 0.1736`},
   {140.3621193`, 0.1777`}, {144.8342553`, 0.1746`}, {148.9573609`, 0.1761`},
   {153.4294969`, 0.1721`}, {157.5526025`, 0.1753`}, {162.0247385`, 0.1721`},
   {166.1478441`, 0.1693`}, {169.3101217`, 0.1668`}, {173.7822577`, 0.1749`},
   {177.9053633`, 0.164`}, {182.3774993`, 0.165`}, {186.5006049`, 0.1655`},
   {190.6237105`, 0.1648`}, {195.0958465`, 0.1605`}, {198.2581241`, 0.1631`},
   {202.7302601`, 0.1597`}, {206.8533657`, 0.159`}, {211.3255017`, 0.1565`},
   {215.4486073`, 0.1578`}, {219.5717129`, 0.1549`}, {223.8693337`, 0.1612`}};

padding = {{50, 50}, {50, 50}};

data =
  ListPlot[mgc, PlotRange → {0.001, 0.3}, PlotStyle → {RGBColor[1, 0, 0], PointSize[0.02]},
   ImageSize -> {300, 300}, ImagePadding → padding];

inidatap = ListPlot[inidata1, DataRange → {0, 220},
   Joined → True, PlotStyle → { Thickness [0.005], RGBColor[0, 1, 0]}];

equdatap = ListPlot[equdata1, DataRange → {0, 220},
   Joined → True, PlotStyle → { Thickness [0.005], RGBColor[0, 0, 1]}];
```

Plot showing the model (mod) with the MgO data and the initial and equilibrium profile.

```
Pl1poi =
 Show[cdatap, data, equdatap, inidatap, ImageSize -> {300, 300}, ImagePadding → padding]
```

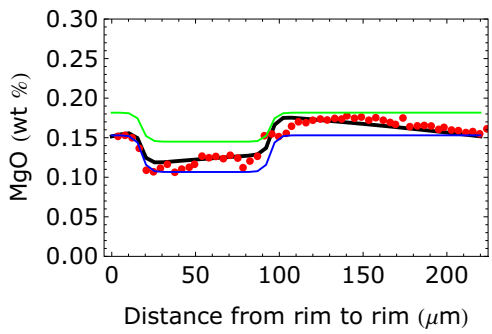

A.6.3: A 1D diffusion plus crystal growth model: Plagioclase

The 1D diffusion model that incorporates crystal growth was used to model the MgO profile in the high anorthite resorbed plagioclase from the Southern Fissure (Section 2.6.2.2.1).

****

Appendix A.6.3: Example of a 1D diffusion plus growth model
A program to model Mg diffusion and growth in one dimension in plagioclase 4205_3 Pl3 from the Southern Fissure. The model assumes the crystal has undergone two growth phases. A core grows from melt 1 containing ~6.3 wt % MgO. The plagioclase is mixed into melt 2 containing ~ 4.3 wt % MgO, and grows a lower Mg rim (rim1). Diffusion of Mg occurs between the core and rim 1 over a period of ~5 weeks as it attemps to internally homogenise. The crystal is then introduced to melt 3 containing ~ 6.3 wt % MgO melt where is grows a higher Mg rim (rim2). Diffusion of Mg occurs between rim1 and rim2 over a period of ~3 weeks.

****

The variables below are 'cleared' to avoid complications from previous values and definitions being associated with them.

In[6028]:=
```
Clear[An1, An2, C10, C20, D1, D2, s, c, f, g, h, r, δx, δt,
 T, t, equi1, equi2, k, AN, ANx, p, j, ceq1, ceq2, ceq3]
```

Temperature (T) is in celsius. The diffusion coefficient for Mg (D1) is in $\mu m^2 s^{-1}$ and is taken from LaTourette and Wasserburg (1998).

Choose a distance step (δx) in microns and a time step (δt) is in seconds. Note, the stability criteria for the explicit method is R*D1 < 0.5.
The variable tf is the number of points in the plagioclase transect, therefore the total length of the transect (s) will equal δx * tf.
The total time for the diffusion model will be δt * ttiter, where ttiter is the number of time iterations used in the model, see below.
A and r are parameters used in the diffusion model below.

In[6029]:= $T = 1200.;$

In[6030]:= $D1 = \left(1.2 * 10^{-6} * \mathrm{Exp}\left[\frac{-266.}{(T + 273.) * 8.3144 * 10^{-3.}}\right]\right) * 10^{12}$

Out[6030]= 0.000443162

In[6031]:= $\delta x = 5.385;\ \delta t = 0.6 * 10\hat{}4;\ R1 = \frac{\delta t}{\delta x^2} D1$

Out[6031]= 0.0916943

In[6032]:= $R = \frac{\delta t}{\delta x^2}$

Out[6032]= 206.909

In[6033]:= $A = 26.1;\ r = 8.314 * 10^{-3.} * (T + 273.);$

In[6034]:= $tf = 127;\ s = 665;$

Import the MgO profile in a text file. Assign the profile to “mgc”

In[6035]:=
```
Import[
  "/Users/Laurencecoogan/Desktop/mathmatica/timescales-4205-3pl3/
    Mg4205_3(1).txt", "Table"];
```

Import::nffil : File not found during Import. ≫

In[6036]:=
```
mgc = {{1, 0.15`}, {2, 0.15`}, {3, 0.15`}, {4, 0.15`}, {5, 0.15`}, {6, 0.15`}, {7, 0.1594996`},
   {8, 0.1522044`}, {9, 0.1377798`}, {10, 0.1462356`}, {11, 0.1422564`}, {12, 0.1432512`},
   {13, 0.1468988`}, {14, 0.1454066`}, {15, 0.1555204`}, {16, 0.1487226`}, {17, 0.144246`},
   {19, 0.145904`}, {20, 0.1478936`}, {21, 0.1480594`}, {22, 0.155023`}, {23, 0.1523702`},
   {24, 0.155852`}, {25, 0.1522044`}, {26, 0.1464014`}, {27, 0.1472304`}, {28, 0.1546914`},
   {29, 0.150878`}, {30, 0.1460698`}, {31, 0.1419248`}, {32, 0.138443`}, {33, 0.1162258`},
   {34, 0.1024644`}, {35, 0.1099254`}, {36, 0.1057804`}, {37, 0.0958324`}, {38, 0.0935112`},
   {39, 0.1071068`}, {40, 0.1056146`}, {41, 0.110257`}, {42, 0.1173864`}, {43, 0.1115834`},
   {44, 0.106941`}, {45, 0.1099254`}, {46, 0.0925164`}, {47, 0.0863818`}, {48, 0.0964956`},
   {49, 0.0916874`}, {50, 0.0913558`}, {51, 0.0958324`}, {52, 0.0948376`}, {53, 0.0948376`},
   {54, 0.0901952`}, {55, 0.093677`}, {56, 0.0896978`}, {57, 0.0933454`}, {58, 0.092019`},
   {59, 0.092019`}, {60, 0.0898636`}, {61, 0.0882056`}, {62, 0.0946718`}, {63, 0.0926822`},
   {64, 0.0916874`}, {65, 0.0931796`}, {66, 0.094506`}, {67, 0.0923506`}, {68, 0.1024644`},
   {69, 0.0996458`}, {70, 0.0950034`}, {71, 0.098651`}, {73, 0.1034592`}, {74, 0.1031276`},
   {75, 0.1037908`}, {76, 0.1013038`}, {77, 0.1006406`}, {78, 0.101967`}, {79, 0.1059462`},
   {80, 0.1099254`}, {81, 0.1084332`}, {82, 0.1100912`}, {83, 0.1203708`}, {84, 0.1192102`},
   {85, 0.1188786`}, {86, 0.1165574`}, {87, 0.1245158`}, {88, 0.1291582`}, {89, 0.1344638`},
   {90, 0.13264`}, {91, 0.1402668`}, {92, 0.1440802`}, {93, 0.1381114`}, {94, 0.1362876`},
   {95, 0.1379456`}, {96, 0.1356244`}, {97, 0.1288266`}, {98, 0.1278318`}, {99, 0.129324`},
   {100, 0.1298214`}, {101, 0.1372824`}, {102, 0.1386088`}, {103, 0.1291582`},
   {104, 0.1344638`}, {105, 0.1338006`}, {106, 0.135956`}, {107, 0.1372824`},
   {108, 0.1369508`}, {109, 0.1344638`}, {110, 0.1357902`}, {111, 0.1371166`},
   {112, 0.1429196`}, {113, 0.14922`}, {114, 0.1497174`}, {115, 0.1432512`},
   {116, 0.143417`}, {117, 0.1386088`}, {118, 0.134298`}, {119, 0.1387746`},
   {120, 0.1397694`}, {121, 0.1470646`}, {122, 0.1349612`}, {123, 0.1344638`},
   {124, 0.1289924`}, {125, 0.1273344`}, {126, 0.1289924`}, {127, 0.131811`}};
```

Plot the MgO data

In[6037]:=
```
data = ListPlot[mgc, PlotRange → {0.001, 0.35},
  PlotStyle → {RGBColor[1, 0, 0], PointSize[0.02]}]
```

Out[6037]=

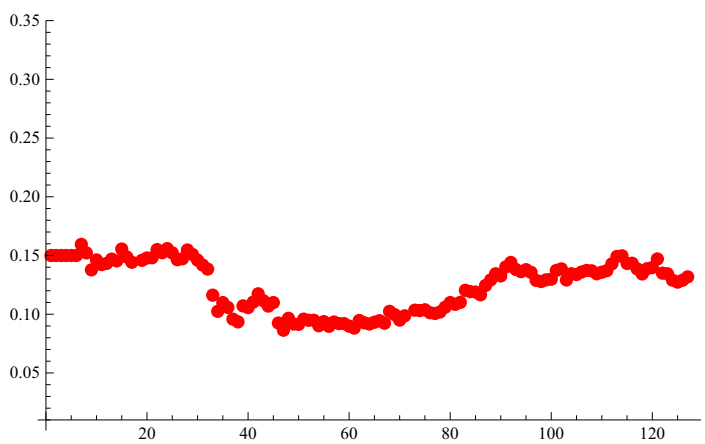

Import the Anorthite (An) profile in a text file. Assign the profile to “An”

In[6038]:=
```
Import["/Users/Kathryngillis/Desktop/Aerona./Desktop/mathmatica/
    Plagioclase/Mg/SF/timescales-4205-3pl3/An4205_3(1).txt",
  "Table"];
```

In[6039]:=
```
An = {{1, 88}, {2, 88}, {3, 88}, {4, 88}, {5, 88}, {6, 88}, {7, 87.18959431`},
   {8, 87.52812293`}, {9, 87.66094342`}, {10, 87.93203488`}, {11, 88.36871114`},
   {12, 87.39995192`}, {13, 86.75427719`}, {14, 87.40772408`}, {15, 87.59870092`},
   {16, 87.10112623`}, {17, 87.95781191`}, {18, 88.03498915`}, {19, 87.89668435`},
   {20, 87.35147658`}, {21, 87.40520549`}, {22, 87.62114204`}, {23, 87.62281657`},
   {24, 87.840521`}, {25, 87.69940168`}, {26, 87.84597383`}, {27, 88.04384397`},
   {28, 87.57929282`}, {29, 87.53637496`}, {30, 87.83046416`}, {31, 89.12513352`},
   {32, 91.30905217`}, {33, 92.54311593`}, {34, 91.04226832`}, {35, 91.57705418`},
   {36, 92.53999538`}, {37, 92.14040726`}, {38, 91.59800222`}, {39, 90.93596343`},
   {40, 91.299772`}, {41, 91.25911619`}, {42, 90.64672955`}, {43, 91.39960063`},
   {44, 92.12584499`}, {45, 92.55721534`}, {46, 93.09269389`}, {47, 93.31109707`},
   {48, 93.86098749`}, {49, 93.07863864`}, {50, 92.59599392`}, {51, 93.27100088`},
   {52, 93.00461856`}, {53, 93.50664748`}, {54, 93.27094838`}, {55, 93.81166162`},
   {56, 93.59332102`}, {57, 92.27202758`}, {58, 93.4209693`}, {59, 93.36549604`},
   {60, 93.43649202`}, {61, 93.02245281`}, {62, 92.96651393`}, {63, 93.31604941`},
   {64, 92.6313807`}, {65, 93.02987742`}, {66, 92.87292648`}, {67, 92.48625686`},
   {68, 93.32417952`}, {69, 92.93257707`}, {70, 92.46232133`}, {71, 92.4363784`},
   {72, 92.31312819`}, {73, 91.9942297`}, {74, 92.40494057`}, {75, 91.92305`},
   {76, 92.05451271`}, {77, 92.61022148`}, {78, 91.7550584`}, {79, 91.99806747`},
   {80, 91.40747417`}, {81, 91.85679475`}, {82, 90.50483768`}, {83, 90.54133102`},
   {84, 91.89449433`}, {85, 91.39606963`}, {86, 90.09376182`}, {87, 90.36830934`},
   {88, 90.11711369`}, {89, 89.74701715`}, {90, 89.03315817`}, {91, 89.60517365`},
   {92, 89.97922444`}, {93, 90.81982025`}, {94, 90.57870873`}, {95, 90.74471127`},
   {96, 91.61372723`}, {97, 91.04740936`}, {98, 91.11905326`}, {99, 90.25186481`},
   {100, 90.59780327`}, {101, 91.39651497`}, {102, 91.30767139`}, {103, 91.11129321`},
   {104, 90.80994747`}, {105, 90.33267873`}, {106, 90.9456601`}, {107, 90.55992813`},
   {108, 91.23918287`}, {109, 91.09531802`}, {110, 90.42236747`}, {111, 90.51169526`},
   {112, 90.7694295`}, {113, 91.05443345`}, {114, 90.18836473`}, {115, 89.87023183`},
   {116, 91.22670988`}, {117, 91.06625152`}, {118, 90.71935091`}, {119, 91.20020063`},
   {120, 91.06951805`}, {121, 90.80803404`}, {122, 91.93665177`}, {123, 92.17912957`},
   {124, 90.710552`}, {125, 91.08721639`}, {126, 90.79607098`}, {127, 90.87109438`}};
```

Plot the An data.

In[6040]:=
```
ListPlot[An, PlotRange → {70, 100}]
```

Out[6040]=

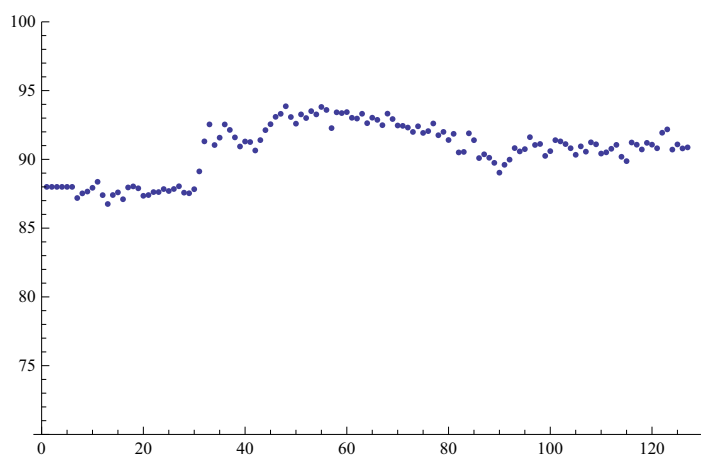

- Graphics -

Convert the Anorthite data to mole fraction.
Determine the diffusion coefficient (DIF) at each point.

The An profile is them smoothed slightly using the diffusion model to remove sharp concentration changes. This will reduce any artifical aritifacts from the spacial resolution of the EMP analyses.

In[6041]:=
```
AN = An[[All, 2]]; AN = An[[All, 2]] / 100.; An;
```

In[6042]:=
```
AN[[tf]] = AN[[tf - 1]] = AN[[tf - 2]] = AN[[tf - 3]];
```

In[6043]:=
```
DIF = Table[0., {tf}];
Do[DIF[[i]] = (1.2 * 10^-6 * Exp[-266. / ((T + 273.) * 8.3144 * 10^-3.)]) * 10^12,
  {i, 1, tf}]; ListPlot[DIF];
```

In[6044]:=
```
Do[ANx = AN;
 Do[AN[[i]] = ANx[[i]] + R DIF[[i]] (ANx[[i + 1]] - 2 ANx[[i]] + ANx[[i - 1]]),
  {i, 2, tf - 1}], {5}]; ListPlot[AN, Joined → True]
```

Out[6044]=

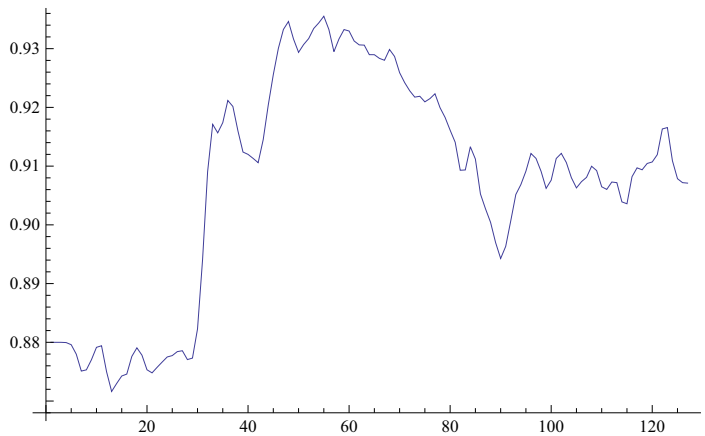

Define the partition coefficient (K). Here the partition coefficient of Mg in plagioclase is taken from Equation (1) in Section 2.4.2.3

In[6045]:=
```
K = Exp[(-21 800 * AN - 26 300) / (8.314 * (T + 273.))];
```

The equilibrium (ceq) profiles are calculated using the parition coefficient of Mg and the plagioclase An profile.
The core is in equilibrium with a 6.3 wt % MgO melt (ceq1)
Rim 2 is in equilibrium with a 4.3 wt % MgO melt (ceq2).
Rim 1 is in equilibrium with a 6.3 wt % MgO melt (ceq3).

In[6046]:=
```
ceq1 = Table[0, {tf}]; Do[ceq1[[i]] = 6.3` K[[i]], {i, 85, tf}];
equi1 = ListPlot[ceq1, Joined → True,
  PlotStyle → {Thickness[0.005`], RGBColor[0, 1, 0]}];
```

In[6047]:=
```
ceq2 = Table[0, {tf}]; Do[ceq2[[i]] = 4.3` K[[i]], {i, 31, 84}];
equi2 = ListPlot[ceq2, Joined → True,
  PlotStyle → {Thickness[0.005`], RGBColor[0, 0, 1]}];
```

In[6048]:=
```
ceq3 = Table[0, {tf}]; Do[ceq3[[i]] = 6.3` K[[i]], {i, 31}];
equi2 = ListPlot[ceq2, Joined → True, PlotStyle → {Thickness[0.005`], RGBColor[0, 0, 1]}];
```

Parameters required for the diffusion model.
ANA and ANO take into account Mg diffusion being driven by the change in An content, and DIFO takes into account Mg diffusion being driven by the change in MgO content.

In[6049]:=
```
ANO = Table[0, {tf}];
```

In[6050]:=
```
Do[ANO[[i]] = AN[[i + 1]] - 2 * AN[[i]] + AN[[i - 1]], {i, 2, tf - 1}]; ANO;
```

In[6051]:=
```
DIFO = Table[0, {tf}];
Do[DIFO[[i]] = ((DIF[[i + 1]] - DIF[[i - 1]]) / 2), {i, 2, tf - 1}]; DIFO;
```

In[6052]:=
```
ANA = Table[0, {tf}];
Do[ANA[[i]] = ((AN[[i + 1]] - AN[[i - 1]])) / 2, {i, 2, tf - 1}]; ANA;
```

****

The following model incorporates diffusion and crystal growth.
The model is split into two stages, the first involves growth of rim 1 from a 4.3 wt % MgO melt. Diffusion occurs at the core-rim1 boundary.
The second stage involves growth of rim 2 from a 6.3 wt % melt. Diffusion occurs at the rim1-rim2 boundary, and continues at the the core-rim1 boundary.

****

1. Growth of rim1 + diffusion

ttiter is the number of iterations used in this first stage of the model

In[6053]:=
```
titer1 = 520;
```

The diffusion plus growth algorithm

The first Do loop excutes the number of iterations (titer) used in the model.

The boundary conditions at the crystal rims are set.
For the growth model the boundary condition on the right side of profile (tf), i.e. the core, is set to equal ceq1 (in equilibrium with a 6.3 wt % mgO melt).
The boundary condition on the left side is set to increase by 10 distance steps every 10 iterations begining at point 85. This will imitate growth of rim 1 from the core (growth progress is right to left). Rim 1 is set to equal ceq2 (in equilibrium with a 4.3 wt % MgO melt). Diffusion occurs between the core and rim 2 during growth.

b=c is set which stores the concentration of MgO after every iteration.
The second Do loop calculates the modelled profile and contains the finite element formulation for the diffusion coefficient which depends on the gradients in the An profile, and the gradients in the MgO profile. This is based on Equation (7) in Costa et al. (2003).

In[6054]:=
```
c = ceq1;
```

In[6055]:=
```
Do[(c[[Ceiling[85 - (j / 10)]]] = ceq2[[32]];
    c[[tf]] = ceq1[[tf]]; b = c; Do[c[[i]] =
      b[[i]] + R * (((DIF[[i]] * b[[i]] * A / r) * ANO[[i]]) + ((1/r DIF[[i]] * A *
            ((b[[i + 1]] - b[[i - 1]]) / 2) + (b[[i]] * A * DIFO[[i]] / r)) *
          ANA[[i]]) + (DIFO[[i]] * ((b[[i + 1]] - b[[i - 1]]) / 2)) +
        DIF[[i]] * (b[[i + 1]] - 2 * b[[i]] + b[[i - 1]])),
     {i, j + 1, tf - 1}]), {j, 10, titer1}];

c;
```

Plot of the modelled profile (black) and the MgO data (red)

In[6057]:=
```
mod = ListPlot[c, PlotRange → {0.02, 0.3`}, AxesOrigin → {0, 0},
  Frame → True, PlotStyle → {Black}]; Show[mod, data]
```

Out[6057]=

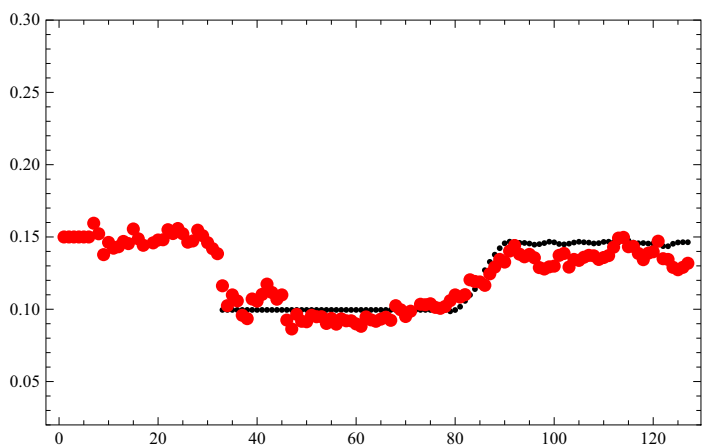

The retrieved time from the first stage

In[6058]:=
```
(titer1 * δt)
```

Out[6058]= 3.12×10^{6}

In[6059]:=
```
timetotalweeks1 = (titer1 * δt) / 604 800
```

Out[6059]= 5.15873

2. Growth of rim 2 + diffusion

A similar diffusion plus growth model as in Stage 1. Here the left boundary (rim2) is set to increase by 10 distance steps every 10 iterations from point 33. This will imitate growth of rim 2 from the first rim (growth is

right to left).
The boundary at rim2 is set to equal ceq3 (in equilibrium with a 6.3 wt % MgO melt). Diffusion of Mg occurs during growth.

In[6060]:=
```
titer3 = 320;
```

In[6061]:=
```
Do[(c[[Ceiling[33 - (j / 10)]]] = ceq3[[1]];
    c[[tf]] = c[[tf]]; b = c; Do[c[[i]] =
      b[[i]] + R * (((DIF[[i]] * b[[i]] * A / r) * ANO[[i]]) + (((1/r) DIF[[i]] * A *
                ((b[[i + 1]] - b[[i - 1]]) / 2) + (b[[i]] * A * DIFO[[i]] / r)) *
            ANA[[i]]) + (DIFO[[i]] * ((b[[i + 1]] - b[[i - 1]]) / 2)) +
          DIF[[i]] * (b[[i + 1]] - 2 * b[[i]] + b[[i - 1]])),
     {i, j + 1, tf - 1}]), {j, 10, titer3}];

c;
```

Plot of the modelled profile (black) and the MgO data (red)

In[6063]:=
```
mod = ListPlot[c, PlotRange → {0, 0.3`},
  AxesOrigin → {0, 0}, Frame → True, Joined → True,
  PlotStyle → {Thickness[0.01`], Black}]; Show[mod, data]
```

Out[6063]=

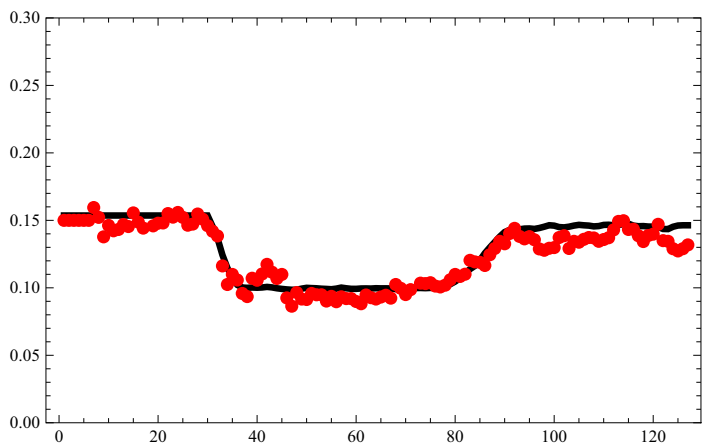

- Graphics -

The retrieved time from the second stage

In[6064]:=
```
timetotalweeks3 = (titer3 * δt) / 604 800
```

Out[6064]= 3.1746